ADAPTIVE WING STRUCTURES FOR AEROELASTIC DRAG REDUCTION AND LOADS ALLEVIATION

A thesis submitted to the University of Manchester for the degree of Doctor of Philosophy in the Faculty of Engineering and Physical Sciences

September 2010

By

Simon J. Miller

School of Mechanical, Aerospace and Civil Engineering

Contents

Final word count: 63,310

List of Tables

List of Figures

Nomenclature

The following is a non-exhaustive list of letters and symbols appearing throughout the thesis. Upper and lower case normal letters and symbols indicate a scalar, bold lower case letters and symbols indicate a vector, and bold upper case letters and symbols indicate a matrix.

$\mathbf{A}$	=	structural inertia matrix
A	=	cross-sectional area of spar, cross-sectional area of wing
$\mathbf{A}_r$	=	aerodynamic disturbance matrix
$\mathbf{a}_r$	=	aerodynamic disturbance vector
a_W	=	lift curve slope
$\mathbf{AIC}_R$	=	matrix of Aerodynamic Influence Coefficients
$\mathbf{AIC}_R^*$	=	reduced matrix of Aerodynamic Influence Coefficients
AIC	=	Aerodynamic Influence Coefficient
$\mathbf{B}$	=	aerodynamic damping matrix
b	=	semi-span of the wing
b_s	=	spar thickness
$\hat{b}$	=	spanwise width of an aerodynamic panel
$\mathbf{C}$	=	aerodynamic stiffness matrix, calibration matrix
C	=	cost/objection function
C_D	=	wing drag coefficient
C_{D_i}	=	wing induced drag coefficient
C_L	=	wing lift coefficient

$\mathbf{c}$	=	vector of circulation strengths of the aerodynamic panels
c	=	wing chord
c_l	=	sectional lift coefficient
$\mathbf{D}$	=	structural damping matrix
d_s	=	spar height
$\mathbf{D}^T$	=	elastic stress-strain operator matrix
D_i	=	induced drag, bearing inner-diameter
$\bar{D}$	=	drag per unit span
$\bar{D}_i$	=	induced drag per unit span
$\mathbf{E}$	=	structural stiffness matrix
E	=	Young's modulus
e	=	distance of elastic axis aft of the aerodynamic centre as a fraction of c
e_O	=	Oswald efficiency factor
$\mathbf{F}$	=	matrix of shape functions
F_i	=	shape function
$\bar{\mathbf{f}}$	=	force per unit length of circulation
f	=	distance of forward spar aft of leading-edge as a fraction of c, natural frequency
f_F	=	flutter frequency
$\mathbf{f}^B$	=	body forces field
$\mathbf{f}^S$	=	surface forces field
G	=	shear modulus
h	=	bending displacement
$\mathbf{I}$	=	identity matrix
I	=	second moment of area about a chordwise axis
I_{xx}	=	polar second moment of area
I_{yy}	=	second moment of area about y-axis
I_{zz}	=	second moment of area about z-axis

$\mathbf{i}$	=	unit vector in the x-direction
J	=	St. Venant torsion constant
$\mathbf{j}$	=	unit vector in the y-direction
k	=	tip device attachment torsional stiffness
K_h	=	flexural rigidity of the wing
k_β	=	torsional stiffness of a rib
K_θ	=	torsional rigidity of the wing
L	=	lift, gene length
l	=	spar length, length of wing
$\bar{L}$	=	lift per unit span
$\bar{\mathbf{l}}$	=	vector of lift per unit span of the aerodynamic panels
L_g	=	gust length
M	=	moment exerted on a rib by a spar, pitching moment
$\bar{M}$	=	pitching moment per unit span about the aerodynamic centre
M_D	=	aerodynamic efficiency effectiveness parameter
M_L	=	lift effectiveness parameter
$M_{\dot{\theta}}$	=	unsteady pitching moment aerodynamic derivative
$\bar{m}_W$	=	mass per unit length of wing
$\bar{\bar{m}}_W$	=	mass per unit area of wing
N_i	=	number of increments
N_{iter}	=	number of iterations
N_{rib}	=	number of ribs
$\mathbf{n}$	=	unit normal vector
P	=	penalty function, load
$\mathbf{p}$	=	load vector
p	=	aeroelastic eigenvalue
p_c	=	probability of crossover
p_m	=	probability of mutation
$\mathbf{q}$	=	vector of generalised coordinates

Q_i	=	generalised forces
q	=	dynamic pressure
q_c	=	distance of aerodynamic centre aft of leading-edge as a fraction of c
q_d	=	divergence dynamic pressure
q_i	=	generalised coordinate
$\mathbf{r}$	=	vector from the midpoint of the vortex segment to point in space
r	=	distance of rear spar aft of leading-edge as a fraction of c, length of vector $\mathbf{r}$
S	=	wing area
s	=	semi-span of the wing
$d\mathbf{s}$	=	vector describing an infinitesimally small segment of a closed curve of fluid velocity
ds	=	length of vector $d\mathbf{s}$
$\mathbf{T}$	=	transformation matrix
T	=	kinetic energy, period
t	=	time, aerofoil thickness as a percentage of c
U	=	air velocity, strain energy, potential energy
U_d	=	divergence speed
U_F	=	flutter speed
U_∞	=	free-stream velocity
δU	=	virtual strain energy
$\mathbf{u}$	=	displacement field, velocity field
u	=	displacement
$\delta\mathbf{u}$	=	virtual displacement field
V	=	wing volume, spar volume, voltage
$\mathbf{v}$	=	vector of voltages
$\delta^* W$	=	virtual work

$\mathbf{w}$	=	induced velocity field, vector of downwashes of the aerodynamic panels
w	=	downwash velocity
w_g	=	gust velocity
x	=	Cartesian coordinate
$\bar{Y}$	=	side force per unit span
y	=	Cartesian coordinate
z	=	Cartesian coordinate
$\boldsymbol{\alpha}$	=	vector of angles of incidence of the aerodynamic panels
α	=	angle of incidence
α_e	=	elastic angle of incidence
α_i	=	induced angle of incidence
$\boldsymbol{\alpha}_r$	=	vector of rigid/wind-off angles of incidence
α_r	=	rigid/wind-off angle of incidence
$\boldsymbol{\beta}$	=	vector of rear spar bending generalised coordinates, vector of wing torsion generalised coordinates
β_b	=	rear spar bending generalised coordinate, wing torsion generalised coordinate
$\Delta\beta$	=	torsional deformation of a rib between two spars
Γ	=	circulation/vortex strength
$\boldsymbol{\gamma}$	=	circulation field
γ	=	rotation/pitch of wing tip device
$\delta\boldsymbol{\varepsilon}$	=	virtual strain field
$\boldsymbol{\zeta}$	=	vector of forward spar bending generalised coordinates, vector of wing bending generalised coordinates
ζ	=	negative damping
ζ_a	=	forward spar bending generalised coordinate, wing bending generalised coordinate
$\boldsymbol{\eta}$	=	vector of generalised coordinates

$\delta\boldsymbol{\eta}$	=	vector of virtual generalised coordinates
θ	=	torsional displacement
Λ	=	wing sweep angle
λ	=	eigenvalue
ν	=	Poisson's ratio
ξ	=	wing geometric dimensionless grouping
ρ	=	air density
ρ_W	=	wing density
$\boldsymbol{\sigma}$	=	stress field
σ	=	stress
τ	=	pulse-width
$\boldsymbol{\Upsilon}$	=	matrix of modified shape functions
$\boldsymbol{\upsilon}$	=	vector of modified shape functions
$\boldsymbol{\phi}$	=	vector of rear spar bending shape functions, vector of wing torsion shape functions
$\boldsymbol{\Phi}^*$	=	matrix of modified rear spar bending shape functions
$\boldsymbol{\phi}^*$	=	vector of modified rear spar bending shape functions
ϕ_b	=	rear spar bending shape function, wing torsion shape function
ϕ_f	=	angle between chordline and the principal axis z' of the forward spar
ϕ_r	=	angle between chordline and the principal axis z' of the rear spar
$\boldsymbol{\Psi}$	=	matrix of influence coefficients
$\boldsymbol{\psi}$	=	vector of forward spar bending shape functions, vector of wing bending shape functions
Ψ	=	influence coefficient
$\boldsymbol{\Psi}^*$	=	matrix of modified forward spar bending shape functions
$\boldsymbol{\psi}^*$	=	vector of modified forward spar bending shape functions
ψ_a	=	forward spar bending shape function, wing bending shape function

$\mathbf{\Omega}$	=	matrix of modified shape functions
$\boldsymbol{\omega}$	=	vorticity field
ω	=	natural frequency
Æ	=	aspect ratio of the wing
∇	=	curl

Subscripts

ac	=	property defined at/about the aerodynamic centre
conv	=	converged value
D	=	property associated with the tip device
e	=	property associated with the elastic axis
h	=	property associated with bending displacement
initial	=	initial value
j	=	integer to distinguish between spars
k	=	integer to distinguish between spanwise sections of a spar
LE	=	property defined at the leading-edge
max	=	maximum
min	=	minimum
p	=	integer to distinguish between aerodynamic panels
panel	=	property associated with an aerodynamic panel
ref	=	reference/target value
s	=	spar property
TE	=	property defined at the trailing-edge
tip	=	property defined at the wing tip
W	=	property associated with the main wing
β	=	property associated with torsional displacement of a rib
γ	=	property associated with the tip device attachment
θ	=	property associated with torsional displacement about a spanwise axis

Adaptive wing structures for aeroelastic drag reduction and loads alleviation

A thesis submitted to the University of Manchester for the degree of Doctor of Philosophy

September 2010

Simon J. Miller

Abstract

An investigation into two distinct novel adaptive structures concepts is performed with a view to improving the aerodynamic efficiency of aircraft wings.

The main focus of the work is on the development of a rotating spars concept that enables the adaptive aeroelastic shape control of aircraft wings in order to reduce drag. By altering the orientation of the internal wing structure, it becomes possible to control the flexural and torsional stiffnesses of the wing, as well as the position of the elastic axis. It follows then that control of the aeroelastic deformation is also possible. Consequently, the aerodynamic performance can be tailored, and more specifically the lift-to-drag ratio can be maximised through continuous adjustment of the structure.

To gain a thorough understanding of the effect of the concept on a wing, an assumed modes static aeroelastic model is developed, and studies are performed using this. These studies establish guidelines with regards to the effective design of a wing incorporating the rotating spars concept. The findings of these studies are then used to establish a baseline design for a wind tunnel model. A finite element model of this is constructed and aeroelastic analyses are used to improve the model and arrive at the final experimental wing design. The wind tunnel tests confirm analytical trends and the robustness of an approach to automatically adapt the structure to maintain an aerodynamic performance objective.

The remainder of the work investigates the application of an all-moving wing tip device with an adaptive torsional stiffness attachment as a passive loads alleviation system. Through consideration of the attachment stiffness and position, it is possible to tune the device throughout flight in order to minimise the loads that are introduced into the aircraft structure in response to a gust or manoeuvre.

A dynamic aeroelastic wing model incorporating the device is developed and used to perform parameter studies; this gives an insight into the sizing and placement of the device. Next, a finite element representation of a conceptual High Altitude Long Endurance (HALE) aircraft is used as a baseline platform for the device. Aeroelastic analyses are performed for the baseline and modified models to investigate the effect of the attachment stiffness and position on the gust response and aeroelastic stability of the system. The reduced loading within the structure of the modified aircraft then enables the model to be optimised in order to reduce the mass of the aircraft.

Declaration

No portion of the work referred to in this thesis has been submitted in support of an application for another degree or qualification of this or any other university or other institute of learning.

Copyright

Copyright in text of this thesis rests with the author. Copies (by any process) either in full, or of extracts, may be made **only** in accordance with instructions given by the author and lodged in the John Rylands University Library of Manchester. Details may be obtained from the librarian. This page must form part of any such copies made. Further copies (by any process) of copies made in accordance with such instructions may not be made without the permission (in writing) of the author.

The ownership of any intellectual property rights which may be described in this thesis is vested in the University of Manchester, subject to any prior agreement to the contrary, and may not be made available for use by third parties without the written permission of the University, which will prescribe the terms and conditions of any such agreement.

Further information on the conditions under which disclosures and exploitation may take place is available from the head of the Department of Mechanical, Aerospace and Civil Engineering.

In loving memory of my dad

Acknowledgements

I would like to thank my supervisor Prof. Jonathan Cooper for his guidance throughout. Special mention goes to Dr. Gareth Vio for his time and assistance as I was getting to grips with the software; his incredible patience and good nature aided me immensely as there was never a minute when he was too busy to help. Thanks to Dr. Richard Gardner for being there to think out loud to.

Many thanks for the support of the technical staff, in particular, Stuart McIntyre for his patience while manufacturing the test wing, Dave Golding for his help setting up test rigs and all the other odd jobs he got roped in to do, Dr. Andrew Kennaugh for his assistance and opinions during the tests, and last but not least, Michael Carroll, for his friendly, approachable and diplomatic nature which made experimental work less stressful and easier. I would also like to acknowledge the guidance and assistance of Prof. Jan Wright and Dr. William Crowther, and the contribution of the Engineering and Physical Sciences Research Council.

Failure to mention the contribution of my parents would be unjust; without their support and encouragement I undoubtedly would have achieved less in life. In particular, my dad's interest and enthusiasm for aviation clearly influenced my career path; despite serious illness midway through my project, his interest in my work never waned until his untimely passing one year ago. Perhaps final mention should be reserved for Mhairi, who had to endure several lonely years while I was working. However, her real moment of truth came during a long summer of testing when she supplied me with an endless chain of homemade snacks and refreshments.

Chapter 1

Introduction

1.1 Background and motivation

Since the early days of flight, the ability of aircraft to adapt to different conditions has been an integral part of the design process. Improving the performance, expanding the flight envelope, increasing capabilities and reducing operating costs require this philosophy. This adaptive technology is evident on almost all examples of aircraft throughout history; the Wright brothers overcame the lack of lateral stability in their Wright Flyer by adapting the twist of the wings to achieve lateral control [15]. This function is performed in most modern aircraft via ailerons, hinged devices that alter the camber of the wing. Similarly, most aircraft employ trailing-edge flaps which are capable of altering the wing camber and area to enable low speed operation, whilst degrading high speed flight performance very little [138]. The increase in activity in the past two decades in the research and development of unconventional aircraft adaptability has led to the term 'morphing' being used to describe this technology [21, 88].

Within the aeronautics community, there is no agreement on the exact definition of morphing [88], with some arguing that it involves large seamless shape changes, and others saying that it must use smart materials and structures technology. Perhaps the less specific definition proposed by Wlezien et al. [139] under

NASA's Morphing project is more useful:

Morphing is efficient, multi-point adaptability and includes macro, micro, structural and/or fluidic approaches.

Further to that, the NATO Research and Technology Organization, Applied Vehicle Technology technical team on morphing vehicles (AVT-168) [88] proposed a similar definition which also addresses the end objective:

Morphing is real-time adaptation to enable multi-point optimized performance.

Despite the lack of a clear definition, most researchers agree on the objective of morphing, and this is mentioned in the latter definition provided above; the primary aim of morphing technologies is to enable aircraft to perform at close to optimum conditions at more than a single point within the flight envelope, even (and especially) if these conditions impose contradictory requirements on the performance [138].

Most aircraft are designed to have optimum aerodynamic characteristics at a single point and fuel condition in the flight envelope. However, the fuel loading and distribution changes throughout flight [21, 95], and aircraft frequently have to fly at sub-optimal conditions for a variety of reasons including take-off and landing configurations and air traffic control restrictions [121]. Additionally, the conventional aircraft configuration that is commonplace today not only performs poorly at off-design points in its flight envelope, but also is typically incapable of operating at all in roles far removed from this design point due to the conflicting performance requirements.

However, in the last couple of decades there has been an effort to tackle these limitations in order to make aircraft more efficient and to expand the flight envelope. This has occurred for a variety of reasons; there is pressure on the civil

aerospace industry to produce greener aircraft. For instance, the ACARE (Advisory Council for Aeronautics Research in Europe) 2020 Vision set goals for the European civil aerospace industry to reduce the 2001 carbon dioxide emission levels by 50% by 2020, nitrogen oxides by 80% and noise by 50% [100]. Additionally, in modern warfare in particular there is a growing requirement for highly capable multi-role aircraft, and the increasing application of unmanned aerial vehicles (UAVs), which are not constrained to physiological limitations, allows for the use of highly unconventional technology [82, 122]. The rapid growth in the last few decades in the research of enabling technologies has also fueled interest in morphing aircraft; this includes advances in the fields of smart materials and structures, biologically-inspired technology and nanotechnology [88].

As already mentioned, morphing aircraft have existed since the dawn of aviation. Examples include trailing-edge flaps, leading-edge slotted slats, variable sweep wings (all to enable low speed flight without compromising high speed performance), retractable landing gear (to reduce drag) and variable pitch propellers (for efficient thrust generation over a wide range of airspeeds). From these examples it is clear that morphing technologies need not weigh less or be less complicated than the systems they replace; use of the technology can be justified provided it offers a net benefit to the aircraft on a system level [88].

The drivers of expanding the flight envelope to allow for different missions and the capability of multi-point optimum performance has resulted in morphing occurring at two distinct scales [138], giving rise to the following categories:

- *Planform morphing*: extreme mission capability adaptability typically requires large changes to the aircraft's planform to achieve efficient multi-role objectives. This includes variation of the wing sweep, area and span [95, 138].

- *Performance morphing*: the ability to tweak the aerodynamic performance throughout the flight envelope to move it closer to the optimum generally does not require large planform changes. Instead, the camber, twist

and thickness properties of the wing can be manipulated, or flow control mechanisms can be applied [95, 138].

1.2 Aircraft morphing - past and present

In this section, a selection of aircraft morphing technologies is presented. This includes examples from the past that were implemented and flown, as well as state-of-the-art technology that is not sufficiently mature for implementation into aircraft.

1.2.1 Planform morphing

Variable sweep

One of the most successful wing morphing technologies is that of variable sweep wings. The motivation for this resulted mainly from the aerodynamically contradictory mission requirements that first surfaced in the 1950s as a consequence of transonic and supersonic capabilities enabled by turbojets [137]. Typical mission requirements were long range/endurance subsonic cruise coupled with high supersonic interception and low altitude transonic strike coupled with the ability to operate from short runways or aircraft carriers.

In order to increase the Mach number at which transonic drag rise occurs, wings are swept which reduces the effective Mach number of the flow over the wing. However, other consequences of swept wings include a higher effective angle of incidence, a lower aspect ratio for a given area and a root-to-tip (rearward swept) spanwise component of flow [160]. These all impact negatively on the low speed performance of the wing, resulting in increased stall speeds, increased subsonic drag as well as a degradation in handling. In this speed range, unswept wings are favourable.

Although the Bell X-5, first flown in 1951, was the first aircraft that used variable sweep wings to provide good performance at both low and high speeds,

the concept had been explored previously [137]. In 1931 the Westland Pterodactyl IV (see figure 1.1a) demonstrated the ability to sweep its wings through 4.75°; however, unlike high speed designs, the Pterodactyl used this feature to trim the aircraft [162]. With a first flight in 1964, the General Dynamics F-111 became the first production aircraft to incorporate variable sweep technology [52]. The following two decades saw the production and successful application of a variety of variable sweep wing aircraft (see figures 1.1b and 1.1c). The Grumman F-14 wing sweep was automatically adjusted to maintain an optimum lift-to-drag ratio at varying Mach numbers [74].

(a) Westland Pterodactyl IV [162].

(b) Mikoyan-Gurevich MiG-23 [144].

(c) Dassault Mirage G8 [169].

Figure 1.1: Examples of variable sweep aircraft.

The most recent production aircraft to employ variable sweep wings, the Tupolev Tu-160, first flew in 1981, three decades ago. The disadvantages associated with variable sweep wings include the heavy gearbox and pivot mechanism [155], which must transmit very large loads, as well as the system complexities such as the necessity to house the leading- and trailing-edges of the wing inside the fuselage [137]. The increased fuel consumption and maintenance requirements associated with variable sweep aircraft has resulted in the technology being phased out from subsequent aircraft [155].

However, the renewed interest in aircraft morphing has resulted in research that attempts to capture the benefits of large sweep change capability with less of the disadvantages of the traditional variable sweep mechanisms. In 2003, the Defense Advanced Research Projects Agency (DARPA) initiated the Morphing Aircraft Structures (MAS) programme that requested proposals for reconfigurable

aircraft wings that are capable of radical shape changes [82]. One of the chosen contractors, NextGen Aeronautics, developed a concept that used a rigid leading- and trailing-edge, as well as wing tip, with a kinematic mid-section attached to a macro-composite flexible skin. This skin was capable of in-plane strain in excess of 100%, whilst withstanding air loads of at least 2.5 g [21]. The internal wing structure, shown in figure 1.2a, was configured into parallelograms, which enabled large area changes with relatively small hydraulic actuators, while providing high out-of-plane rigidity to carry substantial air loads [88]. The concept was successfully tested in a wind tunnel at a range of airspeeds from low subsonic to transonic, as well as on a low subsonic flight demonstrator (figure 1.2b). In addition to substantial aspect ratio, span and area changes, the novel wing design enabled the sweep to be varied between 15° and 45° [21].

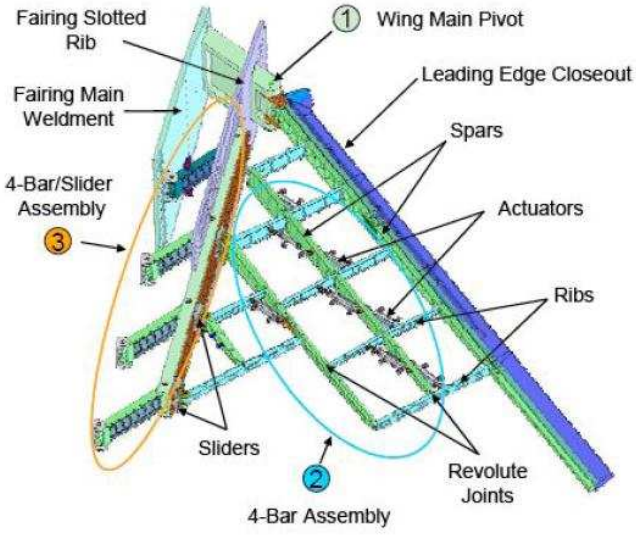

(a) Wing structure [142].

(b) Wind tunnel model [21] and flight demonstrator [88].

Figure 1.2: NextGen Aeronautics Morphing Aircraft Structures concept.

Variable area

For a wing to generate the required lift, L, the following condition [65, 85] must be satisfied:

$$L = qSC_L \tag{1.1}$$

where q is the dynamic pressure, S is the wing area and C_L is the lift coefficient of the wing and is a function of the angle of incidence. This implies that as the airspeed decreases the wing area or lift coefficient must be increased to maintain the required lift. The traditional approach is to increase the lift coefficient by pitching the aircraft to increase the angle of incidence. The use of incidence as a means of trimming the wing is not without its drawbacks however; the induced drag increases with the square of the incidence [108]. As a result, wings that are designed for high speed flight perform poorly during low speed operation.

For fighter aircraft, this poor low speed performance is often degraded further by the requirement of low aspect ratio wings for favourable manoeuvrability. For a fixed wing area, as the aspect ratio decreases, the induced drag increases [108]. The contribution of the induced drag to the total drag decreases with increasing airspeeds (due to the need for higher incidences), and therefore does not affect the high speed performance greatly. However, at low speeds the induced drag contribution is significant.

The Lockheed F-104 (figure 1.3) had a very small area, low aspect ratio wing that was designed for optimal high speed performance with little compromise for its low speed handling. As a consequence, the F-104 possessed poor low speed performance including excessively high take-off and landing speeds as well as unstable flight dynamics at high incidences [157].

Several morphing concepts that enabled wing area changes have been developed over the years, but none have been as universally applied as the Fowler flap. This is a trailing-edge device that was invented in 1924, and used on several Glenn L. Martin Company and Lockheed aircraft during the 1930s [55]. The

Figure 1.3: The small wing area and aspect ratio of the Lockheed F-104 [170].

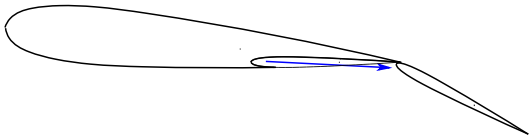

Figure 1.4: Diagram of the Fowler flap operation (reproduced from [85]).

hydraulically-actuated device consists of a hinged tab that can also be extended rearwards (see figure 1.4), therefore not only increasing the camber of the aerofoil, but also the area. The Gouge and Zap flaps were alternative 1930s designs that could similarly increase both camber and area [65]. However, the Fowler flap quickly emerged as the most effective design. Fowler flaps are mechanically complicated and as a result are more expensive and heavier than other high-lift devices; for this reason they are not often used on small aircraft. On the other hand, the low-speed performance benefits they offer to larger aircraft has seen their application to the majority of such aircraft [83].

Another concept that allowed chordwise area increases was found on the LIG-7 by Bakshaev. This technology demonstrator was first flown in 1937 and featured a fixed high aspect ratio wing for high speed flight, as well as manually operated telescoping sections that extended from the fuselage (see figure 1.5) to increase the area at low speeds for improved take-off/landing performance [137]. The success of the concept was evident in that it reduced the take-off distance from 250 m to 135 m and reduced the landing distance from 210 m to 110 m [168].

The main drawback of chordwise area increases is the lowering of the aspect ratio of the wing, and therefore decrease in the lift-to-drag ratio. This effect is greater at lower speeds i.e. the speed regime where wing area increases are most required. The opposite is true of spanwise area increases i.e. for a fixed

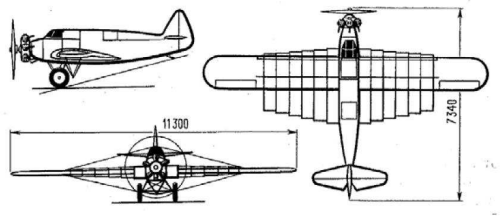

Figure 1.5: Telescoping wing sections of the LIG-7 by Bakshaev for chordwise area increase [137].

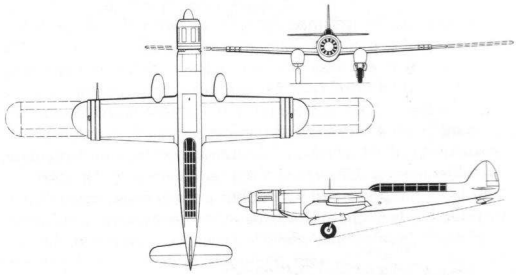

Figure 1.6: Telescoping wing sections of the MAK-123 by Makhonine for spanwise area increase [147].

chord, if the span is increased the lift-to-drag ratio will increase due to the higher aspect ratio. The aerodynamic performance benefits of spanwise area increases over chordwise area increases have been explored since the early days of flight; the MAK-10, designed by Makhonine and first flown in 1931 [147], incorporated a spanwise pneumatic telescoping outer wing section in each wing to allow the aircraft to fly at higher speeds whilst still capable of practical take-off and landing speeds. Improved designs included the MAK-101 (1935) and the MAK-123 (1947) (shown in figure 1.6) [137].

Since these early designs there have been several spanwise telescoping wing aircraft including the Akaflieg Stuttgart FS-29 sailplane, first flown in 1975 [137], which used a large span wing for take-offs and landings as well as climb, and used the retracted smaller span configuration for performance soaring, where the aircraft had to cover a certain distance in the shortest time possible; the higher speed capabilities of the small span arrangement was therefore preferable for this flight condition. More recently (1997), patents were issued to Gevers Aircraft for an aircraft which uses a telescoping wing to almost double the span [49, 118]. In 2007 Samuel and Pines [118] developed a pneumatic telescoping wing. Their design featured two series of pneumatic actuators that doubled as the spars and enabled three different configurations, as shown in figure 1.7, with up to a 230% change in area. Under the SMorph project of which this work is part of, Vale et al. [133] are currently developing a telescoping wing that uses an electric motor

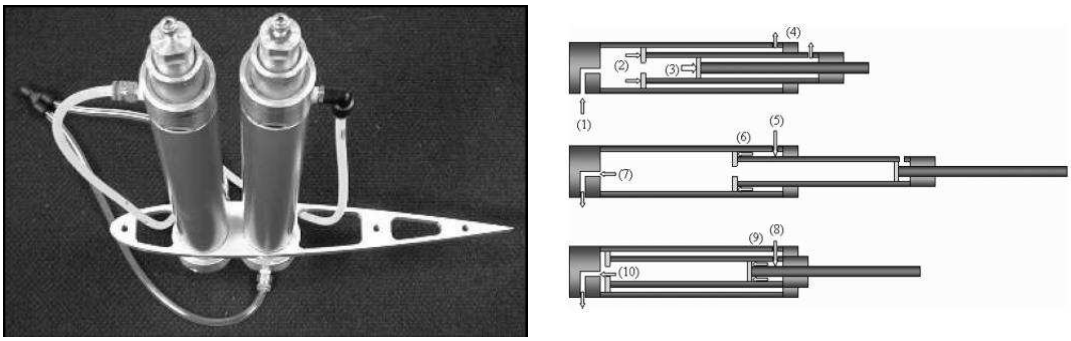

(a) Spars/pneumatic actuators [118]. (b) Configurations [118].

Figure 1.7: A recent spanwise telescoping wing concept [118].

actuated rack and pinion mechanism for deployment. Analytical results show an increase in maximum C_L and lift-to-drag ratio as the span is increased, as expected.

Although telescoping wings do offer good low speed performance and the possibility of roll control, there are several challenges that limit their use. Firstly, typical rack and pinion and cable and pulley actuators are heavy [118], and the need to retract outer wing sections into inner sections makes inner sections heavy due to the increased structural rigidity required [137]. You [142] has proposed the use of variable geometry trusses and deployable box beams, which do not suffer from these problems, as an alternative method to enable spanwise area increases. Additionally these structures can deflect laterally, offering the possibility of variable dihedral wings or winglets. The NextGen Aeronautics concept for DARPA's Morphing Aircraft Structures (MAS) programme was discussed earlier for its variable sweep capabilities. The internal structure in this design (see figure 1.2a) altered its shape in a manner more akin to You's proposed morphing structures. In addition to a 30° variation in sweep [21], the hydraulically actuated NextGen wing could alter its area by up to 40%, the span by up to 73% and the aspect ratio by up to 177% [88].

Folding wings

It has already been demonstrated that an aircraft that is capable of substantial wing area changes will have an increased flight envelope. One less-explored method of enabling this is via the use of a folding wing. Under DARPA's MAS programme, Lockheed Martin developed and wind tunnel tested a UAV which could fold its inboard wing section from the horizontal through 130° to lie flush with the fuselage to reduce the wing area for high speed operation [88, 124]. This operation is demonstrated in figure 1.8. Flexible skins were used at the two

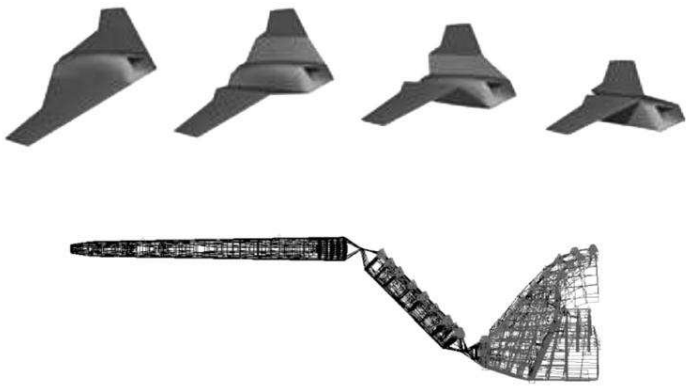

Figure 1.8: Lockheed Martin folding wing concept [124].

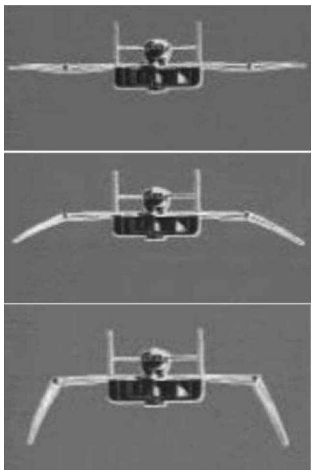

Figure 1.9: Variable anhedral wing tips of the North American XB-70 [82].

fold lines (the root and 30% span) to maintain the aerodynamic shape at these locations and the leading-edge shape was adaptable to enable it to conform with the fuselage. The concept provided the wing with the ability to change its area by up to 200% [124].

Several examples of folding wings can be found throughout aviation history. The earliest and most widespread use of them is for compact storage on carrier vessels. Although the added weight of the mechanism is detrimental to the flight performance of a single aircraft, the benefits of being able to considerably increase the number of aircraft that a carrier can accommodate are significant [137]. This

can be viewed as morphing that enables overall system benefits. The first aircraft to employ folding wings for compact storage was the experimental Short S.41 (1912). Since then, many ship-borne aircraft, and several land-based aircraft have incorporated this space-saving feature.

The prototype North American XB-70 which first flew in 1964 used variable anhedral wing tips to control the aerodynamic performance [82]. Below 300 kts the wings remained horizontal. Between 300 kts and Mach 1.4 the wing tip was folded to 25° below the horizontal, and above Mach 1.4 this angle was increased to 65° below the horizontal [124]. The increased vertical area permitted the use of smaller vertical stabilisers, offset the rearward shift of the aerodynamic centre with increasing airspeed with less need for drag-producing trim corrections and helped to control the compression lift effect during supersonic operation [124]. The XB-70 is shown in its three configurations in figure 1.9.

Research is ongoing at the University of Bristol into morphing winglets. Analytical and experimental studies show how variable dihedral wing tips/winglets may be used as an alternative to conventional control surfaces for aircraft control [19, 20]. In particular, roll control can be achieved with increasing effectiveness at decreasing airspeeds which would enable enhanced low speed manoeuvrability. In another concept, bistable composite wing tips are shown to offer aerodynamic advantages; at low airspeeds the wing tip is aligned with the inboard wing in a stable state, augmenting the lift. At a certain dynamic pressure, the aerodynamically-loaded wing tip passively snaps through to the second stable state, in which it resembles a winglet [46]. This configuration is better suited to higher speeds by decreasing the horizontal area and therefore the drag. One major challenge with this concept is to suppress the substantial excitation of the aircraft modes caused by snap-through [46].

One of the most ambitious folding wing efforts can be found on the prototype IS-1 fighter by Shevchenko, which first flew in 1940. This aircraft used an

unequal-span biplane arrangement for take-off/landing and increased manoeuvrability during combat. However, for high speed flight the lower inboard wings folded into fuselage recesses (similar to the Lockheed Martin MAS concept in figure 1.8), and the lower outboard wings folded into recesses on the underside of the upper wing [137, 161]. The IS-1 is shown in figure 1.10a.

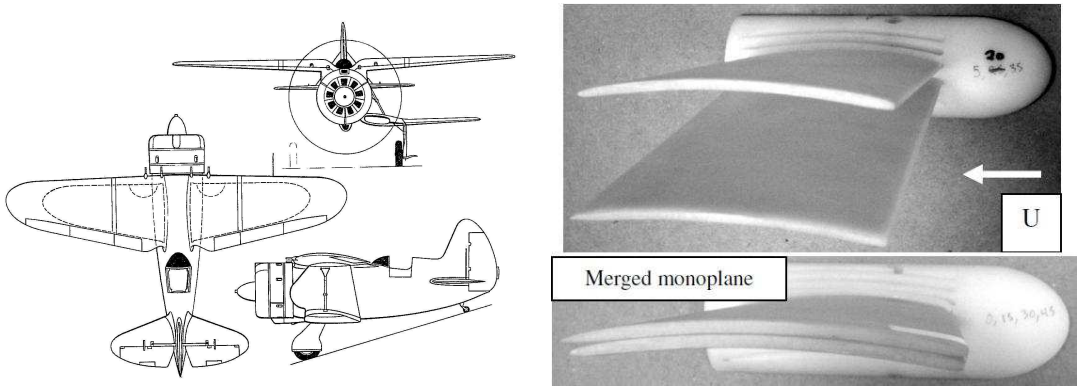

(a) IS-1 by Shevchenko [161]. (b) X-wing by Traub et al. [132].

Figure 1.10: Biplane-to-monoplane morphing examples.

A more recent biplane-to-monoplane morphing method was demonstrated by Traub et al. (2010) [132]. They presented both analytical and experimental results of an X-wing configuration with variable dihedral/anhedral wings; by rotating the lower and upper wings of a biplane towards each other, the two wings can merge (provided they occupy a common root) to form a single monoplane with decreased area, better suited for higher speed flight. The wind tunnel model of the concept is shown in figure 1.10b.

Inflatable wings

Inflatable wings have seen limited application for more than half a century [66]. The Goodyear Inflatoplane, first flown in 1956, was a manned aircraft featuring inflatable wings to enable compact stowage for air-drop behind enemy lines to rescue downed pilots [22, 66]. Around the same time, the M.L. Aviation Company developed a tailless inflatable wing aircraft, the M.L. Utility [22]. In the

1970s, the Apteron flying-wing by ILC Dover became the first UAV to incorporate inflatable wing technology [66], and more recently NASA developed and flight-tested the I2000 inflatable wing UAV technology demonstrator [66]. The deployment sequence for the I2000 is shown in figure 1.11a. The main application of inflatable wing technology is for lightweight portable UAVs. Another proposed use of inflatable wings is to extend fixed surfaces for variable area morphing (see figure 1.11b). The major challenge with this application is the ability to deploy and restow the wings repeatedly during flight; although deployment is straightforward, re-stowage requires mechanisms that will add weight to the aircraft [66].

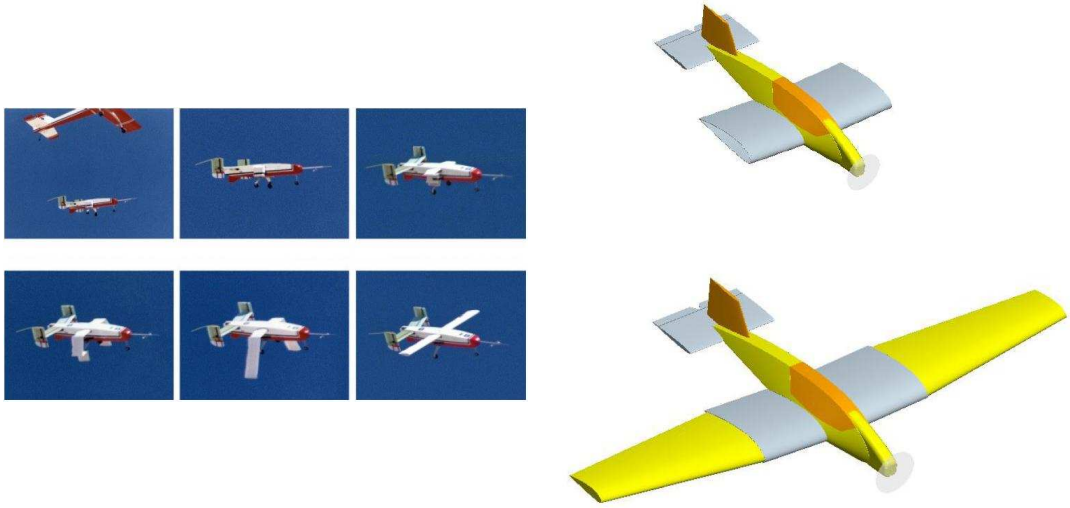

(a) Deployment sequence for NASA's I2000 [66].

(b) Inflatable outboard wing sections for spanwise area increase [66].

Figure 1.11: Inflatable wing examples.

Other planform morphing concepts

Along with trailing-edge flaps, retractable undercarriages (see figure 1.12) are undoubtedly the most common and successful morphing technology found on aircraft. Although they substantially add weight and complexity to the aircraft, above a certain airspeed the drag penalty incurred by fixed landing gear is significant and requires more powerful and therefore heavier engines to compensate

[88]. A retractable undercarriage was first used by Wiencziers in 1911, although the crude mechanism made it impractical [90]. As airspeeds increased there was a greater need for reducing the drag in novel ways and the racing aircraft of the 1920s used retractable undercarriage successfully. Towards the end of the 1920s and early 1930s, commercial aviation and military transport aircraft had embraced this new technology. Despite this, it took until the late 1930s for fighter aircraft designers to be persuaded that the benefits of retractable undercarriages outweighed the penalties they brought with them [90].

Figure 1.12: Retractable undercarriage of a Boeing 787 [145].

Figure 1.13: Variable droop nose on the Aérospatiale-BAC Concorde [149].

Another successfully applied but much less common morphing technology is the variable incidence/droop nose for enhanced pilot visibility, best known for its use on Aérospatiale-BAC Concorde aircraft (see figure 1.13). The origins of this feature can be traced back to the Fairey Delta 2 supersonic research aircraft (1954). One of these was later modified for aerodynamic research under the Concorde programme, and the droop nose subsequently featured on Concorde, which first flew in 1969. The Tupolev Tu-144, the Soviet competitor to Concorde, also incorporated the droop nose feature [72]. All of these aircraft used delta wings which typically impose a very high incidence requirement during landing. This, together with the unusually long noses of these aircraft created limited visibility under certain flight conditions.

A different solution to the high incidence visibility problem was implemented on the Vought F-8 Crusader (1955). This aircraft featured variable incidence wings which allowed the root angle of incidence to be increased by up to 7° to achieve high angles of incidence during take-off and landing whilst maintaining the fuselage at a relatively low incidence [129].

Variable incidence horizontal stabilisers are commonly used on supersonic aircraft, but for a different reason; shockwaves generated during supersonic flight can render conventional trailing-edge elevators ineffective. Instead, stabilators can be employed for pitch control. In this configuration the incidence of the entire horizontal stabiliser can be altered [108].

Vertical and/or Short Take-Off and Landing (V/STOL) enabling technologies are an example of morphing technologies that have struggled to find application in production aircraft, despite offering V/STOL capabilities coupled with higher forward speeds than helicopters. Tiltrotors are aircraft that are capable of altering the orientation of a propeller to enable forward flight (horizontally-aligned) or vertical flight (vertically-aligned). The Transcendental Aircraft Corporation and Bell Aircraft Corporation produced several tiltrotor designs in the early 1950s [75]. Despite various tiltrotor designs since then, only the military Bell-Boeing V-22 (see figure 1.14a), which first flew in 1989, has made it to production. However, the Bell/Agusta BA609 is a civil tiltrotor in the latter stages of development [99].

(a) Bell-Boeing V-22 tiltrotor [148].

(b) Canadair CL-84 tilt wing [154].

(c) Hawker Siddeley Harrier GR7 vectored thrust [153].

Figure 1.14: Examples of V/STOL aircraft.

Around the same period that tiltrotor aircraft first appeared, an alternative

design surfaced too in which the entire wing (with propeller fixed relative to the wing) of the aircraft rotated about a spanwise axis. This tilt wing feature has also appeared on various aircraft (see figure 1.14b) since the 1950s, but has failed to ever be incorporated into production aircraft [81]. As with tiltrotors, the inherent mechanical complexity, added weight and aeroelastic problems associated with tilt wing aircraft has hindered its use [81].

The most successful V/STOL aircraft is the Harrier family (see figure 1.14c), first developed by Hawker Siddeley in the 1960s. Instead of a variable orientation propeller, the Harrier used a vectored thrust turbofan to generate and control the direction of thrust. The less publicised Yakovlev Yak-38 (first flight in 1971) was also a jet powered thrust-vectoring V/STOL aircraft which entered production, and the Lockheed Martin F-35 is currently in the pre-production stage [42].

1.2.2 Performance morphing

Variable camber

In section 1.2.1 it was demonstrated that as the airspeed decreases, a wing must compensate for the decreased dynamic pressure by increasing the area or the lift coefficient. Area-increasing technologies were presented in section 1.2.1. However, the traditional method used for large lift adjustments is to alter the lift coefficient. This is generally achieved by pitching the entire aircraft to a different flight attitude and therefore altering the angle of incidence of the wing. At low airspeeds the angle of incidence becomes critical, however, and a further increase in angle of incidence will stall the wing. To delay the onset of stall (i.e. lowering the stall speed) moderately cambered aerofoils may be used. Relative to the equivalent uncambered aerofoil section, camber increases the maximum achievable lift coefficient, as shown in figure 1.15. Ailerons take advantage of this effect differentially to create a rolling moment.

However, at higher speeds it is desirable to have zero or little camber. The idea for a variable camber wing can be traced back to the invention of the aileron

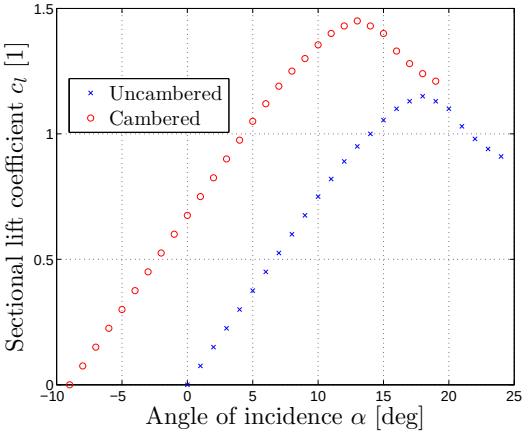

Figure 1.15: Effect of camber on an arbitrary lift curve.

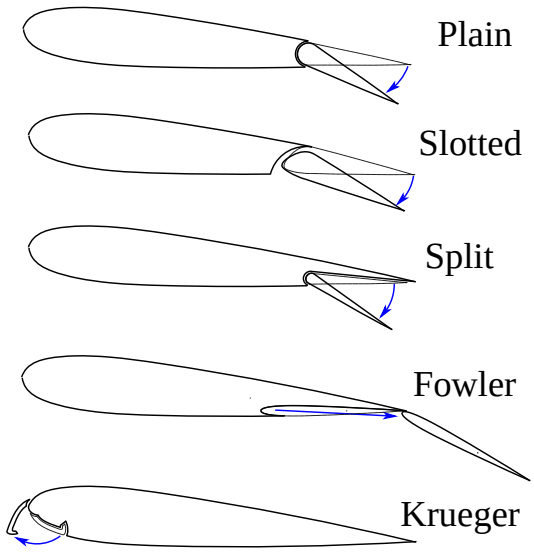

Figure 1.16: Some common flap types (reproduced from [65, 85]).

by Farman in 1908 [55] and led to several World War I aircraft incorporating plain flaps. Despite this, flaps did not see widespread application until the 1930s as a result of the low airspeeds of aircraft of that period, meaning that the devices were redundant. The roots of the differing flap designs in use today were laid down between around 1920 and 1940, with refinements in the devices occurring since [55]. Figure 1.16 shows a variety of common types of modern flaps.

While the conventional flaps described above offer an increase in aerodynamic performance at various points in the flight envelope, they are relatively complex and heavy, and discontinuous surfaces and exposed mechanisms result in large drag penalties. Consequently there has been much research into the development of variable camber wing devices that are more efficient than conventional flaps, and patents for continuous conformal variable camber surfaces exist as early as 1916 (see figure 1.17) [100].

Marques et al. (2009) [84] describe a device which is based on the Fowler flap, producing camber and area increases. However, the key feature of their design is that over the entire deflection range, the flap maintains upper surface continuity; inspection of figure 1.16 reveals that the deflection of conventional flaps results in

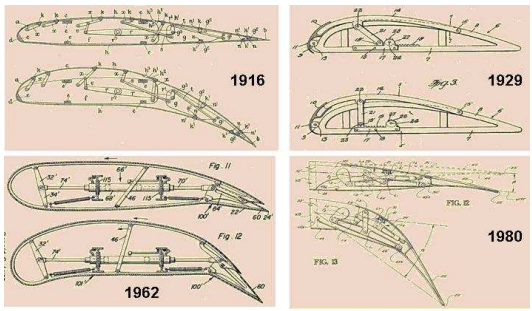

Figure 1.17: Some patented designs for continuous variable camber wings [100].

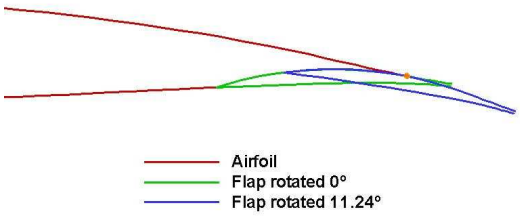

Figure 1.18: Geometry of a traditional jointed mechanism that maintains upper surface continuity [84].

surface discontinuities. These promote flow separation, resulting in higher drag and the earlier onset of stall [48]. Marques et al. optimised the flap geometry to minimise the drag of a low speed UAV. As a result of the continuous upper surface and optimisation procedure, an average drag reduction of 2.7% was achieved, the lift coefficient increase was almost double that achieved by a plain flap, and the actuator energy was only 40% of that of the plain flap. The geometry of the flap is shown in figure 1.18.

The concept by Marques et al. relied on a traditional jointed mechanism. In contrast, NASA's Mission Adaptive Wing (MAW) programme used a concept which can be viewed as compliant in nature. The MAW programme resulted in a wing incorporating leading- and trailing-edge variable camber surfaces which could be deflected in flight to provide close to the optimal camber shape for all flight conditions [112]. The programme commenced in 1971 with analytical studies of smooth variable camber aerofoils, and culminated with six years of flight testing of the technology between 1979 and 1985 [18]. A General Dynamics F-111 platform was used for the flight testing, with the original wings replaced by the MAW. The MAW consisted of internal hydraulically-actuated rods and linkages that were used to elastically deform the leading- and trailing-edges, as shown in figure 1.19, resulting in continuous upper and lower surface deformations, and decreased drag relative to exposed actuators. The results of the MAW

programme showed that a continuous variable camber wing can be used to minimise drag over a range of subsonic, transonic and supersonic flight conditions. Used together with variable sweep, variable camber can minimise penalties for off-design operation [112].

Figure 1.19: The internal structure and actuators of the compliant Mission Adaptive Wing for enabling variable camber with surface continuity [137].

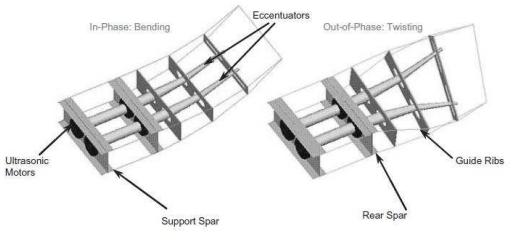

Figure 1.20: Smart Wing ultrasonic piezoelectric motors for high-rate smoothly contoured trailing-edge camber variation [78].

While the MAW programme highlighted the potential aerodynamic benefits of a continuous variable camber wing, on a system level the benefits were marginal due to the heavy and complicated internal mechanical design which used conventional hydraulic actuators [77]. In the mid 1990s, NASA's Morphing project was initiated with the objective of using smart materials and sensors (e.g. Shape Memory Alloys (SMAs), piezoelectrics) to enable aircraft adaptability [86, 87]. As part of this project, the DARPA/AFRL/NASA Smart Wing programme set out to develop a smart materials based concept that would address large deflection, high rate control effectors for aircraft manouevre control [78, 119]. One of the concepts consisted of several smoothly contoured trailing-edge surfaces (similar to the MAW) actuated by SMA wires, forming the flaps and aileron surfaces. When used together, these conformal flaps and ailerons provided up to a 17.3% increase in roll-rate relative to conventional hinged surfaces. However, the increased nose-down pitching moment generated by conformal surfaces leads to a significantly decreased aileron reversal dynamic pressure. To alleviate this, the programme also developed a smoothly contoured variable camber leading-edge, also actuated by SMA wires. Another concept replaced the trailing-edge

SMA wires with ultrasonic piezoelectric motors (see figure 1.20), enabling typical deflection rates required by fighter aircraft [14, 120].

In 2006 FlexSys Inc flight tested the Mission Adaptive Compliant Wing (MACW) which was developed under a Small Business Innovation Research (SBIR) programme with the US Air Force Research Laboratory (AFRL). The wing included an adaptive structures trailing-edge flap that enabled variable geometry reshaping of the upper and lower flap surfaces with no seams or discontinuities (see figure 1.21). As with NASA's MAW, the primary advantage of this was to reduce or eliminate the flow separation associated with conventional flap hinge lines. Relative to these conventional devices, the MACW was able to provide up to a 40% increase in control authority per degree of deflection, and with 25% reduced drag [77].

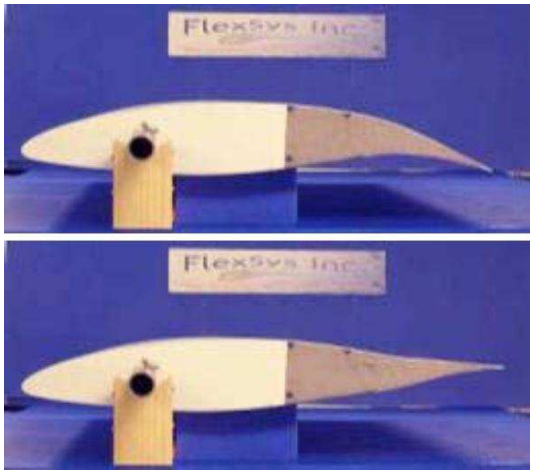

Figure 1.21: Mission Adaptive Compliant Wing trailing-edge demonstrating ±10° deflections [77].

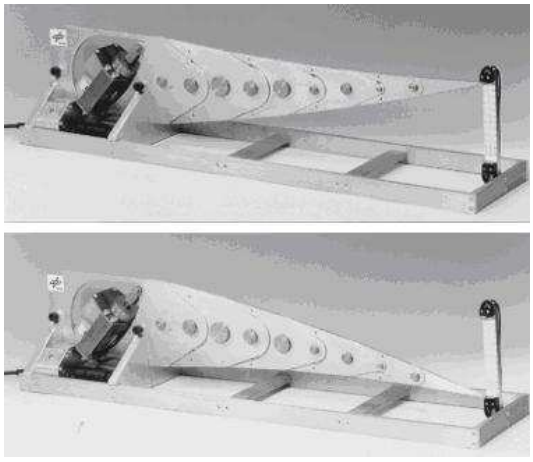

Figure 1.22: A DLR-developed flexible rib to enable conformal trailing-edge camber control [100].

The goal of developing a compliant trailing-edge device for variable camber undoubtedly receives the most attention in present day morphing research. In addition to the concepts already detailed, the German Aerospace Centre (DLR) is active in this area, with one of their concepts shown in figure 1.22. This concept uses an articulated rib composed of plate elements to create a flexible rib on which the skin can glide whilst still being able to transmit the aerodynamic

loads [100].

Variable twist

Variable twist wings for adaptive performance is perhaps the oldest form of morphing. As mentioned previously, the Wright brothers used this method to achieve roll control of their Wright Flyer in 1903 [15]. However, as aircraft became ever faster, the greater dynamic pressures resulted in stiffer wing construction to avoid detrimental aeroelastic effects and consequently conventional aircraft control their aerodynamic performance via alternative methods.

The Active Flexible Wing (AFW) programme was a collaboration between NASA and the USAF which started in the 1980s, before evolving into the Active Aeroelastic Wing (AAW) programme which ended in 2003 [88]. The programme objective was to use conventional leading- and trailing-edge surfaces in a controlled manner at high dynamic pressures to induce substantial twisting of the wing. By performing this differentially on a pair of wings the opposing aeroelastic torsional deflections created a rolling moment therefore improving high speed roll manoeuvrability, which typically suffers as aileron effectiveness decreases with dynamic pressure. The main attraction with this approach is that the energy required to twist the wing is supplied by the airflow. The programme included flight testing of a modified McDonnell Douglas F/A-18A (see figure 1.23), demonstrating the advantages of aeroelastic wing twist for roll control [82, 106].

The European Active Aeroelastic Aircraft Structures (3AS) programme (2002-2005) was similar in its approach to morphing technologies in that it used aeroelastic phenomena to benefit the performance, with the key theme being the use of the aerodynamic loads to deform the structure in a controlled manner [121]. A concept developed by Eller and Heinze [39] within the 3AS framework explored the use of redundant leading- and trailing-edge control surfaces to affect the aeroelastic twist. However, unlike the AAW research, the intention was to

Figure 1.23: Active Aeroelastic Wing subject to torsion tests [146].

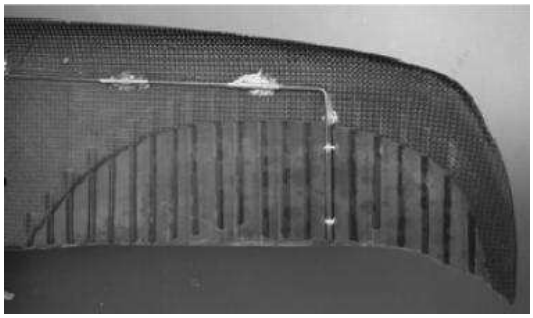

Figure 1.24: Use of an embedded torque rod for active twist roll control of a Micro Air Vehicle [126].

use this to minimise the drag over a range of flight conditions, rather than to augment roll control. Other concepts within 3AS included adaptive internal wing structures to control the elastic axis position, and flexural and torsional rigidities of the wing [3, 4, 6, 7, 29]. Adaptive internal structures therefore provide a mechanism for controlling the aeroelastic shape deformation to influence the aerodynamic performance. It is one of these concepts (rotating spars) that is developed further in the current work.

In addition to the development of conformal variable camber devices described previously, the DARPA/AFRL/NASA Smart Wing programme also explored the use of SMA torque tubes to actively twist the wing. Although not as effective as hoped due to the use of a low aspect ratio wing, the torque tubes were still capable of twisting the wings to increase the lift by 10% [119].

Stanford et al. (2007) [126] developed a system to twist the wings of a Micro Air Vehicle (MAV) differentially for roll control, although this concept is unlikely to be scalable. It consisted of a single torque rod (see figure 1.24) embedded within each of the membrane wings of the MAV and actuated by a single servo. Results show that for MAVs differential wing twisting is a good and practical alternative to ailerons for roll control.

Paluch and Toussaint (2009) [105] developed and tested an active wing box concept. Their design replaced conventional spars and ribs with vertical rods and

hydraulic actuators to affect the twist. Analytical and structural tests proved the feasibility of the concept on a large scale. Vos et al. (2010) [135] tackled the problem of enabling large wing twist deformation whilst maintaining a high load-carrying capability. They achieved this through controlled warping of a torque box structure i.e. cutting the torque box to open it and reattaching it with a sliding mechanism that enabled load-carrying warping (and hence inducing torsional deformation).

Other performance morphing concepts

Flow control is one of more traditional forms of aircraft morphing that enable aircraft the ability to adapt their performance. Lachmann and Handley Page independently invented the wing slot around 1920 to delay flow separation and therefore stall. Lachmann used a long fixed slot near the leading-edge, whereas Handley Page's design was adaptive to alleviate the substantial drag created by slots at high speed; in his concept, a deployable leading-edge section known as a slat created a slot in the wing at low speeds and was retracted at higher speeds to close the slot and lie flush with the leading-edge [55]. The Fowler flap, discussed previously and invented in 1924, was the first trailing-edge device to create a slot. By the late 1930s, double-slotted flaps had been patented, and in 1963 triple-slotted flaps were flown for the first time on a Boeing 727 [55]. Slots delay flow separation of the downstream aerofoil by assisting in turning the flow to provide boundary layer control [80]. For leading-edge slats, this means the main wing can achieve greater angles of incidence, and for trailing-edge flaps this allows the flap to be deflected through a larger angle, therefore increasing the camber.

An externally blown flap, as used on the Boeing C-17, is similar in operation to a conventional slotted flap except airflow through the slot is augmented by the engine exhaust [65]. An improvement on this is upper surface blowing where the exhaust flows over the upper wing and flaps [65]. However, the most effective

high lift device is the internally blown flap; this device bleeds air from the engine compressor which is then blown at supersonic speeds over the trailing-edge flaps. This has been used on fighter aircraft with very small wings (e.g. Lockheed F-104) [65]. Since the late 1960s, research has also been performed into the use of root-to-tip spanwise blowing to delay flow separation [140].

Another concept which applied boundary layer control was explored by Natarajan et al. (2004) [102]. This research involved analytical studies of adaptive bumps on a wing surface in order to promote flow separation in the region of the bump. The work showed that the increased drag due to the separated flow can be used differentially between the wings to generate a substantial yawing moment. Similar work by Barbarino et al. [13] and the German Aerospace Centre (DLR) [100] is ongoing to develop adaptive bumps but for the purpose of reducing transonic drag.

1.3 Evolution of aircraft wing structures

1.3.1 Unstressed wing construction

Early aircraft wings were constructed using an internal framework of spars and ribs covered with a thin flexible skin. The unstressed skin and the ribs act to transmit the aerodynamic loads to the spars, but contribute very little to the structural strength of the wing. The primary structural components in this design are the spar caps/flanges (see figure 1.25a), which resist the concentration of both flexural and torsional loads on the wing [103].

This construction technique is attractive since it is simple and the wing is straightforward to repair and maintain. However, a flexible skin possesses negligible bending load-carrying capability and therefore buckles at a very low dynamic pressure. The stress concentrations which arise from this buckling also make the skin susceptible to low flight cycle fatigue failure. Additionally, a flexible skin can deform into a wave state with relatively large amplitudes and therefore increase

drag forces. As airspeed requirements increased, these problems with unstressed skins became more apparent, and the demand for increasingly lightweight aircraft structures also exposed the relative inefficiency of the unstressed skin design; as the skin can carry only a negligible bending load, a portion of material is not being used and is effectively a dead weight [103].

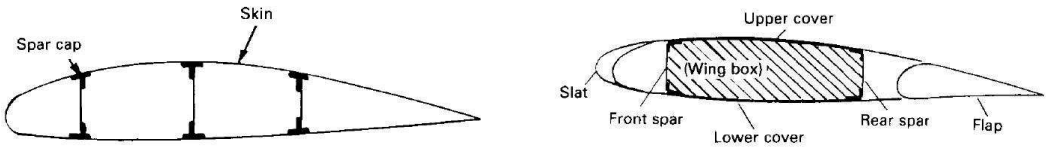

(a) Typical three spar unstressed wing [103]. (b) Typical semi-monocoque wing [103].

Figure 1.25: Wing structures.

1.3.2 Semi-monocoque wing construction

As a consequence of the limitations of unstressed wing construction, semi-monocoque wing construction emerged and has been prevalent since the 1930s. Again, an internal framework of spars and ribs are covered with a skin. However, a stressed skin is used and contributes the majority of the structural strength of the wing, with the spars only acting to reinforce this. Unlike the load concentrations (spar caps) that exist on an unstressed wing, for the semi-monocoque wing (see figure 1.25b) the bending load is distributed around the periphery of the aerofoil profile (skin and spar caps) and the torsional load is distributed throughout the wing box (i.e. the upper and lower skin between the two main spars as well as the spar webs carry shear flow) [103].

Although this type of wing construction requires a heavier skin (50 - 70 % of the structural weight of the wing [103]), the wing is significantly lighter than an equivalent unstressed wing as the material is more efficiently distributed. The weight of the wing is typically reduced further by using a relatively thin stressed skin that employs stringers as spanwise panel stiffeners to prevent buckling [103].

In summary, stressed skin wings are torsionally stiffer, more lightweight and can withstand much higher aerodynamic loads than unstressed skin wings.

The rotating spars concept, which forms the main focus of this work, has been designed for a wing employing unstressed wing construction and therefore significant challenges exist when addressing the scaling-up of the concept. These structural scaling difficulties, as well as other difficulties, will be discussed in more detail in chapter 2.

1.4 Adaptive internal structures

In section 1.2.2 the European 3AS programme was mentioned and, more specifically, efforts to control the wing shape via adaptive internal structures were discussed. The work presented by the author within the SMorph programme are adaptive internal structures concepts and aim at developing these further.

The adaptive internal structures approach employs controlled structural variations to reshape the wing into the configuration that best suits the desired performance. Typical structural parameters that are varied include the wing flexural and torsional rigidities, as well as the position of the elastic axis. This results in a change in the static aeroelastic deformation (bending, h, and torsional, θ, deflections), as shown in figure 1.26, allowing the aerodynamic performance to be tailored. Applications include drag reduction, roll control and loads alleviation. The key idea exploited by the approach is that all the energy required to alter the wing shape and maintain it in position is provided by the airflow.

As with the AFW and AAW programmes discussed in section 1.2.2, the adaptive internal structures approach represents a significant shift in the design methodology; aeroelastic effects are traditionally considered to be detrimental and can be catastrophic, which has led to the acceptance that lifting surfaces should be stiff, and therefore heavy [95]. Adaptive internal structures uses aeroelasticity in a beneficial manner by taking advantage of its deformation effects on

less stiff aerostructures whilst avoiding the classical aeroelastic instabilities such as flutter and divergence.

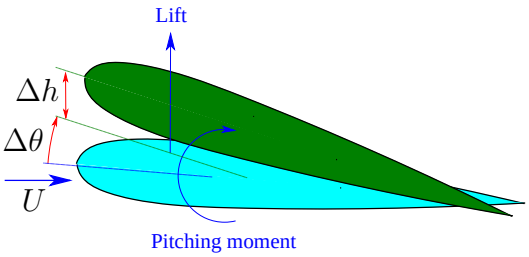

Figure 1.26: Aeroelastic effect on a wing section of altering typical structural properties.

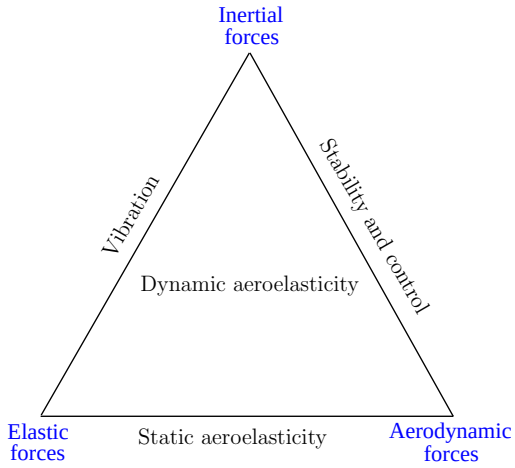

Figure 1.27: Collar's aeroelastic triangle (reproduced from [141]).

1.5 Aeroelasticity

Aeroelasticity is the branch of aircraft design concerning the interactions between the aerodynamic, elastic and inertial forces [15, 37, 45, 61]. Collar [27] presented these three forces as an aeroelastic triangle (see figure 1.27), and this visualisation shows how related interactions are identified by using combinations of any two of these disciplines [37] e.g. the presence of elastic and inertial forces will give rise to vibration of the structure.

Aeroelasticity is traditionally classed as being dynamic or static [141]. Dynamic aeroelasticity concerns the oscillatory effects of the aeroelastic interactions [141]. The most critical effect is the instability known as flutter. Flutter is a collection of aeroelastic phenomena that can be described as unstable self-excited vibration in which the structure extracts energy from the airflow, and is often catastrophic [37, 61]. It is also of interest to predict the transient response of flexible aircraft in unsteady flow conditions, such as gusts, turbulence and manoeuvres [61]. These conditions can introduce large stresses into the structure

and therefore prediction of them is vital to ensure structural integrity. Buffeting, a wake-induced vibration, is another dynamic aeroelastic phenomenon that can cause fatigue damage [61].

Static aeroelasticity concerns the nonoscillatory effects of the aerodynamic forces acting on a flexible aircraft structure [141]. The most important static aeroelastic phenomenon is the instability known as divergence. This involves the moments due to the aerodynamic forces overcoming the elastic restoring moments, resulting in infinite deflections of the wing [61, 141]; in reality, structural failure occurs as the deflections become excessive. Another important static aeroelastic concern is the prediction of the aileron effectiveness at a given airspeed and the associated phenomenon of aileron reversal [61]; typically, as the airspeed increases, ailerons will become less effective and at a certain airspeed will be ineffective. Beyond this, negative effectiveness will occur (aileron reversal). This is caused by the nose-down twist of the wing due to a downwards aileron deflection and vice versa. The remaining focus of static aeroelasticity deals with the static response of the system [61] e.g. an aeroelastic lift prediction is more accurate and may differ significantly from a rigid structure prediction, since the lifting surface may have deflected substantially, redistributing the loads.

The advent of computer-flown aircraft via flight control systems (FCS) has expanded the field to include the additional interaction of the control forces (aeroservoelasticity), and in high temperature environments the heat-induced stresses become significant in the interactions (aerothermoelasticity) [37]. Aeroelastic effects are not limited to aeronautical applications, and occur in other applications too, including civil (e.g. vortex shedding on chimneys) and mechanical (e.g. stall flutter of blades in turbomachinery) [37, 141].

The classic form of the aeroelastic equations of motion can be written as [141]

$$\mathbf{A}\ddot{\boldsymbol{\eta}} + (\rho U\mathbf{B} + \mathbf{D})\,\dot{\boldsymbol{\eta}} + \left(\rho U^2\mathbf{C} + \mathbf{E}\right)\boldsymbol{\eta} = \mathbf{0} \tag{1.2}$$

where **A**, **B**, **C**, **D** and **E** are the structural inertia, aerodynamic damping, aerodynamic stiffness, structural damping and structural stiffness matrices respectively, ρ is the air density, U is the airspeed and $\boldsymbol{\eta}$ are generalised coordinates.

1.6 Aims and objectives

The aim of this work was to advance existing adaptive stiffness wing technologies for the improved aerodynamic performance of morphing aircraft. This aim was realised through the following objectives:

- Analytical exploration of the application of the multiple rotating spars concept and establishment of some design criteria, in particular, confirmation of the suitability of their application to swept wings.
- Implementation of the multiple rotating spars concept on an experimental swept wing model, and comparison of experimental trends with those from the analytical study.
- Development of an approach to automatically alter the spar orientations to achieve and maintain an aerodynamic performance objective.
- Analytical investigation of the application of an adaptive torsional stiffness all-moving wing tip as a loads alleviation device.
- Optimisation of a SensorCraft structure incorporating the loads alleviation device to achieve mass reductions.

1.7 Contribution

The contributions to knowledge presented in this thesis with regards to the multiple rotating spars concept are as follows:

- Implementation of the concept on a sweptback wind tunnel wing; a previous experimental study (unswept) [62] identified the lack of torsional flexibility (in order to satisfy aeroelastic stability requirements) as a limiting factor, and consequently aerodynamic forces could only be varied by less than 10%. This was overcome in the current study with the use of a sweptback wing which promoted aeroelastic stability whilst simultaneously taking advantage of the bending-torsion coupling. This enabled aerodynamic force variations of up to 25% at only 40% of the dynamic pressure of the previous study.

- Integration of actuators into the experimental wing to enable practical control of the orientation of the spars; the previous experimental study used manual adjustment of the spars which required the wind tunnel airspeed to be reduced to zero and the test-section to be opened in order to adjust the spars. Another previous experimental study [3, 7, 29] did use actuators, but only structural tests and proof-of-concept wind tunnel demonstrations were performed with the wing.

- Implementation of a closed-loop system to control the experimental wing; with no user input, the system successfully achieved and maintained several pre-defined aeroelastic objectives, despite deliberate variations in the simulated flight conditions.

- Establishment of design guidelines for an arbitrary wing incorporating two rotating spars.

- Advancement of past trends by performing experimental and analytical parameter studies at a significantly higher resolution; past analytical and experimental aeroelastic studies [3, 7, 29, 62] each considered 9 different spar orientation combinations. The current study used 961 (analytical) and 169 (experimental) combinations to gain an improved insight into the trends.

The contributions to knowledge presented in this thesis with regards to the adaptive wing tip device are as follows:

- Analytical application of the device to reduce gust-induced stresses on a SensorCraft structure.
- Analytical application of the device to reduce the mass of a SensorCraft structure.
- Effect of the device on the aeroelastic stability behaviour of a lifting surface.
- Establishment of design guidelines for an arbitrary wing incorporating the adaptive wing tip device.

1.8 Summary by chapter

The remaining content of the thesis can be summarised:

Chapter 2: The multiple rotating spars concept and the resulting aeroelastic effects are described. The applicability of the concept is discussed, in particular with regards to modern full-size aircraft. Research to date on the concept is summarised to establish the state-of-the-art and gaps in the knowledge.

Chapter 3: Development of a static aeroelastic model for a wing with two rotating spars; this model was developed and coded into MATLAB® to serve as a utility to study the rotating spars concept. The obtained equations of equilibrium are simplified using an assumed modes approach, and the aerodynamics are modelled using the vortex-lattice method.

Chapter 4: Application of the developed static aeroelastic model to perform an analytical study of the rotating spars concept; the model is used to perform a parameter study, establish design guidelines and minimise drag over a range of airspeeds.

Chapter 5: Experimental aeroelastic study of a swept wing incorporating the rotating spars concept; the established guidelines are used to design a wind

tunnel model which is then tested over a range of airspeeds to establish trends. The results of attempts to control the wing in a closed-loop fashion are also presented.

Chapter 6: Analytical study and development of an adaptive wing tip device for loads alleviation; a parameter study is performed using a MATLAB® aeroelastic model of a wing incorporating the device. A case study is then performed on a finite element model to reduce stress and minimise mass.

Chapter 7: Conclusions of the work are presented, which helps to establish suggestions for future directions.

1.9 Related publications

The work contained in this thesis has led to the following publications [31, 91, 92, 93, 94, 95, 96, 97, 166, 167]:

- S. Miller, V. Hodigere-Siddaramaiah, G.A. Vio, and J.E. Cooper. Use of rotating spars for an adaptive aeroelastic wing. *Submitted to Journal of Aircraft*, 2010.

- S. Miller, G.A. Vio, and J.E. Cooper. Gust load alleviation using a wing tip device. *Submitted to Journal of Aircraft*, 2010. a

- S. Miller, G.A. Vio, J.E. Cooper, J. Vale, L. da Luz, A. Gomes, F. Lau, A. Suleman, L. Cavagna, and A. De Gaspari. SMorph - Smart Aircraft Morphing Technologies Project. In 51^{st} *AIAA/ASME/ASCE/AHS/ASC Structures, Structural Dynamics, and Materials Conference*, Orlando, Florida, 2010. a

- S. Miller, V. Hodigere-Siddaramaiah, and J.E. Cooper. Morphing wings using adaptive structures. In *School and Symposium on Smart Structural Systems Technologies*, Porto, Portugal, 2010. a

- S. Miller, V. Hodigere-Siddaramaiah, J.E. Cooper, and G.A. Vio. Control of rotating spars for an adaptive aeroelastic wing. In *AVT-168 Morphing Aircraft Symposium*, Évora, Portugal, 2009. a

- S. Miller, J.E. Cooper, and G.A. Vio. Adaptive wing tip devices for gust alleviation, trim and roll control. In *AVT-168 Morphing Aircraft Symposium*, Évora, Portugal, 2009. a

- S. Miller and J.E. Cooper. Development of an adaptive wing tip device. In 50^{th} *AIAA/ASME/ASCE/AHS/ASC Structures, Structural Dynamics, and Materials Conference*, Palm Springs, California, 2009. a

- S. Miller, G.A. Vio, and J.E. Cooper. Optimisation of a scaled sensorcraft model with passive gust alleviation. In 12^{th} *AIAA/ISSMO Multidisciplinary Analysis and Optimization Conference*, Victoria, British Columbia, 2008. a

- S. Miller and J.E. Cooper. Wing design incorporating a passive loads alleviation device. In *RAeS Aircraft Structural Design Conference*, Liverpool, UK, 2008. a

- J.E. Cooper, V. Hodigere-Siddaramaiah, G.A. Vio, S. Miller and G. Dimitriadis. Adaptive aeroelastic structures for improved aircraft performance. In *World Forum on Smart Materials and Smart Structures Technology*, Chongqing and Nanjing, China, 2007.

Chapter 2

Overview of the rotating spars concept

2.1 Introduction

The rotating spars concept is an adaptive internal structures (see section 1.2.2) approach to wing morphing that relies on variations in the orientation of spars to alter the structural parameters of the wing. More specifically, for non-circular cross-sectional spars, as the spar orientation is varied, the second moment of area and therefore the flexural rigidity of the spar in any given direction will vary. This is illustrated in figure 2.1; in this example the spars have a high aspect ratio rectangular cross-section, and can rotate about an axis parallel to the x-axis. In the red position, the second moment of area of each of the spars about their neutral axis in the Oxz-plane, I_{yy}, is at a maximum, while in the green position it is at a minimum. This corresponds to the maximum and minimum flexural rigidities of the spars in the same direction.

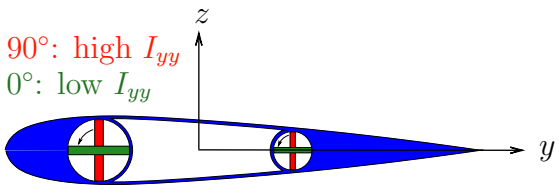

Figure 2.1: Rotating spars concept.

The variation of the flexural rigidity of the spar allows the wing flexural rigidity, torsional rigidity, and elastic axis position to be varied. This enables aeroelastic shape control of the wing, and therefore the ability to alter the aerodynamic performance (lift and drag) in flight. As is demonstrated in chapters 3 - 5, there exists a sinusoidal relationship between the spar orientation and the aeroelastic parameters (structural, wing loads and deflections).

2.2 Wing with a single rotating spar

Consider a wing with a single rotating spar. Typical variations of the aerodynamic performance with spar orientation ϕ are shown in figure 2.2a. It can be seen that it is possible to alter the lift, drag and lift-to-drag ratio of the wing by rotating the spar. This offers the potential to trim the wing to a desired lift value, roll control (through differential variation of the spar orientation of each wing), and loads alleviation. Application of a single rotating spar for roll control was explored in the Variable Stiffness Spar (VSS) concept [24, 41], part of the Active Aeroelastic Wing (AAW) programme mentioned in section 1.2.2. Instead of using a non-circular cross-sectional spar to achieve the stiffness variation, the VSS approach used a segmented circular cross-sectional spar with articulated joints at the connections with the ribs.

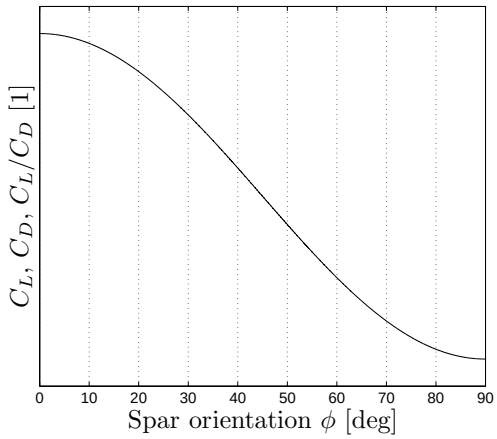

(a) Single rotating spar.

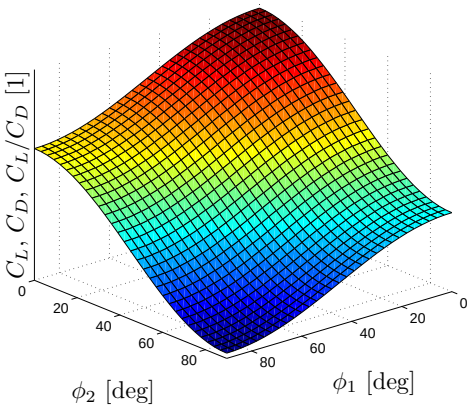

(b) Multiple rotating spars.

Figure 2.2: Typical variation of the aerodynamic performance for wings with single and multiple rotating spars.

2.3 Wing with multiple rotating spars

One limitation of using only a single rotating spar is that the aerodynamic parameters cannot be varied independently e.g. it is not possible to alter the drag without affecting the lift or the lift-to-drag ratio. This can be seen by examining figure 2.2a. However, by employing multiple rotating spars, this becomes a possibility, and enables drag reduction at a fixed lift value (trim). This can be seen in figure 2.2b which shows a typical variation in the aerodynamic behaviour for a wing with two rotating spars. By altering the orientation of both spars, the wing shape can be moved to a new position that maintains the original lift value, but with a reduced drag value, and therefore an increased lift-to-drag ratio. This of course means that a wing with multiple rotating spars can be optimised throughout flight to improve performance and reduce fuel consumption.

2.4 Range of applicability

Since the rotating spars concept works by exploiting changes in the second moment of area of the spars to affect wing structural parameters, it is suited to use in unstressed wings; as discussed in section 1.3, the spars in unstressed wings

account for almost all of the overall wing rigidity.

However, the application of the concept to semi-monocoque wings is not likely to be successful. Again referencing section 1.3, the spars in semi-monocoque wings account for only a small portion of the overall rigidity of the wing, with the stressed skin accounting for the majority of it, and therefore a change in the stiffness of the spars would have only a small effect on the overall rigidity of the wing. Furthermore, the degree of freedom introduced to enable the spars to rotate interrupts the shear flow through the traditional wing torsion box (see figure 1.25b), which has two main effects; firstly, the shear flow is redistributed around the periphery of the aerofoil profile and therefore the skin in the leading- and trailing-edge sections require stiffening, adding weight to the structure. The spar will still carry a portion of the shear flow; however, there are discrete points of entry for this corresponding to the spar bearings, which will therefore experience stress concentrations. Secondly, as the spar webs are carrying very little shear, the concept will have only a negligible effect on the torsional rigidity of the wing.

As all modern aircraft employ a semi-monocoque wing structure, the rotating spars concept is not scalable. The concept also introduces other scaling problems not directly related to the structural issues discussed; to minimise weight and maximise volume, spars also typically double as walls of fuel tanks and the rotating spars would not be capable of this function, creating the need for replacement standalone bulkheads. Furthermore, the clearance required within the wing for rotation of the spars would reduce the volume of usable space; this would undoubtedly reduce fuel capacity and introduce complications for stowage of retractable undercarriage and other flight systems such as actuators for flaps, ailerons and spoilers [103].

Although the rotating spars concept can be used on an wing with unstressed skin to achieve significant changes in the flexural rigidity of the wing, the torsional rigidity and position of the elastic axis is affected much less. Since most aeroelastic phenomena are torsional in nature, the implication of this is that the

concept will be relatively ineffective at tailoring the aerodynamic performance; therefore the flexural behaviour must be used to affect the torsional deflections. This can be achieved by using a wing with rearward sweep, which introduces a beneficial stable bending-torsion coupling. The rotating spars concept is unlikely to be effective on an unswept wing and although a bending-torsion coupling exists on wings with forward sweep, this coupling is unstable leading to a very low divergence dynamic pressure.

In chapter 3, the aeroelastic model that is developed permits inclusion of arbitrary wing sweep for this reason and in chapter 4 the restriction of the concept to sweptback wings will be demonstrated. Chapter 5 goes on to perform wind tunnel tests on a sweptback wing employing the rotating spars concept. Additionally, the wing used in the wind tunnel tests, and the analytical model developed and used in chapters 3 and 4 respectively are representative of an unstressed wing structure.

2.5 Research to date on the concept

Mention has already been made of the Variable Stiffness Spar concept [24, 41], which investigated the use of a single rotating spar for roll control. The primary aim of a multiple rotating spars approach is to achieve drag reduction whilst still maintaining control of the lift. Such a concept has been under development at the University of Manchester for several years. Finite element analyses of unswept wings incorporating two rotating spars suggested that the flexural and torsional rigidities, as well as the elastic axis position of the wing could be varied by adjusting the orientations of the spars [3]. Typical variations of wind-off natural frequencies with the orientations of the spars were also examined and the importance of optimising the wing structure to make best use of the concept was identified [6].

Experimentally, an unswept wing incorporating two rotating spars was constructed and used several stepper motors attached to the ribs to actuate rotation of the spars [3, 7, 29]. Testing was primarily structural, with only a limited insight into the aeroelastic behaviour. The structural benchtests showed clear variations in the flexural and torsional rigidities of the wing as the spar orientations were altered, although concluded that the flexural rigidity could be altered to a much greater extent than the torsional rigidity. Hammer tests were performed to find the natural frequencies of the first six modes, and these agreed well with analytical predictions [4]. Wind tunnel testing did confirm that the aeroelastic twist of the wing could be altered by rotating the spars (a maximum tip twist variation of 0.7° at 15 $m{\cdot}s^{-1}$ and 1.3° at 30 $m{\cdot}s^{-1}$) [3], therefore suggesting the capability of altering the aerodynamic loads.

Later work [62] on the concept included further analytical and experimental studies. The main advances involved optimisation of multiple spar orientations on a finite element model (unswept and sweptback) in order to minimise the drag [63] and wind tunnel testing of an unswept wing, including measurement of the lift and drag forces at several spar orientations.

2.6 Areas identified for development

This initial work on the concept helped to direct the current research to fill gaps in the knowledge and develop the concept further. To summarise the areas identified:

- Perform parameter studies to establish trends that will help in the design of a successful rotating spars concept for drag minimisation.
- Confirm or contradict via analytical studies the finding that the flexural rigidity can be varied substantially more than the torsional rigidity.

- Investigate the application of the concept to swept wings. This will take advantage of the bending-torsion coupling that exists in swept wings by using the variation of both the flexural and torsional rigidities to enable aeroelastic wing shape control.
- Perform optimisation of the wing structure to make best use of the concept.
- Use the findings of these analytical investigations to help design an effective wind tunnel wing model incorporating multiple rotating spars.
- Test the wing in the wind tunnel over a range of airspeeds to collect aeroelastic (loads and deflections) data on the concept.
- Incorporate and demonstrate a form of online control or optimisation to automate the change of spar orientation to meet a desired criteria e.g. drag minimisation at a fixed lift value over a range of airspeeds.

Chapter 3

Development of an aeroelastic model for a rotating spars wing

3.1 Introduction

3.1.1 Motivation

To provide an insight into the rotating spars concept, an analytical study was performed. While finite element (FE) modelling allows an appropriate model to be constructed very quickly, the resulting representation limits its use as an investigative tool; in order to acquire a large amount of data, and to allow optimisation studies to be performed, a requirement of the analytical model was that it should be computationally inexpensive. Aeroelastic finite element analyses are relatively time consuming when multiple analyses are to be performed, especially when the input file requires modification and the output file is to be read between each analysis. Furthermore, the FEA (finite element analysis) software (NASTRAN™) that was considered gives no indication of drag forces [116]. While CFD approaches can calculate drag forces with good accuracy, they are significantly more computationally intensive than FE modelling. Instead, an in-house static aeroelastic wing model was derived from first principles and solved

using MATLAB®; this offered greater flexibility and insight into the aerodynamic forces than is capable with FEA, without the computational expense of CFD.

3.1.2 Chapter overview

The remainder of this chapter derives the governing equations (using the Principle of Virtual Displacements) used for this code, and then manipulates them to make them easily solvable (using the Rayleigh-Ritz method). Next, a steady aerodynamic model is developed (vortex-lattice method (VLM)), and this is then coupled to the structural model. Finally, a comparison is made between solutions obtained using the in-house assumed-modes VLM model code and a finite element doublet-lattice model (NASTRAN™).

3.1.3 Model description

Figure 3.1 illustrates the wing aerodynamics and structure. The wing structure comprises of exactly two spars, but a variable number of ribs. Furthermore, for the theory used to be accurate, the ribs must lie perpendicular to the spars (i.e. the spars are parallel to each other), therefore wing taper is not permitted; the reason for this is that it becomes a great deal more difficult to formulate the structural stiffness matrix when ribs do not meet the spars perpendicularly [127]. The spars are capable of bending and twisting, while the rigid wing cross-section assumption is employed, implying that the ribs are only capable of torsional deformation; this is a reasonable assumption [15, 45]. The entire structure is limited to sharing a single isotropic material (although its properties are variables). A half-wing structure is modelled, although a full-span aerodynamic model is used (by way of reflection about the centreline). Inviscid flow is assumed, which means that only the induced drag component of the total drag can be modelled [65, 70].

The model variables include wingspan, chord, chordwise positions of the spars, spanwise positions of the ribs, number of ribs, second moment of areas of the

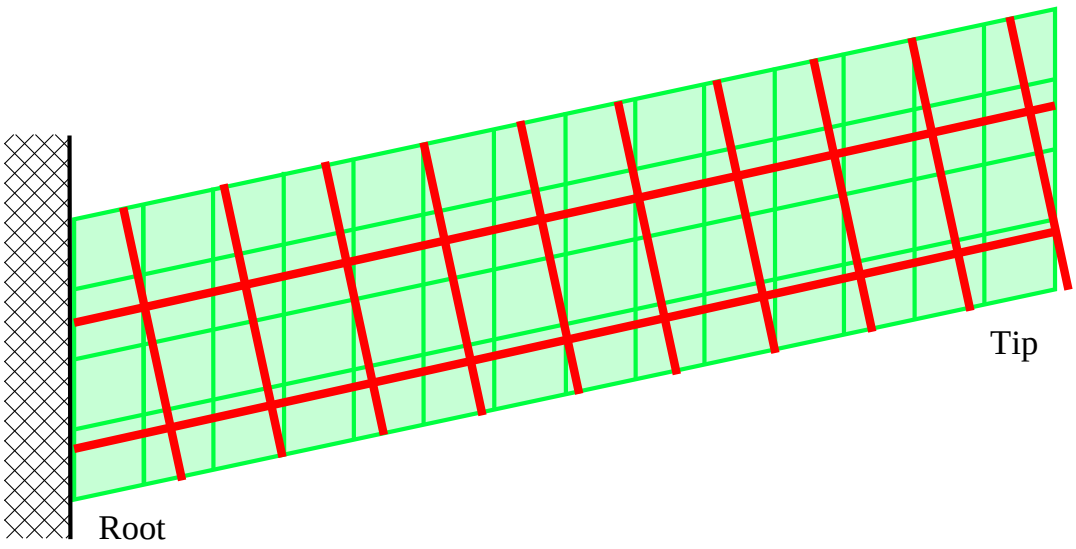

Figure 3.1: The structural model (red) on top of the aerodynamic lifting surface model (green).

spars, torsional constants of the spars and ribs, wing sweep angle, as well as dynamic pressure.

Although the wing is limited to a taper ratio of unity, the other variables will suffice to gain a good insight into this adaptive structures concept. Additionally, it should be remembered that the main objective of this study is to explore the ability of a rotating-spars concept to improve the efficiency of the wing by means of structural optimisation, as well as offering the possibility of roll control without traditional hinged devices (e.g. ailerons). It was therefore decided that a steady aeroelastic analytical model would achieve this goal, without the complexity of a full unsteady model. As stated previously, the induced drag is the only contribution to drag forces that the VLM is capable of computing, and even this becomes less accurate for swept (and tapered) wings [65, 101]. Although these limitations prevent accurate drag modelling and unsteady flow phenomenon such as flutter from being present in the analysis, and therefore result in an incomplete model, it is nevertheless a useful tool to perform steady aeroelastic analyses with.

3.2 Structural model

To construct an analytic aeroelastic wing model, the first step is to obtain the governing equations of equilibrium. For the steady aerodynamic case these will contain structural stiffness terms and aerodynamic stiffness terms.

There are various common methods that can be used to obtain the equations of motion for an aeroelastic system. However, in aircraft structures there are constraints which limit the motion of the structure e.g. motion of the wing root relative to the fuselage is constrained. Such constraints can introduce difficulties into the equations of motion; for instance, the constraint forces may appear as an additional set of unknowns that make solving the equations more challenging [114, 128]. The Principle of Virtual Displacements is a method that allows the equations of motion to be formulated in such a way as to eliminate these problems (there are other approaches too e.g. Lagrange's equations of motion, as applied in section 6.3.2) [110, 114].

3.2.1 Principle of Virtual Displacements

The Principle of Virtual Displacements (PVD) is a method that can be used to obtain the equations of motion of linear elastic structures [33, 128], and in doing so avoid dealing with unknown constraint forces. Let us introduce a virtual displacement $\delta\mathbf{u}$ which vanishes on $\mathbf{S}_u$ (the restraint surface i.e. the wing root) in order to satisfy the boundary condition, but is otherwise arbitrary. This virtual displacement must have a virtual work associated with it (in order for the elastic surface to have been displaced). The virtual displacement $\delta\mathbf{u}$ must satisfy [33, 64]

$$\delta\boldsymbol{\varepsilon} = \mathbf{D}^T\delta\mathbf{u} \tag{3.1}$$

where $\delta\boldsymbol{\varepsilon}$ is the virtual strain and $\mathbf{D}^T$ is the elastic stress-strain operator matrix. For a wing the PVD is defined as [33, 128]

$$\text{virtual strain energy} + \text{virtual inertial energy} = \text{virtual work} \tag{3.2}$$

and these three energies can be found from

$$\text{virtual strain energy} = \int_V \boldsymbol{\sigma}^T \delta\boldsymbol{\varepsilon}\, dV \tag{3.3}$$

$$\text{virtual inertial energy} = \int_V \rho_W\, \delta\mathbf{u}^T \frac{\partial^2 \mathbf{u}}{\partial t^2}\, dV \tag{3.4}$$

$$\text{virtual work} = \int_S \delta\mathbf{u}^T \mathbf{f}^S\, dS + \int_V \delta\mathbf{u}^T \mathbf{f}^B\, dV \tag{3.5}$$

In the equations above, V is the volume of the wing, S is the area of the wing, $\boldsymbol{\sigma}$ is the stress, ρ_W is the density of the wing, $\mathbf{f}^S$ are surface forces acting on the wing (e.g. aerodynamic pressures), and $\mathbf{f}^B$ are body forces acting on the wing (e.g. gravity). So using Eqs. 3.2 - 3.5

$$\int_V \boldsymbol{\sigma}^T \delta\boldsymbol{\varepsilon}\, dV = \int_S \delta\mathbf{u}^T \mathbf{f}^S\, dS + \int_V \delta\mathbf{u}^T \mathbf{f}^B\, dV - \int_V \rho_W\, \delta\mathbf{u}^T \frac{\partial^2 \mathbf{u}}{\partial t^2}\, dV \tag{3.6}$$

PVD applied to a framework wing

For a plate wing the displacement field $\mathbf{u}$ will contain both bending and torsional contributions, with the displacements being measured about the wing's elastic axis. However, the wing modelled herein is not solid and instead is a framework of ribs and spars. This can be modelled using a local displacement field for each spar.

Displacement field

A Cartesian coordinate system is defined for the spar swept back at an angle Λ from the flow normal, as shown in figure 3.2. The subscript j has been introduced

to denote a parameter in axes placed on the j^{th} spar. Note that the x_j-axis coincides with the neutral axis of the spar, but that the y_j- and z_j-axes are not fixed relative to the spar as it rotates, and instead are fixed relative to the wing. Firstly, assumptions about the displacement field $\mathbf{u_j}$ must be made; it is

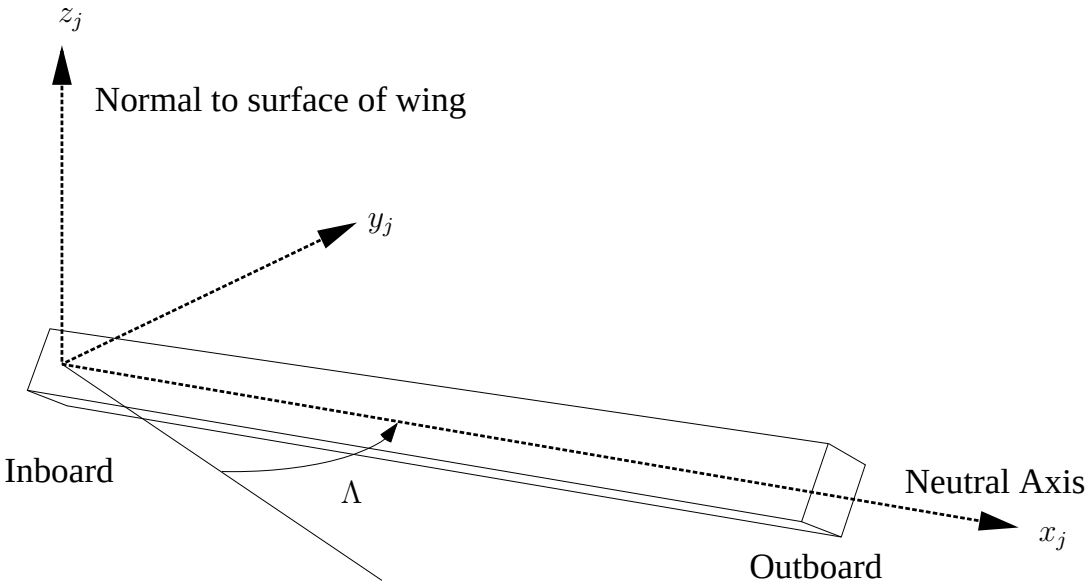

Figure 3.2: Cartesian coordinate system for j^{th} rotating spar.

assumed that any given spar has a high aspect ratio (with reference to figure 3.2, this implies its dimension in the x_j-direction >> dimensions in the Oy_jz_j-plane), allowing it to be treated as a beam, thus the kinematic assumptions of Euler-Bernoulli beam theory [143] may be applied:

1. Beam (spar) cross-section is non-deformable.

2. Transverse/bending displacement limited to Ox_jz_j-plane, where the z_j-axis is a normal to the wing's surface.

3. Axial displacements result from rotation of cross-section only i.e. shear deformation is neglected.

Using the above assumptions allows the displacement field for the spar to be defined as follows.

Spar bending contribution

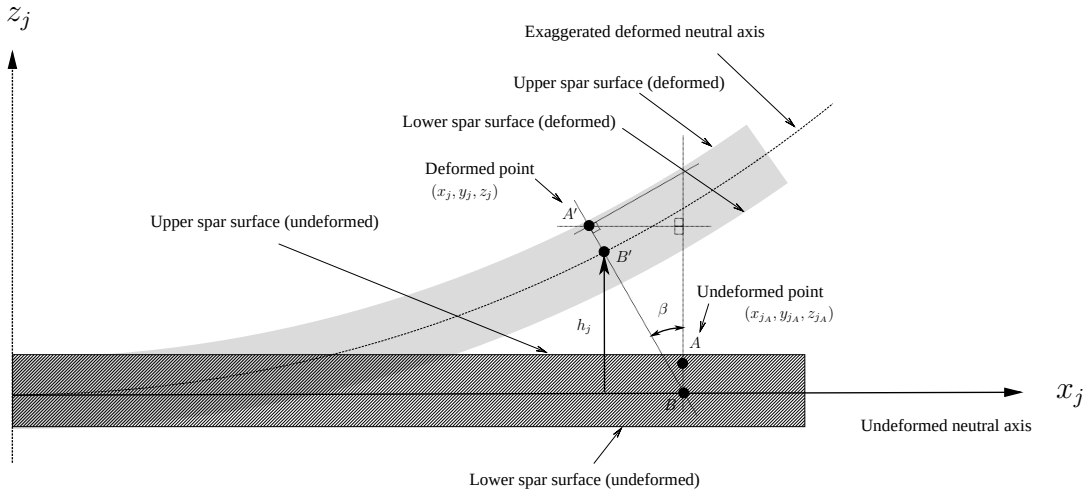

Figure 3.3: Spar bending in Ox_jz_j-plane.

Consider the spar bending in the Ox_jz_j-plane, as shown in figure 3.3. Point A is offset in the z_j-direction from a point B on the neutral axis (x_j-axis) of the undeformed spar. After bending, point A moves to point A' in the Cartesian coordinate system, and B moves to B'. $h_j(x_j, t)$ is the bending displacement of the neutral axis at the deformed x_j coordinate. Using the figure, an approximate expression for the displacement field due to pure bending can be derived. Firstly, the exact expression for the displacement field can be written as

$$\mathbf{u}_j(x_j, y_j, z_j, t) = [(x_j - x_{j_A}), (y_j - y_{j_A}), (z_j - z_{j_A})]^T \tag{3.7}$$

At this point Lagrange's notation shall be introduced for convenience i.e.

$$\frac{\partial(\ )}{\partial x} = (\ )' \qquad \frac{\partial^2(\ )}{\partial x^2} = (\ )'' \qquad \frac{\partial^3(\ )}{\partial x^3} = (\ )''' \qquad \frac{\partial^4(\ )}{\partial x^4} = (\ )'''' \qquad \text{etc.}$$

The slope of the deformed neutral axis at any spanwise location is (applying the small angle/slope assumption)

$$\begin{aligned} \arctan \frac{\partial h_j}{\partial x_j} &\approx \frac{\partial h_j}{\partial x_j} \\ &= h_j' \end{aligned} \tag{3.8}$$

By approximating the x_j coordinate of A' as the same as B', the slope of line A'-B is the same as that of the deformed neutral axis at B' (i.e. h_j'). Hence $\beta = h_j'$. So

$$\begin{aligned} x_j - x_{j_A} &= \left(x_{j_A} - z_j \tan h_j'\right) - x_{j_A} \\ &\approx -z_j h_j' \end{aligned} \tag{3.9}$$

From the second assumption stated previously

$$y_j - y_{j_A} = 0 \tag{3.10}$$

Finally

$$\begin{aligned} z_j - z_{j_A} &= \left(h_j + z_{j_A} \cos h_j'\right) - z_{j_A} \\ &\approx h_j + z_{j_A} - z_{j_A} \\ &= h_j \end{aligned} \tag{3.11}$$

Hence the displacement field due to pure bending of the spar is given approximately by

$$\mathbf{u}_j = \begin{bmatrix} -z_j h_j' & 0 & h_j \end{bmatrix}^T \tag{3.12}$$

Spar torsion contribution

Consider the cross-section of the spar deformed through a nose-up pitch angle of θ_j in the Oy_jz_j-plane, at some arbitrary spanwise location on the x_j-axis, as

shown in figure 3.4. After twisting, point A moves to point A'. Using this figure,

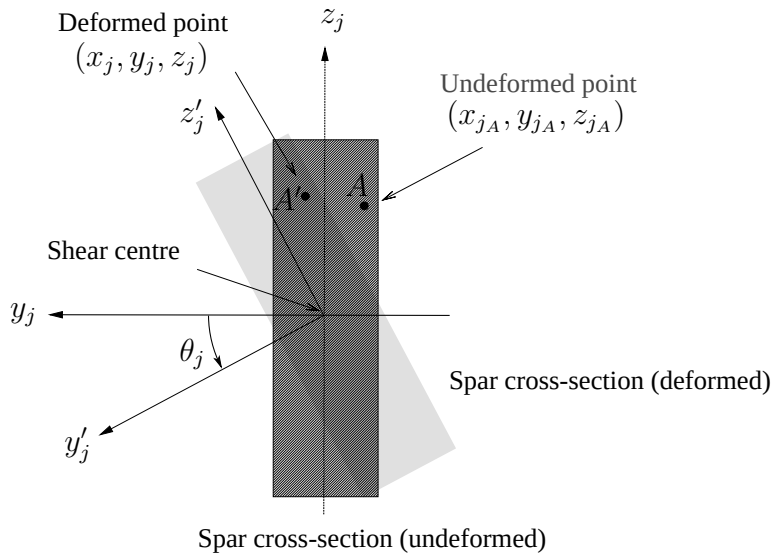

Figure 3.4: Spar twisting in Oy_jz_j-plane.

an approximate expression for the displacement field due to pure torsion can be derived.

Point A' defined in coordinate system $Ox'_jy'_jz'_j$ will have the same coordinate values as point A defined in coordinate system $Ox_jy_jz_j$. So with A and A' written in $Ox_jy_jz_j$ coordinates

$$A = \mathbf{T}A' \tag{3.13}$$

where $\mathbf{T}$ is the transformation matrix from coordinate system $Ox'_jy'_jz'_j$ to coordinate system $Ox_jy_jz_j$, defined as

$$\mathbf{T} = \begin{bmatrix} 1 & 0 & 0 \\ 0 & \cos\theta_j & \sin\theta_j \\ 0 & -\sin\theta_j & \cos\theta_j \end{bmatrix} \tag{3.14}$$

And the displacement field is defined in coordinate system $Ox_jy_jz_j$ as

$$\mathbf{u}_j(x_j, y_j, z_j, t) = [(x_j - x_{j_A}), (y_j - y_{j_A}), (z_j - z_{j_A})]^T \tag{3.15}$$

So

$$x_j - x_{j_A} = 0 \tag{3.16}$$

and

$$y_j - y_{j_A} = y_j \cos\theta_j + z_j \sin\theta_j - y_j \tag{3.17}$$

which becomes (upon application of the small angle approximation)

$$y_j - y_{j_A} \approx z_j \theta_j \tag{3.18}$$

and finally

$$\begin{aligned} z_j - z_{j_A} &= -y_j \sin\theta_j + z_j \cos\theta_j - z_j \\ &\approx -y_j \theta_j \end{aligned} \tag{3.19}$$

Hence the approximate displacement field due to pure torsion of the spar is

$$\mathbf{u}_j = \begin{bmatrix} 0 & z_j\theta_j & -y_j\theta_j \end{bmatrix}^T \tag{3.20}$$

Spar bending and torsion together

The general displacement field for the j^{th}spar bending and twisting simultaneously is simply the sum of the bending and torsion contributions (i.e. the sum of Eqs. 3.12 and 3.20):

$$\mathbf{u}_j = \begin{bmatrix} -z_j h_j' & z_j\theta_j & (h_j - y_j\theta_j) \end{bmatrix}^T \tag{3.21}$$

Virtual strain energy in spars

The elastic stress-strain operator matrix for the spar coordinate system is given by [23]

$$\mathbf{D}_j = \begin{bmatrix} \dfrac{\partial}{\partial x_j} & 0 & 0 & \dfrac{\partial}{\partial y_j} & 0 & \dfrac{\partial}{\partial z_j} \\ 0 & \dfrac{\partial}{\partial y_j} & 0 & \dfrac{\partial}{\partial x_j} & \dfrac{\partial}{\partial z_j} & 0 \\ 0 & 0 & \dfrac{\partial}{\partial z_j} & 0 & \dfrac{\partial}{\partial y_j} & \dfrac{\partial}{\partial x_j} \end{bmatrix} \tag{3.22}$$

So substituting Eq. 3.21 (modified for a *virtual* displacement) and Eq. 3.22 into Eq. 3.1 gives the virtual strain of the spar as

$$\delta\boldsymbol{\varepsilon}_j = \begin{bmatrix} -z_j\,\delta h_j'' & 0 & 0 & z_j\,\delta\theta_j' & 0 & -y_j\,\delta\theta_j' \end{bmatrix}^T \tag{3.23}$$

Now, stress is the product of linear strains ($\delta\boldsymbol{\varepsilon}(1:3)$) and Young's modulus E, plus the product of shearing strains ($\delta\boldsymbol{\varepsilon}(4:6)$) and shear modulus G [23, 58] i.e.

$$\boldsymbol{\sigma}_j = \begin{bmatrix} -z_j E h_j'' & 0 & 0 & z_j G\theta_j' & 0 & -y_j G\theta_j' \end{bmatrix}^T \tag{3.24}$$

So the virtual strain energy (from Eq. 3.3) for the j^{th} spar is

$$\int_V \boldsymbol{\sigma}_j^T \delta\boldsymbol{\varepsilon}_j\, dV = \int_V \begin{bmatrix} -z_j E h_j'' & 0 & 0 & z_j G\theta_j' & 0 & -y_j G\theta_j' \end{bmatrix} \begin{bmatrix} -z_j\,\delta h_j'' \\ 0 \\ 0 \\ z_j\,\delta\theta_j' \\ 0 \\ -y_j\,\delta\theta_j' \end{bmatrix} dV$$

$$= \int_V \left(z_j^2 E h_j''\,\delta h_j'' + z_j^2 G\theta_j'\,\delta\theta_j' + y_j^2 G\theta_j'\,\delta\theta_j' \right) dV$$

$$= \int_V z_j^2 E h_j'' \, \delta h_j'' \, dV + \int_V \left(z_j^2 + y_j^2\right) G\theta_j' \, \delta\theta_j' \, dV$$

$$= \int_A z_j^2 \, dA \int_0^l E h_j'' \, \delta h_j'' \, dx_j + \int_A \left(z_j^2 + y_j^2\right) dA \int_0^l G\theta_j' \, \delta\theta_j' \, dx_j$$

$$= \int_0^l \left(E I_{y_j y_j} h_j'' \, \delta h_j'' + G I_{x_j x_j} \theta_j' \, \delta\theta_j'\right) dx_j \tag{3.25}$$

In Eq. 3.25 V, A and l are the volume, cross-sectional area and length of the spar respectively. $I_{y_j y_j}$ is the second moment of area of the spar about its neutral axis in the $Ox_j z_j$-plane, and is defined as [57, 130]

$$I_{y_j y_j} = \int_A z_j^2 \, dA \tag{3.26}$$

The yy subscript will be dropped and replaced with s to indicate a spar parameter. $I_{x_j x_j}$ is the polar second moment of area of the spar, defined as [130]

$$I_{x_j x_j} = \int_A \left(z_j^2 + y_j^2\right) dA \tag{3.27}$$

In general, torsion of a beam will be accompanied by warping (with a few exceptions that do not apply here e.g. circular cross-section, axial restraint at free-end to ensure sections remain plane); this warping distorts the torsional rigidity of the spar, and the polar second moment of area has to be replaced by the St. Venant torsion constant J_{s_j} for Eq. 3.25 to be accurate [59, 76, 136].

Second moment of area about an inclined axis

Note that in general, for a rotating spars wing, none of the spars' principal axes will coincide with the wing-orientated y_j-axes (about which I_{s_j} is defined). Referring to figure 3.5, I_{s_j} is given by [58, 130]

$$I_{s_j} = I_{y_j y_j} = I_{y_j' y_j'} \cos^2 \phi_j - I_{z_j' y_j'} \sin 2\phi_j + I_{z_j' z_j'} \sin^2 \phi_j \tag{3.28}$$

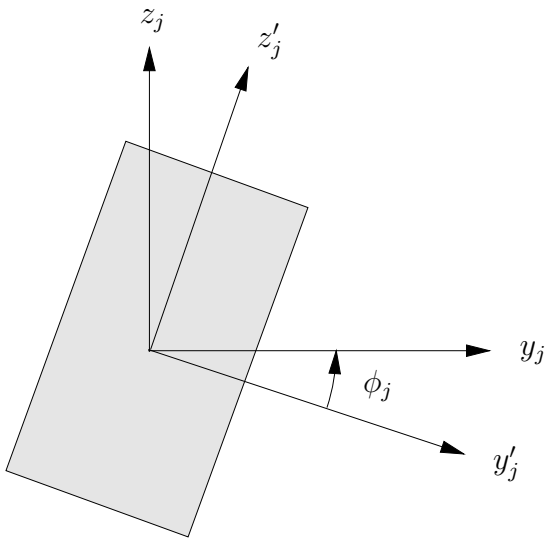

Figure 3.5: Second moment of area about inclined axes.

where $I_{z'_j z'_j}$ is the second moment of area of the spar about its neutral axis in the $Ox'_j y'_j$-plane, $I_{y'_j y'_j}$ is the second moment of area of the spar about its neutral axis in the $Ox'_j z'_j$-plane, and $I_{y'_j z'_j}$ is the product moment of area of the spar about its neutral axis, and since y'_j and z'_j are the principal axes of the cross-section, $I_{y'_j z'_j} = 0$.

It is assumed Young's modulus E, and shear modulus G are uniform throughout the spar. Additionally, the second moment of area I_{s_j} and St. Venant's torsion constant J_{s_j} are limited to being constant at all locations along spar j, although, in general, these parameters will be different for any given spar j. Separating Eq. 3.25 into the virtual strain energy from the bending of the spar δU_{h_j}, and the virtual strain energy from the torsion of the spar δU_{θ_j} gives

$$\delta U_{h_j} = EI_{s_j} \int_0^l h''_j \, \delta h''_j \, dx_j \tag{3.29}$$

$$\delta U_{\theta_j} = GJ_{s_j} \int_0^l \theta'_j \, \delta \theta'_j \, dx_j \tag{3.30}$$

As discussed in section 3.2.2, the displacement field will be approximated using suitable interpolation functions. As the wing comprises of two spars, the wing

deflections can be approximated by using two matrices of interpolation functions (one per spar, modelling the bending deflections of the spars, $h_1(x_1, t)$ and $h_2(x_2, t)$); this is sufficient and manipulation of the spars' bending deflections allows spar torsion and rib torsion to be accurately described also.

Therefore, Eqs. 3.29 and 3.30 must firstly be expressed in terms of $h_1(x_1, t)$ and $h_2(x_2, t)$. These can be easily substituted into Eq. 3.29, to obtain expressions for the bending virtual strain energy of spar 1 and spar 2

$$\delta U_{h_1} = EI_{s_1} \int_0^l h_1'' \, \delta h_1'' \, dx_1 \tag{3.31}$$

$$\delta U_{h_2} = EI_{s_2} \int_0^l h_2'' \, \delta h_2'' \, dx_2 \tag{3.32}$$

which gives the total virtual strain energy due to the bending deformation of the spars as

$$\delta U_h = EI_{s_1} \int_0^l h_1'' \, \delta h_1'' \, dx_1 + EI_{s_2} \int_0^l h_2'' \, \delta h_2'' \, dx_2 \tag{3.33}$$

However, obtaining an expression for the torsional virtual strain energy is more involved.

Using figure 3.6, Eq. 3.30 can be written in terms of h_1 and h_2. The spar axis from which h_1 is defined (forward spar) is positioned at a distance fc aft of the leading-edge and that from which h_2 is defined (rear spar) at a distance rc aft of the leading-edge, where c is the wing chord.

Assuming that the wing will twist through a small angle θ and that the wing has a rigid cross-section

$$\theta\left(x_1, x_2\right) \approx \left(\frac{1}{c\left(r-f\right)}\right)\left(h_1\left(x_1\right) - h_2\left(x_2\right)\right) \tag{3.34}$$

Noting that the spars are twisted by bending moments at junctions with the ribs (i.e. discrete point loads corresponding to the spanwise positions of the ribs), the torsional displacement θ_j of the spar will follow a linear relationship between

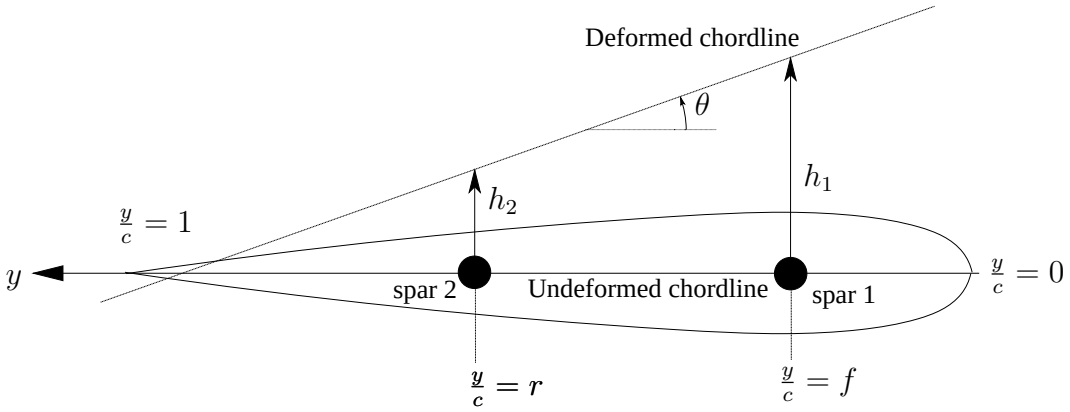

Figure 3.6: Spars' bending deflection h_1 and h_2.

adjacent ribs i.e.

$$\theta_j = Ax_j + C \tag{3.35}$$

In Eq. 3.35, A and C are constants which will be different between different pairs of ribs. Consider a section of spar between two ribs (a and b). At rib a

$$\theta_j\left(x_{j_a}\right) = Ax_{j_a} + C \tag{3.36}$$

Note that for values of x_j corresponding to a rib location, the expression for θ given in Eq. 3.34 holds also for θ_j. Substituting this into Eq. 3.36 gives

$$Ax_{j_a} + C = \frac{h_1\left(x_{j_a}\right) - h_2\left(x_{j_a}\right)}{c\left(r - f\right)} \tag{3.37}$$

Similarly at rib b

$$Ax_{j_b} + C = \frac{h_1\left(x_{j_b}\right) - h_2\left(x_{j_b}\right)}{c\left(r - f\right)} \tag{3.38}$$

Subtracting Eq. 3.37 from Eq. 3.38 yields

$$A\left(x_{j_b} - x_{j_a}\right) = \frac{h_1\left(x_{j_b}\right) - h_1\left(x_{j_a}\right) + h_2\left(x_{j_a}\right) - h_2\left(x_{j_b}\right)}{c\left(r - f\right)} \tag{3.39}$$

So

$$A = \frac{h_1\left(x_{j_b}\right) - h_1\left(x_{j_a}\right) + h_2\left(x_{j_a}\right) - h_2\left(x_{j_b}\right)}{c\left(r - f\right)\left(x_{j_b} - x_{j_a}\right)} \tag{3.40}$$

Now, substituting Eq. 3.40 into Eq. 3.37 gives

$$C = \frac{h_1\left(x_{j_a}\right) - h_2\left(x_{j_a}\right)}{c\left(r-f\right)} - Ax_{j_a} \tag{3.41}$$

So for the j^{th} spar, which can be separated into a number of sections, where each section has a rib (or the wing root) at either end, for the k^{th} section

$$\theta_{j_k}\left(x_j\right) = A_k x_j + C_k \tag{3.42}$$

where

$$A_k = \frac{h_1\left(x_{j_{k+1}}\right) - h_1\left(x_{j_k}\right) + h_2\left(x_{j_k}\right) - h_2\left(x_{j_{k+1}}\right)}{c\left(r-f\right)\left(x_{j_{k+1}} - x_{j_k}\right)} \tag{3.43}$$

and

$$C_k = \frac{h_1\left(x_{j_k}\right) - h_2\left(x_{j_k}\right)}{c\left(r-f\right)} - Ax_{j_k} \tag{3.44}$$

Finally, differentiating Eq. 3.42 once with respect to x_j gives

$$\theta'_{j_k} = A_k \tag{3.45}$$

Substituting Eq. 3.45 into Eq. 3.30, and noting that the expression has been modified slightly to account for the step changes in A_k along the spar which has m ribs (i.e. m spar sections),

$$\delta U_{\theta_j} = GJ_{s_j} \sum_{k=1}^{m} A_k\, \delta A_k \int_{x_{j_k}}^{x_{j_{k+1}}} dx_j \tag{3.46}$$

Substituting Eq. 3.43 into Eq. 3.46, and evaluating the integral gives

$$\begin{aligned}\delta U_{\theta_j} = \frac{GJ_{s_j}}{c^2\left(r-f\right)^2} \sum_{k=1}^{m} \frac{1}{\left(x_{j_{k+1}} - x_{j_k}\right)^2} \big(&h_{1_{k+1}}\,\delta h_{1_{k+1}} - h_{1_{k+1}}\,\delta h_{1_k} + h_{1_{k+1}}\,\delta h_{2_k} \\ &- h_{1_{k+1}}\,\delta h_{2_{k+1}} - h_{1_k}\,\delta h_{1_{k+1}} + h_{1_k}\,\delta h_{1_k} - h_{1_k}\,\delta h_{2_k} + h_{1_k}\,\delta h_{2_{k+1}} \\ &+ h_{2_k}\,\delta h_{1_{k+1}} - h_{2_k}\,\delta h_{1_k} + h_{2_k}\,\delta h_{2_k} - h_{2_k}\,\delta h_{2_{k+1}} - h_{2_{k+1}}\delta h_{1_{k+1}} \\ &+ h_{2_{k+1}}\,\delta h_{1_k} - h_{2_{k+1}}\,\delta h_{2_k} + h_{2_{k+1}}\,\delta h_{2_{k+1}}\big)\left(x_{j_{k+1}} - x_{j_k}\right)\end{aligned} \tag{3.47}$$

The k and $k+1$ subscripts attached to h_j and δh_j indicate the position where h_j and δh_j are to be evaluated e.g. h_{2_k} implies that h_2 is to be evaluated at x_{2_k}. Additionally, notice that

$$\sum_{k=1}^{m} \left(x_{j_{k+1}} - x_{j_k} \right) = l \tag{3.48}$$

where l is the length of the spar. Following the geometric constraints stated in the introduction to this chapter, both spars have the same length. The torsional virtual strain energy of both spars is then

$$\begin{aligned} \delta U_\theta = \frac{G\left(J_{s_1} + J_{s_2}\right)}{c^2 \left(r-f\right)^2 l} \sum_{k=1}^{m} \big(& h_{1_{k+1}} \delta h_{1_{k+1}} - h_{1_{k+1}} \delta h_{1_k} + h_{1_{k+1}} \delta h_{2_k} \\ & - h_{1_{k+1}} \delta h_{2_{k+1}} - h_{1_k} \delta h_{1_{k+1}} + h_{1_k} \delta h_{1_k} - h_{1_k} \delta h_{2_k} + h_{1_k} \delta h_{2_{k+1}} \\ & + h_{2_k} \delta h_{1_{k+1}} - h_{2_k} \delta h_{1_k} + h_{2_k} \delta h_{2_k} - h_{2_k} \delta h_{2_{k+1}} - h_{2_{k+1}} \delta h_{1_{k+1}} \\ & + h_{2_{k+1}} \delta h_{1_k} - h_{2_{k+1}} \delta h_{2_k} + h_{2_{k+1}} \delta h_{2_{k+1}} \big) \end{aligned} \tag{3.49}$$

Virtual strain energy in ribs

Modelling the ribs as torsional springs, the strain energy for rib k is [59, 76]

$$U_{\beta_k} = \frac{1}{2} M_k \Delta\beta_k \tag{3.50}$$

In Eq. 3.50 M_k is the moment exerted on rib k by the spars at either end, and $\Delta\beta_k$ is the torsional deformation of the rib between the spars. For rib k meeting spar 1 at position x_{1_k} and spar 2 at x_{2_k}

$$\Delta\beta_k \left(x_{1_k}, x_{2_k}\right) = h_1' \left(x_{1_k}\right) - h_2' \left(x_{2_k}\right) \tag{3.51}$$

Rearranging Eq. 3.34 gives

$$h_1 \left(x_1\right) - h_2 \left(x_2\right) \approx c \left(r-f\right) \theta \left(x_1, x_2\right) \tag{3.52}$$

Hence

$$h_1'(x_1) - h_2'(x_2) \approx c(r-f)\,\theta'(x_1, x_2) \tag{3.53}$$

So substituting Eq. 3.53 into Eq. 3.51 gives

$$\Delta\beta_k \approx c(r-f)\,\theta' \tag{3.54}$$

Now, the moment M_k exerted on the k^{th} rib by the spars is equivalent to the product of the rib's torsional stiffness k_{β_k} (assumed constant along the length of the rib) and the torsional deformation of the rib i.e.

$$M_k = k_{\beta_k}\,\Delta\beta_k = k_{\beta_k} c(r-f)\,\theta' \tag{3.55}$$

Substituting Eqs. 3.54 and 3.55 into Eq. 3.50 gives

$$U_{\beta_k} = \frac{1}{2} k_{\beta_k} c^2 (r-f)^2\,\theta'^2 \tag{3.56}$$

To express the above as the *virtual* strain energy associated with the virtual displacement $\delta\theta$ it is manipulated as follows [33, 128]:

$$\begin{aligned}
\delta U_{\beta_k} &= \frac{d}{d\theta'} U_{\beta_k}\,\delta\theta' \\
&= \frac{d}{d\theta'}\left(\frac{1}{2} k_{\beta_k} c^2 (r-f)^2\,\theta'^2\right)\delta\theta' \\
&= k_{\beta_k} c^2 (r-f)^2\,\theta'\,\delta\theta'
\end{aligned} \tag{3.57}$$

The rib's torsional stiffness is simply [59, 76]

$$k_{\beta_k} = \frac{G J_{r_k}}{c(r-f)} \tag{3.58}$$

where J_{r_k} is the St. Venant torsion constant of the k^{th} rib. Substituting Eq. 3.58 into Eq. 3.57 gives

$$\delta U_{\beta_k} = G J_{r_k} c(r-f)\,\theta'\,\delta\theta' \tag{3.59}$$

Using Eq. 3.34 allows Eq. 3.59 to be expressed in terms of h_1 and h_2 as

$$\delta U_{\beta_k} = \frac{GJ_{r_k}}{c\,(r-f)}\Big(h_1'\,(x_{1_k}) - h_2'\,(x_{2_k})\Big)\Big(\delta h_1'\,(x_{1_k}) - \delta h_2'\,(x_{2_k})\Big) \tag{3.60}$$

So for the wing (all m ribs), the total virtual strain energy associated with twisting deformations of the ribs is given by

$$\delta U_{\beta} = \frac{G}{c\,(r-f)}\sum_{k=1}^{m} J_{r_k}\Big(h_1'\,(x_{1_k}) - h_2'\,(x_{2_k})\Big)\Big(\delta h_1'\,(x_{1_k}) - \delta h_2'\,(x_{2_k})\Big) \tag{3.61}$$

The total virtual strain energy is the sum of the individual contributions:

$$\delta U = \delta U_h + \delta U_\theta + \delta U_\beta \tag{3.62}$$

Virtual inertial energy

The wing is being considered under static aerodynamic conditions therefore (virtual) inertial energy is zero.

Virtual work

Assuming the wing's undisplaced position accounts for gravity acting on the mass of the wing, the only virtual work contributions are from the surface forces ($\mathbf{f}^B = \mathbf{0}$) i.e. lift per unit span $\bar{L}$ and pitching moment per unit span about the aerodynamic centre $\bar{M}_{ac}$ (both acting along/about the aerodynamic centre). Drag is unimportant since it acts in the Ox_jy_j-plane, in which zero structural deformation is assumed. An alternative definition of the virtual work to that given by Eq. 3.5 is the product of forces and the resulting virtual bending deformation, plus the product of moments and the resulting virtual torsional deformation [158]. For a wing with a spanwise variation in lift and pitching moment, this can be expressed as

$$\delta^* W = \int_0^l \bar{L}\cos\Lambda\,\delta h_{ac}\,dx_{ac} + \int_0^l \bar{M}_{ac}\cos\Lambda\,\delta\theta\,dx_{ac} \tag{3.63}$$

The cosine terms are required in Eq. 3.63 since the aerodynamic centre x_{ac} along which the integrals are evaluated lies at an angle of Λ (wing sweep angle) to the spanwise direction along which $\bar{L}$ and $\bar{M}_{ac}$ are defined. The simplification is made that the aerofoil being modelled is symmetric about its chordline i.e. $\bar{M}_{ac} = 0$. So

$$\delta^* W = \int_0^l \bar{L} \cos\Lambda \, \delta h_{ac} \, dx_{ac} \tag{3.64}$$

The next step is to express Eq. 3.64 in terms of h_1 and h_2. Let $q_c c$ be the distance that the wing aerodynamic centre lies aft of the leading-edge. Then using Eq. 3.34

$$\begin{aligned} h_{ac} &= h_1(x_1) + c(f - q_c)\sin\theta \\ &\approx h_1(x_1) + c(f - q_c)\theta \\ &= h_1(x_1) + \frac{f - q_c}{r - f}\Big(h_1(x_1) - h_2(x_2)\Big) \end{aligned} \tag{3.65}$$

Let

$$\xi = \frac{f - q_c}{r - f} \tag{3.66}$$

Substituting Eq. 3.66 into Eq. 3.65 and then that in terms of *virtual* displacements in turn into Eq. 3.64 gives

$$\delta^* W = (1 + \xi) \int_0^l \bar{L} \cos\Lambda \, \delta h_1(x_1) \, dx_1 - \xi \int_0^l \bar{L} \cos\Lambda \, \delta h_2(x_2) \, dx_2 \tag{3.67}$$

3.2.2 Rayleigh-Ritz method

The governing PVD equation can be written as

$$\delta U_h + \delta U_\theta + \delta U_\beta = \delta^* W \tag{3.68}$$

into which Eqs. 3.33, 3.49, 3.61 and 3.67 must be substituted. Inspection of these expressions reveals that the governing PVD equation will be a partial differential equation, which is difficult to solve. The Rayleigh-Ritz method allows partial differential equations to be easily solved as an approximate finite solution (alternative methods include Galerkin and Lagrange characteristic) [114], in this case by separating the displacement field of the spars into a spatial and a time-dependent part i.e.

$$\begin{aligned}\mathbf{u}_j(x,y,z,t) &\approx \mathbf{F}^T(x,y,z)\mathbf{q}(t) \\ &= \sum_{i=1}^{n} F_i(x,y,z)q_i(t) \end{aligned} \tag{3.69}$$

$\mathbf{F}$ is a $nx3$ matrix containing appropriate shape/interpolation functions F_i (assumed modes), which satisfy the wing geometric boundary conditions, and $\mathbf{q}$ is a vector of length n containing unknown functions of time q_i. Therefore $\mathbf{q}$ is the set of generalised coordinates for the model. Generalised coordinates are a set of independent parameters which are sufficient to describe the system's motion [158] and for an assumed modes approach they define the amount of each assumed mode present in the motion [141]. The products of each shape function and generalised coordinate are summed to provide an approximation to the true mode. The approximation will become more accurate as the number of included functions n is increased. Also, as the shape functions become closer to the exact modes of the system, the number of functions required to obtain a given degree of accuracy will decrease [114].

Expressing the equations of equilibrium in terms of shape functions

To apply the Rayleigh-Ritz method to the displacement field herein, it is noted that instead of describing the displacement field with a single variable in terms of its x, y and z coordinates, it is being describing using two variables (h_1 and h_2) representing bending along two different spanwise wing axes, both of which are

only dependent on either x_1 or x_2. Hence it becomes necessary to introduce two arbitrary and distinct matrices of interpolation functions as well as two unknown vectors of generalised coordinates (since this is a steady model, these are not functions of time):

$$\begin{aligned} h_1(x_1,t) &\approx \boldsymbol{\psi}^T(x_1)\boldsymbol{\zeta} \\ &= \sum_{a=1}^{A} \psi_a(x_1)\zeta_a \end{aligned} \tag{3.70}$$

$$\begin{aligned} h_2(x_2,t) &\approx \boldsymbol{\phi}^T(x_2)\boldsymbol{\beta} \\ &= \sum_{b=1}^{B} \phi_b(x_2)\beta_b \end{aligned} \tag{3.71}$$

In this case $\boldsymbol{\psi}$ and $\boldsymbol{\phi}$ are Ax1 and Bx1 matrices (i.e. vectors) containing appropriate shape/ interpolation functions ψ_a and ϕ_b respectively, and $\boldsymbol{\zeta}$ and $\boldsymbol{\beta}$ are vectors of length A and B containing unknown generalised coordinates ζ_a and β_b respectively. Substituting Eqs. 3.70 and 3.71 firstly into Eq. 3.33 gives

$$\delta U_h = \delta\boldsymbol{\eta}^T \begin{bmatrix} EI_{s_1}\int_0^l \boldsymbol{\psi}''\boldsymbol{\psi}''^T\,dx_1 & \mathbf{0}_{A,B} \\ \mathbf{0}_{B,A} & EI_{s_2}\int_0^l \boldsymbol{\phi}''\boldsymbol{\phi}''^T\,dx_2 \end{bmatrix} \boldsymbol{\eta} \tag{3.72}$$

where

$$\boldsymbol{\eta}^T = \begin{bmatrix} \boldsymbol{\zeta}^T & \boldsymbol{\beta}^T \end{bmatrix} \tag{3.73}$$

and next into Eq. 3.49:

$$\delta U_\theta = \frac{G\left(J_{s_1}+J_{s_2}\right)}{c^2\left(r-f\right)^2 l}\delta\boldsymbol{\eta}^T \ldots$$

$$\ldots \sum_{k=1}^{m} \begin{bmatrix} \begin{pmatrix} \boldsymbol{\psi}_{k+1}\boldsymbol{\psi}_{k+1}^T - \boldsymbol{\psi}_{k+1}\boldsymbol{\psi}_k^T \\ -\boldsymbol{\psi}_k\boldsymbol{\psi}_{k+1}^T + \boldsymbol{\psi}_k\boldsymbol{\psi}_k^T \end{pmatrix} & \begin{pmatrix} \boldsymbol{\psi}_{k+1}\boldsymbol{\phi}_k^T - \boldsymbol{\psi}_{k+1}\boldsymbol{\phi}_{k+1}^T \\ -\boldsymbol{\psi}_k\boldsymbol{\phi}_k^T + \boldsymbol{\psi}_k\boldsymbol{\phi}_{k+1}^T \end{pmatrix} \\ symmetric & \begin{pmatrix} \boldsymbol{\phi}_{k+1}\boldsymbol{\phi}_{k+1}^T - \boldsymbol{\phi}_{k+1}\boldsymbol{\phi}_k^T \\ -\boldsymbol{\phi}_k\boldsymbol{\phi}_{k+1}^T + \boldsymbol{\phi}_k\boldsymbol{\phi}_k^T \end{pmatrix} \end{bmatrix} \boldsymbol{\eta} \tag{3.74}$$

The ellipsis indicate that the two terms should be read together i.e. the first term multiplied by the second term. Next, Eqs. 3.70 and 3.71 are substituted into Eq. 3.61 giving

$$\delta U_\beta = \frac{G}{c\left(r-f\right)}\delta\boldsymbol{\eta}^T \sum_{k=1}^{m} J_{r_k} \begin{bmatrix} \boldsymbol{\phi}_k'\boldsymbol{\phi}_k'^T & -\boldsymbol{\phi}_k'\boldsymbol{\psi}_k'^T \\ symmetric & \boldsymbol{\psi}_k'\boldsymbol{\psi}_k'^T \end{bmatrix} \boldsymbol{\eta} \tag{3.75}$$

In Eqs. 3.74 and 3.75 the k and $k+1$ subscripts attached to $\boldsymbol{\psi}$ and $\boldsymbol{\phi}$ indicate the positions where $\boldsymbol{\psi}$ and $\boldsymbol{\phi}$ are to be evaluated e.g. $\boldsymbol{\phi}_k$ implies that $\boldsymbol{\phi}$ is to be evaluated at x_{2_k}. Finally, Eqs. 3.70 and 3.71 are substituted into Eq. 3.67

$$\delta^* W = \cos\Lambda\,\delta\boldsymbol{\eta}^T \begin{bmatrix} (1+\xi)\int_0^l \boldsymbol{\psi}\bar{L}\,dx_1 \\ -\xi\int_0^l \boldsymbol{\phi}\bar{L}\,dx_2 \end{bmatrix} \tag{3.76}$$

Substituting Eqs. 3.72 - 3.76 into Eq. 3.68 yields

$$\delta\boldsymbol{\eta}^T \left(\begin{bmatrix} EI_{s_1}\int_0^l \boldsymbol{\psi}''\boldsymbol{\psi}''^T\,dx_1 & \mathbf{0}_{A,B} \\ \mathbf{0}_{B,A} & EI_{s_2}\int_0^l \boldsymbol{\phi}''\boldsymbol{\phi}''^T\,dx_2 \end{bmatrix}$$

$$+\frac{G\left(J_{s_1}+J_{s_2}\right)}{c^2\left(r-f\right)^2 l}\sum_{k=1}^{m}\begin{bmatrix}\begin{pmatrix}\boldsymbol{\psi}_{k+1}\boldsymbol{\psi}_{k+1}^T-\boldsymbol{\psi}_{k+1}\boldsymbol{\psi}_k^T\\-\boldsymbol{\psi}_k\boldsymbol{\psi}_{k+1}^T+\boldsymbol{\psi}_k\boldsymbol{\psi}_k^T\end{pmatrix} & \begin{pmatrix}\boldsymbol{\psi}_{k+1}\boldsymbol{\phi}_k^T-\boldsymbol{\psi}_{k+1}\boldsymbol{\phi}_{k+1}^T\\-\boldsymbol{\psi}_k\boldsymbol{\phi}_k^T+\boldsymbol{\psi}_k\boldsymbol{\phi}_{k+1}^T\end{pmatrix}\\ symmetric & \begin{pmatrix}\boldsymbol{\phi}_{k+1}\boldsymbol{\phi}_{k+1}^T-\boldsymbol{\phi}_{k+1}\boldsymbol{\phi}_k^T\\-\boldsymbol{\phi}_k\boldsymbol{\phi}_{k+1}^T+\boldsymbol{\phi}_k\boldsymbol{\phi}_k^T\end{pmatrix}\end{bmatrix}$$

$$+\frac{G}{c\left(r-f\right)}\sum_{k=1}^{m}J_{r_k}\begin{bmatrix}\boldsymbol{\phi}_k'\boldsymbol{\phi}_k'^T & -\boldsymbol{\phi}_k'\boldsymbol{\psi}_k'^T\\ symmetric & \boldsymbol{\psi}_k'\boldsymbol{\psi}_k'^T\end{bmatrix}\Bigg)\boldsymbol{\eta}$$

$$=\delta\boldsymbol{\eta}^T\cos\Lambda\begin{bmatrix}\left(1+\xi\right)\int_0^l\boldsymbol{\psi}\bar{L}\,dx_1\\-\xi\int_0^l\boldsymbol{\phi}\bar{L}\,dx_2\end{bmatrix} \tag{3.77}$$

Choice of interpolation functions

Since the shape functions are modelling the bending deflections of the spars, any set of functions capable of jointly representing the boundary conditions and bending modes of a beam are acceptable [114]. In general, the closer the functions are to the exact modes, the lower the number of terms are required for convergence. An investigation was performed to compare the convergence of using polynomial shape functions against exact expressions for beam bending modes. For the model studied herein, no obvious advantage was observed by using the exact modes, whereas the assumed polynomial modes representation is considerably easier to code and significantly less computationally expensive. Therefore, it was decided to use a set of polynomial functions as the assumed modes:

$$\psi_a=\left(\frac{x_1}{l}\right)^{a+1} \tag{3.78}$$

$$\phi_b=\left(\frac{x_2}{l}\right)^{b+1} \tag{3.79}$$

To solve the system described in Eq. 3.77, the first step is to develop an expression for the lift per unit span $\bar{L}$. Strip theory was considered too inaccurate here as it neglects tip effects, and instead assumes 2D flow [15]. Alternatively, a vortex-lattice aerodynamic model provides an accurate representation of steady 3D flow [85, 141]; section 3.3 explains and describes this method.

3.2.3 Note on spar efficiency and lateral buckling

Typically the main spars in aircraft wings are I-beams or C-channel beams; these structures perform well at resisting bending loads. The flange sections of the beam contain most of the material and are designed to resist axial compression and tension loads, whilst the thin web is designed to carry shear loads. Consequently, by using I- or C-shaped cross-sections, spars can offer the required flexural rigidity whilst having a relatively low weight [103].

The analytical model that has been developed in this section is applicable to a spar of any cross-sectional shape (for simplicity, the figures used depicted spars of rectangular cross-section) provided the spanwise dimension is large relative to the cross-sectional dimensions, therefore allowing Euler-Bernoulli beam theory to be applied.

Despite this, both the analytical study presented in chapter 4 and the experimental wing model in chapter 5 use spars of rectangular cross-section; this is convenient as a proof-of-concept since it is a simple shape, offers a high ratio of spar second moments of area $I_{y'y'}/I_{z'z'}$, which improves the effectiveness of the concept (see section 4.3.3), and for the experimental stage is easier to integrate with bearings.

However, beams of rectangular cross-section are not only inefficient at resisting bending loads, they are also much more susceptible to lateral buckling; for any beam, at a critical bending load value, the beam will become unstable and buckle laterally. Typically, this failure mode need not be examined as the yield point is reached first. However, for beams where the flexural rigidity in the plane

of bending is large in comparison with the lateral flexural rigidity (i.e. large $I_{y'y'}/I_{z'z'}$), and for beams where the length of the beam is much greater than the cross-sectional dimensions, lateral buckling instability is a possibility [131].

While beyond the scope of the current work, future studies should concentrate on spar cross-sectional shape design in order to improve the efficiency of them (by making them more lightweight) whilst maintaining a large ratio $I_{y'y'}/I_{z'z'}$, and also on the inclusion of a lateral buckling stability check in the analytical model to ensure that buckling is not possible. In section 5.2.5, the spars of the experimental wing model are predicted to be safe from lateral buckling throughout the range of test speeds.

3.3 Aerodynamic model

One advantage of a vortex-lattice method aerodynamic model over strip theory is its ability to compute the downwash velocity at a point in the flowfield (which is induced by the flow at all other points in space) and model the wake; this leads to a more accurate representation of the aerodynamics. However, to do this, some fundamental concepts of fluid dynamics must be revised.

3.3.1 Fluid dynamics

Circulation

Definition

The circulation (or vortex strength) Γ is the line integral around a closed curve C of fluid velocity [70] as shown in figure 3.7. It is defined as

$$\Gamma = -\oint_C \mathbf{u} \cdot d\mathbf{s} \tag{3.80}$$

$d\mathbf{s}$ is a vector describing an infinitesimally small segment of C, and $\mathbf{u}$ is the velocity vector.

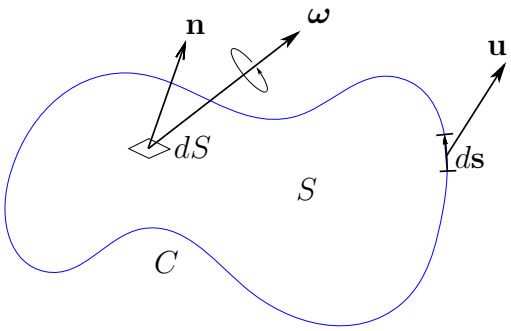

Figure 3.7: Circulation.

Vorticity related to circulation

Vorticity is the circulation per unit area, taken around an infinitesimal loop. Circulation can be related to vorticity by Stokes' theorem, which integrates the vorticity over a surface S [70]

$$-\Gamma = \int\int_S (\nabla \times \mathbf{u}) \cdot \mathbf{n}\, dS = \int\int_S \boldsymbol{\omega} \cdot \mathbf{n}\, dS \tag{3.81}$$

In Eq. 3.81 $\mathbf{n}$ is a unit vector normal to dS, and vorticity is defined as the curl of the velocity [70]

$$\boldsymbol{\omega} = \nabla \times \mathbf{u} \tag{3.82}$$

Biot-Savart law

For aerodynamic applications, the Biot-Savart law allows the velocity induced at a point in space due to a vortex filament to be found [70, 141] (see figure 3.8). For

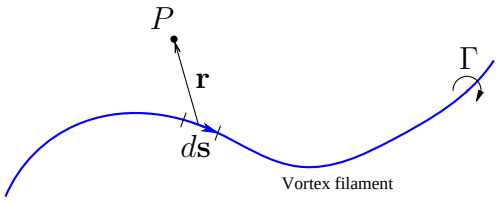

Figure 3.8: The influence of a vortex filament segment at a point P in space.

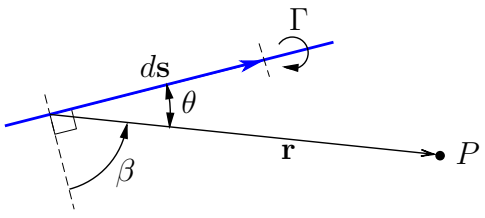

Figure 3.9: Definition of the angles θ and β.

an infinitesimally small segment of the vortex filament $d\mathbf{s}$, the induced velocity at point P is

$$d\mathbf{w}_P = \frac{\Gamma}{4\pi}\frac{d\mathbf{s}\times\mathbf{r}}{\|\mathbf{r}\|^3} \tag{3.83}$$

where Γ is the vortex strength (circulation) and $\mathbf{r}$ is a vector from the midpoint of the vortex segment to point P in space. $d\mathbf{w}_P$ will lie perpendicular to both $d\mathbf{s}$ and $\mathbf{r}$. This can also be written as

$$d\mathbf{s}\times\mathbf{r} = \|d\mathbf{s}\|\|\mathbf{r}\|\sin\theta\frac{\mathbf{w}_P}{\|\mathbf{w}_P\|} \tag{3.84}$$

where θ is the smaller angle between $d\mathbf{s}$ and $\mathbf{r}$ (i.e. $0 \leq \theta \leq \pi$) and is shown in figure 3.9. Substituting Eq. 3.84 into Eq. 3.83 gives

$$d\mathbf{w}_P = \frac{\Gamma}{4\pi}\frac{\|d\mathbf{s}\|\|\mathbf{r}\|\sin\theta}{\|\mathbf{r}\|^3}\frac{\mathbf{w}_P}{\|\mathbf{w}_P\|} \tag{3.85}$$

So

$$d\mathbf{w}_P = \frac{\Gamma}{4\pi}\frac{\mathbf{w}_P}{\|\mathbf{w}_P\|}\frac{\sin\theta}{r^2}ds \tag{3.86}$$

where

$$r = \|\mathbf{r}\| \tag{3.87}$$

and

$$ds = \|d\mathbf{s}\| \tag{3.88}$$

Now

$$\sin\theta = \sin\left(\frac{\pi}{2}-\beta\right) = \cos\beta \tag{3.89}$$

β is the angle (defined positive counter-clockwise) from a line perpendicular to $d\mathbf{s}$ (lying in a plane containing both $d\mathbf{s}$ and $\mathbf{r}$) to $\mathbf{r}$ defined as in figure 3.9, and it follows that $-\pi/2 \leq \beta \leq \pi/2$. Hence Eq. 3.86 can be written as

$$d\mathbf{w}_P = \frac{\Gamma}{4\pi}\frac{\mathbf{w}_P}{\|\mathbf{w}_P\|}\frac{\cos\beta}{r^2}ds \tag{3.90}$$

3.3.2 Obtaining the aerodynamic forces

Kutta-Joukowski theorem

The Kutta-Joukowski theorem [79, 141] relates the circulation vector $\boldsymbol{\gamma}$ to the resultant force per unit length $\bar{\mathbf{f}}$ of the circulation and is given by

$$\bar{\mathbf{f}} = \rho \mathbf{u} \times \boldsymbol{\gamma} \tag{3.91}$$

where ρ is the fluid density. The circulation vector describes the direction of the circulation strength along the vortex filament i.e.

$$\boldsymbol{\gamma} = \Gamma \frac{d\mathbf{s}}{\|d\mathbf{s}\|} \tag{3.92}$$

and $\bar{\mathbf{f}}$ acts normal to $\mathbf{u}$ and $\boldsymbol{\gamma}$.

Two-dimensional wing

With reference to figure 3.10a, for the case of circulation around a 2D/infinite span wing of sweepback angle Λ inclined at an angle of incidence α to the airflow, and where vectors are defined in the aerodynamic coordinate system $Oxyz$, which has its origin at the centreline

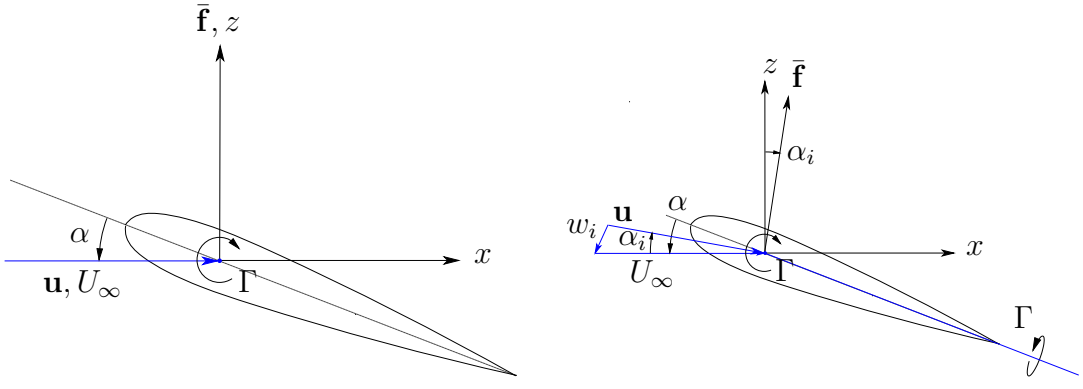

(a) 2D wing. (b) 3D wing.

Figure 3.10: Resultant force vectors.

$$\mathbf{u} = \begin{bmatrix} U_\infty & 0 & 0 \end{bmatrix} \tag{3.93}$$

And for circulation corresponding to spanwise locations $y < 0$ i.e. left wing

$$\boldsymbol{\gamma}_{LHS} = \begin{bmatrix} -\Gamma \sin\Lambda & \Gamma\cos\Lambda & 0 \end{bmatrix} \tag{3.94}$$

while for circulation corresponding to spanwise locations $y > 0$ i.e. right wing

$$\boldsymbol{\gamma}_{RHS} = \begin{bmatrix} \Gamma \sin\Lambda & \Gamma\cos\Lambda & 0 \end{bmatrix} \tag{3.95}$$

therefore, using Eqs. 3.93 - 3.95 with Eq. 3.91 gives, for all spanwise locations

$$\bar{\mathbf{f}} = \begin{bmatrix} 0 & 0 & \rho U_\infty \Gamma \cos\Lambda \end{bmatrix} \tag{3.96}$$

where U_∞ is the free-stream velocity. This is the force per unit length of circulation (i.e. $d\mathbf{f}/ds$). To express it as a force per unit span (i.e. $d\mathbf{f}/dy$) Eq. 3.96 must be divided by $\cos\Lambda$. Now, lift per unit span $\bar{L}$ and drag per unit span $\bar{D}$ are the components of the force per unit span in the z- and x-directions respectively, so

$$\bar{L} = \rho U_\infty \Gamma \tag{3.97}$$

and

$$\bar{D} = 0 \tag{3.98}$$

Finite wing

Unlike the 2D wing, for 3D/finite wings the trailing vortex sheet induces a downwash w_i on the wing, which gives $\mathbf{u}$ a downwards $(-z)$ component and consequently $\bar{\mathbf{f}}$ a rearward $(+x)$ component [65]. w_i is perpendicular to the mean chord surface and is defined as positive in the $-z$-direction (see figure 3.10b)

$$\mathbf{u} = \begin{bmatrix} (U_\infty - w_i \sin\alpha) & 0 & -w_i \cos\alpha \end{bmatrix} \tag{3.99}$$

and as before

$$\boldsymbol{\gamma}_{LHS} = \begin{bmatrix} -\Gamma \sin\Lambda & \Gamma\cos\Lambda & 0 \end{bmatrix} \tag{3.94}$$

and:

$$\boldsymbol{\gamma}_{RHS} = \begin{bmatrix} \Gamma \sin\Lambda & \Gamma\cos\Lambda & 0 \end{bmatrix} \tag{3.95}$$

Hence, for $y < 0$ the resultant force per unit length of circulation is

$$\bar{\mathbf{f}}_{LHS} = \rho \begin{bmatrix} w_i\Gamma\cos\alpha\,\cos\Lambda & w_i\Gamma\cos\alpha\,\sin\Lambda & (U_\infty - w_i\sin\alpha)\,\Gamma\cos\Lambda \end{bmatrix} \tag{3.100}$$

And for $y > 0$ the resultant force per unit length of circulation is

$$\bar{\mathbf{f}}_{RHS} = \rho \begin{bmatrix} w_i\Gamma\cos\alpha\,\cos\Lambda & -w_i\Gamma\cos\alpha\,\sin\Lambda & (U_\infty - w_i\sin\alpha)\,\Gamma\cos\Lambda \end{bmatrix} \tag{3.101}$$

Therefore, for a finite wing in inviscid flow, the lift and drag forces per unit span are given respectively by

$$\bar{L} = \rho\,(U_\infty - w_i\sin\alpha)\,\Gamma \tag{3.102}$$

and

$$\bar{D} = \bar{D}_i = \rho w_i \Gamma\cos\alpha \tag{3.103}$$

$\bar{D}_i$ is the induced drag per unit span. The Oxz-plane component of the angle by which the velocity and force vectors are altered is called the induced angle of incidence α_i [79, 85] (see figure 3.10b) and using Eqs. 3.102 and 3.103 can be expressed as

$$\begin{aligned} \tan\alpha_i &= \frac{\bar{D}}{\bar{L}} \\ &= \frac{w_i\cos\alpha}{U_\infty - w_i\sin\alpha} \end{aligned} \tag{3.104}$$

From Eqs. 3.100 and 3.101 another 3D aerodynamic effect is apparent; for swept wings a side force exists (inwards towards the centreline for sweptback wings, and outwards away from the centreline for sweptforward wings). For $y < 0$, this side force per unit span is given by

$$\bar{Y}_{LHS} = \rho w_i \Gamma \cos\alpha \tag{3.105}$$

and for $y > 0$

$$\bar{Y}_{RHS} = -\rho w_i \Gamma \cos\alpha \tag{3.106}$$

For a full-span wing these side forces are equal and opposite and so their contribution can be ignored. Additionally, from the previously-stated assumption of Euler-Bernoulli beam theory [143], structural deformation in the $Ox_j y_j$ (spar structural coordinate system), in which $\bar{Y}$ acts, is assumed to be zero and therefore the side forces have no bearing on the aeroelastic deformation of the wing.

Linearising the aerodynamic forces for the aeroelastic model

For a analysis of the finite wing with the assumption of a rigid structure (i.e. known angle of incidence α) the steady aerodynamic forces and induced angle of incidence are given by Eqs. 3.102 - 3.106. However, for the equivalent analysis of an elastic structure the angle of incidence is unknown and is obtained by solving the static aeroelastic equations of equilibrium for the unknown deflections. This becomes very difficult to perform if the aeroelastic forces are nonlinear in nature, as in Eqs. 3.102 - 3.106. However, for most practical applications these expressions can be linearised; firstly, the small angle approximation can be applied to the angle of incidence α and, secondly, it can be assumed that $w_i \ll U_\infty$ [79]. Therefore, from Eqs. 3.102 and 3.103 respectively the lift and drag forces per unit span simplify to

$$\bar{L} = \rho U_\infty \Gamma \tag{3.107}$$

and

$$\bar{D} = \bar{D}_i = \rho w_i \Gamma \tag{3.108}$$

Similarly, for $y < 0$ locations, the side force per unit span (from Eq. 3.105) becomes

$$\bar{Y}_{LHS} = \rho w_i \Gamma \tag{3.109}$$

and for $y > 0$ (from Eq. 3.106)

$$\bar{Y}_{RHS} = -\rho w_i \Gamma \tag{3.110}$$

Finally, the induced angle of incidence given by Eq. 3.104 reduces to

$$\alpha_i = \frac{w_i}{U_\infty} \tag{3.111}$$

3.3.3 The horseshoe vortex

The flow field around a wing can be represented by any solution that satisfies all flow constraints. The vortex filament is one such solution to model the steady aerodynamics of a wing. The vortex filament system has a constant circulation Γ in accordance with Helmholtz' first theorem [79]:

The strength of a vortex filament is constant along its length.

Additionally, the vortex filament contains a finite bound segment that represents the circulatory flow around the wing, and two semi-infinite filaments that extend from the ends of the bound segment to infinity behind the wing, thereby modelling the wake. The trailing segments must extend to infinity to satisfy Helmholtz' second theorem [79]:

A vortex filament cannot end in a fluid; it must extend to the boundaries of

the fluid or form a closed path.

Due to the arrangement of these vortex filament segments, the vortex filament is traditionally known as a horseshoe vortex [79]. In this section, the Biot-Savart law given by Eq. 3.90 will be applied to develop expressions for the induced velocity at a point due to these vortex filament segments, and then applied to a wing represented with a horseshoe vortex. The unknown circulation and hence aerodynamic forces will then be found by application and solution of the boundary conditions. To aid development of these expressions, firstly the expression for the induced velocity at a point due to an infinitely long vortex line will be developed.

Infinite vortex line

Consider a vortex line of infinite length as shown in figure 3.11. As previously, β is defined positive counter-clockwise in figures 3.11 - 3.14. From the diagram it

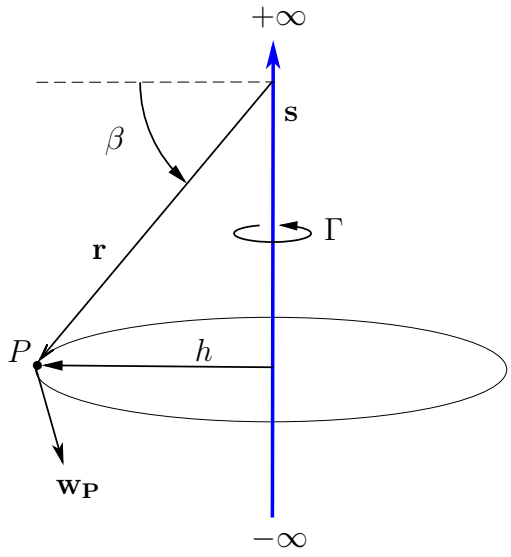

Figure 3.11: Infinite vortex line.

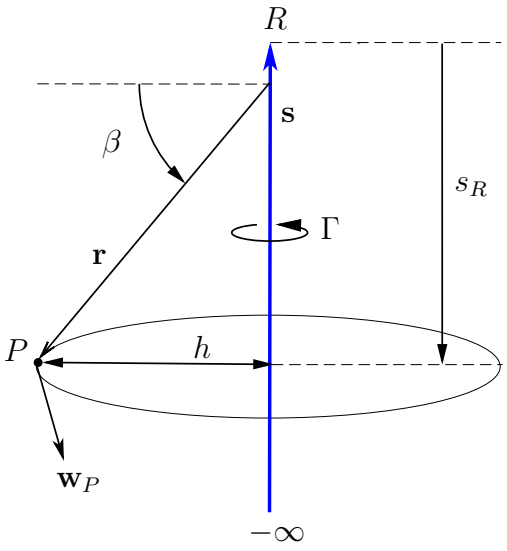

Figure 3.12: Semi-infinite vortex line.

can be seen that

$$\|\mathbf{r}\| = r = \frac{h}{\cos\beta} \tag{3.112}$$

h is the perpendicular distance between the vortex line and P, and is always positive.

$$s = h \tan \beta \tag{3.113}$$

Eq. 3.90 is

$$\mathbf{w}_P = \frac{\Gamma}{4\pi} \frac{\mathbf{w}_P}{\|\mathbf{w}_P\|} \int_{-\infty}^{\infty} \frac{\cos \beta}{r^2} ds \tag{3.90}$$

which, upon substitution of Eq. 3.112 becomes

$$\mathbf{w}_P = \frac{\Gamma}{4\pi} \frac{\mathbf{w}_P}{\|\mathbf{w}_P\|} \int_{-\infty}^{\infty} \frac{\cos^3 \beta}{h^2} ds \tag{3.114}$$

Now, Eq. 3.113 gives

$$\frac{ds}{d\beta} = \frac{h}{\cos^2 \beta} \tag{3.115}$$

So

$$ds = \frac{h \, d\beta}{\cos^2 \beta} \tag{3.116}$$

Substituting Eq. 3.116 into Eq. 3.115 gives

$$\mathbf{w}_P = \frac{\Gamma}{4\pi h} \frac{\mathbf{w}_P}{\|\mathbf{w}_P\|} \int_{-\frac{\pi}{2}}^{\frac{\pi}{2}} \cos \beta \, d\beta \tag{3.117}$$

So

$$w_P = \frac{\Gamma}{2\pi h} \tag{3.118}$$

The direction of w_P is given from $\mathbf{s} \times \mathbf{r}$, with $\mathbf{r}$ being a vector describing a line from any point on the straight vortex filament to the point of interest P.

Semi-infinite vortex line

Comparison of figure 3.12 with figure 3.11 allows Eq. 3.117 to be used for the semi-infinite vortex line, but with different limits of integration

$$\mathbf{w}_P = \frac{\Gamma}{4\pi h} \frac{\mathbf{w}_P}{\|\mathbf{w}_P\|} \int_{-\frac{\pi}{2}}^{\beta_R} \cos \beta \, d\beta \tag{3.119}$$

In Eq. 3.119 β_R is the angle β taken from point R on the vortex line. This gives

$$\mathbf{w}_P = \frac{\Gamma}{4\pi h}\frac{\mathbf{w}_P}{\|\mathbf{w}_P\|}(\sin\beta + 1) \tag{3.120}$$

And it can be seen that

$$\sin\beta = \frac{s_R}{\|\mathbf{r}\|} \tag{3.121}$$

where s_R is the distance parallel to the vortex line between P and R (positive in direction of arrow). Hence

$$\mathbf{w}_P = \frac{\Gamma}{4\pi h}\frac{\mathbf{w}_P}{\|\mathbf{w}_P\|}\left(\frac{s_R}{\|\mathbf{r}\|} + 1\right) \tag{3.122}$$

which, from the Pythagorean theorem, can be written as

$$\mathbf{w}_P = \frac{\Gamma}{4\pi h}\frac{\mathbf{w}_P}{\|\mathbf{w}_P\|}\left(\frac{s_R}{\sqrt{h^2 + {s_R}^2}} + 1\right) \tag{3.123}$$

Alternatively

$$w_P = \frac{\Gamma}{4\pi h}\left(\frac{s_R}{\sqrt{h^2 + {s_R}^2}} + 1\right) \tag{3.124}$$

And the direction of w_P, as before, is given from $\mathbf{s} \times \mathbf{r}$. For a semi-infinite vortex line from $+\infty$ rather than $-\infty$, the resulting expression is identical to Eq. 3.124.

Finite vortex line

Comparison of figure 3.13 with figure 3.11 allows Eq. 3.117 to be used for the finite vortex line, but with different limits of integration

$$\mathbf{w}_P = \frac{\Gamma}{4\pi h}\frac{\mathbf{w}_P}{\|\mathbf{w}_P\|}\int_{\beta_S}^{\beta_R}\cos\beta\, d\beta \tag{3.125}$$

where β_R and β_S are the angles β taken from points R and S on the vortex line respectively, as shown in figure 3.14. This gives

$$\mathbf{w}_P = \frac{\Gamma}{4\pi h}\frac{\mathbf{w}_P}{\|\mathbf{w}_P\|}(\sin\beta_R - \sin\beta_S) \tag{3.126}$$

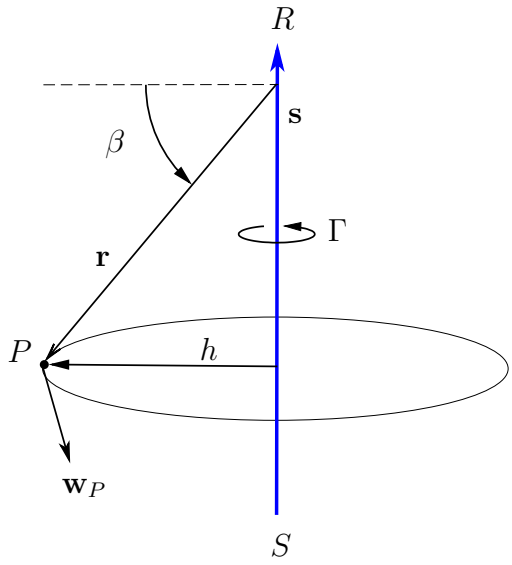

Figure 3.13: Finite vortex line.

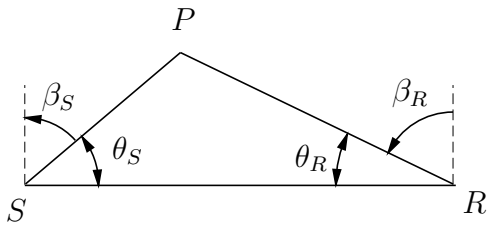

Figure 3.14: Finite vortex line angles.

From figure 3.14

$$\sin\beta_R = \sin\left(\frac{\pi}{2} - \theta_R\right) = \cos\theta_R \tag{3.127}$$

and

$$\sin\beta_S = \sin\left(-\frac{\pi}{2} + \theta_S\right) = -\cos\theta_S \tag{3.128}$$

So

$$w_P = \frac{\Gamma}{4\pi h}\left(\cos\theta_R + \cos\theta_S\right) \tag{3.129}$$

And the direction of w_P, as before, is given from $\mathbf{s} \times \mathbf{r}$.

Applied to a wing as a single horseshoe

The finite and semi-infinite vortex segments can now be placed on a wing as a crude representation of the aerodynamics. As shown later, to solve the resulting equations, it is necessary to define boundary conditions. For each horseshoe vortex (corresponding to a single aerodynamic panel), the boundary condition is specified at a single point known as the control point (or collocation point) [85, 141]. Here, an expression shall be formulated for the downwash at the control point of a wing with a single vortex filament placed on it. A horseshoe vortex is

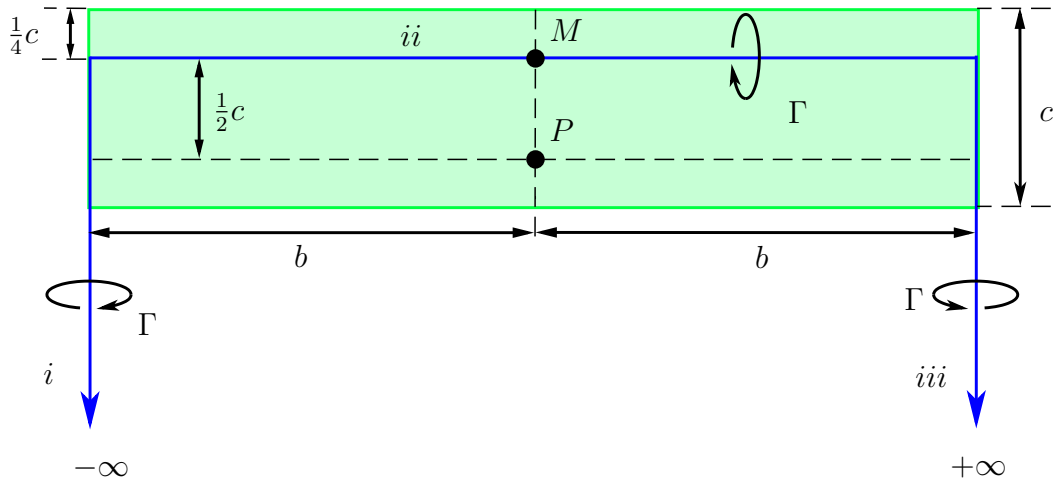

Figure 3.15: Wing with single horseshoe vortex.

placed on the wing (chord c, span $2b$) with the finite segment running along the quarter-chord (corresponding to the aerodynamic centre of subsonic thin-aerofoil theory [15, 70]) and the two semi-infinite segments extending behind the tips to represent the trailing vortices. For the solution to agree exactly with subsonic thin-aerofoil theory, the control point P is placed $0.5c$ (semi-chord) behind the finite segment at the mid-span [70] (see figure 3.15). Point M is located on the mid-span of the bound vortex segment and is used for induced drag calculations.

The induced downwash velocity at the control point P is simply the summation of the individual contributions from each of the three segments at the control point

$$w_P = w_{P_i} + w_{P_{ii}} + w_{P_{iii}} \tag{3.130}$$

From Eq. 3.124

$$w_{P_i} = w_{P_{iii}} = \frac{\Gamma}{4\pi b}\left(\frac{\left(\frac{c}{2}\right)}{\sqrt{b^2 + \left(\frac{c}{2}\right)^2}} + 1\right) \tag{3.131}$$

and from Eq. 3.129

$$w_{P_{ii}} = \frac{\Gamma}{4\pi\left(\frac{c}{2}\right)}(\cos\theta_R + \cos\theta_S) \tag{3.132}$$

Examining the geometry of the finite segment (figure 3.16)

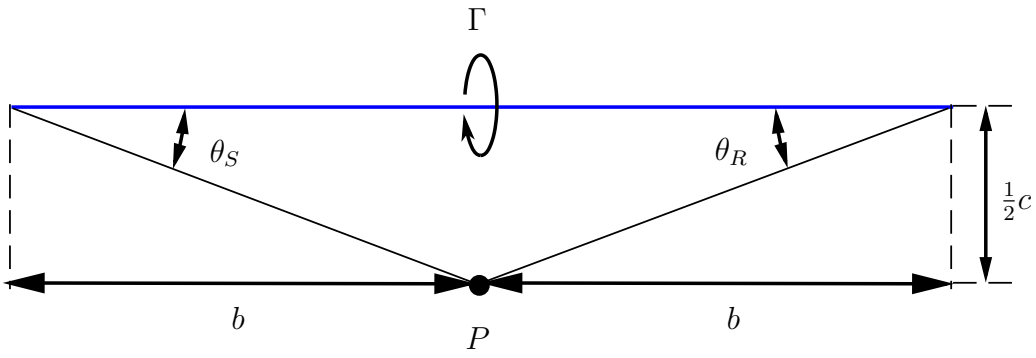

Figure 3.16: Geometry of finite segment of horseshoe vortex.

$$\cos\theta_R = \frac{b}{\sqrt{b^2 + \left(\frac{c}{2}\right)^2}} \tag{3.133}$$

and

$$\cos\theta_S = \frac{b}{\sqrt{b^2 + \left(\frac{c}{2}\right)^2}} \tag{3.134}$$

So $w_{P_{ii}}$ becomes

$$w_{P_{ii}} = \frac{\Gamma}{4\pi\left(\frac{c}{2}\right)}\left(\frac{2b}{\sqrt{b^2 + \left(\frac{c}{2}\right)^2}}\right) \tag{3.135}$$

Substituting Eqs. 3.131 and 3.135 into Eq. 3.130 gives

$$w_P = \frac{2\Gamma}{4\pi b}\left(\frac{\left(\frac{c}{2}\right)}{\sqrt{b^2+\left(\frac{c}{2}\right)^2}}+1\right)+\frac{\Gamma}{4\pi\left(\frac{c}{2}\right)}\left(\frac{2b}{\sqrt{b^2+\left(\frac{c}{2}\right)^2}}\right) \tag{3.136}$$

So

$$w_P = \frac{\Gamma}{2\pi b}\left(\frac{c}{2\sqrt{b^2+\left(\frac{c}{2}\right)^2}}+1\right)+\frac{\Gamma}{\pi c}\left(\frac{b}{\sqrt{b^2+\left(\frac{c}{2}\right)^2}}\right) \tag{3.137}$$

or

$$w_P = \Psi_P \Gamma \tag{3.138}$$

In Eq. 3.138 Ψ_P is the influence coefficient for P (scalar for a single vortex). To solve this equation, a boundary condition must be introduced at the control point P. A suitable boundary condition is that the sum of the resulting downwash due to the horseshoe vortex and the velocity contribution from the airflow must be zero (i.e. no penetration condition at the wall) [70, 141]; this will be examined in greater depth in the next section.

Satisfying control point boundary conditions

To be able to use the expressions for the aerodynamic forces (Eqs. 3.107 and 3.108) requires the unknown vortex strength Γ to be found. As mentioned previously, there is a no penetration condition at the wall. Since the vortex-lattice method represents the lifting surface as an infinitesimally thin sheet coinciding with a plane that passes through the mid-chord of the true aerofoil, it should be noted that this is not the physical surface of the aerofoil, but rather a mean surface; this is distinct from other panel methods, which apply the boundary conditions to the actual physical surface [70]. The no penetration condition implies that at the control point the sum of downwashes due to all vortices and the

freestream must equal zero; firstly, using figure 3.17a the freestream contribution will be considered:

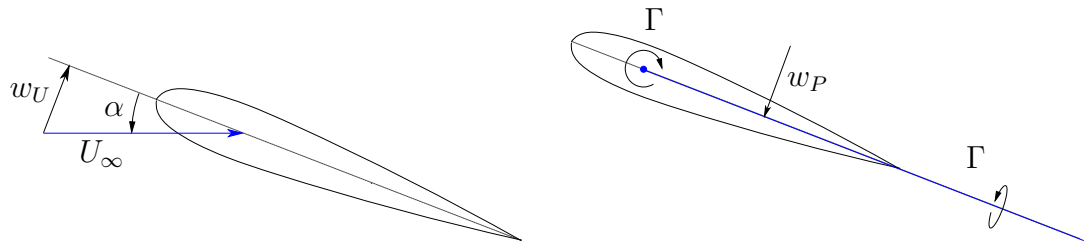

(a) Downwash due to the freestream. (b) Downwash due to the vortices.

Figure 3.17: Downwash contributions.

$$w_U = U_\infty \sin\alpha \tag{3.139}$$

Assuming small angles of incidence

$$w_U = U_\infty \alpha \tag{3.140}$$

and now, the downwash due to the vortices (at the control point), as shown in figure 3.17b is given by Eq. 3.138 as

$$w_P = \Psi_P \Gamma \tag{3.138}$$

So to satisfy the boundary condition of flow-tangency at the mean chord

$$U_\infty \alpha + \Psi_P \Gamma = 0 \tag{3.141}$$

Eq. 3.141 is then used to find the vortex strength Γ for a given airspeed, incidence, and wing geometry (the geometry determines the influence coefficient Ψ). Then, using Eqs. 3.107 and 3.108 integrated over the span, $2b$, of the wing, the total wing lift is

$$L = \int_{-b}^{b} \rho U_\infty \Gamma \, dy \tag{3.142}$$

and the total wing induced drag is

$$D_i = \int_{-b}^{b} \rho w_i \Gamma \, dy \tag{3.143}$$

where y is the spanwise axis in the aerodynamic coordinate system. w_i can be found from

$$w_i = \Psi_M \Gamma \tag{3.144}$$

in which Ψ_M is derived in an identical manner to Ψ_P in Eq. 3.138, but at point M on the mid-point of the bound vortex segment instead of point P [10, 79] (see figure 3.15). Note that carrying out this derivation will result in an infinite downwash contribution from the bound vortex segment at M; this problem is overcome by setting this contribution to zero [40].

3.3.4 Vortex-lattice aerodynamics

The simple single-horseshoe approximation of the aerodynamics of a wing can be taken a step further to obtain a more accurate representation; here, the wing is divided into several quadrilateral aerodynamic panels and a horseshoe vortex is placed on each to form a discrete lattice lifting-surface representation. As the number of panels is increased, so too is the accuracy of the aerodynamic model. To illustrate this method, a wing which has been divided into four aerodynamic panels will be considered.

Example: Wing with four aerodynamic panels

Consider figure 3.18 which illustrates the discrete approximation of a wing aerodynamic model using four horseshoe vortices.

All finite vortex lines are placed at the quarter chord of each aerodynamic panel. The control point P_i for the i^{th} panel is located at the three-quarter chord

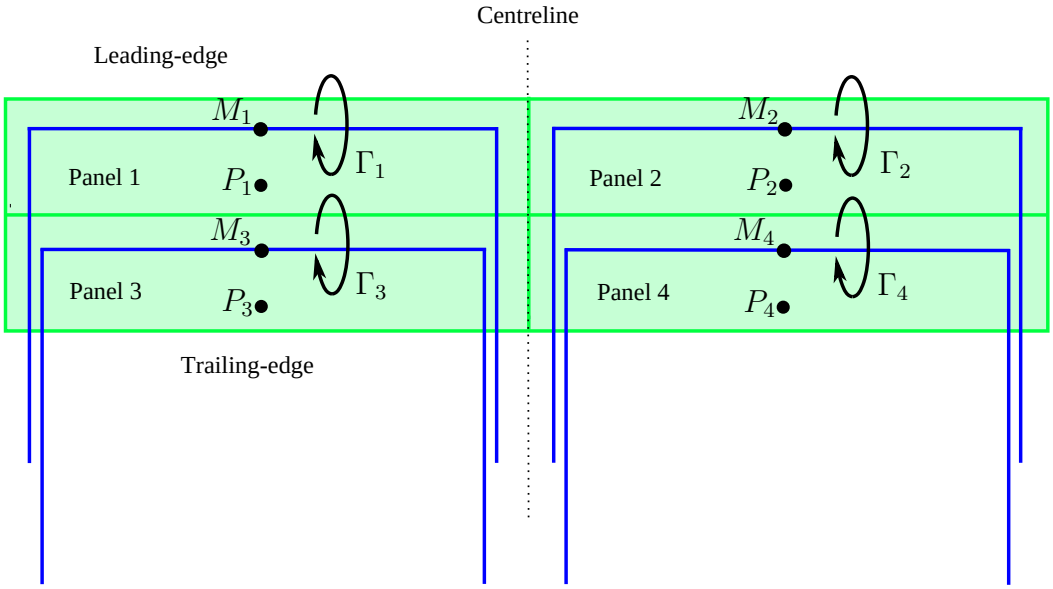

Figure 3.18: Wing with four aerodynamic panels.

and semi-span of the panel. For the i^{th} control point Eq. 3.138 becomes

$$w_{P_i} = \Psi_{i1}\Gamma_1 + \Psi_{i2}\Gamma_2 + \Psi_{i3}\Gamma_3 + \Psi_{i4}\Gamma_4 \tag{3.145}$$

in which the P subscript for the Ψ values has been dropped for brevity. So for all four aerodynamic panels Eq. 3.138 is

$$\mathbf{w}_P = \begin{bmatrix} w_{P_1} \\ w_{P_2} \\ w_{P_3} \\ w_{P_4} \end{bmatrix} = \begin{bmatrix} \Psi_{11} & \Psi_{12} & \Psi_{13} & \Psi_{14} \\ \Psi_{21} & \Psi_{22} & \Psi_{23} & \Psi_{24} \\ \Psi_{31} & \Psi_{32} & \Psi_{33} & \Psi_{34} \\ \Psi_{41} & \Psi_{42} & \Psi_{43} & \Psi_{44} \end{bmatrix} \begin{bmatrix} \Gamma_1 \\ \Gamma_2 \\ \Gamma_3 \\ \Gamma_4 \end{bmatrix} = \mathbf{\Psi}_P \mathbf{c} \tag{3.146}$$

So, for instance, $\Psi_{23}\Gamma_3$ is the downwash at P_2 due to the horseshoe vortex placed on aerodynamic panel 3. In Eq. 3.146 $\mathbf{c}$ is the vector of circulation strengths. As before, the zero normal flow boundary condition at all the control points must be satisfied

$$\mathbf{\Psi}_P \mathbf{c} + U_\infty \boldsymbol{\alpha} = \mathbf{0} \tag{3.147}$$

where $\boldsymbol{\alpha}$ is the vector of angles of incidence of the aerodynamic panels. Eq. 3.147 can be solved to find the unknown vortex strengths $\mathbf{c}$, allowing the aerodynamic forces to be calculated as before. Alternatively it can be manipulated as follows [141]:

$$\boldsymbol{\Psi}_P \mathbf{c} = -U_\infty \boldsymbol{\alpha} \tag{3.148}$$

so

$$\mathbf{c} = -\boldsymbol{\Psi}_P^{-1} U_\infty \boldsymbol{\alpha} \tag{3.149}$$

Multiplying through by $\rho U_\infty/2$

$$\frac{\rho U_\infty \mathbf{c}}{2} = -\frac{\rho U_\infty^2}{2} \boldsymbol{\Psi}_P^{-1} \boldsymbol{\alpha} \tag{3.150}$$

Using Eq. 3.107 allows the vector of panel lift per unit span for a finite wing to be expressed as

$$\bar{\mathbf{l}} = \rho U_\infty \mathbf{c} \tag{3.151}$$

So using Eq. 3.150 with Eq. 3.151 gives

$$\bar{\mathbf{l}} = -\frac{\rho U_\infty^2}{2} 2\boldsymbol{\Psi}_P^{-1} \boldsymbol{\alpha} \tag{3.152}$$

or

$$\bar{\mathbf{l}} = \frac{\rho U_\infty^2}{2} \mathbf{AIC}_R \boldsymbol{\alpha} \tag{3.153}$$

where $\mathbf{AIC}_R = -2\boldsymbol{\Psi}_P^{-1}$ is the matrix of Aerodynamic Influence Coefficients. $\mathbf{AIC}_R$ is real for steady aerodynamics hence the R subscript, but complex for unsteady aerodynamics.

Comparison with strip theory

For the four-panel wing, strip theory [15] gives the lift L_{panel} on each panel, area S_{panel} as

$$L_{\text{panel}} = \frac{\rho U_\infty^2}{2} a_W \alpha_{\text{panel}} S_{\text{panel}} \tag{3.154}$$

where a_W is the lift curve slope (assumed to be uniform for the wing). In terms of chord c and span $2s$, Eq. 3.154 is

$$\begin{aligned} L_{\text{panel}} &= \frac{\rho U_\infty^2}{2} a_W \alpha_{\text{panel}} \frac{1}{4} 2sc \\ &= \frac{\rho U_\infty^2}{2} a_W \alpha_{\text{panel}} \frac{1}{2} sc \end{aligned} \tag{3.155}$$

Hence the lift per unit span for each panel is simply given by

$$\bar{L}_{\text{panel}} = \frac{\rho U_\infty^2}{2} a_W \alpha_{\text{panel}} \frac{c}{2} \tag{3.156}$$

and so for the whole wing the lift per unit span is

$$\bar{\mathbf{l}} = \begin{bmatrix} \bar{L}_{\text{panel 1}} \\ \bar{L}_{\text{panel 2}} \\ \bar{L}_{\text{panel 3}} \\ \bar{L}_{\text{panel 4}} \end{bmatrix} = \frac{\rho U_\infty^2}{2} \frac{c a_W}{2} \begin{bmatrix} 1 & 0 & 0 & 0 \\ 0 & 1 & 0 & 0 \\ 0 & 0 & 1 & 0 \\ 0 & 0 & 0 & 1 \end{bmatrix} \begin{bmatrix} \alpha_{\text{panel 1}} \\ \alpha_{\text{panel 2}} \\ \alpha_{\text{panel 3}} \\ \alpha_{\text{panel 4}} \end{bmatrix} \tag{3.157}$$

Bearing in mind that $\mathbf{AIC}_R = -2\boldsymbol{\Psi}_P^{-1}$, comparison of Eq. 3.157 with Eq. 3.153 shows that strip theory is over simplified in that there exists no cross-coupling between aerodynamic panels (see Eq. 3.146 for the expanded $\boldsymbol{\Psi}_P$ matrix in which this cross-coupling exists), as it assumes the flow at any given location in space is independent from the flow at another distinct location.

Downwash singularities

The Biot-Savart law contains a singularity that can cause problems if unaccounted for; from Eq. 3.83 it can be seen that if the point at which the downwash is being calculated coincides with $d\mathbf{s}$, the infinitesimally small segment of the vortex filament, then $\|\mathbf{r}\| = 0$ and the theory breaks down by predicting an infinite induced velocity at the point. In reality a vortex does not induce any velocity on

itself [40]. This problem can occur frequently for a vortex-lattice surface; calculation of the downwash at the mid-bound vortex points M (for the induced drag calculation) due to the contribution of all bound vortex segments that can be projected through M cause this singularity to occur. Additionally, for a swept wing it is possible that the projection of some of the bound vortices will pass through control points P also resulting in singularities. The solution is to set these contributions to zero.

3.4 Aeroelastic coupling

To couple the aerodynamic model to the structural model an expression for the vector of lift per unit span of each panel $\bar{\mathbf{l}}$ needs to be substituted into the equilibrium equations given by Eq. 3.77; the appropriate expression is given by Eq. 3.153. It is at this point however, for two reasons, that difficulties arise if Eq. 3.153 is used directly in Eq. 3.77 without any manipulation:

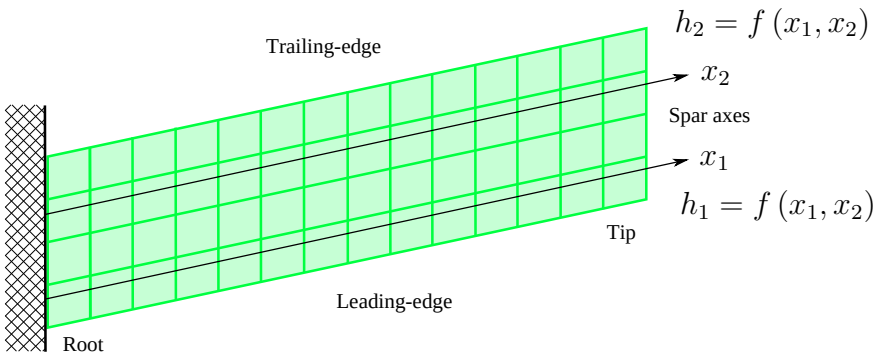

Figure 3.19: The continuous structural model lies on top of the discretised aerodynamic lifting surface model (green).

1. The structural model is a continuous system whereas the aerodynamic model is discretised, as demonstrated in figure 3.19. The solution is to evaluate the integrals of virtual work (right-hand side of Eq. 3.77) between spanwise locations coinciding with the aerodynamic panel edges, between which the lift per unit span $\bar{L}$ is constant, and then sum. In this way $\bar{L}$

becomes a discretised step function of x_1 and x_2, the axial coordinates of the two spars in the structural coordinate system.

2. For an elastic wing, the vector of angles of incidence for each panel $\boldsymbol{\alpha}$ is unknown and so must be expressed in terms of the vector of generalised coordinates $\boldsymbol{\eta}$.

3.4.1 Discretising the virtual work for use with the aerodynamic model

The aerodynamic loads and deflections corresponding to a symmetric half-wing model are being represented, but to construct the $\mathbf{AIC}_R$ matrix, consideration of the full-span aerodynamic model is necessary (see figure 3.20). From this illustration, it can be seen that the total number of aerodynamic panels for the full-span model is 28. So, Eq. 3.153 can be expanded to

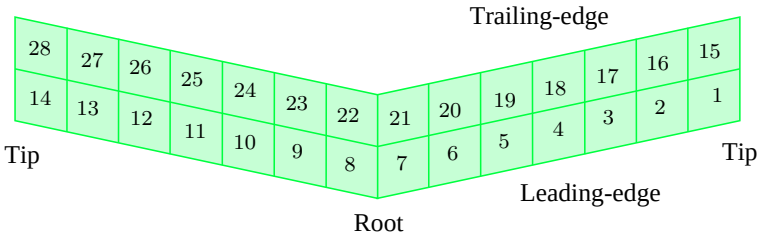

Figure 3.20: Aerodynamic panel numbering convention for $\mathbf{AIC}_R$ matrix.

$$\begin{bmatrix} \bar{L}_{\text{panel 1}} \\ \bar{L}_{\text{panel 2}} \\ \vdots \\ \bar{L}_{\text{panel 28}} \end{bmatrix} = \frac{\rho U_\infty^2}{2} \begin{bmatrix} AIC_{1\,1} & AIC_{1\,2} & \cdots & AIC_{1\,28} \\ AIC_{2\,1} & AIC_{2\,2} & \cdots & AIC_{2\,28} \\ \vdots & \vdots & \ddots & \vdots \\ AIC_{28\,1} & AIC_{28\,2} & \cdots & AIC_{28\,28} \end{bmatrix} \begin{bmatrix} \alpha_{\text{panel 1}} \\ \alpha_{\text{panel 2}} \\ \vdots \\ \alpha_{\text{panel 28}} \end{bmatrix} \tag{3.158}$$

Symmetry can now be exploited to reduce the size of the vectors and matrix in Eq. 3.158 [70]; firstly, only the loads from the half-span model are of interest

(although the influence of the entire model is required):

$$\begin{bmatrix} \bar{L}_{\text{panel 1}} \\ \bar{L}_{\text{panel 2}} \\ \vdots \\ \bar{L}_{\text{panel 7}} \\ \bar{L}_{\text{panel 15}} \\ \bar{L}_{\text{panel 16}} \\ \vdots \\ \bar{L}_{\text{panel 21}} \end{bmatrix} = \frac{\rho U_\infty^2}{2} \begin{bmatrix} AIC_{1\,1} & AIC_{1\,2} & \cdots & AIC_{1\,28} \\ AIC_{2\,1} & AIC_{2\,2} & \cdots & AIC_{2\,28} \\ \vdots & \vdots & \ddots & \vdots \\ AIC_{7\,1} & AIC_{7\,2} & \cdots & AIC_{7\,28} \\ AIC_{15\,1} & AIC_{15\,2} & \cdots & AIC_{15\,28} \\ AIC_{16\,1} & AIC_{16\,2} & \cdots & AIC_{16\,28} \\ \vdots & \vdots & \ddots & \vdots \\ AIC_{21\,1} & AIC_{21\,2} & \cdots & AIC_{21\,28} \end{bmatrix} \begin{bmatrix} \alpha_{\text{panel 1}} \\ \alpha_{\text{panel 2}} \\ \vdots \\ \alpha_{\text{panel 28}} \end{bmatrix} \tag{3.159}$$

Next, the symmetry in $\boldsymbol{\alpha}$ is noted i.e. $\alpha_{\text{panel 1}} = \alpha_{\text{panel 14}}$, $\alpha_{\text{panel 2}} = \alpha_{\text{panel 13}}$ etc, so

$$\begin{bmatrix} \bar{L}_{\text{panel 1}} \\ \bar{L}_{\text{panel 2}} \\ \vdots \\ \bar{L}_{\text{panel 7}} \\ \bar{L}_{\text{panel 15}} \\ \bar{L}_{\text{panel 16}} \\ \vdots \\ \bar{L}_{\text{panel 21}} \end{bmatrix} = \frac{\rho U_\infty^2}{2} \begin{bmatrix} \mathbf{AIC}_a & \mathbf{AIC}_b \end{bmatrix} \begin{bmatrix} \alpha_{\text{panel 1}} \\ \alpha_{\text{panel 2}} \\ \vdots \\ \alpha_{\text{panel 7}} \\ \alpha_{\text{panel 15}} \\ \alpha_{\text{panel 16}} \\ \vdots \\ \alpha_{\text{panel 21}} \end{bmatrix} \tag{3.160}$$

In Eq. 3.160, the modified $\mathbf{AIC}_R$ matrix has been expressed in terms of two matrices $\mathbf{AIC}_a$ and $\mathbf{AIC}_b$ simply for presentation purposes (due to the size of

the full matrix), where

$$\mathbf{AIC}_a = \begin{bmatrix} (AIC_{1\,1} + AIC_{1\,14}) & (AIC_{1\,2} + AIC_{1\,13}) & \cdots & (AIC_{1\,7} + AIC_{1\,8}) \\ (AIC_{2\,1} + AIC_{2\,14}) & (AIC_{2\,2} + AIC_{2\,13}) & \cdots & (AIC_{2\,7} + AIC_{2\,8}) \\ \vdots & \vdots & \ddots & \vdots \\ (AIC_{7\,1} + AIC_{7\,14}) & (AIC_{7\,2} + AIC_{7\,13}) & \cdots & (AIC_{7\,7} + AIC_{7\,8}) \\ (AIC_{15\,1} + AIC_{15\,14}) & (AIC_{15\,2} + AIC_{15\,13}) & \cdots & (AIC_{15\,7} + AIC_{15\,8}) \\ (AIC_{16\,1} + AIC_{16\,14}) & (AIC_{16\,2} + AIC_{16\,13}) & \cdots & (AIC_{16\,7} + AIC_{16\,8}) \\ \vdots & \vdots & \ddots & \vdots \\ (AIC_{21\,1} + AIC_{21\,14}) & (AIC_{21\,2} + AIC_{21\,13}) & \cdots & (AIC_{21\,7} + AIC_{21\,8}) \end{bmatrix} \tag{3.161}$$

and

$$\mathbf{AIC}_b = \begin{bmatrix} (AIC_{1\,15} + AIC_{1\,28}) & (AIC_{1\,16} + AIC_{1\,27}) & \cdots & (AIC_{1\,21} + AIC_{1\,22}) \\ (AIC_{2\,15} + AIC_{2\,28}) & (AIC_{2\,16} + AIC_{2\,27}) & \cdots & (AIC_{2\,21} + AIC_{2\,22}) \\ \vdots & \vdots & \ddots & \vdots \\ (AIC_{7\,15} + AIC_{7\,28}) & (AIC_{7\,16} + AIC_{7\,27}) & \cdots & (AIC_{7\,21} + AIC_{7\,22}) \\ (AIC_{15\,15} + AIC_{15\,28}) & (AIC_{15\,16} + AIC_{15\,27}) & \cdots & (AIC_{15\,21} + AIC_{15\,22}) \\ (AIC_{16\,15} + AIC_{16\,28}) & (AIC_{16\,16} + AIC_{16\,27}) & \cdots & (AIC_{16\,21} + AIC_{16\,22}) \\ \vdots & \vdots & \ddots & \vdots \\ (AIC_{21\,15} + AIC_{21\,28}) & (AIC_{21\,16} + AIC_{21\,27}) & \cdots & (AIC_{21\,21} + AIC_{21\,22}) \end{bmatrix} \tag{3.162}$$

Defining the reduced $\mathbf{AIC}_R$ matrix as

$$\mathbf{AIC}_R^* = \begin{bmatrix} \mathbf{AIC}_a & \mathbf{AIC}_b \end{bmatrix} \tag{3.163}$$

Eqns. 3.160 and 3.163 give

$$\bar{\mathrm{l}} = q\mathbf{AIC}_R^* \boldsymbol{\alpha} \tag{3.164}$$

where $q = \rho U_\infty^2/2$ is the dynamic pressure. From the right-hand side of Eq. 3.77, the virtual work is given by

$$\delta^* W = \delta\boldsymbol{\eta}^T \cos\Lambda \begin{bmatrix} (1+\xi)\int_0^l \boldsymbol{\psi}\bar{L}\, dx_1 \\ -\xi \int_0^l \boldsymbol{\phi}\bar{L}\, dx_2 \end{bmatrix} \tag{3.165}$$

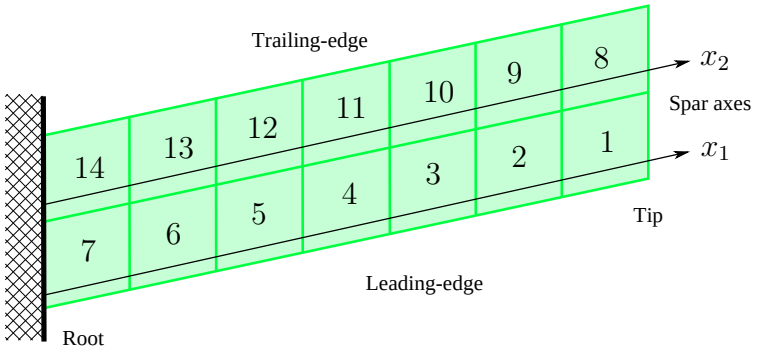

Figure 3.21: Aerodynamic panel numbering convention referenced by panel p.

where $\boldsymbol{\eta}$ is the vector of generalised coordinates, $\boldsymbol{\psi}$ and $\boldsymbol{\phi}$ are the vectors of assumed modes and ξ is the wing geometric dimensionless grouping defined in Eq. 3.66. As explained earlier, the expression for lift per unit force in Eq. 3.164 cannot be directly substituted into Eq. 3.165 since Eq. 3.164 does not express $\bar{L}$ in terms of x_1 and x_2 and rather gives a discretised expression for $\bar{L}$ at each aerodynamic panel. Instead, the integrals of virtual work (right-hand side of Eq. 3.77) will be evaluated between spanwise locations coinciding with the aerodynamic panel edges, between which the lift per unit span $\bar{L}$ is constant, and then this expression shall be summed across all the half-span aerodynamic panels. So for a half-span (reduced to half-span via symmetry) aerodynamic model represented by $g \times h$ panels (g spanwise by h chordwise, see figure 3.21 for panel numbering where $g = 7$ and $h = 2$)

$$\delta^* W = \delta\boldsymbol{\eta}^T q \cos\Lambda \sum_{p=1}^{g\times h} \begin{bmatrix} (1+\xi_p)\int_p \boldsymbol{\psi}\, dx_1 \\ -\xi_p \int_p \boldsymbol{\phi}\, dx_2 \end{bmatrix} \mathbf{AIC}^*_{R_p} \boldsymbol{\alpha} \tag{3.166}$$

where $\mathbf{AIC}^*_{R_p}$ is the p^{th} row of the matrix $\mathbf{AIC}^*_R$, and the integration limits are the x_1 or x_2 values of the bound vortex ends of the p^{th} panel. ξ has also been modified from its definition in Eq. 3.66, and is given by

$$\xi_p = \frac{f - q_{c_p}}{r - f} \tag{3.167}$$

where, q_{c_p} is the distance that the aerodynamic centre of the p^{th} panel (i.e. bound vortex) lies aft of the leading-edge of the wing, and f and r are the chordwise positions of the spars, as defined in figure 3.6. Next, an expression is required for $\boldsymbol{\alpha}$, the vector of angles of incidence for each panel. As this is an elastic model, α for any given panel depends on the loads and therefore it must be expressed in terms of w_1 and w_2, or more correctly, $\boldsymbol{\psi}$ and $\boldsymbol{\phi}$, and $\boldsymbol{\eta}$.

3.4.2 Angle of incidence for a swept elastic wing [37, 61] as a function of the unknown amplitudes

The angle of incidence is composed of a rigid contribution and an elastic contribution i.e.

$$\alpha = \alpha_r + \alpha_e \tag{3.168}$$

For the general case of a wing with non-zero sweep angle Λ, the elastic angle of incidence comprises of a torsional component, plus a bending component that is due to the sweep. With reference to figure 3.22, the angle of incidence is a

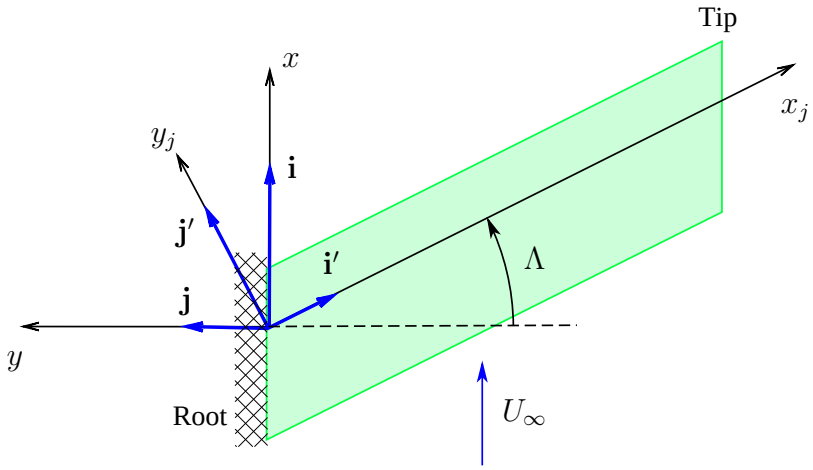

Figure 3.22: Angle of incidence for a swept wing.

rotation of the wing about the y-axis, perpendicular to the flow. So in order to get α_e aeroelastic rotations must be transformed from structural (Ox_jy_j) to aerodynamic (Oxy) axes. Let $\mathbf{i}'$, $\mathbf{j}'$, $\mathbf{i}$ and $\mathbf{j}$ be the unit vectors in the x_j-, y_j-,

x- and y-directions respectively. Then the angle of incidence is a rotation in the j-direction, given by

$$\mathbf{j} = -\mathbf{i}' \cos\Lambda + \mathbf{j}' \sin\Lambda \tag{3.169}$$

Twisting of the wing due to torsion is about the x_j-axis (-$\mathbf{i}'$-direction) and is $-\theta_j$. Rotation of the wing due to bending is about the y_j-axis ($-\mathbf{j}$'-direction) and is $-\frac{\delta h_j}{\delta x_j} = -h_j'$, where h_j is the bending displacement of the j^{th} axis. So, applied to panel p

$$\alpha_p = \alpha_{r_p} + \theta_p \cos\Lambda - h_p' \sin\Lambda \tag{3.170}$$

Using a similar expansion to Eq. 3.65 allows Eq. 3.170 to be expressed in terms of h_1 and h_2, the bending displacements of the two spars

$$\begin{aligned} \alpha_p = \alpha_{r_p} &+ \left(\frac{h_1\left(x_{1_p}\right) - h_2\left(x_{2_p}\right)}{c\left(r-f\right)\cos\Lambda} \right) \cos\Lambda \\ &- \left(h_1'\left(x_{1_p}\right) + \xi_p \Big(h_1'\left(x_{1_p}\right) - h_2'\left(x_{2_p}\right) \Big) \right) \sin\Lambda \end{aligned} \tag{3.171}$$

Cancelling the two cosine terms and substituting in the shape functions from Eqs. 3.70, 3.71 and 3.73, and switching notation from x_{1_p} and x_{2_p} to p gives

$$\begin{aligned} \alpha_p = \alpha_{r_p} &+ \frac{1}{c\left(r-f\right)} \begin{bmatrix} \boldsymbol{\psi}_p^T & -\boldsymbol{\phi}_p^T \end{bmatrix} \boldsymbol{\eta} \\ &- \begin{bmatrix} \left(1+\xi_p\right)\boldsymbol{\psi}_p'^T & -\xi_p \boldsymbol{\phi}_p'^T \end{bmatrix} \sin\Lambda\, \boldsymbol{\eta} \end{aligned} \tag{3.172}$$

which can be written

$$\alpha_p = \alpha_{r_p} + \left[\boldsymbol{\psi}_p^{*T} - \boldsymbol{\phi}_p^{*T} \right] \boldsymbol{\eta} \tag{3.173}$$

where

$$\boldsymbol{\psi}_p^* = \frac{1}{c\left(r-f\right)} \boldsymbol{\psi}_p - \left(1+\xi_p\right) \sin\Lambda\, \boldsymbol{\psi}_p' \tag{3.174}$$

and

$$\boldsymbol{\phi}_p^* = \frac{1}{c\left(r-f\right)} \boldsymbol{\phi}_p - \xi_p \sin\Lambda\, \boldsymbol{\phi}_p' \tag{3.175}$$

So, for all panels

$$\boldsymbol{\alpha} = \boldsymbol{\alpha}_r + \left[\boldsymbol{\Psi}^{*\mathbf{T}} - \boldsymbol{\Phi}^{*\mathbf{T}}\right]\boldsymbol{\eta} \tag{3.176}$$

where

$$\boldsymbol{\alpha}_r = \begin{bmatrix} \alpha_{r_1} & \alpha_{r_2} & \cdots & \alpha_{r_{gh}} \end{bmatrix}^T \tag{3.177}$$

$$\boldsymbol{\Psi}^* = \begin{bmatrix} \boldsymbol{\psi}_1^* & \boldsymbol{\psi}_2^* & \cdots & \boldsymbol{\psi}_{gh}^* \end{bmatrix} \tag{3.178}$$

$$\boldsymbol{\Phi}^* = \begin{bmatrix} \boldsymbol{\phi}_1^* & \boldsymbol{\phi}_2^* & \cdots & \boldsymbol{\phi}_{gh}^* \end{bmatrix} \tag{3.179}$$

Substituting Eq. 3.176 into 3.166 gives

$$\delta^* W = \delta\boldsymbol{\eta}^T q \cos\Lambda \sum_{p=1}^{g\times h} \begin{bmatrix} (1+\xi_p)\int_p \boldsymbol{\psi}\, dx_1 \\ -\xi_p \int_p \boldsymbol{\phi}\, dx_2 \end{bmatrix} \mathbf{AIC}_{R_p}^* \left(\boldsymbol{\alpha}_r + \left[\boldsymbol{\Psi}^{*\mathbf{T}} - \boldsymbol{\Phi}^{*\mathbf{T}}\right]\boldsymbol{\eta}\right) \tag{3.180}$$

Let

$$\boldsymbol{\upsilon}_p = \begin{bmatrix} (1+\xi_p)\int_p \boldsymbol{\psi}\, dx_1 \\ -\xi_p \int_p \boldsymbol{\phi}\, dx_2 \end{bmatrix} \tag{3.181}$$

and let

$$\boldsymbol{\Omega} = \left[\boldsymbol{\Psi}^{*\mathbf{T}} - \boldsymbol{\Phi}^{*\mathbf{T}}\right] \tag{3.182}$$

Then

$$\delta^* W = \delta\boldsymbol{\eta}^T q \cos\Lambda \sum_{p=1}^{g\times h} \boldsymbol{\upsilon}_p \mathbf{AIC}_{R_p}^* \boldsymbol{\alpha}_r + \delta\boldsymbol{\eta}^T q \cos\Lambda \sum_{p=1}^{g\times h} \boldsymbol{\upsilon}_p \mathbf{AIC}_{R_p}^* \boldsymbol{\Omega}\boldsymbol{\eta} \tag{3.183}$$

Alternatively, the summation can be omitted by using the full $\mathbf{AIC}_R^*$ matrix

$$\delta^* W = \delta\boldsymbol{\eta}^T q \cos\Lambda\, \boldsymbol{\Upsilon}\, \mathbf{AIC}_R^* \boldsymbol{\alpha}_r + \delta\boldsymbol{\eta}^T q \cos\Lambda\, \boldsymbol{\Upsilon}\, \mathbf{AIC}_R^* \boldsymbol{\Omega}\boldsymbol{\eta} \tag{3.184}$$

where

$$\boldsymbol{\Upsilon} = \begin{bmatrix} \boldsymbol{\upsilon}_1 & \boldsymbol{\upsilon}_2 & \cdots & \boldsymbol{\upsilon}_{gh} \end{bmatrix}^T \tag{3.185}$$

3.4.3 The complete equilibrium equations

Substituting Eq. 3.184 into the PVD equilibrium equations Eq. 3.77 gives

$$\delta\boldsymbol{\eta}^T \left(\begin{bmatrix} EI_{s_1}\int_0^l \boldsymbol{\psi}''\boldsymbol{\psi}''^T\,dx_1 & \mathbf{0}_{A,B} \\ \mathbf{0}_{B,A} & EI_{s_2}\int_0^l \boldsymbol{\phi}''\boldsymbol{\phi}''^T\,dx_2 \end{bmatrix} \right.$$

$$+ \frac{G\left(J_{s_1}+J_{s_2}\right)}{c^2\left(r-f\right)^2 l}\sum_{k=1}^{m} \begin{bmatrix} \begin{pmatrix} \boldsymbol{\psi}_{k+1}\boldsymbol{\psi}_{k+1}^T - \boldsymbol{\psi}_{k+1}\boldsymbol{\psi}_k^T \\ -\boldsymbol{\psi}_k\boldsymbol{\psi}_{k+1}^T + \boldsymbol{\psi}_k\boldsymbol{\psi}_k^T \end{pmatrix} & \begin{pmatrix} \boldsymbol{\psi}_{k+1}\boldsymbol{\phi}_k^T - \boldsymbol{\psi}_{k+1}\boldsymbol{\phi}_{k+1}^T \\ -\boldsymbol{\psi}_k\boldsymbol{\phi}_k^T + \boldsymbol{\psi}_k\boldsymbol{\phi}_{k+1}^T \end{pmatrix} \\ symmetric & \begin{pmatrix} \boldsymbol{\phi}_{k+1}\boldsymbol{\phi}_{k+1}^T - \boldsymbol{\phi}_{k+1}\boldsymbol{\phi}_k^T \\ -\boldsymbol{\phi}_k\boldsymbol{\phi}_{k+1}^T + \boldsymbol{\phi}_k\boldsymbol{\phi}_k^T \end{pmatrix} \end{bmatrix}$$

$$\left. + \frac{G}{c\left(r-f\right)}\sum_{k=1}^{m} J_{r_k} \begin{bmatrix} \boldsymbol{\phi}_k'\boldsymbol{\phi}_k'^T & -\boldsymbol{\phi}_k'\boldsymbol{\psi}_k'^T \\ symmetric & \boldsymbol{\psi}_k'\boldsymbol{\psi}_k'^T \end{bmatrix} \right) \boldsymbol{\eta}$$

$$= \delta\boldsymbol{\eta}^T q\cos\Lambda\,\boldsymbol{\Upsilon}\,\mathbf{AIC}_R^*\boldsymbol{\alpha}_r + \delta\boldsymbol{\eta}^T q\cos\Lambda\,\boldsymbol{\Upsilon}\,\mathbf{AIC}_R^*\boldsymbol{\Omega}\boldsymbol{\eta} \tag{3.186}$$

i.e.

$$\delta\boldsymbol{\eta}^T\mathbf{E}\boldsymbol{\eta} = \delta\boldsymbol{\eta}^T\rho U^2\mathbf{A}_r\boldsymbol{\alpha}_r - \delta\boldsymbol{\eta}^T\rho U^2\mathbf{C}\boldsymbol{\eta} \tag{3.187}$$

where

$$\mathbf{E} = \begin{bmatrix} EI_{s_1}\int_0^l \boldsymbol{\psi}''\boldsymbol{\psi}''^T\,dx_1 & \mathbf{0}_{A,B} \\ \mathbf{0}_{B,A} & EI_{s_2}\int_0^l \boldsymbol{\phi}''\boldsymbol{\phi}''^T\,dx_2 \end{bmatrix}$$

$$+ \frac{G\left(J_{s_1}+J_{s_2}\right)}{c^2\left(r-f\right)^2 l}\sum_{k=1}^{m} \begin{bmatrix} \begin{pmatrix} \boldsymbol{\psi}_{k+1}\boldsymbol{\psi}_{k+1}^T - \boldsymbol{\psi}_{k+1}\boldsymbol{\psi}_k^T \\ -\boldsymbol{\psi}_k\boldsymbol{\psi}_{k+1}^T + \boldsymbol{\psi}_k\boldsymbol{\psi}_k^T \end{pmatrix} & \begin{pmatrix} \boldsymbol{\psi}_{k+1}\boldsymbol{\phi}_k^T - \boldsymbol{\psi}_{k+1}\boldsymbol{\phi}_{k+1}^T \\ -\boldsymbol{\psi}_k\boldsymbol{\phi}_k^T + \boldsymbol{\psi}_k\boldsymbol{\phi}_{k+1}^T \end{pmatrix} \\ symmetric & \begin{pmatrix} \boldsymbol{\phi}_{k+1}\boldsymbol{\phi}_{k+1}^T - \boldsymbol{\phi}_{k+1}\boldsymbol{\phi}_k^T \\ -\boldsymbol{\phi}_k\boldsymbol{\phi}_{k+1}^T + \boldsymbol{\phi}_k\boldsymbol{\phi}_k^T \end{pmatrix} \end{bmatrix}$$

$$+\frac{G}{c\,(r-f)}\sum_{k=1}^{m} J_{r_k}\begin{bmatrix} \boldsymbol{\phi}'_k\boldsymbol{\phi}_k^{'T} & -\boldsymbol{\phi}'_k\boldsymbol{\psi}_k^{'T} \\ symmetric & \boldsymbol{\psi}'_k\boldsymbol{\psi}_k^{'T} \end{bmatrix} \tag{3.188}$$

is the structural stiffness matrix,

$$\mathbf{A}_r = \frac{\cos\Lambda}{2}\,\boldsymbol{\Upsilon}\,\mathbf{AIC}_R^* \tag{3.189}$$

is a matrix of aerodynamic disturbances (which result from a wind-off non-zero angle of incidence i.e. the rigid contribution), and

$$\mathbf{C} = -\frac{\cos\Lambda}{2}\,\boldsymbol{\Upsilon}\,\mathbf{AIC}_R^*\boldsymbol{\Omega} \tag{3.190}$$

is the aerodynamic stiffness matrix. Since $\delta\boldsymbol{\eta}^T$ is arbitrary, Eq. 3.187 simplifies to

$$\left(\rho U^2\mathbf{C}+\mathbf{E}\right)\boldsymbol{\eta} = \rho U^2\mathbf{A}_r\boldsymbol{\alpha}_r \tag{3.191}$$

which is the classic form of the static aeroelastic equations of equilibrium (compare with Eq. 1.2), altered to include a vector of aerodynamic disturbance forces.

3.4.4 Solving the equilibrium equations

The first step is to use Eq. 3.191 to find the vector of generalised coordinates $\boldsymbol{\eta}$. For a dynamic aeroelastic analysis these are functions of time, but constant for the static analysis

$$\boldsymbol{\eta} = \left[\rho U^2\mathbf{C}+\mathbf{E}\right]^{-1}\rho U^2\mathbf{A}_r\boldsymbol{\alpha}_r \tag{3.192}$$

To obtain the total lift for the half-wing, Eq. 3.182 is substituted into Eq. 3.176 and then this expression is used for $\boldsymbol{\alpha}$ in Eq. 3.164. This then must be multiplied by $\hat{b}$ (spanwise width of each aerodynamic panel) to obtain the lift force rather than the lift per unit span for each panel. Finally, the lift for each panel is

summed to find the total lift,

$$L = q\hat{b}\sum_{p=1}^{g\times h} \mathbf{AIC}^{*}_{R_p}\left(\boldsymbol{\alpha}_r + \boldsymbol{\Omega\eta}\right) \tag{3.193}$$

The 3D/global lift coefficient is given by [65, 85]

$$C_L = \frac{L}{qS} \tag{3.194}$$

where S is the half-wing area. Substituting the same expression for $\boldsymbol{\alpha}$ into Eq. 3.149 allows the vector of unknown vortex strengths to be found from

$$\mathbf{c} = -\boldsymbol{\Psi}_P^{-1} U_\infty \left(\boldsymbol{\alpha}_r + \boldsymbol{\Omega\eta}\right) \tag{3.195}$$

This can then be substituted into Eq. 3.144 (expressed in vector format for multiple vortices) to find the vector of induced downwashes at point M on all bound vortices

$$\mathbf{w}_i = -\boldsymbol{\Psi}_M \boldsymbol{\Psi}_P^{-1} U_\infty \left(\boldsymbol{\alpha}_r + \boldsymbol{\Omega\eta}\right) \tag{3.196}$$

To find the induced drag, the p^{th} entry of vectors $\mathbf{c}$ and $\mathbf{w}_i$ (i.e. Γ_p and w_{i_p}) are substituted into Eq. 3.108 and multiplied by $\hat{b}$ to obtain the drag force rather than the drag per unit span for each panel. Finally, the drag for each panel is summed to find the total (induced) drag,

$$D_i = \rho\hat{b}\sum_{p=1}^{g\times h} \Gamma_p w_i \tag{3.197}$$

The 3D/global induced drag coefficient is given by [65, 85]

$$C_{D_i} = \frac{D_i}{qS} \tag{3.198}$$

The divergence dynamic pressure q_d can be found from the lowest real and positive solution to the matrix eigenvalue problem [15] (from Eq. 3.192)

$$|\mathbf{E} - q_d(-2\mathbf{C})| = 0 \tag{3.199}$$

The bending of the forward spar $h_1(x_1)$ and rear spar $h_2(x_2)$ can be found by substituting the known values of $\boldsymbol{\zeta}$ and $\boldsymbol{\beta}$ (from $\boldsymbol{\eta}$) back into Eqs. 3.70 and 3.71.

3.5 Validation and verification

To evaluate the accuracy of the developed model, a comparison with a representative finite element model using NASTRAN™ was performed. Three distinct comparisons were done; structural (i.e. deformation under point loads) to investigate the accuracy of the stiffness matrix, aerodynamic (i.e. rigid structure), and full aeroelastic. Additionally, a further aerodynamic comparison with Tornado (a vortex-lattice method code developed by the Royal Institute of Technology in Sweden and the University of Bristol in the UK [165]) was performed, mainly to validate the induced drag calculation which NASTRAN™ has no capability of analysing [116].

From this point forward the angle of orientation of each spar in the 2-spar rotating spars wing will be described by $[\phi_f \ \phi_r]$, the angle in degrees between the wing chordline and the principal axis z' of the spar for the forward and rear spar respectively, where $I_{z'z'} \leq I_{y'y'}$ e.g. [90 90] is the spar combination required for maximum wing bending stiffness, and [0 0] is required for the minimum wing bending stiffness.

3.5.1 Structural comparison

A finite element (FE) model was made using NASTRAN™ with the same parameters as the model herein. A force and moment were applied at the tip of

the forward spar and deflections at thirty evenly-spaced spanwise locations for each spar were obtained using a linear static solution sequence (SOL 101). This was done for a variety of spar orientations ([90 0], [0 90], [25 75]). An identical analysis was performed using the Rayleigh-Ritz (RR) assumed modes structural model, with 11 trial functions used for each spar (i.e. up to 12^{th} order polynomial terms), which was more than sufficient for convergence of the solution (a convergence plot is shown in section 3.5.3). Figures 3.23 and 3.24 show the percentage difference between the two approaches for bending and twisting deflections, and figures 3.25 and 3.26 show their respective true deformations. Both plots show a

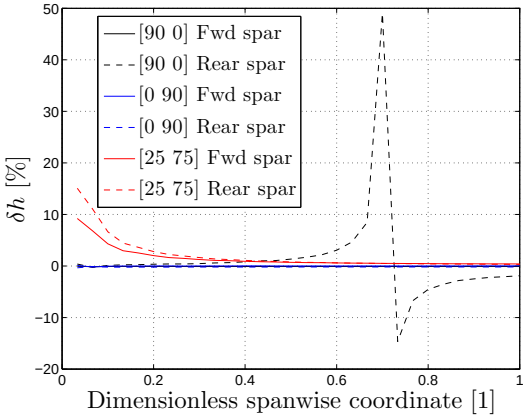

Figure 3.23: Difference in bending deflection δh of spars under point loads.

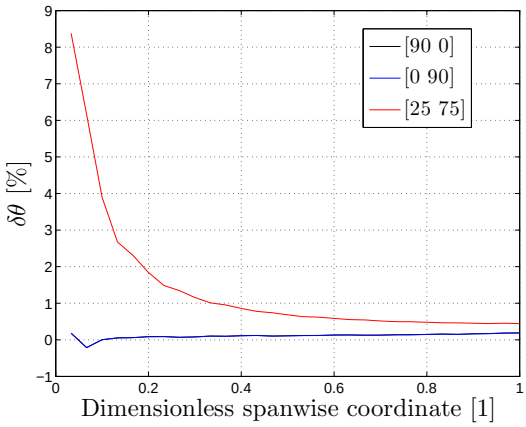

Figure 3.24: Difference in twisting deflection $\delta\theta$ of wing under point loads.

good comparison, generally with errors less than 1% from the FE model for most of the span. The large error spike that does occur (the rear spar during case [90 0]) in the bending comparison plot (figure 3.23) at around 70% span is due to the bending deflection passing through zero as shown in figure 3.25, and therefore, when calculating the percentage error, a zero exists on the denominator resulting in an infinite percentage error. Note that this spike is not present in the plot of actual bending deflection (figure 3.25). The other significant error occurs at the root of the wing, in both bending and twisting. As can be seen from figures 3.23 and 3.24, this does not occur in the [0 90] or [90 0] cases, only in the [25 75] case. The source of this error is due to a non-zero value for $I_{y_j z_j}$ (i.e. product

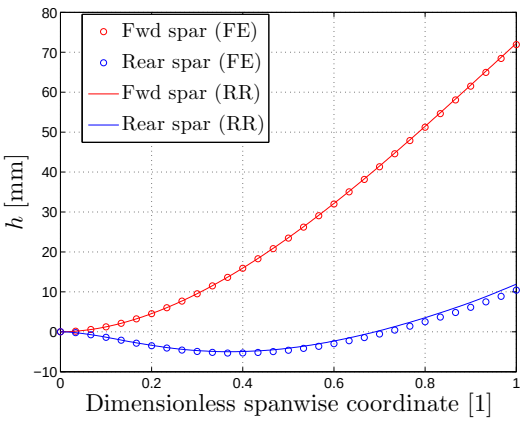

Figure 3.25: Bending deflection of spars under point loads.

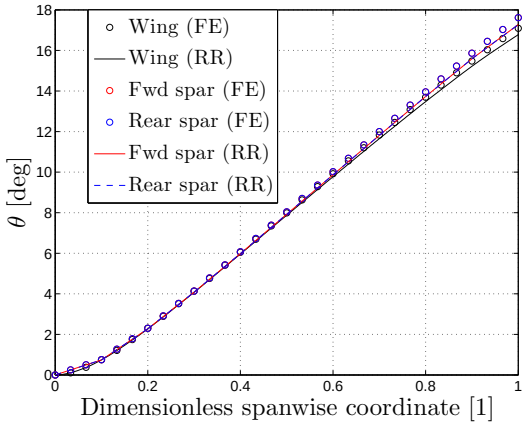

Figure 3.26: Twisting deflection of wing under point loads.

moment of area about wing axes, *not* $I_{y'_j z'_j}$ which is about the spars' principal axes and for this investigation was always zero) for cases when the spars are not oriented a 0° or 90°; for non-principal directions, the coupling of $I_{y_j z_j}$ gives the spar deflection a component in the plane of the wing. There is work associated with this translation and so less work is available to move the spar in the vertical direction, therefore less displacement is observed in this direction than predicted by the RR assumed modes model which assumes zero movement in the plane of the wing. To confirm this as the cause of the error, the comparison was repeated with all the nodes in the FE model constrained in motion in the plane of the wing. Figures 3.27 and 3.28 show that the large root errors for the non-principal orientations of the spars have been eliminated, therefore reinforcing that this is the only significant source of error in the structural model. In section 3.5.3 it will be seen that this model discrepancy has an insignificant effect on both the aeroelastic loads and deflections, and is only noticeable when a linear static analysis is performed. From this comparison it can be concluded that the derived stiffness matrix is sufficiently accurate, and that the interpolation functions used (polynomial) represent the modes well.

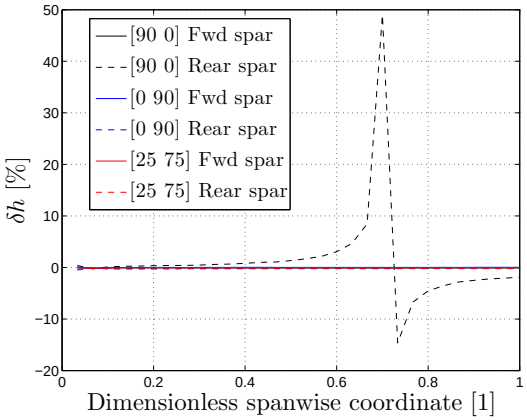

Figure 3.27: Difference in bending deflection of spars under point loads (constrained FE model).

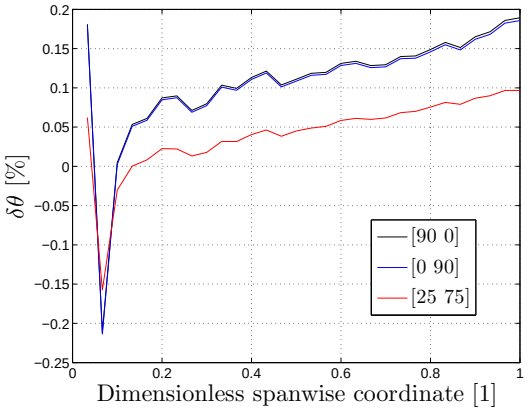

Figure 3.28: Difference in twisting deflection of wing under point loads (constrained FE model).

3.5.2 Aerodynamic comparison

Required number of aerodynamic panels for convergence

As with any discrete method, the vortex-lattice method becomes more accurate as the number of panels used increases. However, as the numbers of panels used increases, so too does the computational time. As a consequence, a compromise is usually found which offers relatively accurate solutions without being overly computationally expensive.

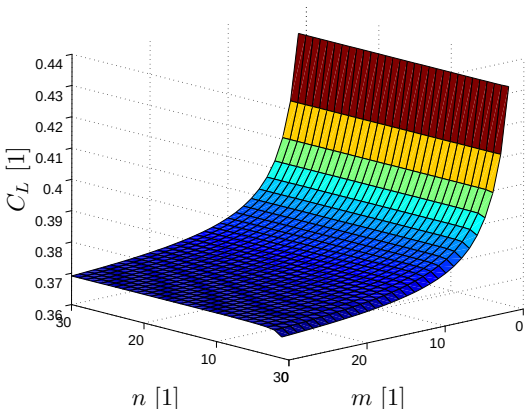

Figure 3.29: Convergence of C_L with number of panels.

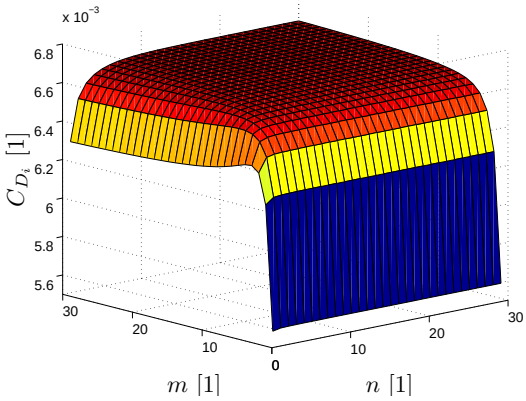

Figure 3.30: Convergence of C_{D_i} with number of panels.

To investigate the convergence of the lift and induced drag solutions, the

number of semi-spanwise m and chordwise n aerodynamic panels were varied, with the results shown in figures 3.29 and 3.30. This was done for an arbitrary swept planform with a rigid structure. The plots clearly show that as the number of chordwise panels increases, the aerodynamic forces converge quickly, relative to the rate of convergence for the number of spanwise panels. Figure 3.31 illustrates the corresponding variation in computation time. From this plot the need for a compromise in the number of panels used becomes clear; for one-off analyses, it is acceptable to use many panels ($m \geq 30$, $n \geq 30$), with associated computation times in excess of 20 s, but with high accuracy. For parameter studies and optimisation runs where many analyses are necessary, a lower number of panels (chordwise in particular) are recommended (e.g. $m = 25$, $n = 10$) resulting in fairly accurate solutions and fast computation times of less than 1.5 s.

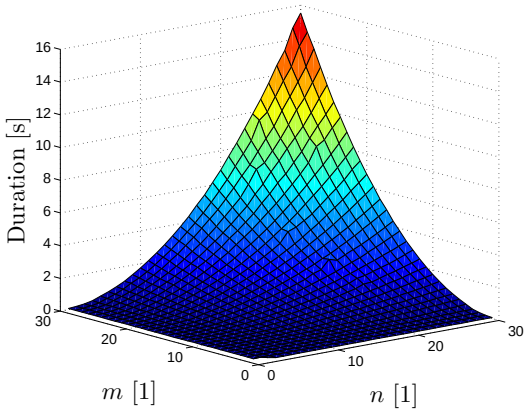

Figure 3.31: Variation of computation time with number of panels.

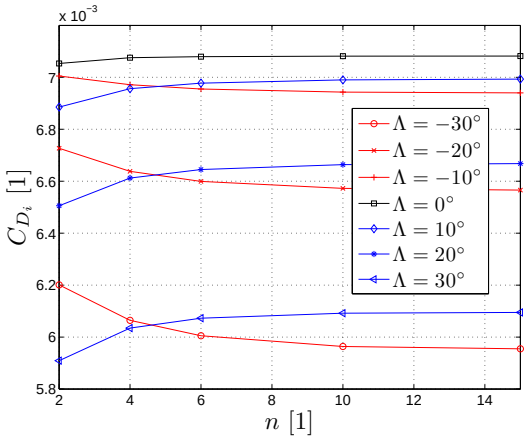

Figure 3.32: Effect of sweep on convergence of C_{D_i} in chordwise direction.

One disadvantage of the vortex-lattice method is the inaccuracy of the induced-drag prediction for swept planforms; as the sweep angle moves further away from zero, the rate of convergence of the number of chordwise panels decreases (see figure 3.32). This is caused by the kink in the bound vortices at mid-span which causes an induced downwash that tends to infinity near the kink. Such velocity gradients are not found in nature and a more realistic vortex sheet for swept planforms would have smooth curved bound vortices at inboard locations [65, 101];

this is beyond the scope of this model. However, from figure 3.32) it can be seen that it is possible to use less aerodynamic panels (e.g. $m = 25$, $n = 5$) for unswept planforms than was previously stated without affecting the accuracy.

Comparison of lift and induced drag

To gain an insight into the accuracy of the vortex-lattice method (VLM) aerodynamic model used, three FE models were made and aerodynamics were added using the doublet-lattice method (DLM) provided by NASTRAN™ [116]; an unswept wing, a wing with sweepback ($\Lambda = 20°$), and a wing with forward sweep ($\Lambda = -20°$). Using a static aeroelastic analysis (solution sequence SOL 144), a rigid trim analysis was requested for each of the planforms with the (rigid) angle of incidence α_r set to 5°. Similar models were made in the VLM aerodynamic model and the lift coefficient results were compared. Identical analyses were also performed using Tornado (a vortex-lattice method code developed as a collaboration between the Royal Institute of Technology in Sweden and the University of Bristol in the UK [165]); this provided another independent source to compare lift coefficients to. However, more significantly, the Tornado code also offered induced drag coefficients for comparison which NASTRAN™ does not do [116]. For all three approaches, an aerodynamic grid of 25 spanwise and 10 chordwise aerodynamic panels was used.

Table 3.1: Comparison of rigid lift coefficient between the VLM and DLM.

Λ [deg]	$C_{L_{\text{DLM}}}$ [1]	$C_{L_{\text{VLM}}}$ [1]	ΔC_L [%]
0	0.38458	0.38500	+0.10921
20	0.35610	0.35667	+0.16007
-20	0.35530	0.35606	+0.2139

Table 3.1 summarises the comparison of the 3D lift coefficient C_L for the various models. For all three planforms it can be seen that the VLM prediction is in excellent agreement with the finite element method, with less than 0.25% error.

Table 3.2: Comparison of rigid lift coefficient between the VLM and Tornado code.

Λ [deg]	$C_{L_{\text{Tornado}}}$ [1]	$C_{L_{\text{VLM}}}$ [1]	ΔC_L [%]
0	0.38403	0.38500	+0.25258
20	0.36898	0.35667	-3.3362
-20	0.36834	0.35606	-3.3339

Table 3.2 shows the same comparison of the 3D lift coefficient C_L, but against the Tornado values instead of the NASTRAN™ values. Once again, agreement between the two is generally good, although the difference is more notable on swept planforms, indicating that the Tornado code deals with swept wing aerodynamics slightly differently to both NASTRAN™ and the vortex-lattice model developed by the author.

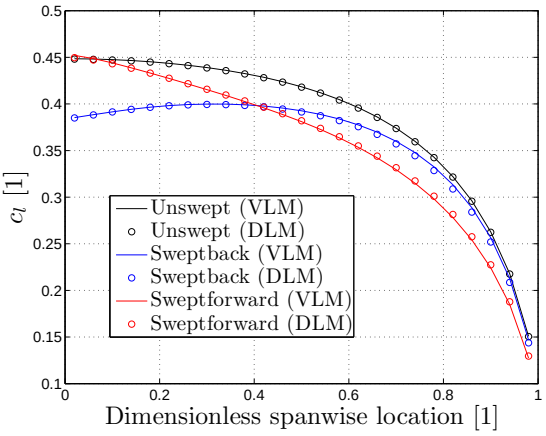

Figure 3.33: Lift distribution for a rigid wing.

Figure 3.33 shows the lift distribution across the span for the three cases (for DLM and VLM only) and again the results agree well with the DLM aerodynamic model.

Table 3.3 shows the comparison of the 3D induced drag coefficient C_{D_i} between the developed vortex-lattice model and the Tornado code. Agreement between the two is good for the unswept case ($< 0.75\%$ error). However, for the swept cases the error is more substantial (5 - 6%); this error is not unexpected given the results of the lift comparison (tables 3.1 and 3.2) which suggest that the

Tornado code deals with swept wing aerodynamics differently to the other two approaches considered. Nevertheless, the values of induced drag are relatively accurate within the scope of the theory (see the part of this section on required number of aerodynamic panels for convergence for details of the limitation of induced drag modelling via vortex-lattice based approaches).

Table 3.3: Comparison of rigid induced drag coefficient between the VLM and Tornado code.

Λ [deg]	$C_{D_{i_{\text{Tornado}}}}$ [1]	$C_{D_{i_{\text{VLM}}}}$ [1]	ΔC_{D_i} [%]
0	0.0070299	0.0070814	+0.73259
20	0.0066157	0.0069563	+5.1484
-20	0.0065245	0.0068994	+5.7460

The good results of the aerodynamic comparison are as expected, since the doublet-lattice method supplied by NASTRAN™ has zero reduced frequency for the steady case and therefore becomes equivalent to the vortex-lattice method [116], and Tornado uses the vortex-lattice method also [165], although clearly there is some discrepancy in the aerodynamic calculations of swept wings between Tornado and the other two methods.

3.5.3 Aeroelastic comparison

To check the accuracy of the coupling/splining of the aerodynamic model to the structural model, a full aeroelastic comparison was performed also. The same three FE models as in section 3.5.2 were used (i.e. an unswept wing, a wing with sweepback ($\Lambda = 20°$), and a wing with forward sweep ($\Lambda = -20°$)). However, this time an elastic trim analysis was requested with the rotating spars set to [25 75], but with the same rigid angle of incidence α_r of 5°. All three FE models were also analysed with the constraint mentioned in section 3.5.1 in place i.e. all nodes constrained in movement in the plane of the wing; this was done to investigate the validity of this assumption/simplification in the assumed modes model. No comparison of aeroelastic induced drag was performed as NASTRAN™ is not

capable of calculating drag, and Tornado is only an aerodynamic model i.e. no ability to couple to a structure.

Table 3.4: Comparison of aeroelastic lift coefficient between the RR\VLM model and FE\DLM model.

Λ [deg]	$C_{L_{\mathrm{DLM}}}$ [1]	$C_{L_{\mathrm{DLM}_c}}$ [1]	$C_{L_{\mathrm{VLM}}}$ [1]	ΔC_L [%]	ΔC_{L_c} [%]
0	0.55314	0.54869	0.54826	-0.88159	-0.078454
20	0.44711	0.44575	0.45275	+1.2613	+1.5706
-20	0.51980	0.51634	0.50969	-1.9443	-1.2886

In table 3.4, the c subscript indicates an FE analysis with the constraint described above in place. For the unconstrained comparison, the results show very good agreement in the values of C_L for the cases considered, with less than 2% error. In general, there is a small increase in the error from the rigid aerodynamic comparison presented in table 3.1, and this is due mainly to slight differences between the VLM/RR and the DLM/FE models in the way that the aerodynamic model is splined to the structural model. There is also a small source of error from the zero deflection in the plane of the wing assumption; it can be seen that, in general, the results improve slightly with this constraint in place in the FE analysis too.

Table 3.5 shows that the divergence behaviour compares well too. At worst, the difference is less than 1.75%. This is an acceptable error, especially as this translates as less than 1.5% error in the divergence speed. As with C_L, the accuracy of the divergence analysis improves if the FE model is constrained as above. Importantly though, it is clear from both these tables that the effect of this assumption on the accuracy of the aeroelastic model is almost insignificant compared to the effect it has on the accuracy of a non-aerodynamic loading as presented in section 3.5.1.

Figure 3.34 shows the lift distribution for all three wing planforms. Comparison with figure 3.33 allows the impact of an elastic structure on the lift distribution to be clearly seen. At a glance, it is apparent from these two figures

Table 3.5: Comparison of divergence dynamic pressure between the RR\VLM model and FE\DLM model.

Λ [deg]	$q_{d_{\mathrm{DLM}}}$ [Pa]	$q_{d_{\mathrm{DLM}_c}}$ [Pa]	$q_{d_{\mathrm{VLM}}}$ [Pa]	Δq_d [%]	Δq_{d_c} [%]
0	1543.3	1566.0	1568.4	+1.6242	+0.15227
20	2428.5	2457.1	2470.6	+1.7325	+0.54848
-20	1429.5	1445.1	1450.8	+1.4950	+0.40004

that the aeroelastic lift model is less accurate than the rigid lift model, reinforcing the results in table 3.4, and it can be seen here that this inaccuracy occurs almost uniformly over the span.

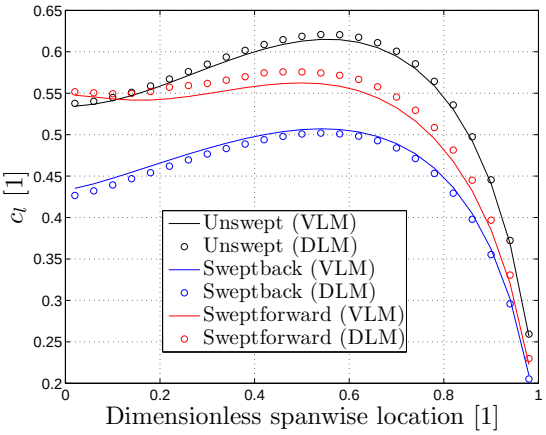

Figure 3.34: Lift distribution for an elastic wing.

Figures 3.35a - 3.35d illustrate the accuracy of the resulting structural deformations due to the aeroelastic loads. The first three of these plots show that there is good agreement in the bending deformations of the spars (and therefore the wing) for all planforms considered. There is a small but noticeable (at the tip) error that occurs, most likely due to the splining differences mentioned previously. Figure 3.35d shows the wing twist (calculated from the bending deflections of the two spars) deformation for the three cases, and it is clear from this that the small errors in the bending deflection combine to form more substantial errors in the twisting deformations, although they are still acceptable at less than 3%.

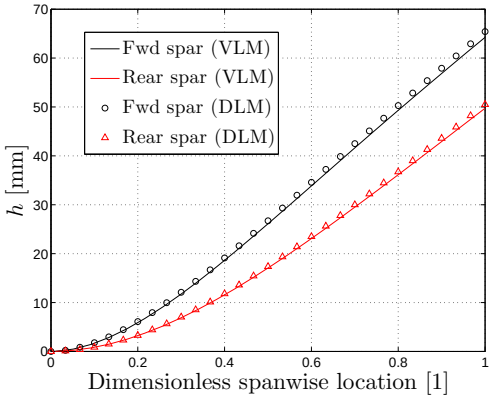

(a) Bending deflection of spars for an unswept wing.

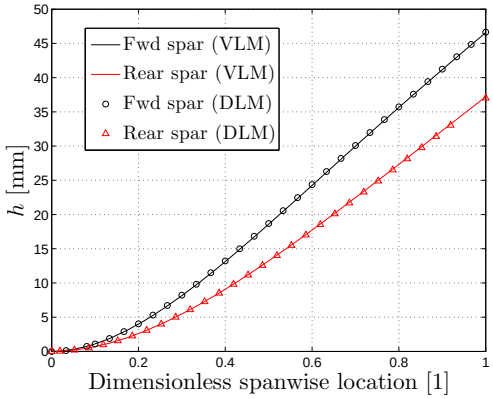

(b) Bending deflection of spars for a swept-back wing.

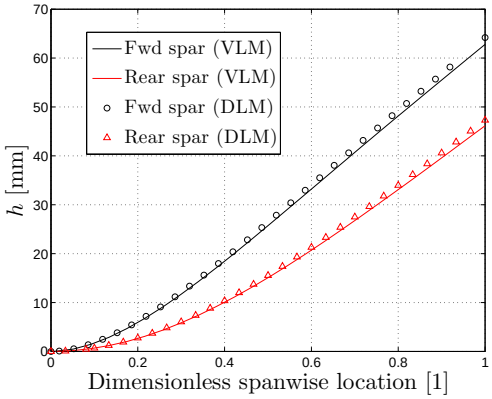

(c) Bending deflection of spars for a swept-forward wing.

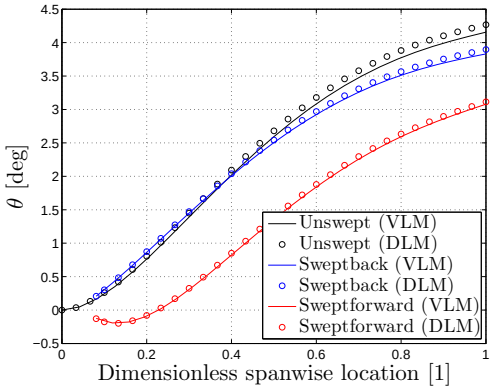

(d) Twisting deflection of wing (all cases).

Figure 3.35: Comparison of aeroelastic deflections.

Required number of shape functions for convergence

The number of shape functions required for each spar to achieve convergence of the solution is of course dependent on the structure itself. For instance, for wing torsion, as the ribs are given higher torsional stiffness values, the polynomial shape functions will be very different to the modes of the system, and therefore more shape functions will be required for convergence. However, for realistic ranges of spar and rib stiffnesses, the number of shape functions required for convergence will not vary much. Figures 3.36a - 3.36c illustrate the convergence of the lift coefficient, induced drag coefficient and divergence dynamic pressure respectively for a wing with realistic values of these stiffness terms.

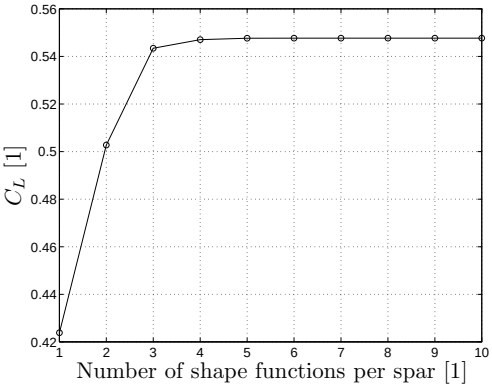

(a) Convergence of lift coefficient with number of RR shape functions.

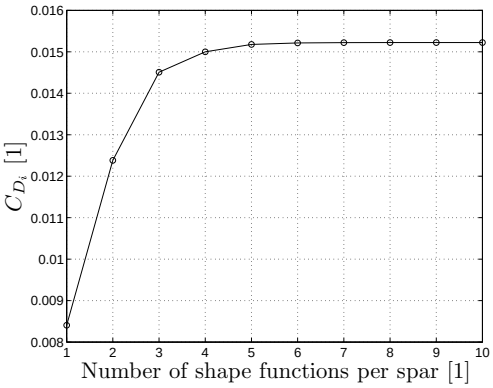

(b) Convergence of induced drag coefficient with number of RR shape functions.

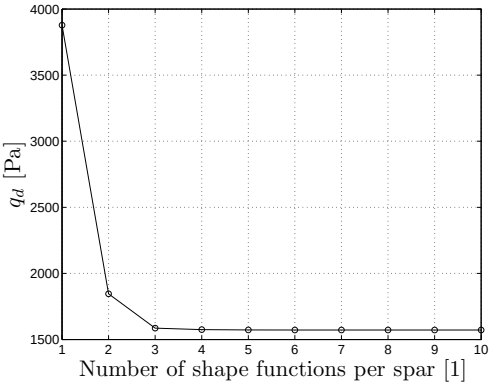

(c) Convergence of divergence dynamic pressure with number of RR shape functions.

Figure 3.36: Convergence of solution with number of Rayleigh-Ritz shape functions per spar.

It can be seen that the lift coefficient converges to a solution with 4 or 5 shape functions per spar, while the induced drag coefficient requires perhaps an additional higher order term for satisfactory convergence (5 or 6 shape functions per spar). The divergence dynamic pressure converges the quickest, after only 3 shape functions. With this in mind it is the recommendation of the author that at least 7 shape functions be used, thereby introducing an error margin. However, the full aeroelastic analysis, when tested, took an average of 1.61 s to run with 7 shape functions (with 25 spanwise and 10 chordwise aerodynamic panels), and 1.63 s to run with the maximum number of shape functions (limited to 11 due to rounding errors becoming significant in matrix inversion in MATLAB®) therefore

11 shape functions were used for all subsequent analyses.

3.6 Conclusions

In this chapter, an assumed modes vortex-lattice method static aeroelastic model has been developed from first principles. The equations of equilibrium were obtained using the Principle of Virtual Displacements, and then it was shown how the task of solving these could be made less challenging by approximating the system modes with assumed modes (Rayleigh-Ritz method). Next, a static aeroelastic model was derived using the vortex-lattice method, and this model and the structural model were then manipulated in order for the aerodynamics to spline correctly to the structure. Finally, a comparison with an equivalent finite element model showed that the theory behind the developed aeroelastic model is correct, and that the assumptions made were valid.

Chapter 4

An analytical study using the rotating spars aeroelastic model

4.1 Introduction

The static aeroelastic model developed in chapter 3 was used to perform a comprehensive analytical investigation to gain further insight into the rotating spars concept and to establish trends that will aid in the design of a wing incorporating this technology.

Firstly, a parameter study was carried out; the main aim of this was to investigate the effect that the rotating spars' orientations have on various aeroelastic parameters.

Next, an investigation was performed to establish how various wing and spar design parameters impact the effectiveness of the concept. This study was made more realistic by defining constraints in the analysis.

The results of these studies were carried through into further work on the concept to enable an efficient and successful design (see chapter 5).

As the results of the parameter study and effectiveness study will show, the design of a rotating spars wing is not straightforward due to the many conflicting design variables that impact the effectiveness of the concept, as well as the

constraints already mentioned that further complicate the design. Optimisation is a tool well suited to overcoming such a problem, and therefore an optimisation procedure (a genetic algorithm) was employed in conjunction with the static aeroelastic assumed modes model in order to arrive at an analytical wing design that was capable of effectively minimising induced drag and altering its lift.

This wing design was then used as the platform to perform a trim optimisation exercise (via the method of steepest descent/ascent); the goal of this study was to trim the wing to a fixed C_L value whilst using the rotating spars to minimise the induced drag.

The model was described in section 3.1, but to briefly re-cap, the wing planform used was full-span and limited to zero taper, and the structure consisted of exactly two spars but a variable number of ribs (which had to lie perpendicular to the spars). The structure was limited to sharing a single isotropic material. The aerodynamics used were implemented via a vortex-lattice lifting-surface approach and therefore steady inviscid flow was assumed, along with a zero wing thickness simplification. Assumptions that apply to the model were detailed throughout chapter 3, but the main constraints that were implemented are:

1. Spars were assumed to be of high aspect ratio such that the spanwise dimension of a spar is much greater than dimensions in other directions.

2. Ribs were assumed to be rigid in bending.

3. Reasonable angles of incidence were assumed since the aerodynamics have been linearised.

4. Inviscid flow was assumed, therefore the only contribution to the drag was the induced drag.

4.2 Parameter study

4.2.1 Structural behaviour

Since the rotating spars concept is an adaptive structures approach to morphing, it is intuitive that as the spars' orientations are altered, trends are most likely to be distinguishable in the structural behaviour. Naturally, trends will also appear in the aeroelastic behaviour of the wing, but these will be more difficult to explain with any certainty since the aeroelastic model contains many more variables than the basic structural model. Therefore, it was of interest to investigate the response of the structural model as the variables (forward and rear spar orientations) were altered, and the results of this may allow for a better explanation of the trends in the aeroelastic behaviour.

To perform a structural investigation, the aerodynamics were removed from the full model developed in chapter 3 and a static load vector replaced it such that Eq. 3.191, given by

$$\left(\rho U^2 \mathbf{C} + \mathbf{E}\right) \boldsymbol{\eta} = \rho U^2 \mathbf{A}_r \boldsymbol{\alpha}_r \tag{3.191}$$

became

$$\mathbf{E}\boldsymbol{\eta} = \mathbf{p} \tag{4.1}$$

where $\mathbf{p}$ is the vector of loads. For simplicity, only the unswept structure was considered, except for the study of the elastic axis position.

Chordwise position of the shear centre

The effect of the adaptive structures concept on the chordwise position of the shear centre of a wing section was of course of interest; in short, this is a major factor in determining the amount the wing will twist due to the aerodynamic loads i.e. the greater the distance between the aerodynamic and shear centres, the greater the moment arm.

To find the position of the shear centre of any given section, the wing was loaded (vertical force) near the leading-edge of the section to produce a non-zero twist, and then it was loaded near the trailing-edge of the section to produce a non-zero twist in the opposite direction. Plotting twist angle against chordwise loading point and assuming a rigid cross-section allowed the shear centre of the section to be found as the point where the projected twist is zero (see figure 4.1). This loading procedure was performed at the tip section for an arbitrary wing

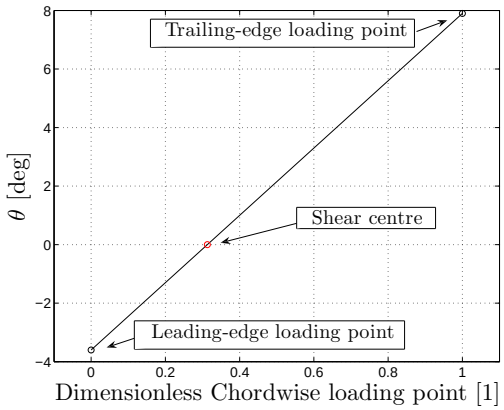

Figure 4.1: Locating the shear centre of a wing section.

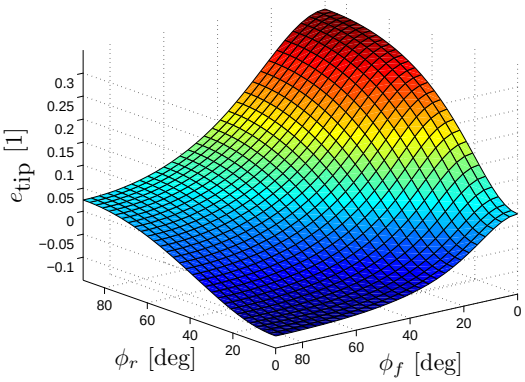

Figure 4.2: Variation a wing section (tip) shear centre position with spars' orientations.

setup for various forward ϕ_f and rear ϕ_r spar orientations (3° increments between 0° and 90° for both spars) and the results plotted in figure 4.2. The forward spar was given larger stiffness values than the rear spar, since this is more realistic (aerodynamic loading higher towards leading-edge and aerofoil thicker towards leading-edge).

As mentioned in section 3.5, the angle of orientation of each spar in the 2-spar rotating spars wing is described by $[\phi_f \ \phi_r]$, the angle in degrees between the wing chordline and the principal axis z' of the spar for the forward and rear spar respectively, where $I_{z'z'} \leq I_{y'y'}$ e.g. the wing's bending stiffness is maximum at the [90 90] configuration, and is minimum at the [0 0] configuration.

The results are fairly intuitive; the shear centre (e_{tip} is the fractional chordwise distance aft of the aerodynamic centre) is closest to the leading-edge at the [90

0] configuration, since this corresponds to a maximum forward spar bending stiffness and a minimum rear spar bending stiffness. In this region, the negative e_{tip} values imply that the shear centre lies ahead of the aerodynamic centre; the aeroelastic implication of this is that classical torsional divergence is impossible. As the forward spar is rotated towards 0°, and/or the rear spar is rotated towards 90°, the shear centre moves aft, being closest to the trailing-edge at the [0 90] configuration i.e. minimum forward spar bending stiffness and maximum rear spar bending stiffness.

For this example, a large variation in the chordwise position of the shear centre is possible (approximately a semi-chord variation). The main factors influencing the achievable range of the shear centre are the ratio of local bending stiffnesses for each of the spars i.e. $I_{y'y'}/I_{z'z'}$, the chordwise location of each of the spars (throughout chapter 5 this was described by the variables f and r for the forward and rear spars respectively), and the extent to which the rotating spars contribute towards the torsional rigidity of the wing; in the model considered in this investigation, this is close to 100% since the ribs are assumed to have a comparatively low contribution, and there are no other spars in the model. For realistic designs (such as the experimental model described in chapter 5) there will also be additional non-rotating spars, and the bending and torsional stiffnesses of these will contribute significantly towards the overall torsional rigidity of the wing, leading to a smaller variation in the chordwise position of the shear centre (see figure 5.21 in section 5.5.3).

Chordwise position of the elastic axis

The locus of shear centres at various spanwise locations is known as the elastic axis. For an unswept wing with uniform structural properties along its span, there will be no spanwise variation in the shear centre (i.e. figure 4.2 is valid along the entire length of the wing) and the elastic axis is a straight line. However, for a swept wing this is not true. To gain an insight into this behaviour, the

shear centres were found for a highly swept ($\Lambda = 40°$) wing at various spanwise locations, and various spar configurations. The results are shown in figure 4.3. The green shading represents the wing planform, and the solid blue lines represent the two spars. For ease of inspection, the plot is not to scale and the true aspect ratio of the wing was 6.67.

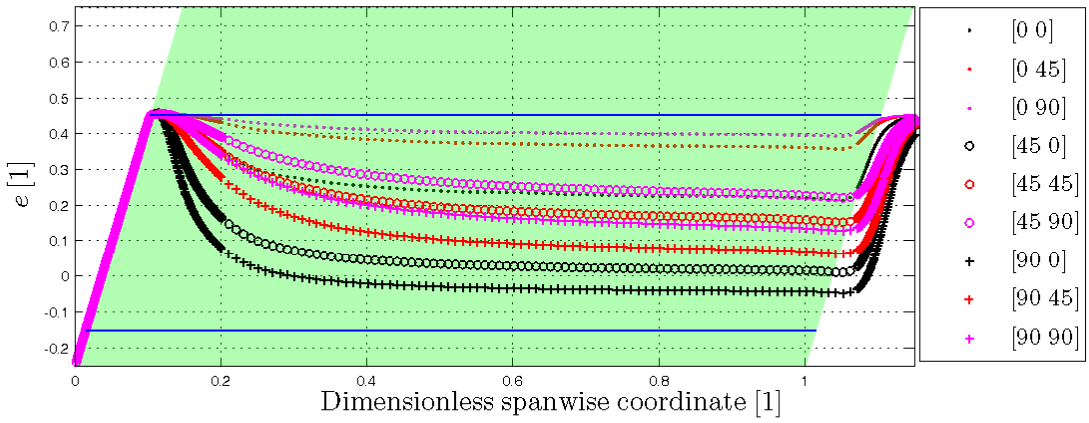

Figure 4.3: Variation of wing elastic axis position with spars' orientations for a swept wing.

The chordwise variation with the spar orientations follows the same relationship as presented in figure 4.2. However, it can be seen that for any given spar configuration, the shear centres deviate away from the unswept straight elastic axis prediction in the root and tip regions. More specifically, in the root region they curve towards the rear spar, meeting it at the wing root, before following a path along the root towards the leading-edge. In the tip region the shear centres curve towards the rear spar. The deviation of the elastic axes from a straight line is larger for larger sweep angles and smaller aspect ratios. The trend reverses for sweptforward wings i.e. the elastic axes curve towards the forward spar in the root and tip regions.

Flexural rigidity

The variation of the wing's flexural rigidity as the spars' orientations are altered is also of interest; for swept wings the bending deflection contributes towards the angle of incidence of the wing (see section 3.4.2) and therefore a coupling exists between the bending and torsional behaviour of the wing.

Using the results of the elastic axis investigation, for any given $[\phi_f \ \phi_r]$ the wing was again loaded with a vertical force on a point at the tip passing through the elastic axis. In this way, the resulting deflection was pure bending and zero torsion. Since the wing has uniform properties along its span, the wing flexural rigidity is given by [47]

$$K_h = \frac{Pl^3}{3h_{\text{tip}}} \tag{4.2}$$

where P is the point force, l is the length of the wing in structural axes i.e. along a spar, and h_{tip} is the resulting bending deflection of the elastic axis at the tip. This was done for the same arbitrary wing setup as the elastic axis investigation, for 3° increments between 0° and 90° for both spars. The results are shown in figure 4.4.

Once again, the results are intuitive; the wing's flexural rigidity is at its greatest at the [90 90] configuration, since both spars have greatest bending stiffness in this setup. Similarly, the lowest value of flexural rigidity is attained at the [0 0] configuration. The reason that the [90 0] configuration gives the wing a greater flexural rigidity than the [0 90] configuration is that the forward spar has larger cross-sectional dimensions than the rear spar, as already mentioned. The flexural rigidity of the wing can be altered by up to 900%, which is very substantial. This agrees with the following argument: the flexural rigidity of the wing can also be written as

$$K_h = EI_{yy} \tag{4.3}$$

where E is Young's modulus, and I_{yy} is the second moment of area of the wing in the bending plane. Variation of the spars' orientations does not affect E,

but does influence I_{yy}. Therefore $K_h \propto I_{yy}$, and so examination of the behaviour of I_{yy} will give an indication of the behaviour of K_h. The analysis assumed rectangular spars, and for the j^{th} spar the dimensions were given by b_{s_j} and d_{s_j}, where $d_{s_j} \geq b_{s_j}$. Therefore, for spar j, the maximum value for the second moment of area [89] in the wing bending plane is

$$I_{y_j y_j}\big|_{\max} = \frac{b_{s_j} d_{s_j}^3}{12} \tag{4.4}$$

and the minimum value is

$$I_{y_j y_j}\big|_{\min} = \frac{d_{s_j} b_{s_j}^3}{12} \tag{4.5}$$

For the wing containing two spars ($j = 1, 2$), it can then be shown that the maximum variation in I_{yy} is

$$\frac{I_{y_j y_j}\big|_{\max}}{I_{y_j y_j}\big|_{\min}} = \frac{b_{s_1} d_{s_1}^3 + b_{s_2} d_{s_2}^3}{d_{s_1} b_{s_1}^3 + d_{s_2} b_{s_2}^3} \times 100\% \tag{4.6}$$

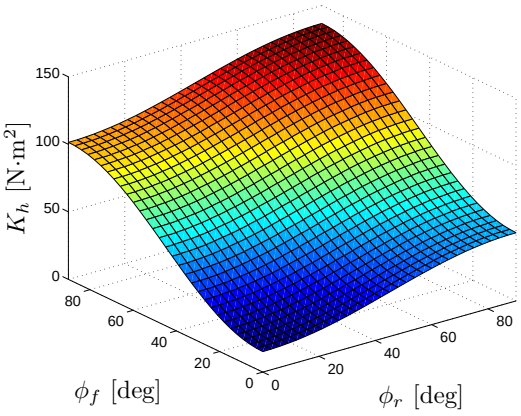

Figure 4.4: Variation of wing flexural rigidity with spars' orientations.

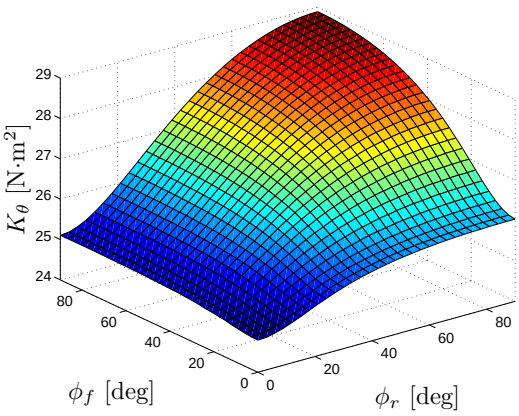

Figure 4.5: Variation of wing torsional rigidity with spars' orientations.

The analysis used a forward spar 5×15 mm and a rear spar 4×12 mm. This predicts that the flexural rigidity can be varied by 900%, which agrees with the

results of the analysis. As before, for a realistic wing the presence of non-rotating spars will decrease this value significantly.

Torsional rigidity

The variation of the wing's torsional rigidity as the spars' orientations are altered is the final structural aspect that is of interest; for all planforms, the torsional deflection contributes towards the angle of incidence of the wing (see section 3.4.2) and so its associated rigidity is important in determining the aerodynamic loads.

For a given $[\phi_f \ \phi_r]$ the wing was loaded with a pitching moment on a point at the tip. In this way, the resulting deflection was purely torsional and zero bending. Since the wing has uniform properties along its span, the wing torsional rigidity is given by [47]

$$K_\theta = \frac{Ml}{\theta_{\text{tip}}} \tag{4.7}$$

where M is the pitching moment, l is the length of the wing as before, and θ_{tip} is the resulting torsional deflection of the wing at the tip. This was done for the same arbitrary wing setup as the elastic axis investigation, for 3° increments between 0° and 90° for both spars. The results are shown in figure 4.5.

The results are slightly less intuitive this time. Understanding the contributions to the wing's torsional rigidity does help; as the wing twists, the displacement of the structure can be separated into three contributions: differential bending of the spars (one up, one down), torsion of the spars, and torsion of the ribs. Of these, it is only the bending of the spars which the adaptive structures concept can exploit; the bending displacement of spar j results in a vertical restoring force which is proportional to I_{s_j} (the second moment of area for spar j about a chordwise axis). This causes an equal and opposite moment about the wing's elastic axis for the two spars. The position of the elastic axis e varies with the spars' orientations also, therefore I_{s_1}, I_{s_2} and e all influence K_θ. For this reason it is difficult to explain the trends observed in figure 4.5, although a

maximum stiffness does occur at the [90 90] configuration, and the lowest value of wing torsional stiffness occurs at the [0 0] configuration. The torsional stiffness of the wing can be altered by up to around 20%. The reason that this is substantially lower than for the bending stiffness is that the rotating spars concept does not alter the torsional stiffnesses of the spars and ribs, which are significant portions of the wing's overall torsional stiffness. As before, for a realistic wing the presence of non-rotating spars will further decrease this value.

4.2.2 Aeroelastic behaviour

The main aims of the rotating spars concept are to, firstly, minimise drag for any given flight condition, and secondly, to achieve roll-control with a conformable (and therefore lower-drag) device. Consequently, the effect that the concept has on several related aeroelastic parameters are of interest.

In this section, three arbitrary wing planforms were used (unswept $\Lambda = 0°$, sweptback $\Lambda = 20°$, sweptforward $\Lambda = -20°$) at three different airspeeds (20 $m{\cdot}s^{-1}$, 25 $m{\cdot}s^{-1}$, and 15 $m{\cdot}s^{-1}$ respectively) and the forward and rear spar angles, ϕ_f and ϕ_r, were varied at 3° increments between 0° and 90°. The semi-span was set to $b = 0.9$ m and the chord was $c = 0.27$ m. The full static aeroelastic model developed in chapter 3 was used to obtain a range of outputs, with the results shown in figures 4.6a - 4.24.

The reason different airspeeds were used for each of the three planforms is because it is trends and not values that are of interest here and as the sweep angle is altered, the airspeed needs to be adjusted also to cause similar aeroelastic loads and deflections e.g. for a given sweptforward wing at 5 $m{\cdot}s^{-1}$, aeroelastic loads and deflections are large enough to observe trends. However, for the same wing with rearward sweep, trends are difficult to establish at 5 $m{\cdot}s^{-1}$. This becomes obvious if a sweptforward wing is operating near its divergence speed, resulting in very large deflections and loads, while at the same airspeed the equivalent sweptback wing has much more moderate loads and deflections.

The results shown here are separated into three categories: deflections/instabilities (divergence dynamic pressure q_d, wing tip twist θ, and forward and rear spar tip bending displacement h_1 and h_2), loads (C_L and C_{D_i}), and aerodynamic efficiencies (inviscid lift-to-drag ratio C_L/C_{D_i} and Oswald efficiency factor e_{O}).

Deflections/instabilities

The variation of forward and rear spar tip bending displacement ($h_{1_{\mathrm{tip}}}$ and $h_{2_{\mathrm{tip}}}$ respectively) with the spars' orientations for the three cases is shown in figures 4.6a - 4.6f.

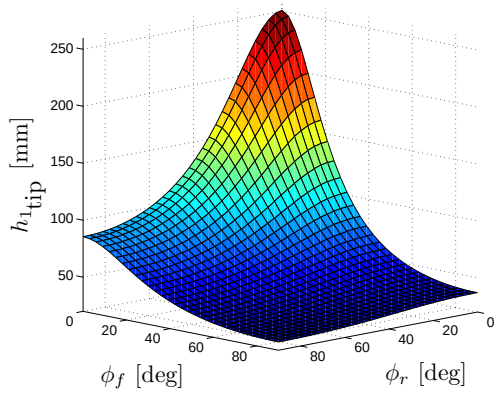

(a) Variation of $h_{1_{\mathrm{tip}}}$ with spars' orientations.

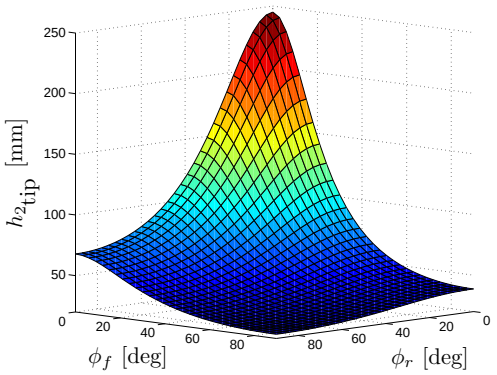

(b) Variation of $h_{2_{\mathrm{tip}}}$ with spars' orientations.

Figure 4.6: Variation of bending deflections (unswept).

It is clear at a glance that for each of the three planforms the spar (and hence wing) bending trends are very similar; as anticipated, the trends are the opposite of those identified in figure 4.4, the variation of the wing's flexural rigidity as the spars' orientations are varied i.e. maximum bending deflection occurs at the [0 0] configuration (minimum flexural rigidity), and minimum bending occurs at the [90 90] configuration (maximum flexural rigidity).

There are two contributing factors why the [0 90] configuration produces larger aeroelastic bending deflections than the [90 0] configuration; firstly, for this particular wing, the [90 0] configuration is stiffer in bending than the [0

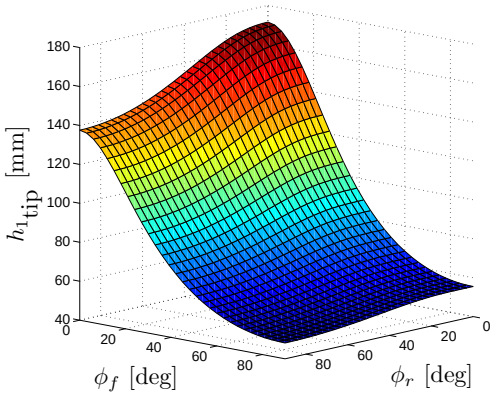

(c) Variation of $h_{1_{\text{tip}}}$ with spars' orientations.

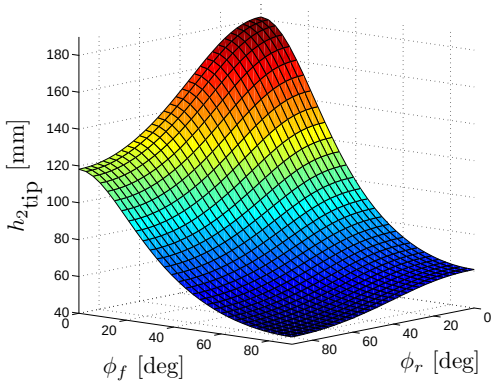

(d) Variation of $h_{2_{\text{tip}}}$ with spars' orientations.

Figure 4.6: Variation of bending deflections (sweptback).

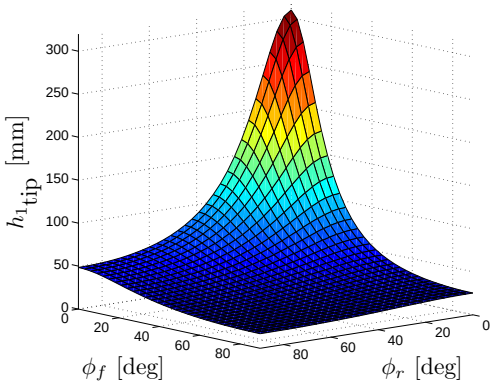

(e) Variation of $h_{1_{\text{tip}}}$ with spars' orientations.

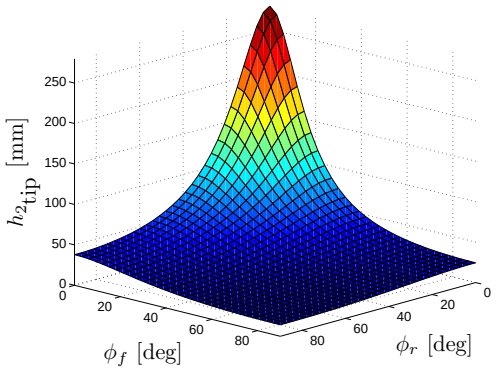

(f) Variation of $h_{2_{\text{tip}}}$ with spars' orientations.

Figure 4.6: Variation of bending deflections (sweptforward).

90] configuration (see section 4.2.1 for explanation). Secondly, the elastic axis is positioned further aft for the [0 90] configuration than for the [90 0] configuration (see figure 4.2) and so a greater lift force will be acting on the wing (greater moment arm, so greater twist, therefore greater angle of incidence).

From figures 4.6a - 4.6f it can be seen that as the wing is swept back the sensitivity of the bending deflections to changes in the spars' orientations becomes less, whereas sweeping the wing forward destabilises the bending behaviour (wing close to diverging in figures 4.6e and 4.6f) at the [0 0] configuration. This is because for swept wings, there is a contribution to the angle of incidence from the

bending deflection (see Eq. 3.170) and for sweptforward wings this is positive (destabilising), whereas for sweptback wings this is negative (stabilising).

The variation of wing tip torsional displacement, θ_{tip}, with the spars' orientations for the three cases is shown in figures 4.7, 4.9, and 4.11.

There are several factors that influence the aeroelastic torsional deflection including position of the elastic axis, wing torsional stiffness and sweep angle. However, from the plots it is clear that the main driver is the position of the elastic axis; for all three planforms the maximum torsional deflection occurs at the [0 90] configuration (corresponding to furthest aft elastic axis (see figure 4.2) and so largest pitching moment that acts to twist the wing). Similarly the minimum torsional deflection corresponds to when the elastic axis is at its furthest forward location i.e. the [90 0] configuration.

For the [90 90] and [0 0] configurations the elastic axis position is approximately the same; however, inspection of the other influencing factors allows the torsional deflection behaviour to be explained. From figure 4.5 it can be seen that the wing torsional stiffness is greater for the [90 90] configuration than for the [0 0] configuration. Therefore a greater torsional deflection can be expected for the [0 0] configuration for the unswept wing (see figure 4.7).

For swept wings there is also a bending contribution to the angle of incidence (from figures 4.6c - 4.6f, larger at [0 0] than [90 90] configuration); for the forward swept wing this is a positive contribution and causes a significant increase in lift force on the wing at the [0 0] configuration. This results in a positive contribution to the torsional deflection therefore augmenting the torsional stiffness contribution mentioned above and so the [0 0] configuration will clearly twist more than the [90 90] configuration (see figure 4.11). However, for the sweptback wing the bending contribution is negative and acts to oppose the torsional stiffness contribution, and for this particular wing figure 4.9 shows that the aeroelastic twist is actually slightly less at the [0 0] configuration than for the [90 90] configuration

for the rearward swept wing.

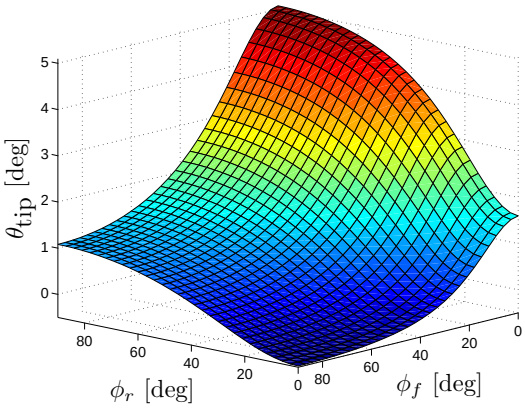

Figure 4.7: Variation of tip twist with spars' orientations (unswept).

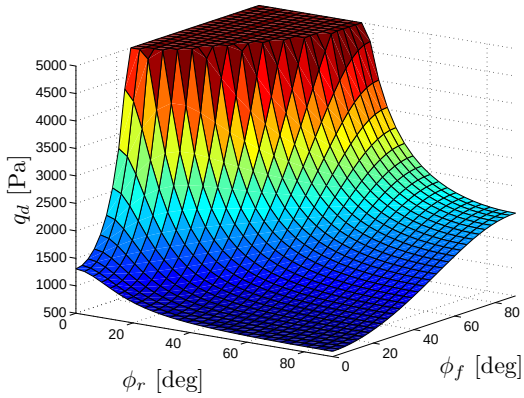

Figure 4.8: Variation of q_d with spars' orientations (unswept).

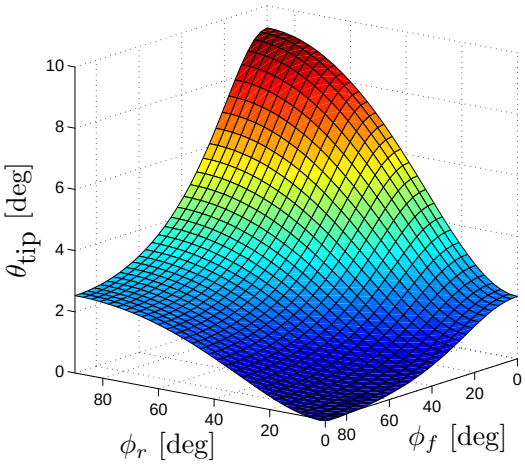

Figure 4.9: Variation of tip twist with spars' orientations (sweptback).

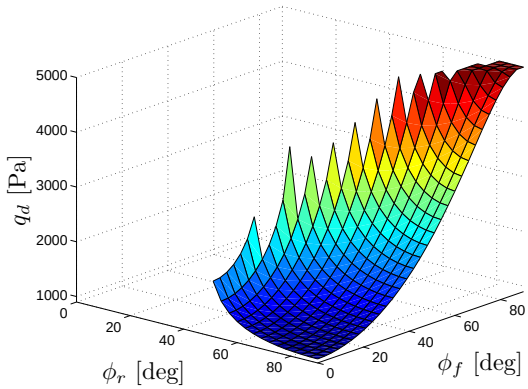

Figure 4.10: Variation of q_d with spars' orientations (sweptback).

Next, the divergence dynamic pressure q_d trends are discussed. In figure 4.8 the divergence plot abruptly plateaus off at 5000 Pa; this indicates a divergence dynamic pressure greater than or equal to 5000 Pa. In figure 4.10 there is an area of no data; this is because no real solutions were found for the corresponding spar configurations i.e. divergence is impossible.

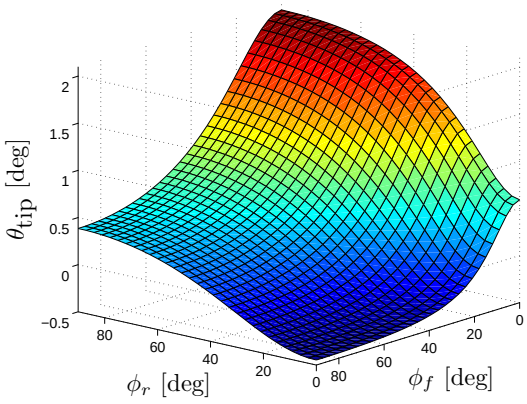

Figure 4.11: Variation of tip twist with spars' orientations (sweptforward).

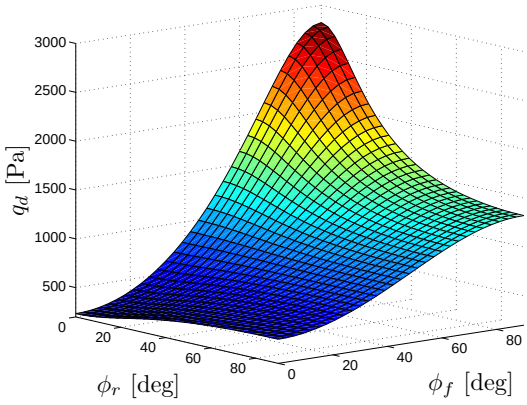

Figure 4.12: Variation of q_d with spars' orientations (sweptforward).

Unsurprisingly, the trends of divergence dynamic pressure (figures 4.8, 4.10, and 4.12) closely follow the inverse of the torsional deflection trends, indicating that the elastic axis position is the main driver; the explanation follows the same argument as for the torsional deflection trends. The only exception is for the sweptforward wing where the minimum divergence dynamic pressure occurs at the [0 0] configuration instead of the [0 90] configuration; as mentioned above, for forward swept wings the bending deflection has a destabilising effect and for the [0 0] configuration the bending deflections are at a maximum.

As expected, the most statically stable wing is the sweptback wing where for the majority of spar configurations aeroelastic divergence is impossible, and even at its most unstable arrangement the divergence dynamic pressure is approximately 1000 Pa (see figure 4.10). The unswept wing is less stable with a minimum divergence dynamic pressure of around 500 Pa, and divergence is a theoretical possibility for all configurations (although well above typical test speeds for many spar configurations) (see figure 4.8). As already mentioned, the forward swept wing is the most statically unstable of the planforms with a minimum divergence dynamic pressure of less than 250 Pa and a maximum of less than 3000 Pa.

Loads

The variation of C_L with the spars' orientations for the three cases is shown in figures 4.13, 4.15 and 4.17, and the corresponding variation of C_{D_i} is shown in figures 4.14, 4.16 and 4.18.

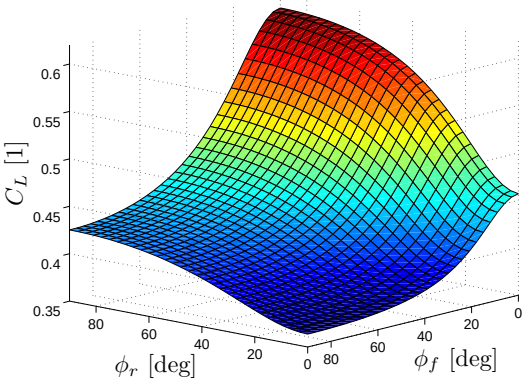

Figure 4.13: Variation of C_L with spars' orientations (unswept).

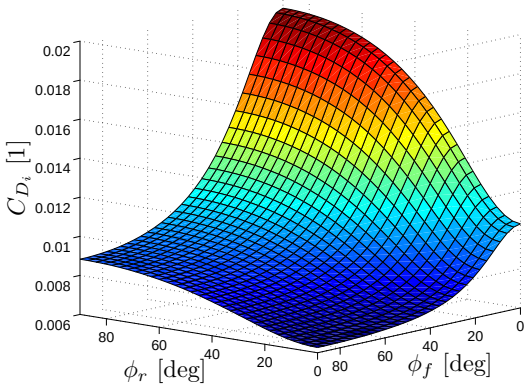

Figure 4.14: Variation of C_{D_i} with spars' orientations (unswept).

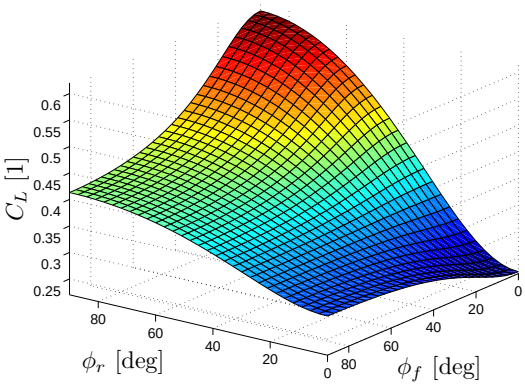

Figure 4.15: Variation of C_L with spars' orientations (sweptback).

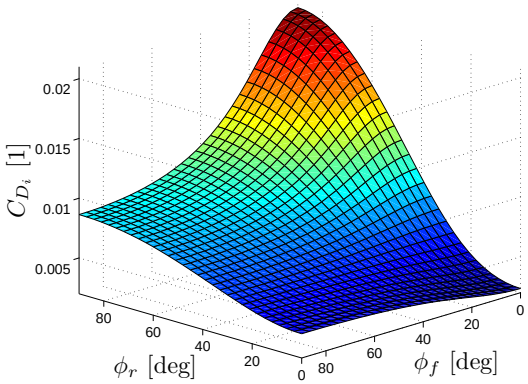

Figure 4.16: Variation of C_{D_i} with spars' orientations (sweptback).

It is clear at a glance that for each of the planforms the lift and induced drag trends are very similar. This is as expected since for a wing in inviscid flow [108]

$$C_{D_i} = C_D = \frac{C_L^2}{\pi \mathcal{A} \mathcal{R} e_{\mathrm{O}}} \tag{4.8}$$

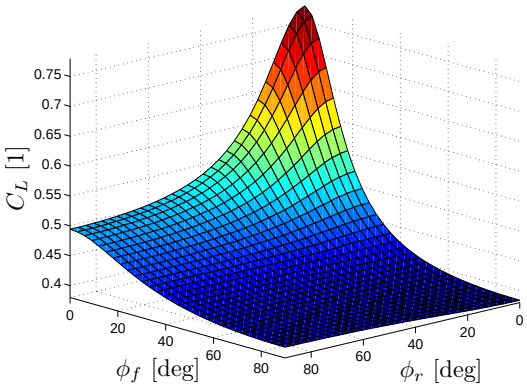

Figure 4.17: Variation of C_L with spars' orientations (sweptforward).

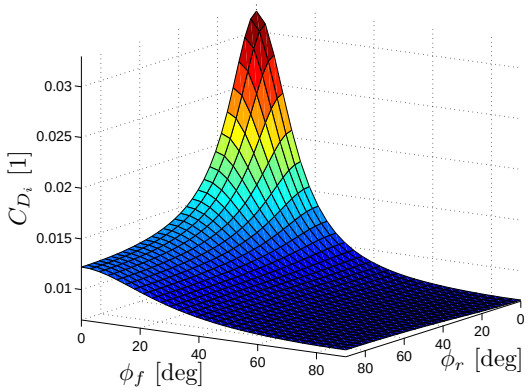

Figure 4.18: Variation of C_{D_i} with spars' orientations (sweptforward).

where $\mathcal{A}$R is the aspect ratio of the wing, and since the Oswald efficiency factor e_{O} is almost constant (some elastic variation [117], see figure 4.20) for a given planform, then clearly the induced drag is proportional to the square of the lift.

Besides the rigid angle of incidence, the main contributions to the angle of incidence and therefore aerodynamic forces are the wing's torsional deflection, and for a swept wing the wing's bending deflection. Therefore, for the unswept wing (see figures 4.13 and 4.14) the reason that C_L and C_{D_i} are maximum for the [0 90] configuration is because this coincides with the maximum wing twist (caused by furthest aft elastic axis). Similarly the minimum aerodynamic forces coincide with minimum twist (and furthest forward elastic axis) i.e. the [90 0] configuration.

For the sweptback wing the negative contribution to the aeroelastic forces from the bending deflection must be considered; this becomes significant for large bending deflections (e.g. close to the [0 0] configuration) and so does not affect the location of the maximum C_L and C_{D_i} values ([0 90]) where bending deflection is low. However, for the [0 0] configuration the lift and drag are decreased by this contribution to such an extent that it becomes lower than the lift value at the [90 0] configuration (where the bending deflection is low), and so the minimum aerodynamic loads for the sweptback wing occur at the [0 0] configuration (see

figures 4.15 and 4.16).

Conversely, for the sweptforward wing the bending deflection provides a positive contribution to the aeroelastic forces; once again, this effect is minimal for small bending deflections (e.g. [0 90], [90 0]) and so the minimum C_L and C_{D_i} values still occur at the [90 0] configuration. However, the large bending deflections that occur for low wing bending stiffnesses (e.g. [0 0]) provide a large increase in loads and at the [0 0] configuration the increase is large enough to surpass the loads at the [0 90] configuration, such that the maximum aerodynamic loads for the sweptforward wing occur at the [0 0] configuration (see figures 4.17 and 4.18).

Aerodynamic efficiencies

The effect the rotating spars concept has on the aerodynamic efficiency of the wing will be investigated in this section. This is of course an important aspect of the parameter study since the main goal of the concept is to maximise the efficiency. Here, two different efficiencies will be considered; the lift-to-drag ratio (aerodynamic efficiency), defined as C_L/C_{D_i} for a wing in inviscid flow, and the Oswald efficiency factor which indicates how close the lift distribution is to the optimum (elliptical) [108] and for the inviscid case is given by

$$e_{\mathrm{O}} = \frac{C_L^2}{\pi \mathcal{AR} C_{D_i}} \tag{4.9}$$

Substituting the expression for C_{D_i} given by Eq. 4.8 into the expression for the inviscid lift-to-drag ratio, C_L/C_{D_i} gives

$$\frac{C_L}{C_{D_i}} = \frac{\pi \mathcal{AR} e_{\mathrm{O}}}{C_L} \tag{4.10}$$

Given that e_{O} will vary very little relative to C_L as the spars are rotated allows the prediction to be made that the lift-to-drag ratio will approximately

follow the trends of the corresponding C_L values, inverted i.e.

$$\frac{C_L}{C_{D_i}} \propto \frac{1}{C_L} \tag{4.11}$$

Comparison of figures 4.19, 4.21 and 4.23 with figures 4.13, 4.15 and 4.17 respectively reveals that this is indeed the case; for all cases the spar configuration required for maximum lift-to-drag ratio coincides with the minimum lift configuration, and similarly the spar configuration required for minimum lift-to-drag ratio coincides with the maximum lift configuration. In general however, this will not be true for the same wing in viscous flow where the induced drag is only part of the overall drag. Additionally, for viscous flow, the lift-to-drag ratios will be considerably lower.

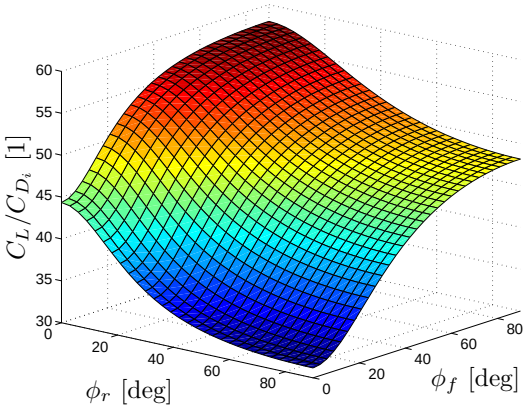

Figure 4.19: Variation of lift-to-drag ratio with spars' orientations (unswept).

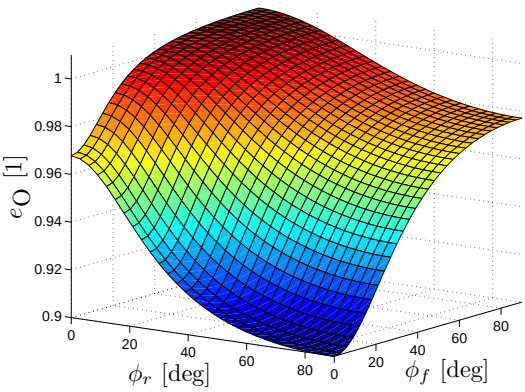

Figure 4.20: Variation of Oswald efficiency factor with spars' orientations (unswept).

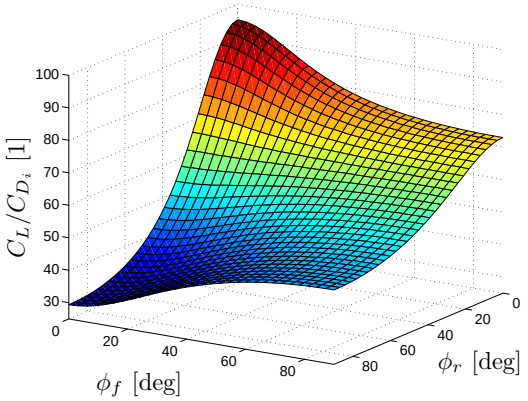

Figure 4.21: Variation of lift-to-drag ratio with spars' orientations (sweptback).

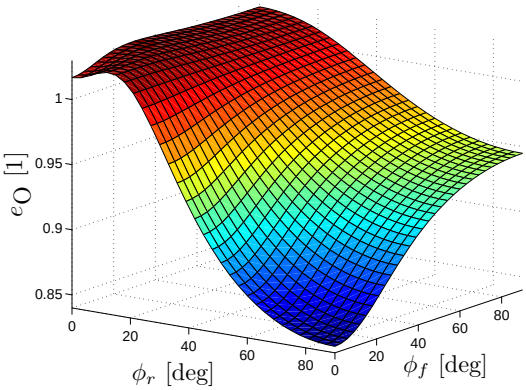

Figure 4.22: Variation of Oswald efficiency factor with spars' orientations (sweptback).

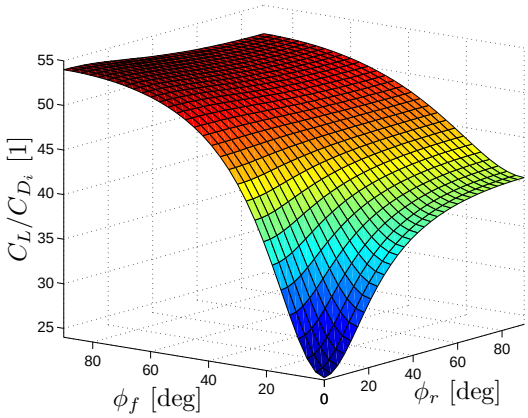

Figure 4.23: Variation of lift-to-drag ratio with spars' orientations (sweptforward).

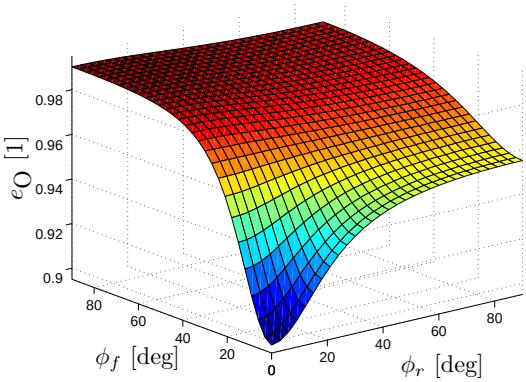

Figure 4.24: Variation of Oswald efficiency factor with spars' orientations (sweptforward).

The plots of Oswald efficiency factor e_O as a function of the spars' orientations (figure 4.20, 4.22, and 4.24) follow the trends of the lift-to-drag ratio plots closely, although there is one major discrepancy; figure 4.22 shows that for the sweptback case the trend deviates from the equivalent lift-to-drag ratio trend (figure 4.21) close to the [0 0] configuration. The large influence that the bending deflections have on the aerodynamics for the sweptback [0 0] configuration is most likely having an effect, and the implications of this become apparent in section 4.5.

4.3 Establishing design guidelines

4.3.1 Procedure

The parameter study carried out in section 4.2 is useful to identify trends and the expected behaviour of a wing incorporating the rotating spars adaptive internal structures concept. However, it provides only a limited insight into the feasibility of the concept for an arbitrary wing and no rules of thumb for positioning and sizing the rotating spars.

Basic design guidelines are outlined in this section, and to do this a measure of the effectiveness of the concept will now be defined; as stated previously, there are two primary objectives for developing the rotating spars concept; firstly, to minimise drag throughout the flight envelope i.e. for a given C_L value at various atmospheric conditions, the spars' orientations are varied to minimise C_D, and secondly to use the rotating spars to achieve roll control without the use of conventional hinged surfaces i.e. differential variation of C_L. For these two aims, two corresponding effectiveness parameters are defined respectively as

$$M_D = \frac{\left.\frac{C_L}{C_D}\right|_{\max}}{\left.\frac{C_L}{C_D}\right|_{\min}} \tag{4.12}$$

and

$$M_L = C_L|_{\max} - C_L|_{\min} \tag{4.13}$$

where the effectiveness parameters are calculated at a fixed flight condition and for a wing with fixed parameters; the only variables that are used to establish the above parameters are the forward and rear spar angles of orientation. The C_D values used above will of course be induced drag coefficients due to the inviscid flow limitation. As an additional indication of the effectiveness of the concept, maximum airspeeds will be monitored.

In terms of suitability to a wing, the major planform parameters that will

have a large impact on the success of the concept will be investigated (wing sweep and aspect ratio). The drivers for these parameters will be the role of the aircraft and not the rotating spars i.e. the aim is to determine the type of aircraft that could benefit from the concept, not to redesign all wing types so that the concept works well with them, as this would degrade the ability of certain aircraft to successfully perform their role.

The results of this will then be used to establish guidelines for designing the spars i.e. a suitable planform will be chosen and the major spar design variables will be investigated (chordwise position of the two spars, and ratio of spar second moments of area).

It is also important to employ analysis constraints at this point to make the investigation more realistic. Admittedly, a major constraint in the full model will be the dynamic instability of flutter, but this is beyond the scope of the current model. The two constraints identified for the linear static model that will prevent the model achieving the theoretical behaviour involve large deflections; firstly, sufficiently large twist angles will cause the wing to stall and also invalidate the small angles assumption used by the model theory, and secondly, large bending deflections will also contribute to flow stall for sweptforward wings, but more significantly cause large static friction (stiction) forces to be present between the rotating spars and their mountings; large bending deformations result in large restoring forces which are transmitted from the spars to the ribs via their mountings perpendicular to the plane of rotation of the spars. For any surface where friction is present, these perpendicular forces will give rise to the requirement for a threshold of force parallel to the surface to be applied in order to overcome the static friction [68]. These are the forces that actuators have to overcome to re-orient the spars. For actuators with given maximum torque values there will exist points in the flight envelope at which they are incapable of overcoming the stiction forces.

To deal with these two problems, two constraints are defined; twisting deflections at the wing tip are limited to being equal to or less than a certain pre-defined value $\theta_{\text{tip}}|_{\text{max}}$, and the slope of the bending deflections of both spars are limited to being equal to or less than a certain pre-defined value $h'_{\text{tip}}\big|_{\text{max}}$. All other solutions are discarded i.e. solutions are limited to the ranges given by

$$\theta_{\text{tip}} \leq \theta_{\text{tip}}|_{\text{max}} \tag{4.14}$$

and

$$h'_{1_{\text{tip}}}, h'_{2_{\text{tip}}} \leq h'_{\text{tip}}\big|_{\text{max}} \tag{4.15}$$

Both of these constraints also deal with the onset of static instability (divergence). It was established in section 4.2 that the maxima and minima defined in Eqs. 4.12 and 4.13 will occur at any of the four spar configurations of [0 0], [90 90], [90 0] and [0 90]. With this in mind the effectiveness study analysis routine can be summarised with the following steps (using the example of aspect ratio $\mathcal{A}$R as the parameter of interest):

1. Choose an initial value of aspect ratio $\mathcal{A}\text{R}_1$ and an initial airspeed U_1.

2. For $\mathcal{A}\text{R}_1$ and U_1, run the static aeroelastic analysis for the spar configurations [0 0], [90 90], [90 0], [0 90].

3. At each of these four configurations check whether any of the θ_{tip} values exceed the constraint $\theta_{\text{tip}}|_{\text{max}}$, and whether any of the $h'_{1_{\text{tip}}}, h'_{2_{\text{tip}}}$ values exceed the constraint $h'_{\text{tip}}\big|_{\text{max}}$.

4. If none of the constraints are violated for the set of spar configurations, increase the airspeed to U_2.

5. Repeat steps 2 - 4 until a constraint is violated.

6. Converge on the maximum possible airspeed that does not violate a constraint, U_{max}, by alternating an increase and decrease in the airspeed, and

by using smaller increments. At $U_{\max}$ calculate the effectiveness parameters M_D and M_L from Eqs. 4.12 and 4.13 respectively. Since these are calculated at the maximum speed $U_{\max}$, these can be written $M_D\left(U_{\max}\right)$ and $M_L\left(U_{\max}\right)$.

7. Increment the aspect ratio to a new arbitrary value, $\text{Æ}\text{R}_2$. Set the new initial airspeed to equal $U_{\max}$ corresponding to $\text{Æ}\text{R}_1$.

8. Repeat steps 2 - 7 for all aspect ratio values of interest..

9. Plot $M_D\left(U_{\max}\right)$, $M_L\left(U_{\max}\right)$, and $U_{\max}$ against Æ R.

The above steps were performed for all parameters (sweep Λ, aspect ratio Æ R, chordwise position of forward spar f, chordwise position of rear spar r, and the ratio of spar second moments of area i.e. $I_{y'y'}/I_{z'z'}$). For f and r the procedure was combined to obtain results for various combinations of f and r, and then $M_D\left(U_{\max}\right)$, $M_L\left(U_{\max}\right)$, and $U_{\max}$ were plotted against f and r i.e. 3D plots. Firstly though, values were chosen for $\theta_{\text{tip}}\big|_{\max}$ and $h'_{\text{tip}}\big|_{\max}$, the constraints; exact values were not too important provided they were consistent as this allowed a valid comparison between different wings to be made. However, attempts were made to set them to realistic values and so 15° was chosen for both as this preserves the assumptions of linearity within the model, allows fairly large torsional deflections without stall occurring, and allows for realistic bending deflections (the bending constraint of course depends on the output torque of the actuator). The results are discussed in sections 4.3.2 and 4.3.3.

4.3.2 Suitability for planform

As mentioned in section 4.3.1, to determine what category of wings the rotating spars concept is most suitable for, the wing aspect ratio and sweep was varied and a measure of the effectiveness of the concept calculated and plotted. All other wing parameters were fixed.

To establish the effectiveness of the concept, the iterative procedure described at the end of section 4.3.1 was used with the sweep Λ and then the aspect ratio $\mathcal{AR}$ as the parameter p.

Effect of wing sweep

Figure 4.25 shows the influence of wing sweep on the effectiveness of the rotating spars concept. With reference to this figure, to clarify the meaning of the three output parameters, for $\Lambda = 30°$ the rotating spars concept allows the lift coefficient to be changed by up to around 0.37 ($M_L\,(U_{\max})$), the (inviscid) lift-to-drag ratio, C_L/C_{D_i}, can be changed by up to approximately 360% ($M_D\,(U_{\max}) \approx 3.6$), and these changes occur at at speed of around 27 $\text{m}\cdot\text{s}^{-1}$ ($U_{\max}$). At lower speeds for the same wing, the variation in lift and lift-to-drag ratio will be lower (since at a lower dynamic pressure). For the same sweep angle, it is possible to achieve speeds beyond 27 $\text{m}\cdot\text{s}^{-1}$ but an increasing number of spar configurations will trigger a constraint. To deal with this problem in order to safely increase the flight envelope would require an intelligent feedback loop. Essentially 27 $\text{m}\cdot\text{s}^{-1}$ is the maximum speed for this sweep angle that all the possible spar configurations are safely accessible.

From the plots it is clear to see that the rotating spars concept is most suitable to wings that are sweptback; as the sweep angle increases the maximum speed that the wing can use the concept in all configurations increases. This is not a surprising result since it is well known that sweeping a wing rearwards provides static stability, whereas sweeping it forwards has the opposite effect [15]. As a result of this it can be expected that the effectiveness parameters M_L and M_D will be higher for larger sweep angles; this is in part true, but clearly at around $\Lambda = 22°$ a maximum is reached for both $M_L\,(U_{\max})$ and $M_D\,(U_{\max})$ and beyond this the effectiveness decreases again. It can also be seen that a minimum is reached at around $\Lambda = -6°$ and for lower values of sweep the effectiveness increases again. These two anomalies are most likely due to the influence of the

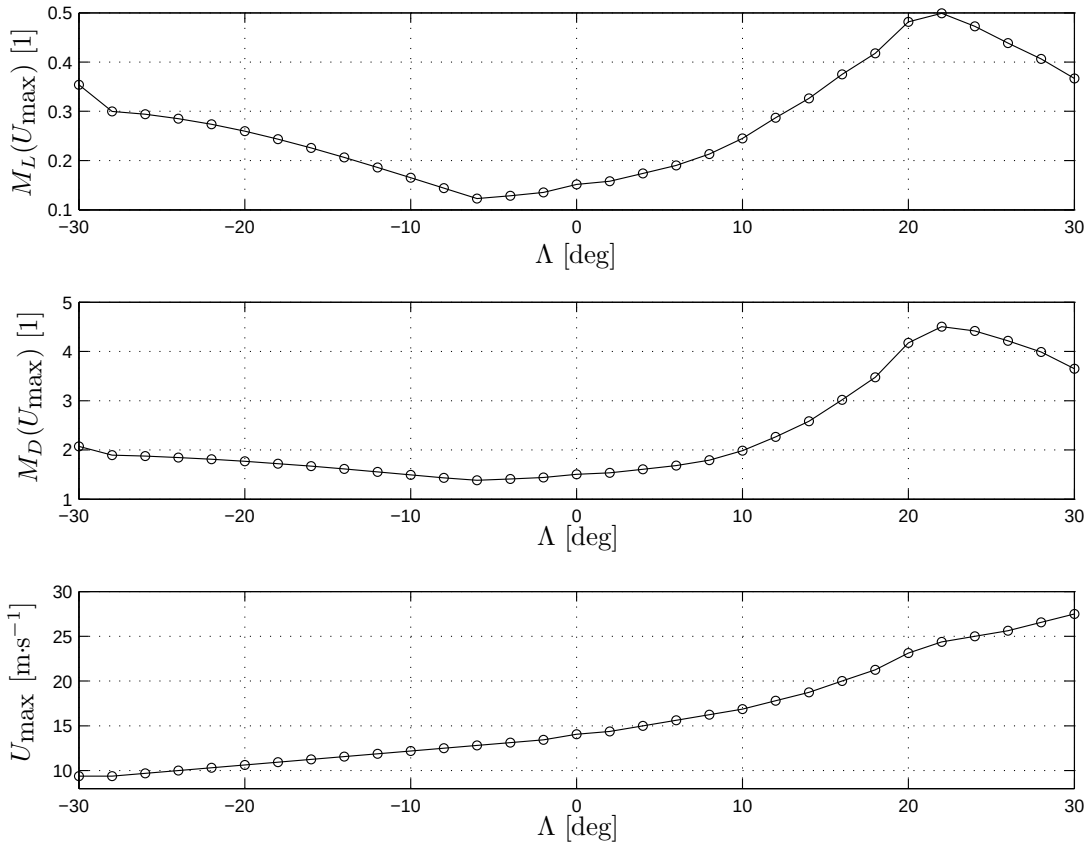

Figure 4.25: Variation of morphing effectiveness parameters at maximum airspeed with wing sweep.

coupling effect that bending deflections have with the aerodynamics for swept wings. Note that in general the optimum sweep angle will not be 22° and this will be dependent on many other model variables.

Although dynamic effects are not included in the current model, it is well known that rearward sweep provides dynamic aeroelastic stability in addition to the static stability already mentioned, and therefore it can be expected that if flutter were included as an additional constraint, the results would still indicate that the concept is most suitable to sweptback planforms [15].

Effect of wing aspect ratio

Figure 4.26 shows the influence of the wing aspect ratio $\mathcal{A}\mathrm{R}$ on the effectiveness of the rotating spars concept. To clarify

$$\mathcal{A}\mathrm{R} = \frac{2b}{c} = \frac{4b^2}{S} \tag{4.16}$$

where b is the wing semi-span, c is the chord, and S is the full-span wing area. Although the previous section established that the rotating spars concept is most suitable for sweptback wings, the results for the unswept and sweptforward analyses are also shown ($\Lambda = 0°, 20°, -20°$).

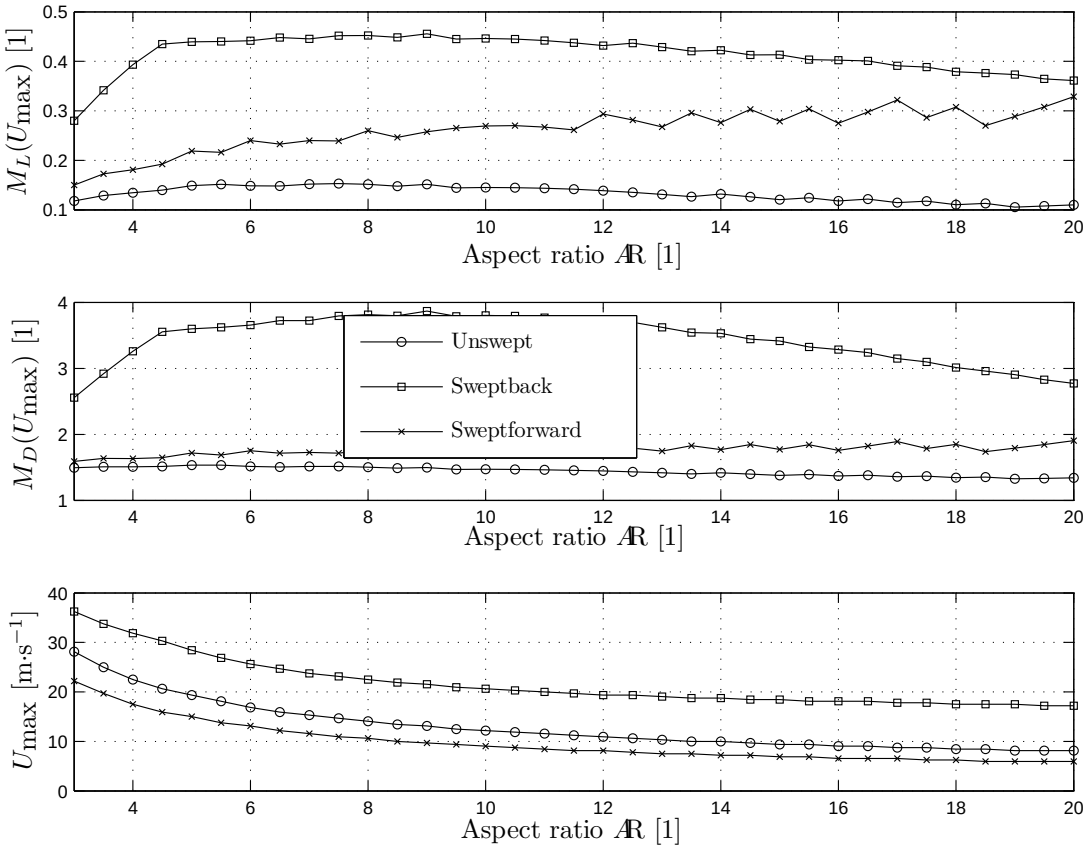

Figure 4.26: Variation of morphing effectiveness parameters at maximum airspeed with wing aspect ratio.

Figure 4.26 reinforces the findings of the sweep investigation that the concept is by far more suitable to sweptback wings; for sweptback wings, as the aspect

ratio increases, $U_{\max}$ decreases, effectively decreasing the size of the flight envelope. It can also be seen that at very low aspect ratios the effectiveness of the concept is poor. This increases quickly as the aspect ratio is increased towards around $AR = 9$, and then decreases again very gradually as the aspect ratio is further increased, but with no significant loss in effectiveness for the range of aspect ratios considered. As before, this optimum value for the aspect ratio is in general specific to the wing setup and varies as all the other parameters vary.

4.3.3 Rotating spar placement and sizing

Using the results of section 4.3.2, a wing planform was used that lends itself well to the rotating spars concept. This model was used to carry out an investigation into how the local stiffness ratio of the spars, as well as the chordwise placement of them affects the effectiveness of the concept.

Effect of ratio of spar second moments of area

At a fundamental level, the rotating spars alter the structure and therefore aeroelastic behaviour by varying I_{s_1} and I_{s_2}, the second moment of area of the two spars about a chordwise axis. For spar j this relies on a variable orientation ϕ_j as well as non-equal values of $I_{y'_j y'_j}$ and $I_{z'_j z'_j}$, the second moments of area of spar j about its principal axes (see Eq. 3.28 in section 3.2.1). It is this second parameter, the ratio of spar second moments of area, that will be discussed in this section.

Using a model based on results from section 4.3.2 i.e. sweep of 20° and aspect ratio of 8, the iteration procedure described in section 4.3.1 was used to investigate how the ratio of spar second moments of area influences the effectiveness of the concept. The ratio of spar second moments of area for both spars was varied simultaneously and for spar j is given by $I_{y'_j y'_j}/I_{z'_j z'_j}$, where $I_{y'_j y'_j} \geq I_{z'_j z'_j}$. $I_{y'_j y'_j}$ is a fixed value (sized to fit inside a typical wing thickness), and variation of the ratio of spar second moments of area is achieved by varying $I_{z'_j z'_j}$. The results for

the unswept and sweptforward wing are also shown in figure 4.27 alongside the sweptback wing for comparison.

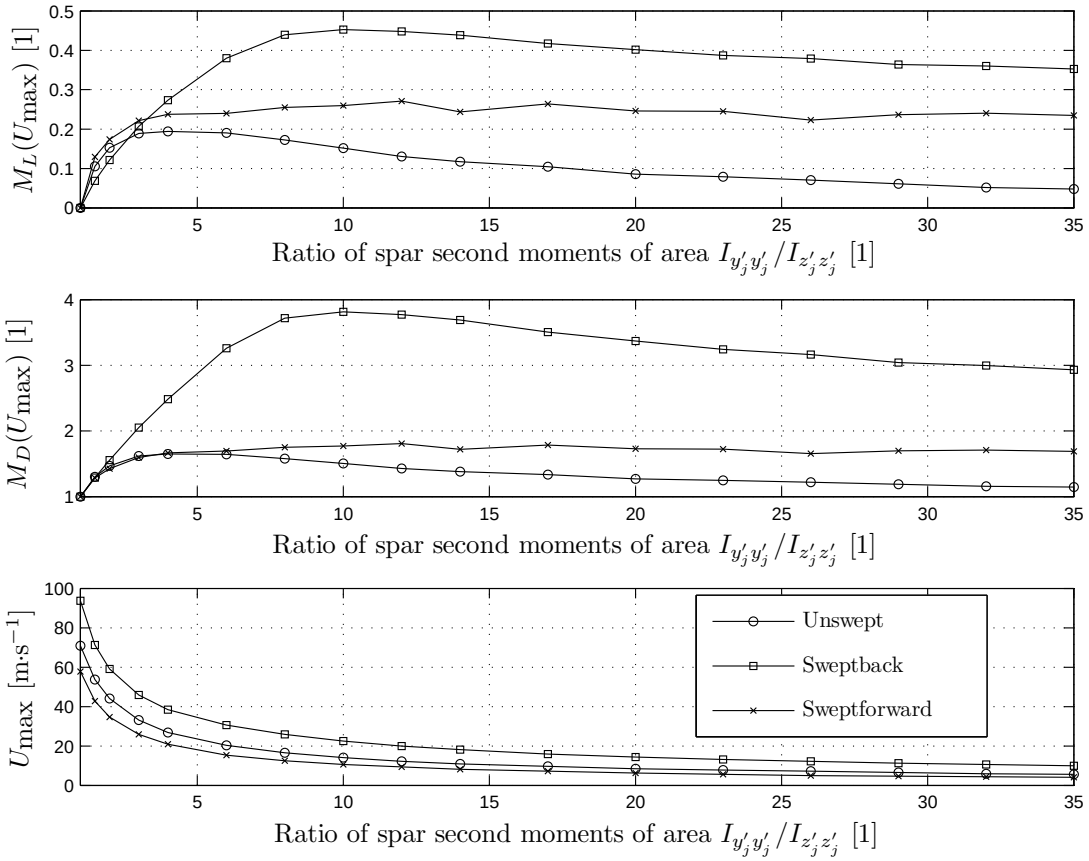

Figure 4.27: Variation of morphing effectiveness parameters at maximum speed with rotating spars' ratio of second moments of area.

As before, it is clear that the rotating spars concept is far more suitable for use on sweptback wings than unswept and sweptforward wings. Intuitively, it could be expected that as the ratio of spar second moments of area increases, the effectiveness of the concept will increase, since this implies a greater variation in the elastic axis position and wing stiffnesses; however, this is not the case with the effectiveness peaking for a ratio of approximately 10, before gradually decreasing again. This is due to the inclusion of the constraints outlined by Eqs. 4.14 and 4.15; as the ratio of spar second moments of area increases, $I_{z'_j z'_j}$ decreases, while $I_{y'_j y'_j}$ remains fixed. Consequently, the spar second moment of area about a

chordwise axis I_{s_j} will decrease resulting in a lower wing bending and torsional stiffness. This will of course cause the wing to bend and twist to larger values, therefore eventually violating one or both of the mentioned constraints.

In other words, at a given speed, a high ratio of spar second moments of area will offer higher effectiveness parameters M_L and M_D than a low stiffness ratio, but will also result in higher deflections and therefore be more likely to violate the constraints, and so a compromise must be found. For this wing, figure 4.27 identifies this as the wing with a ratio of spar second moments of area of 10.

The plots also show that if ratios below this optimum value are used, the effectiveness sharply decreases. The conflicting argument, however, is that as the ratio increases from 1, the highest speed that all possible spar configurations can be realistically used (i.e. $U_{\max}$) decreases rapidly, although this is augmented by using rearward sweep.

Effect of spars' chordwise placement

It has already been shown in section 4.2 that a large variation in the elastic axis position of the wing is integral to the success of the rotating spars adaptive structures concept. The degree to which this can be achieved largely depends on the ratio of spar second moments of area, as discussed in the previous section, as well as how far apart in a chordwise direction that the two spars are placed. In this section the latter is investigated for a model based on results from section 4.3.2 i.e. sweep of 20° and aspect ratio of 8.

The iteration procedure described in section 4.3.1 was used with a slight adjustment to investigate how the chordwise placement of the spars affects the effectiveness of the concept. The modified procedure included an extra loop in order to obtain values $U_{\max}$ and the corresponding maximum effectiveness parameters i.e. $M_L\left(U_{\max}\right)$ and $M_D\left(U_{\max}\right)$ for a range of combinations of f and r, the dimensionless chordwise position of the forward and rear spars respectively. $M_L\left(U_{\max}\right)$, $M_D\left(U_{\max}\right)$ and $U_{\max}$ were then plotted against f and r (see figures

4.28 - 4.30). For a wing of chord c, fc is the chordwise distance that the forward

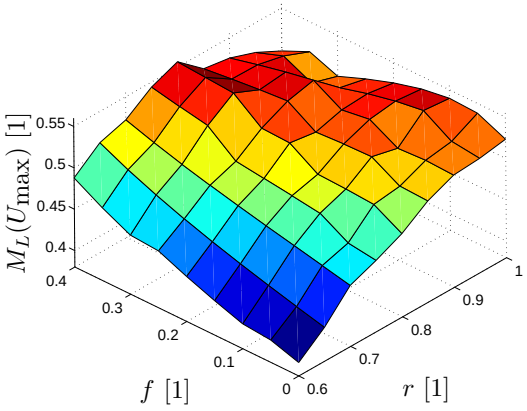

Figure 4.28: Variation of morphing effectiveness parameter $M_L\,(U_{\max})$ with chordwise placement of rotating spars.

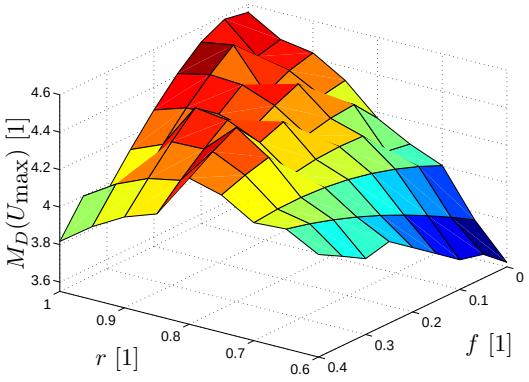

Figure 4.29: Variation of morphing effectiveness parameter $M_D\,(U_{\max})$ with chordwise placement of rotating spars.

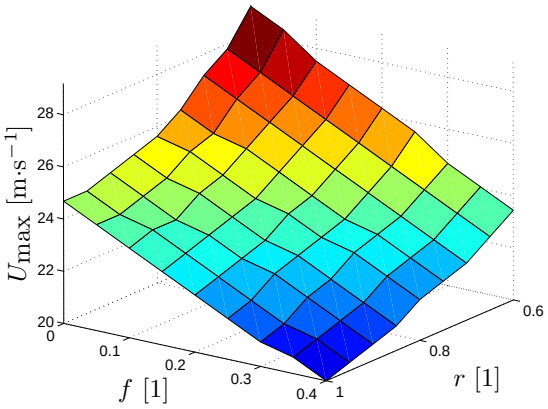

Figure 4.30: Variation of $U_{\max}$ with chordwise placement of rotating spars.

spar lies behind the leading-edge, and similarly rc is the chordwise distance that the rear spar lies behind the leading-edge.

Unsurprisingly, the wing with the spars located furthest apart i.e. $f = 0$, $r = 1$, in general, has the potential to have the most effective rotating spars, and as the spars are positioned closer to one another the effectiveness drops. There are a few exceptions to this trend however; when the spars are closest together i.e. $f = 0.4$, $r = 0.6$ the effectiveness parameters corresponding to maximum speed $M_L\,(U_{\max})$ and $M_D\,(U_{\max})$ are larger than when the spars are

further apart for $f = 0$ and $r = 0.6$. This is because the effectiveness of the concept is more precisely related to the distance that the elastic axis can vary by *relative to* the aerodynamic centre (at the quarter chord), rather than simply just the total distance that the elastic axis can vary by. It can be assumed therefore that for the arrangement $f = 0$ and $r = 0.6$, the elastic axis does vary by a larger distance than for the $f = 0.4$, $r = 0.6$ arrangement, but it is passing through the aerodynamic centre with a smaller change in aeroelastic moment arm. Additionally, the torsional stiffness of the wing will be less when the spars are closer together and therefore aeroelastic deflections will be greater.

Despite this theoretical result that suggests the forward spar should be placed at the leading-edge of the wing, and the rear spar on the trailing-edge, a realistic wing will have problems achieving this for a number of reasons, the main one being that a spar on the trailing-edge will have to have very small dimensions to fit inside the aerofoil section, and therefore its stiffness values and hence contribution to the adaptive structures concept will be minimal. A more realistic design will have the forward spar around the 0.1 chord position, and the rear spar perhaps at the 0.7 to 0.8 chord position.

Inspection of the $U_{\max}$ plot (figure 4.30) reveals that it loosely follows the inverse of the trends observed in figures 4.28 and 4.29, the effectiveness plots, and that as f and r are altered to improve the effectiveness, the maximum speed at which the wing can achieve all possible spar orientation combinations will decrease.

Although trends have been established in sections 4.2 and 4.3, it has also been shown that several of the parameter values that produce optimum behaviour are model-dependent. With a model with multiple variables such as this one, the solution is to perform an optimisation routine to arrive at the most suitable design. This will be the focus of the next section.

4.4 Design of a rotating spars wing using a genetic algorithm

4.4.1 Introduction

As demonstrated in the previous section, the performance of the rotating spars concept is dependent on multiple variables. Several of these, such as the chordwise position of the spars, will be altered to achieve optimum performance, while others will be pre-determined for a given wing depending on its role (e.g. sweep angle, aspect ratio).

This section deals with finding optimum values for these variables, and assumes that the wing is completely designed around the rotating spars; making this assumption allowed those variables such as sweep and aspect ratio that are usually pre-determined to be altered to help achieve an effective adaptive structures design. Although this is perhaps an unrealistic approach to designing a wing, for the purpose of a technology demonstrator it is ideal.

The objective was to vary the wing design in order to maximise the effectiveness of the concept, measured using the parameters M_D and M_L (given respectively by Eqs. 4.12 and 4.13). The analysis was subject to constraints. Due to the large number of variables, and the possibility of several valid solutions, an optimisation routine was the obvious approach to solving this problem. To begin with, an introduction to optimisation will be presented.

4.4.2 Optimisation overview

Optimisation is the process of obtaining the most suitable solution to a problem. For some problems, there exists only a single solution, but it may be difficult or even impossible to solve this explicitly. For other problems, there are multiple solutions. Regardless, optimisation is the process of attempting to find the 'best' solution. By 'best', it is implied that the solution is, in general, not exact, but is

sufficiently close to the exact solution [104].

For all approaches to optimisation, the problem is rearranged such that a maximum or minimum corresponds to the desired solution [104] e.g. consider the equation

$$z = f(x, y) \tag{4.17}$$

and the problem is to find appropriate values of x and y such that $z = z_T$. For optimisation approaches the problem can then be set-up as

$$C(x, y) = |z_T - f(x, y)| \tag{4.18}$$

where C is known as the objective or cost function [104]. The aim then is to minimise C.

Exhaustive search [56]

The exhaustive search approach to optimisation is the simplest but least efficient method. In this approach, no intelligent observations are made to speed up the search. Instead, a sufficiently high resolution of samples are taken of the cost function (e.g. for the example given by Eq. 4.18, many different x and y combinations) to construct a 'map' of the cost function, and then by comparing the cost functions for each sample, a minimum/maximum is found. The idea is that enough samples are taken to have confidence that this is the global minimum/maximum, and not a local minimum/maximum. This requirement for the cost function to be evaluated a large number of times makes the exhaustive search trial-and-error process extremely computationally expensive and therefore slow.

A refinement is to start with a low resolution to produce a coarse 'map' of the cost function, and then narrow in on areas of interest. This will speed up the routine to some extent, but the likelihood of missing the global minimum/maximum inevitably increases.

Gradient methods [104]

The so-called gradient methods work by calculating gradients of the cost function and using this information to direct the search towards minima/maxima. This makes gradient methods superior to exhaustive search approaches. There are a variety of different gradient based approaches that work differently from each other:

- Method of steepest descent/ascent. This is a simple and robust routine, but is slow to converge [26]. This approach is used in section 4.5.4.
- Newton's method. Speeds up convergence, but at the expense of robustness. It is unreliable unless the starting point is in the vicinity of the global minimum/maximum. Furthermore, Newton's method requires that second order derivatives also be calculated [53, 104].
- Conjugate gradient methods e.g. Fletcher-Reeves algorithm [111].
- Variable metric (quasi-Newton) methods e.g. Davidon-Fletcher-Powell (DFP) algorithm, Broyden-Fletcher-Goldfarb-Shanno (BFGS) algorithm [113].

The last two methods are similar to Newton's method, but avoid calculating second-order derivatives explicitly and instead use approximations. This makes them more efficient and robust, but they are difficult to implement [28].

One major drawback to gradient methods is that they converge on the minimum/maximum closest to the starting point, which may not be the global extreme. Additionally, gradient methods cannot deal with cost functions that are not differentiable at all points and have discontinuities, since gradients are undefined for these features, and they also struggle to succeed for a large number of input variables [56].

Metaheuristics [51, ?]

The gradient methods improve on the exhaustive search technique by using an intelligent search pattern; they look for clues that point them in the most likely direction of a minimum/maximum value. However, these approaches do not improve the chances of finding the global minimum/maximum instead of a local one.

Methods of optimisation known as metaheuristics have surfaced in recent years that offer fast and robust methods of finding the solution in a manner that increases the likelihood of that solution being the global minimum/maximum. These methods create new points to search by applying statistical operators to previous points. Unlike gradient methods, derivatives of the cost function are not necessary and so metaheuristics can deal with discrete variables and noncontinuous cost functions. However, as with other methods there is no guarantee that the optimal solution will be found. Methods include:

- Simulated annealing (SA) [73].
- Particle swarm optimisation (PSO) [38, 71].
- Ant colony optimisation (ACO) [35, 36].
- Evolutionary algorithms (EA) including genetic algorithms (GA) [34, 56].
- Neural network metamodel based optimisation [51, 54, 113].
- Kriging metamodel based optimisation [25, 134].

A genetic algorithm will be used as the tool to search the design variables in the rotating spars wing for an optimum solution, since it copes well with a large set of variables, has a reputation for locating 'good' solutions in relatively few iterations (even for difficult objective functions), and is a well developed and understood method [28, 56, 98].

4.4.3 Genetic algorithms

A genetic algorithm (GA) is an optimisation and search technique that is based on the Darwinian theory of natural selection, a primary element in evolution [69].

Natural selection is the process that makes certain traits of an organism (e.g. human, animal, insect, plant etc.) more common in the population over multiple generations. These traits that are passed down through generations are those that are well suited to the organisms' environment, and therefore reflect the survivability of that organism, hence the phrase "survival of the fittest" [123].

The basic steps in the GA routine are [28, 56, 98]:

1. Random generation of individuals to form an initial *population*.

2. Evaluation of the fitness/survivability of each individual in the population.

3. *Selection*: Randomly select pairs of individuals, biased towards fitter individuals. An individual can be present in more than one pair. This procedure is often referred to as *roulette wheel selection*, with the size of the slots in the wheel proportional to the fitness of the individuals i.e. fittest individuals are most likely to be selected, but there is no guarantee that this will occur or that the least fit individuals will not be selected. This is in contrast to the rarely used *truncation selection* method where all individuals fitter than a certain threshold are selected, and all others are not [123].

4. Reproduction: In a high probability procedure known as *crossover*, the pairs breed. If no crossover occurs for a given pair then exact copies of the parents are made. The *offspring* are then subject to the low probability procedure of *mutation*. The original generation become *parents*.

5. Formation of the second generation: The bulk of the offspring then replace their parents in the population. However, a small portion of the most

fit parents (*elite*) remain in order to preserve individuals that have the potential to be the fittest over successive generations.

6. Steps 2 - 5 are repeated over multiple generations and the overall fitness of a generation will increase over successive generations until it has reached a maximum (*convergence*).

7. *New blood*: This optional procedure can be thought of as the introduction of an individual from an environment completely different to the one that the successive individuals exist in. If this procedure is used then every so often (e.g. every tenth generation), the offspring of the least fit pairs of parents from the previous generation are replaced by new randomly-produced individuals. The idea is to introduce an unbiased solution into the population that has not inherited any of the previous generations' traits; this tends to enhance the genetic diversity of the population, and can result in the exploration of search space not previously covered. Sometimes this can nudge the solution away from convergence occurring in a local minimum/maximum and therefore aids the search for the global solution [12]. The mechanisms of new blood and mutation are used to prevent the population from stagnating [67].

Implementation

Applying the process to input variables rather than organisms is done using abstract representations of the potential solutions; traditionally, but not exclusively, a set of binary strings are used [123]. The reason for this approach is to create a representation of the potential solution that is more alike to genetic models found in nature. At this point some terminology will be defined:

- *Gene*: a binary string that represents a potential solution.

- *Cell*: a single element in the binary string, which therefore will have the value 0 or 1.

- *Pool*: a collection of binary strings that together are equivalent to a single generation of organisms in nature. All genes (binary strings) in the generation and in fact in all generations must contain the same number of cells for the algorithm to function.

The implementation will be explained using a simplified example: consider the problem of designing a two-spar wing with the objective of minimising the maximum bending deflection $h_{\max}$ of the wing at a specific flight condition, where $h_{\max} = g(\Lambda, f, r)$ i.e. the design variables are the wing sweep Λ, and chordwise position of the two spars f and r, and g is a function that relates the variables to the maximum bending deflection. The first step is to decide the range of possible values and resolution to use for each variable, shown in table 4.1.

Table 4.1: Variable range and increments.

Range	N_i	Increment
$-35^\circ \leq \Lambda \leq 35^\circ$	2^4	4.667°
$0.10 \leq f \leq 0.40$	2^2	0.1
$0.50 \leq r \leq 0.85$	2^2	0.11667

Since the optimisation routine trials discrete values, careful consideration of the search space resolution should be made. This is indicated in table 4.1 via the number of increments, N_i, which must be a power of 2. If the resolution is too large, the routine can miss minima, whereas if it is too small convergence may take a long time.

As the routine represents the search space with binary strings, the variable ranges must be modelled by positive integer values e.g. r currently runs between 0.50 and 0.85 with 2^2 increments of 0.11667; this must be adjusted so that it

begins at 0 with increments of 1. A simple transformation can easily be derived to do this, given by

$$\hat{x} = (x - x_{\min}) \times \frac{N_i - 1}{x_{\max} - x_{\min}} \tag{4.19}$$

where x is an any one of the variables, and $\hat{x}$ is the transformed variable. The transformed variable ranges are given in table 4.2.

Table 4.2: Transformed variable range and increments.

Range	N_i	Increment
$0 \leq \hat{\Lambda} \leq 15$	2^4	1
$0 \leq \hat{f} \leq 3$	2^2	1
$0 \leq \hat{r} \leq 3$	2^2	1

With N_i shown as a power of 2, the exponent indicates the length of the binary string (or gene) that will represent that particular variable i.e. $\hat{\Lambda}$ will be represented by a gene with 4 cells, and $\hat{f}$ and $\hat{r}$ by genes with 2 cells each.

For problems with more than one variable (as in this example), the genes are combined (in any order) e.g. $\underbrace{1011}_{\hat{\Lambda}}\underbrace{11}_{\hat{f}}\underbrace{10}_{\hat{r}}$. This eight cell gene is then treated as a single binary string for the reproduction processes that follow. Extraction of $\hat{\Lambda}$, $\hat{f}$ and $\hat{r}$ for evaluation of cost functions is done simply by dividing the gene up into its constituent components i.e. $\hat{r}$ is represented by cells one and two (where the first cell is the right-most cell), $\hat{f}$ is represented by cells three and four, and $\hat{\Lambda}$ is represented by cells five through to eight.

With this information an initial pool (generation) can be created; the population depends on the problem, but for this example a population of six will be used. Six genes are then generated randomly, each representing different combinations of $\hat{\Lambda}$, $\hat{f}$, and $\hat{r}$ (see table 4.3). Also shown in the table are the variable values that they represent. Eq. 4.19 was used to convert back from the transformed variables to the actual variables.

Table 4.3: Representation of possible solutions with binary strings and conversion back to transformed and actual variable decimal values.

ID	Gene	$\hat{\Lambda}$ [1]	$\hat{f}$ [1]	$\hat{r}$ [1]	Λ [deg]	f [1]	r [1]
A	10110010	11	0	2	16.333	0.1	0.7333
B	00110111	3	1	3	-21	0.2	0.85
C	00000011	0	0	3	-35	0.1	0.85
D	01111001	7	2	1	-2.333	0.3	0.6167
E	01100000	6	0	0	-7	0.1	0.5
F	11100110	14	1	2	30.333	0.2	0.7333

Next the fitness of each gene in the pool is evaluated using the cost (fitness) function $h_{\max} = g(\Lambda, f, r)$. This is presented in table 4.4.

Table 4.4: Fitness of each gene.

ID	Gene	Fitness $h_{\max}$ [mm]
A	10110010	67
B	00110111	34
C	00000011	131
D	01111001	12
E	01100000	46
F	11100110	58

Selection [123]

The genes are then paired in preparation for 'mating'. A gene can be present in multiple pairs, and the likelihood of a gene being present in a pair depends on its fitness; genes that are fittest (in this case lowest values of $h_{\max}$) are most likely to be present in a pair. In the example, gene D is most likely to be present in one or both of the pairs, and gene C is least likely to appear. Assume that the biased random pairing of genes pairs genes D and B together, genes D and

A together, and genes E and F together Mating then occurs between the genes in each pair through the mechanisms of crossover, mutation and translation.

Crossover [123]

The pairs that have been created then mate to produce two offspring each. The main mechanism at work here is a procedure known as crossover. For any given pair in a generation, there is a high user-defined probability p_c (usually around 0.9 [60], although sometimes $1/L$ is used, where L is the length of a gene [123]) that crossover will occur. Various crossover techniques are available, but the traditional one point crossover [123] will be demonstrated here; a random coinciding point in the two genes is chosen and the cell values beyond this point swap over between genes. For example, assume crossover does occur for the pair of genes D and B, with a crossover point between the fifth and sixth cells, and for the pair of genes D and A, with a crossover point between the second and the third cells. Assume the pair of genes E and F are not selected for crossover. Table 4.5 summarises the crossover procedure; notice that the offspring of genes E and F are copies of their parents.

Table 4.5: Crossover of genes.

ID	Original gene	Post-crossover
D	011 11001	011 10111
B	001 10111	001 11001
D	011110 01	011110 10
A	101100 10	101100 01
E	01100000	01100000
F	11100110	11100110

Mutation [123]

Next, the offspring from the crossover procedure are exposed to the possibility of mutation. There are a variety of mutation techniques that can be employed; here the inversion and translation techniques will be demonstrated. There is a low user-defined probability p_m (e.g. 0.01 [60]) of either of these mutation procedures occurring to a given offspring gene.

If inversion [123] does occur within a gene, a random cell within the gene changes value (i.e. 0 become 1, or 1 becomes 0). For demonstration purposes, assume that inversion occurs in the second and third of the post-crossover genes, and that this occurs at the fourth and eighth cells respectively (see table 4.6).

Table 4.6: Inversion of genes.

Post-crossover	Post-inversion
01110111	01110111
0011(1)001	0011(0)001
(0)1111010	(1)1111010
10110001	10110001
01100000	01100000
11100110	11100110

If translation [28] occurs, a random point in the gene is chosen and all cells after this point are moved before this point and vice versa. For demonstration purposes, assume that translation occurs in the first and second of the post-inversion genes, and that this occurs between the third and the fourth cells, and the fourth and the fifth cells respectively (see table 4.7).

Table 4.7: Translation of genes.

Post-inversion	Post-translation
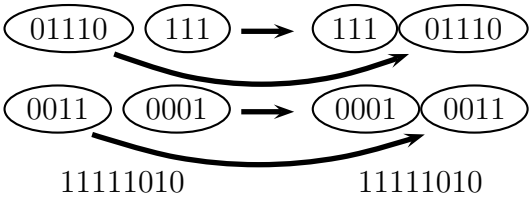	
11111010	11111010
10110001	10110001
01100000	01100000
11100110	11100110

New blood [12]

In an optional procedure known as introducing new blood, infrequently a completely random set of genes is introduced into the gene pool. The idea of this is to introduce genes into the gene pool that do not have any of the previous generations' traits. This procedure can sometimes move a solution away from incorrect convergence at a local minimum/maximum and therefore aids convergence at a global minimum/maximum. Usually many generations evolve between the introduction of this new blood (e.g. every 15 loops), and only a small portion of the genepool will be replaced by these randomly generated genes. Table 4.8 shows the introduction of new blood for the current example, with only one of the post-translation genes being replaced by new blood.

Table 4.8: Introduction of new blood.

Post-translation	Post- new blood
11101110 →	00100010
00010011	00010011
11111010	11111010
10110001	10110001
01100000	01100000
11100110	11100110

Preserving the elite genes [123]

To prevent losing possible 'best' solutions (i.e. those with the lowest/highest fitness) between successive generations, a small portion (e.g. 20%) of the most fit genes in each generation are carried over to the next generation.

For the current example, it is assumed that only a single gene is carried over. From table 4.4 the gene with the best fitness for the current objective (minimise $h_{\max}$) is gene D, represented by the binary string 01111001; this replaces one of the offspring genes (see table 4.9).

Table 4.9: Carry-over of elite gene from previous generation.

Post-new-blood	Post-carry-over
00100010	00100010
00010011	00010011
11111010	11111010
10110001	10110001
01100000	01100000
11100110 →	01111001

The column on the right in table 4.9 i.e. post-carry-over represents the final gene pool of the offspring. This mating process is then repeated for the offspring until satisfactory convergence of the cost function occurs.

4.4.4 Optimisation of the rotating spars wing to maximise effectiveness parameters

The genetic algorithm optimisation routine described in section 4.4.3 was used to find parameter values for the rotating spars adaptive structures wing concept in order to maximise the effectiveness parameters defined in section 4.3.1 (these parameters give an indication of the effectiveness of the rotating spars concept). This was performed using the MATLAB® static aeroelastic model (developed in chapter 3) in conjunction with a genetic algorithm routine, also written in MATLAB®. The objective was to establish an effective model that was then used for further analytical work in section 4.5.

Cost function

The primary aim of the design optimisation was to arrive at a wing design that would effectively minimise drag for a given lift value throughout the flight envelope i.e. maximise M_D (as explained in section 4.3.1, M_D gives an indication of the range of lift-to-drag ratios that are possible at a given flight condition by varying only the spars' orientations). As an additional benefit, a rotating spars wing that achieves a large value of M_D will also be able to vary the lift substantially and so roll control is a possibility; this variation in lift is measured by M_L (M_L gives an indication of the range of lift that is achievable at a given flight condition by varying only the spars' orientation).

Since maximising M_D was the primary objective, and an increase in M_D will in general increase M_L, the cost function for the optimisation task was to maximise M_D. Out of interest a separate optimisation was performed where the cost function was to maximise M_L; as this is not the main aim of the concept

the results of this were not taken any further.

Design variables

There were a large number of wing/structural parameters that could be varied in order to alter the effectiveness of the concept; it is for this reason that an optimisation approach was used to find a 'good' design. These parameters are shown in table 4.10; the range in which they were allowed to vary, as well as the number of increments N_i considered is also shown.

Table 4.10: Parameter ranges and number of increments.

Parameter	Min. value	Max. value	N_i
Wing aspect ratio $\mathcal{AR}$ [1]	3	20	2^4
Wing sweep Λ [deg]	-45	45	2^6
Fwd spar position f [1]	0.05	0.40	2^5
Rear spar position r [1]	0.60	0.95	2^5
Ratio of spar second moments of area for each of the two spars $\frac{I_{y'_j y'_j}}{I_{z'_j z'_j}}$ [1]	1	35	2^5
Rib torsional constant for each of the 10 ribs J_{r_k} [$\mathrm{m}^4 \times 10^{-10}$]	1.0	2.0	2^3

Design constants

A number of basic model parameters had to be assigned values before the optimisation routine could be performed. These values are presented in table 4.11.

Table 4.11: Basic fixed parameter values.

Parameter	Value
Wing area (full-span) S [m^2]	0.5
Aerofoil thickness t [%]	12
Number of ribs N_{rib} [1]	10
Young's modulus E [GPa]	69
Poisson's ratio ν [1]	0.33
Airspeed U [$m{\cdot}s^{-1}$]	30
Air density ρ [$kg{\cdot}m^{-3}$]	1.225
Rigid angle of incidence α_r [deg]	5

The thickness of the wing t does not affect the aerodynamics since thin-aerofoil theory assumptions are being used for the aerodynamic model. Instead it is used to size the height of the spars d_{s} (a rectangular cross-section is used for the spars). A NACA four-series aerofoil is assumed so that, using the thickness given in table 4.11 along with the governing equation for the NACA four-series aerofoil, the wing thickness at any chordwise location can be assessed. So the height of the forward spar (located at the chordwise location f) is defined as the thickness of the aerofoil at f, and similarly for the rear spar. The thickness of the spar b_{s_j} for spar j is then calculated using the ratio of spar second moments of area $I_{y'_j y'_j}/I_{z'_j z'_j}$.

Constraints

To make the design process more realistic, several constraints were enforced. As described in section 4.3.1, large wing twist angles cause the wing to stall in reality and invalidate the small angles assumption used during the development of the analytical model in chapter 3, and large bending deflections also contribute towards stall for sweptforward wings. The aerodynamic model is linear and does not account for stall.

Additionally, in reality, large bending deflections cause large stiction forces to be present between the rotating spars and their mountings, and for an actuator with a given maximum torque value there will exist a bending deflection at which it is incapable of overcoming the stiction force.

Furthermore, large twist and bending deflections indicate the onset of a divergence instability. The analytical model was restricted from operating in these conditions by specifying a maximum wing tip twist angle $\theta_{\text{tip}}|_{\text{max}}$ and a maximum slope for the bending deflections of each spar at the wing tip $h'_{\text{tip}}\big|_{\text{max}}$.

The final constraint that was introduced was to specify a minimum thickness $b_{\text{s}}|_{\text{min}}$ for the spars; this prevented convergence of a solution where the spar was so thin that it could not be easily manufactured. The actual values used for these three constraints is not too significant assuming they are consistent for the complete analysis. Care was taken to use realistic values however, and table 4.12 displays these.

Table 4.12: Optimisation constraints for the design of the rotating spars wing.

Constraint	Value
$\theta_{\text{tip}}\|_{\text{max}}$ [deg]	15
$h'_{\text{tip}}\big\|_{\text{max}}$ [deg]	15
$b_{\text{s}}\|_{\text{min}}$ [mm]	2

The constraints were enforced in the GA optimisation routine with the use of a penalty function P; this is a discrete function that significantly alters the cost function C to ensure that the solution cannot converge whenever a constraint is violated e.g. for the routine where the objective was to maximise M_D, the unconstrained routine was to maximise $C = M_D$. The constrained optimisation was then set up such that the objective was to maximise $C = M_D/P$, with P either several orders of magnitude greater than the expected order of magnitude

of M_D, or equal to 1:

$$P = 1, \qquad \text{constraints not violated} \tag{4.20}$$

$$P = 10,000, \qquad \text{constraint(s) violated} \tag{4.21}$$

Results

For both design objectives (i.e. maximise M_D and maximise M_L) the optimisation was carried out three times (runs D_1 to D_3, and L_1 to L_3 respectively) in order to assess whether convergence occurred each time at a global maximum, and if it did not, to decide whether the local maximum solution was acceptable.

For the genetic algorithm, an initial gene pool of 25 genes was created, and the optimisation was allowed to run through 50 generations/iterations. The results for all three cases are shown in table 4.13. The units of J_{r_k}, not displayed in the table for brevity, are $\mathrm{m}^4 \times 10^{-10}$.

Table 4.13: GA optimisation results.

Variable	Cost function					
	Maximise M_D			Maximise M_L		
	Run D_1	Run D_2	Run D_3	Run L_1	Run L_2	Run L_3
$M_{D_{\text{conv}}}$ [1]	4.9982	3.5129	4.5747	2.9929	2.7074	2.7694
$M_{L_{\text{conv}}}$ [1]	0.60162	0.40208	0.52504	0.38161	0.34440	0.39387
$\mathcal{A}$R [1]	7.5	14.3	10.9	15.5	16.6	16.6
Λ [deg]	16.4	29.3	15.0	23.6	22.1	29.3
f [1]	0.073	0.400	0.163	0.400	0.366	0.400
r [1]	0.634	0.679	0.657	0.736	0.645	0.690
$\frac{I_{y_1'y_1'}}{I_{z_1'z_1'}}$ [1]	29.5	32.8	27.3	18.5	15.3	22.9
$\frac{I_{y_2'y_2'}}{I_{z_2'z_2'}}$ [1]	32.8	13.1	25.1	10.9	27.3	17.5
J_{r_1}	1.3	1.6	1.6	1.1	1.7	1.9
J_{r_2}	1.1	1.0	1.0	1.0	1.6	1.1
J_{r_3}	1.0	1.0	1.1	1.1	1.6	1.6
J_{r_4}	1.4	1.0	1.3	1.6	1.1	1.1
J_{r_5}	1.1	1.1	1.0	1.3	1.4	1.7
J_{r_6}	1.1	1.1	1.6	1.1	1.6	1.6
J_{r_7}	1.3	1.3	1.3	1.1	1.3	1.1
J_{r_8}	1.9	1.6	1.3	1.4	1.9	1.1
J_{r_9}	1.1	1.0	1.3	1.4	1.9	1.6
$J_{r_{10}}$	1.1	1.6	1.4	1.0	1.7	1.3

From the results of all the cases it is unclear as to whether any of the six solutions represents the global maximum, as no two solutions share near-identical parameter sets. Figure 4.31 shows a typical iteration history (run D_1) for the five best genes/solutions,

Despite the cost function in runs L_1 to L_3 being set up to maximise M_L,

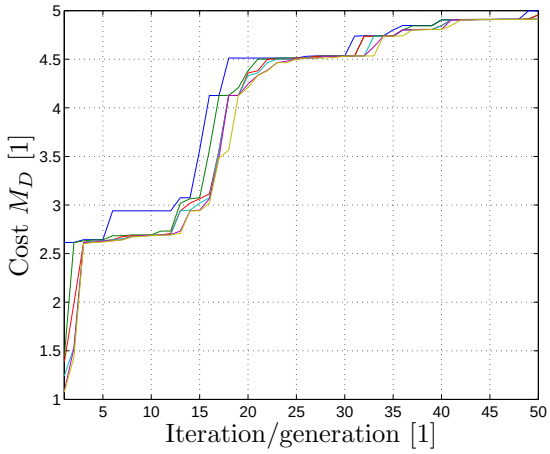

Figure 4.31: Convergence of morphing effectiveness parameter M_D for the five best genes/solutions.

it can be seen that the converged values of both M_D and M_L are consistently higher for runs D_1 to D_2 where the cost function is set up to maximise M_D. One possible explanation is that the cost function for maximising M_L has more local maxima than the equivalent cost function for maximising M_D, and the routine may benefit from an increased number of iterations.

Although the converged design variables are not identical, trends can be observed that reinforce the results of section 4.3; a medium-to-high aspect ratio wing with a sweepback angle between 15° and 30° seems to work well. A high aspect ratio increases the lift, as well as the lift-to-drag ratio and so increases the range that these can be varied by (i.e. M_L and M_D), but as the aspect ratio is further increased the deflections become substantial and violate the constraints. Additionally, rearward sweep delays divergence and therefore excessive deflections and so M_L and M_D will be higher as the sweep angle is increased. At sufficiently large sweep angles the stabilising bending-torsion coupling that exists will begin to reduce M_L and M_D.

It has been recommended (see section 4.3) that the rotating spars be placed either as far apart in a chordwise sense as possible, or close together. It was also mentioned that, in reality, the thickness of the aerofoil towards the trailing-edge will prevent the rear spar being located there, and a more realistic position for

it will be at 0.7 or 0.8 chord. From the table it can be seen that all solutions placed the rear spar close to 0.7 chord, and two of the solutions (runs D_1 and D_3) placed the forward spar towards the leading-edge, while the other four solutions placed it approximately as far aft as possible (0.4 chord).

The results also confirm that relatively large ratios of spar second moments of area make the concept more effective. All of the converged values are greater than 10, and the majority of them are close to 30. This is equivalent to spar heights d_s in excess of five times the spar thicknesses b_s. These large ratios enable the wing to substantially alter the position of the elastic axis.

Most of the torsional stiffnesses of the ribs have converged to low values (closer to 1×10^{-10} m^4 than 2×10^{-10} m^4). This is not surprising given that a contribution of the wing's torsional stiffness comes from the torsional stiffnesses of the ribs, and therefore by reducing the torsional stiffnesses of the ribs the wing's torsional stiffness will also reduce, allowing greater control over the aeroelastic deflections.

Run D_1 is clearly the best solution in terms of maximising both M_D and M_L. The wing described by the solution parameters of run D_1 will be used in the next section to carry out a trim study.

4.5 Trim study

4.5.1 Introduction

Since the main aim of the rotating spars adaptive structures concept is to minimise drag throughout the flight envelope, a study was performed to gain an insight into how the spar orientations affect the drag for a constant C_L, since this is a required condition for straight and level flight which aircraft operate at for the majority of flight. The wing model described by the optimisation results of case D_1 in section 4.4.4 was used as the platform for the study since this design has been optimised to make best use of the rotating spars concept.

To simulate the flight envelope, the airspeed was varied, and a trim analysis

was performed; more specifically, a target C_L value was defined, and at each airspeed the rigid angle of incidence as well as the spars' orientations were varied in order to match the target C_L. This allowed plots of the spars' orientations against drag at the trim state to be constructed for each airspeed. These plots highlight the requirement for different combinations of spar orientations in order to achieve minimum drag at the trim state.

To conclude this study, a steepest descent optimisation algorithm was implemented in order to determine the required spar orientations for minimum induced drag at each airspeed.

4.5.2 Trimming the wing

With the assumption that the rigid angle of incidence α_r is the only variable, and noting that the analytical aeroelastic model is linear, and therefore has a linear lift-curve slope (approximately correct for small angles of incidence) which passes through the origin (symmetric aerofoil so zero lift for zero incidence), the following procedure can be followed to trim the wing:

1. Define a target C_L value, $C_{L_{\text{ref}}}$. This is the value of C_L that the wing will be trimmed to.

2. At an arbitrary trial rigid angle of incidence $\alpha_{r_{\text{trial}}}$ calculate the lift coefficient $C_{L_{\text{trial}}}$ for the current airspeed.

3. The required rigid angle of incidence $\alpha_{r_{\text{trim}}}$ to trim the wing to $C_{L_{\text{ref}}}$ at the current airspeed is simply given by

$$\alpha_{r_{\text{trim}}} = \alpha_{r_{\text{trial}}} \frac{C_{L_{\text{ref}}}}{C_{L_{\text{trial}}}} \tag{4.22}$$

4. The above procedure is repeated for all required airspeeds.

4.5.3 Effect of rotating spars on the trim state

The trim procedure described was performed for various combinations of the spars' orientations (3° increments between 0° and 90° for both spars) and airspeeds (20, 40 and 60 m·s^{-1}). The reference C_L was 0.0777 (corresponding to $U = 10$ m·s^{-1}, $\alpha_r = 1°$, and spar configuration [60 60]). The results are shown in figures 4.32 - 4.37.

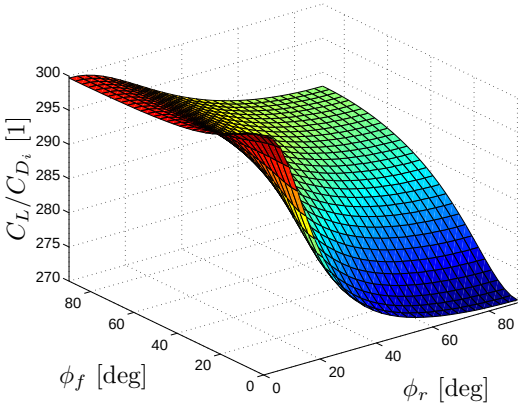

Figure 4.32: Variation of C_L/C_{D_i} at 20 m·s^{-1} with spars' orientations (trim state).

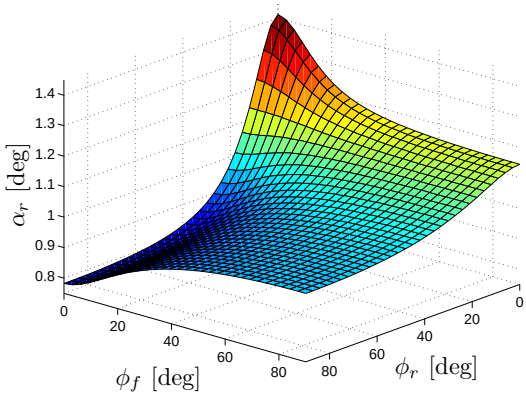

Figure 4.33: Variation of rigid angle of incidence at 20 m·s^{-1} with spars' orientations (trim state).

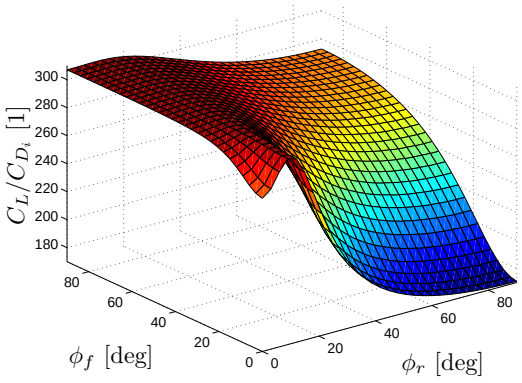

Figure 4.34: Variation of C_L/C_{D_i} at 40 m·s^{-1} with spars' orientations (trim state).

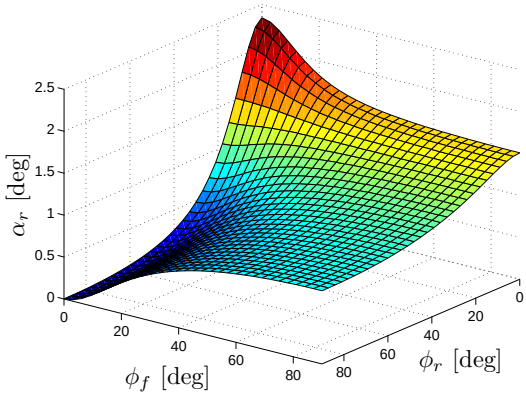

Figure 4.35: Variation of rigid angle of incidence at 40 m·s^{-1} with spars' orientations (trim state).

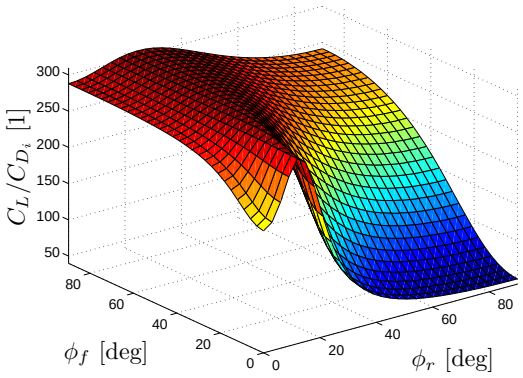

Figure 4.36: Variation of C_L/C_{D_i} at 60 m·s^{-1} with spars' orientations (trim state).

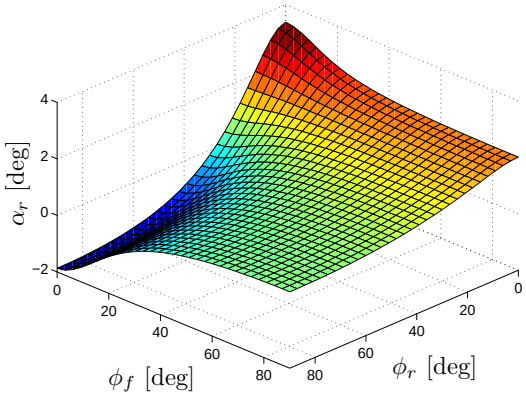

Figure 4.37: Variation of rigid angle of incidence at 60 m·s^{-1} with spars' orientations (trim state).

The inviscid lift-to-drag ratio C_L/C_{D_i} was related to the Oswald efficiency factor e_{O} and the lift coefficient C_L in Eq. 4.10 i.e.

$$\frac{C_L}{C_{D_i}} = \frac{\pi A \mathrm{R} e_{\mathrm{O}}}{C_L} \tag{4.10}$$

In section 4.2.2 the assumption was made that e_{O} varies very little relative to C_L; this is in general true. However, for a trim analysis C_L is fixed and so

$$\frac{C_L}{C_{D_i}} \propto e_{\mathrm{O}} \tag{4.23}$$

Comparison of figures 4.32, 4.34, and 4.36 with figure 4.22 (the plot of the spars' orientations against the Oswald efficiency factor for a sweptback wing) confirms the relationship given by Eq. 4.23. The physical reasoning behind this trend can be understood by examining the expression for the angle of incidence for a swept wing, given by

$$\alpha = \alpha_r\left(x_1, x_2\right) + \theta\left(x_1, x_2\right)\cos\Lambda - h'\left(x_1, x_2\right)\sin\Lambda \tag{4.24}$$

where θ is the torsional displacement of the wing, h' is the slope of the bending displacement of the wing, Λ is the rearward sweep angle, and x_1 and x_2 are the

spanwise coordinates along each of the two spars. Note that bending deflections will be larger towards the tip than torsional deflections will since these deflections will be similar to the mode shapes of a cantilever beam which, in general, follow this trend.

In the [0 90] configuration, the elastic axis is far aft and the bending and torsional stiffnesses are moderate resulting in large torsional displacements θ, but low to moderate bending deflections (therefore bending gradients h'). In the [90 90] configuration, θ is slightly less, but h' is noticeably less. In the [90 0] configuration, the forward placed elastic axis and fairly high stiffnesses will result in low values of θ, and low to moderate values of h', while in the [0 0] configuration, the lower stiffness values will result in moderate values of θ and high values of h'.

Using Eq. 4.24 in a qualitative manner with these predictions suggests that relative to the inboard angles of incidence, the [0 90] configuration is likely to have the highest outboard angles of incidence (highest induced drag and lowest efficiencies), and the [0 0] or [90 0] configuration is likely to have the lowest outboard angles of incidence (lowest induced drag and highest efficiencies). Therefore it is probable that for a rearward-swept elastic wing

$$\begin{aligned} & e_{\mathrm{O}}|_{[0\,90]} < e_{\mathrm{O}}|_{[90\,90]} < e_{\mathrm{O}}|_{[90\,0]} < e_{\mathrm{O}}|_{[0\,0]} \\ \text{or} \quad & e_{\mathrm{O}}|_{[0\,90]} < e_{\mathrm{O}}|_{[90\,90]} < e_{\mathrm{O}}|_{[0\,0]} < e_{\mathrm{O}}|_{[90\,0]} \end{aligned} \tag{4.25}$$

and

$$\begin{aligned} & \left.\frac{C_L}{C_{D_i}}\right|_{[0\,90]} < \left.\frac{C_L}{C_{D_i}}\right|_{[90\,90]} < \left.\frac{C_L}{C_{D_i}}\right|_{[90\,0]} < \left.\frac{C_L}{C_{D_i}}\right|_{[0\,0]} \\ \text{or} \quad & \left.\frac{C_L}{C_{D_i}}\right|_{[0\,90]} < \left.\frac{C_L}{C_{D_i}}\right|_{[90\,90]} < \left.\frac{C_L}{C_{D_i}}\right|_{[0\,0]} < \left.\frac{C_L}{C_{D_i}}\right|_{[90\,0]} \end{aligned} \tag{4.26}$$

These statements agree with the plots of e_{O} (figures 4.20, 4.22 and 4.24) and C_L/C_{D_i} (figures 4.19, 4.21 and 4.23). The pattern of these statements is also

likely to hold true for the total elastic angle of incidence given by

$$\alpha_e(x_1, x_2) = \theta(x_1, x_2)\cos\Lambda - h'(x_1, x_2)\sin\Lambda \tag{4.27}$$

although the pattern will be reversed i.e.

$$\begin{aligned} & \alpha_e|_{[0\,90]} > \alpha_e|_{[90\,90]} > \alpha_e|_{[90\,0]} > \alpha_e|_{[0\,0]} \\ \text{or} \quad & \alpha_e|_{[0\,90]} > \alpha_e|_{[90\,90]} > \alpha_e|_{[0\,0]} > \alpha_e|_{[90\,0]} \end{aligned} \tag{4.28}$$

and therefore in order to trim the wing to a fixed C_L, the rigid angle of incidence α_r must be adjusted to compensate and so it can be expected that

$$\begin{aligned} & \alpha_r|_{[0\,90]} < \alpha_r|_{[90\,90]} < \alpha_r|_{[90\,0]} < \alpha_r|_{[0\,0]} \\ \text{or} \quad & \alpha_r|_{[0\,90]} < \alpha_r|_{[90\,90]} < \alpha_r|_{[0\,0]} < \alpha_r|_{[90\,0]} \end{aligned} \tag{4.29}$$

and inspection of figures 4.33, 4.35, and 4.37 reveals this to be the case, although there is a clear peak at [0 0] which is consistent at all airspeeds, unlike the peaks in the C_L/C_{D_i} trends.

As the airspeed increases, a larger range of lift-to-drag ratios are available, and the range that the rigid angle of incidence needs to be varied by to trim the wing also increases. This is due to a larger range of aeroelastic deflections caused by the higher dynamic pressures.

Notice that as the airspeed changes, the shape/trend of the C_L/C_{D_i} plot changes; in particular, the peak (global maximum) which represents the optimal spar configuration for minimising induced drag appears to shift. This manifests itself as a ridge which moves in the positive ϕ_r-direction as the speed increases. Figure 4.36 clearly shows the bulge of the graph which runs approximately between the [0 15] configuration and the [90 25] configuration. This is a feature of swept wings only and is a result of the conflicting contributions to the angle of incidence distribution from the bending and twisting displacements. The peak of

the graph indicates that at that particular airspeed and trim C_L, the corresponding spar configuration produces a lift distribution that minimises drag. This leads to a minimum induced drag 'corridor' or 'valley' that shifts with airspeed. The objective then is to exploit this feature by varying the spar orientations throughout flight to maintain a minimum drag state.

4.5.4 Minimisation of induced drag at the trim state via a steepest descent optimisation algorithm

Introduction

To find the spar configuration that minimises induced drag at the trim state, a steepest descent optimisation algorithm was written and the trim procedure was included in it with induced drag as the cost function. As mentioned in section 4.4.2, this method is simple to implement and fairly robust. Disadvantages of this method include slow convergence, particularly in the region near the minimum/maximum, and susceptibility to zig-zagging down/up valleys which, of course, is inefficient. Routines with many variables can also be problematic, and complicated cost functions can present difficulties [109, 113].

However, the cost function in this study (the trend is the inverse of the C_L/C_{D_i} plots at the trim condition - see figures 4.32, 4.34, and 4.36) is fairly straightforward, with a single minimum (although the boundaries may be treated as such), and is a function of only two variables, and therefore convergence difficulties are not expected. For these reasons, and given the ease of coding, it was decided that the method of steepest descent was the most suitable choice of optimisation method, rather than use other more complicated methods that may not necessarily offer faster convergence. As is clear from the plots, the cost function does contain a valley and so some zig-zagging can be expected; this was not anticipated to be a major problem. Had it been then the conjugate gradient or quasi-Newton approaches mentioned in section 4.4.2 would have been more appropriate.

Implementation of a steepest descent algorithm

A steepest descent algorithm was written in MATLAB®, and was coupled with the trim routine that controls the static aeroelastic wing model develop in chapter 3, and also written in MATLAB®. The following procedure describes the optimisation routine that was implemented:

1. Define a target lift coefficient value, $C_{L_{\text{ref}}}$. This is the value of C_L that the wing will be trimmed to.

2. At an arbitrary initial spar configuration $[\phi_{f_1}\ \phi_{r_1}]$, at an arbitrary trial rigid angle of incidence $\alpha_{r_{\text{trial}}}$, calculate the lift coefficient $C_{L_{\text{trial}}}$.

3. The required rigid angle of incidence $\alpha_{r_{\text{trim}}}$ to trim the wing to $C_{L_{\text{ref}}}$ at the current airspeed was given in Eq. 4.22 as

$$\alpha_{r_{\text{trim}}} = \alpha_{r_{\text{trial}}} \frac{C_{L_{\text{ref}}}}{C_{L_{\text{trial}}}} \tag{4.22}$$

   and the corresponding coefficient of induced drag is C_{D_i}.

4. Increment ϕ_{f_1} by a small amount $\partial\phi_f$ and repeat steps 2 - 3 for $[(\phi_{f_1} + \partial\phi_f)\ \ \phi_{r_1}]$, with the incremented coefficient of induced drag at the trim condition being $C_{D_i}(\partial\phi_f)$. The gradient of the induced drag in the ϕ_f-direction is then approximated by

$$\frac{\partial C_{D_i}}{\partial \phi_f} \approx \frac{C_{D_i}(\partial\phi_f) - C_{D_i}}{\partial\phi_f} \tag{4.30}$$

5. Step 4 is then repeated for a small increment $\partial\phi_r$ i.e. $[\phi_{f_1}\ \ (\phi_{r_1} + \partial\phi_r)]$, with the incremented coefficient of induced drag at the trim condition being $C_{D_i}(\partial\phi_r)$. The gradient of the induced drag in the ϕ_r-direction is then approximated by

$$\frac{\partial C_{D_i}}{\partial \phi_r} \approx \frac{C_{D_i}(\partial\phi_r) - C_{D_i}}{\partial\phi_r} \tag{4.31}$$

6. The next spars' orientations are then calculated from

$$\phi_{f_2} = \phi_{f_1} - \frac{\frac{\partial C_{D_i}}{\partial \phi_f}}{\left\{\left(\frac{\partial C_{D_i}}{\partial \phi_f}\right)^2 + \left(\frac{\partial C_{D_i}}{\partial \phi_r}\right)^2\right\}^{0.5}} \partial \phi_f \tag{4.32}$$

and

$$\phi_{r_2} = \phi_{r_1} - \frac{\frac{\partial C_{D_i}}{\partial \phi_r}}{\left\{\left(\frac{\partial C_{D_i}}{\partial \phi_f}\right)^2 + \left(\frac{\partial C_{D_i}}{\partial \phi_r}\right)^2\right\}^{0.5}} \partial \phi_r \tag{4.33}$$

which can be written for convenience as

$$\phi_{f_2} = \phi_{f_1} - \Delta\phi_f \tag{4.34}$$

and

$$\phi_{r_2} = \phi_{r_1} - \Delta\phi_r \tag{4.35}$$

This ensures that a path of steepest descent is chosen.

7. Steps 2 - 6 are then repeated until satisfactory convergence of C_{D_i}

Handling the solution boundaries

At certain points in the domain, the optimisation procedure described previously would have attempted to move the solution over the boundaries of the input e.g. a trial solution at [2 87] would calculate the gradients of C_{D_i} in both directions and may have attempted to move it by $-5°$ in the ϕ_f-direction, and $5°$ in the ϕ_r-direction; this would have resulted in the solution moving to [-3 92], which is of course outside the range of ϕ_f and ϕ_r since $0 \leq \phi_f \leq 90$ and similarly $0 \leq \phi_r \leq 90$. As a result, the following was enforced:

$$\begin{aligned} &\phi_{f_{i+1}} = \phi_{f_i} - \Delta\phi_f, && 0 \leq \left(\phi_{f_{i+1}} - \Delta\phi_f\right) \leq 90 \\ &\phi_{f_{i+1}} = 0, && \left(\phi_{f_{i+1}} - \Delta\phi_f\right) < 0 \\ &\phi_{f_{i+1}} = 90, && \left(\phi_{f_{i+1}} - \Delta\phi_f\right) > 90 \end{aligned} \tag{4.36}$$

and similarly in the ϕ_r-direction.

Improving the convergence speed for cost functions containing 'valleys'

The cost function in this study (the trend is the inverse of the C_L/C_{D_i} plots at the trim condition - see figures 4.32, 4.34, and 4.36) contains a well-defined 'valley' at higher airspeeds, which runs almost parallel to the ϕ_f-direction. The gradient in the ϕ_f-direction is very small relative to the 'sides' of the valley. Such a feature in the cost function causes convergence to be slow because the solution follows a tight zig-zag path down the valley, with much of the movement almost perpendicular to the direction of the optimum solution. This behaviour is caused by the algorithm attempting to follow the path of steepest descent, which in the case of such a valley, is not the most efficient.

To alleviate this problem, information from a number of consecutive gradients was used to detect valleys, which resulted in the algorithm no longer following the path of steepest descent; instead, movement was divided equally between the ϕ_f- and ϕ_r-directions. This was effective in speeding up the movement of the solution down a valley. If the path exited the valley, the algorithm returned to a steepest descent approach.

Improving the accuracy of the converged solution

To improve the accuracy of the solution, information about successive gradients was stored and used to detect troughs (i.e. potential optimum solutions) and this resulted in $\partial\phi_f$ and/or $\partial\phi_r$ decreasing in order to home in on a more accurate solution. If this turned out to be a false trough, the original increment size was reinstated.

Tackling problematic iteration patterns

An awkward terrain can occasionally cause the method to move the solution to a worse position than before. Generally, over the course of successive iterations,

this is not a problem. However, sometimes this can cause the algorithm to get stuck in a repeated path from which it does not escape or converge. This usually occurs in the region of the optimum solution and the path loops around the minima, but never gets close enough to consider it as convergence. To get around this problem, a small random perturbation was added to both ϕ_f and ϕ_r in step 2 of the procedure described previously.

Optimisation results

The optimisation procedure was used to find the optimum spar configuration at the trim state for a range of airspeeds (1 m·s^{-1} increments between 5 m·s^{-1} and 60 m·s^{-1}). The reference C_L was 0.0777 (corresponding to $U = 10$ m·s^{-1}, $\alpha_r = 1°$, and spar configuration [60 60]). The initial spar configuration for each optimisation procedure was [45 45] and the spar orientation increments used were 5° for both spars. Figure 4.38 summarises the converged parameters over the range of airspeeds, and figures 4.39a and 4.39b show a typical convergence history for a single airspeed ($U = 60$ m·s^{-1}).

The most significant feature to note is that the optimum spar configuration alters with airspeed, quantitatively confirming the results of section 4.5.3. This behaviour corresponds to the minimum induced drag 'corridor' mentioned in that section, which moves as the airspeed changes. These results highlight the benefit of the rotating spars concept.

As the airspeed increases, a general increase in the rigid angle of incidence required to trim the wing is also evident. This is fairly intuitive, since the increasing bending deflections couple in the sweptback wing to decrease the angle of incidence as the dynamic pressure increases. The rigid angle of incidence therefore must increase to return the wing to the trim state.

An increase in the maximum C_L/C_{D_i} achievable is noted as the airspeed increases. This is due to the increasing bending deflections creating a more efficient lift distribution over the wing.

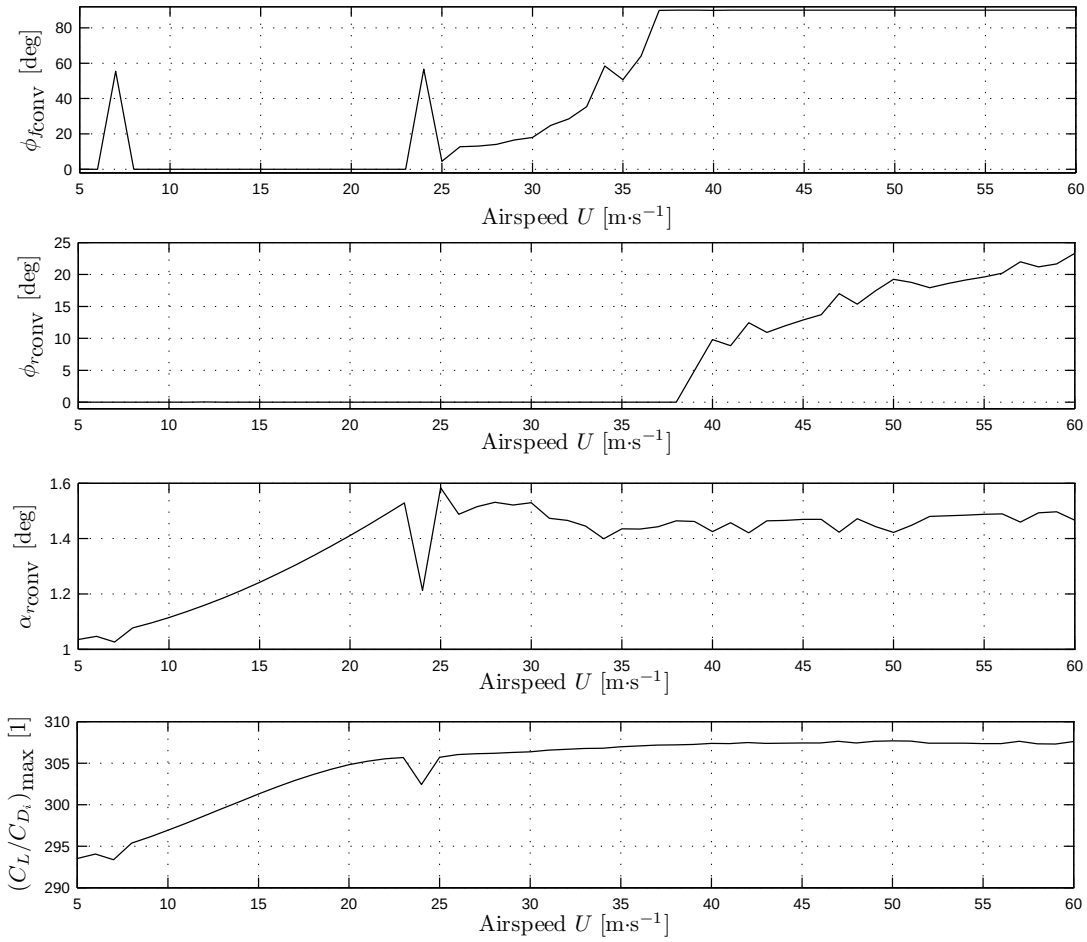

Figure 4.38: Variation of the converged parameters at the trim state.

Figure 4.39a shows a typical convergence history of the spars' orientations. It is clear that the algorithm takes the solution into a near optimum solution (corresponding to the valley feature of the cost function) relatively quickly, but then slows down as it travels down the valley. Zig-zag behaviour is fairly limited due to the inclusion of the tool to counter this behaviour (mentioned previously), and it can be seen that the valley runs almost parallel to the ϕ_f-direction, confirming the observations in section 4.5.3.

Figure 4.39b shows the corresponding convergence history of the cost function, C_{D_i}. Convergence to a near minimum value of C_{D_i} is rapid (approximately ten iterations), and at this point the solution enters the valley feature in the cost function. The remaining 45 iterations are used to improve the accuracy of

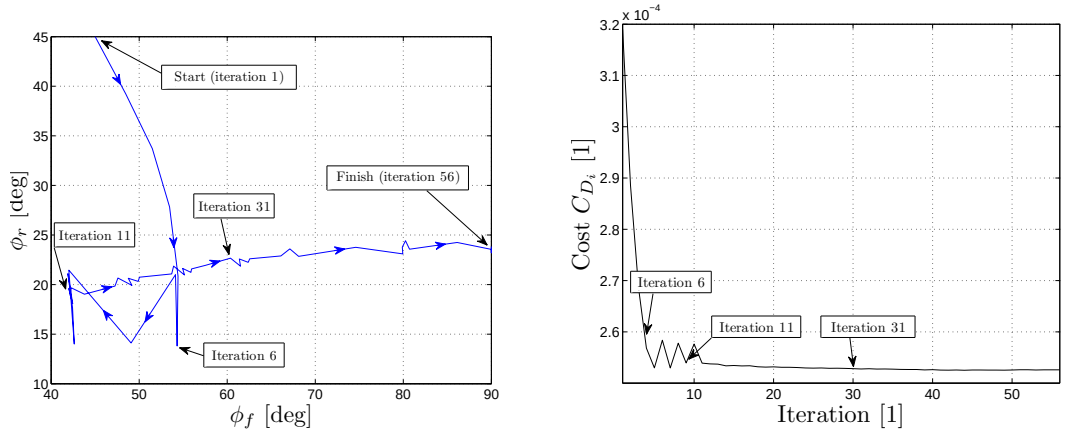

(a) Spars' orientations iteration history for a typical run.

(b) Cost history for a typical run.

Figure 4.39: Convergence of spar orientations and cost.

the optimum configuration of $[\phi_f \ \phi_r]$, despite there being only a relatively small improvement in the cost function.

Ability to handle noise in the data

A random time-varying perturbation was added to the cost function to gain an insight into the ability of the optimisation routine to converge successfully in less simulated environments. The results suggest that when this noise exceeds around 10% of the range of the cost function, the algorithm will struggle to converge. This is shown experimentally in chapter 5 where the algorithm does not converge when the load readings (low signal-to-noise ratios) are used as the cost function, but does converge when the deflections (higher signal-to-noise ratios) are used instead.

4.6 Conclusions

This chapter has demonstrated that the position of the wing's elastic axis and the its bending stiffness are the main structural parameters that are affected by the rotating spars adaptive internal structures concept. The wing's torsional stiffness

is much less sensitive to changes in the spars' orientations. A conclusion that occurs throughout this study is that the rotating spars concept is better suited to sweptback wings, and the fundamental reason for this is that the concept allows much more control over the wing's bending stiffness (which contributes to aeroelastic loads for swept wings) than its torsional stiffness.

Additionally it has been established that all aeroelastic parameters have extremes, unsurprisingly, when the two spars are at a configuration of 0° or 90° i.e. [0 0], [90 90], [0 90], or [90 0]. These trends are likely to remain if the study is repeated in viscous flow.

This chapter has also established the following basic guidelines for assessing the suitability of the rotating spars concept for use on an arbitrary wing:

- In terms of effectiveness, the concept is unlikely to offer much benefit to wings that are unswept or sweptforward; on the other hand, wings sweptback to between 15° and 30° lend well to the mechanisms involved.

- The concept will work best with wings of medium-to-high aspect ratio ($7 \leq \mathcal{A}\mathrm{R} \leq 15$), and will be largely ineffective if applied to very low aspect ratio wings, such as those found on supersonic fighter aircraft.

Additionally, the following basic design guidelines with respect to the spars have been established:

- The ratio of spar second moments of area should be relatively large (≥ 10), although above a certain ratio (≈ 30) the effectiveness of the concept will decrease again.

- In general, the two rotating spars should be positioned as far apart as possible in the chordwise direction.

These guidelines are all likely to hold true if the analysis is made more realistic by considering the viscous drag contributions and using a dynamic aeroelastic

model, although the resultant introduction of flutter as a constraint could have a large impact on these trends.

An overview of genetic algorithm optimisation was also presented and the results of a process to optimise a rotating spars wing (using a genetic algorithm) to maximise the effectiveness of the procedure was shown. This resulted in a wing design well suited to the concept, that was then used as the platform for carrying out a trim study. It was shown (qualitatively) that the spar configuration required to minimise the induced drag at the trim state for this wing changes as the airspeed changes, and then the results of an steepest descent optimisation routine to locate this configuration were presented, therefore quantifying the previous conclusion, and demonstrating how the online control of a rotating spars wing might, in practice, be implemented. With the exception of additional constraints, the procedures employed for optimising the design and trim state are unlikely to change if a complete dynamic aeroelastic model were used in viscous flow. The optimum solutions, on the other hand, would most likely be different.

Chapter 5

Wind tunnel tests of a rotating spars wing

5.1 Introduction

The results of chapter 4 dictated several design guidelines that were then used as the basis for the design of a wind tunnel model that could be used to perform similar tests to those performed in chapter 4, but on an experimental level. This was an important stage in the development of the concept as it allowed the viability of it to be explored to some degree and identified several design challenges that would have to be overcome that were not immediately clear from the analytical study.

Firstly, the basic model design was identified and will be described in this chapter. From this, the baseline model was produced; essentially this involved identifying all the constraints in the design, build and test phases and applying them early on in order to narrow-down the design. Finally, to fine-tune the baseline design to the final design, a finite element representation of the baseline design was made and several aeroelastic analyses were performed using it; this focussed on maximising the effectiveness of the concept with regards to maximising the range of lift achievable, whilst simultaneously ensuring that the critical

flutter and divergence dynamic pressures of the wing were significantly higher than the test range dynamic pressures.

Next, the chapter will describe the construction phase; this involved all components of the wing model that had to be designed and built and specific features of these components will be discussed.

Before the tests are discussed and the results presented, a section of this chapter is devoted to describing the equipment that was used to perform these tests.

Finally, the tests and results will be presented. This begins with examining the integrity of the channels to explain why noise was a problem throughout much of the testing, and what was done to alleviate it as much as possible. The assembly that supported the wing protruded into the test-section and therefore its effect on the aerodynamic loads had to be removed; the results of this calibration are shown. Next the parameter study is presented; this involved a structural investigation, and also an aeroelastic investigation. The results of these studies agreed, in general, with analytical predictions and the trends established in chapter 4.

Attempts to use the rotating spar concept to accurately control the aerodynamic loads involved polynomial curve fitting as well as feedback approaches via optimisation. Both of these approaches failed, primarily due to the aforementioned noise problems. The curve fit approach was also found to lack robustness. Conversely, the robustness of the optimisation approach was proven using deflections in place of loads as the inputs, and therefore the conclusion was reached that the rotating spars could accurately control the aerodynamic loads via the optimisation approach provided that the loads could be measured with a sufficiently high signal-to-noise ratio. Although the optimisation approach takes a relatively long time to reach desired values, the application of this concept would be for low-frequency applications and therefore it is a suitable control method.

5.2 Design of the model using an analytical approach

5.2.1 Basic structural layout

It was important to produce a design that was reasonably simple in order to aid the ease of fabrication, performance, repair and robustness. Figure 5.1 shows a CAD model of the proposed structure.

Figure 5.1: CAD model of the wing design.

The key points to emphasise are:

- Two fixed spars at the leading- and trailing-edges to maintain the planform shape.
- Two rotating spars between the fixed spars.
- Thin ribs, spaced equidistant from one another with a relatively small gap between adjacent ribs in order to maintain the aerofoil shape along the span.
- Roller-bearings used to provide low-friction rotation for the spars. The

bearings were substantially thicker than the ribs into which they were inserted in order to provide good contact with the spars with minimal free-play.

- The rotating spars had a rectangular cross-section except at locations where they contact the bearings where they were cylindrical. This removed the requirement for an inner-race in the bearings since the spar itself became the inner-race, therefore allowing the spars to have larger cross-sectional dimensions. Fabricating the rotating spars was identified as the most challenging part of the manufacturing process and for this reason it was decided to make them identical to each other.

- Shrink-wrap skin supported by low stiffness rib-caps (not shown in figure 5.1).

- Ribs perpendicular to the spars and a rectangular planform, regardless of the sweep angle. This made fabrication substantially simpler and less time-consuming, and did not affect the demonstration of the concept.

- Half-span model only (not clear from figure 5.1).

5.2.2 Establishing a baseline wing

Introduction

Naturally there are many variables that need to be considered during the design of any wind tunnel wing model; for instance, the wingspan, operating airspeed and construction materials will all affect the performance of the wing.

However, the decision-making process can be simplified by recognising constraints that will exist either during the manufacturing process or in the test environment and using these to reduce the number of possibilities.

Design guidelines

The guidelines established in section 4.3 were used as the basis of a wing design with two rotating spars:

1. Medium-to-high wing sweepback angle ($15° \leq \Lambda \leq 30°$).
2. Medium-to-high wing aspect ratio ($7 \leq AR \leq 15$).
3. High bending stiffness ratios for the rotating spars ($10 \leq I_{y'_j y'_j}/I_{z'_j z'_j} \leq 30$) i.e. the second moment of area of a rotating spar was much larger in one direction that in the perpendicular direction.
4. The two rotating spars were to be placed as far apart as possible in the chordwise direction.

Choice of airspeed

Several factors influenced the airspeed range for the tests:

- the maximum wind tunnel airspeed was approximately 50 $m{\cdot}s^{-1}$.
- airflow patterns due to the less-than-ideal placement of the wind tunnel caused resonance of the entire tunnel structure limiting the operating ranges to 0 $m{\cdot}s^{-1} < U < 28$ $m{\cdot}s^{-1}$, 32 $m{\cdot}s^{-1} < U < 34$ $m{\cdot}s^{-1}$, and 37 $m{\cdot}s^{-1} < U < 50$ $m{\cdot}s^{-1}$. The second of these ranges was far too small and therefore only the lower and upper speed ranges were considered.
- higher airspeeds result in a larger range of aerodynamic loads and so the signal-to-noise ratio of trends would be better at higher speeds.
- as the airspeed increases, actuators for the rotating spars would require a greater torque to overcome the increasing stiction forces.

The use of the upper speed range would involve passing through tunnel resonance twice whilst accelerating the airflow, and therefore test airspeeds within

the lower range were favoured for an initial design (maximum of 25 $m \cdot s^{-1}$), with the option of redesigning for the upper speed range should the original design be evaluated as ineffective at an early stage.

Choice of planform parameters

Several factors of the test environment dictated certain aspects of the wing planform as follows:

1. The wing geometry was dictated by the wind tunnel test-section geometry. A diagram of the test-section is depicted in figure 5.2a. For a medium-to-high aspect ratio wing the largest dimension will be the wingspan, therefore, from figure 5.2b, which shows the cross-sectional dimensions of the test-section, the span of a horizontally aligned half-wing model had to be less than 1095 mm, and the span of a vertically-aligned half-wing model had to be less than 870 mm. Additionally, it was recognised that if the model was too small it might be challenging to manufacture and sourcing off-the-shelf components may also be difficult. For this reason, a horizontally-aligned wing was chosen. It was decided that a wing of span 730 mm (perpendicular to the flow direction) located centrally within the test-section would provide sufficient root clearance for housing the actuators whilst being large enough not to present problems during manufacture.

2. The wing had to be designed such that the loads produced were not in excess of the load balance range, not only to accurately measure the loads but also to prevent damage to the load balance. The six-component balance was limited to the following maximum loads in the channels of interest; lift: 220 N, drag: 67 N.

3. To allow elastic aerodynamic effects to occur free from stall, a low-to-moderate wind-off angle of incidence of 5° was used, which also represented a realistic value. A chord of 250 mm was chosen, which offered adequate

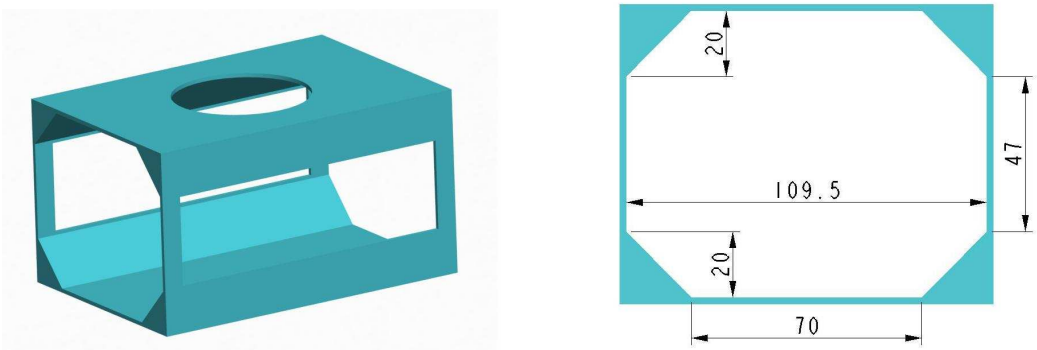

(a) With side panel windows and roof disc removed.

(b) Cross-sectional dimensions. All dimensions in centimetres.

Figure 5.2: Diagrams of the wind tunnel test-section.

space inside the wing for mechanisms etc., while still providing an aspect ratio of 5.84, which is in keeping with the earlier recommendation of a medium-to-high aspect ratio. With a lift-curve slope of 2π, the model parameters stated so far predicted the rigid lift would not exceed 40 N, and the lift-to-drag ratio was expected to be approximately 5, suggesting maximum drag values of 8 N, both of these liberal estimates falling well below the maximum range of the load balance. Again, in keeping with the planform recommendations, the wing was sweptback to an angle of 15°.

Choice of structural parameters

The fabrication process dictated certain aspects of the wing structure as follows:

1. Aluminium was selected as the wing structural material for its low-cost, availability, high strength-to-weight ratio, isotropic properties (making analytical predictions more straightforward), and ease of machining. This provided the following structural parameters: Young's modulus $E = 69$ GPa, shear modulus $G = 26$ GPa.

2. A NACA 0012 aerofoil section was chosen for the wing as it is widely used and is symmetric making analytical predictions simpler and more accurate.

The thickness of this aerofoil provided the upper limits for the spar heights. For a chord of 250 mm the maximum wing thickness is 30 mm. However, to achieve a large range of possible chordwise spar placement locations, wing thicknesses as small as 25 mm had to be considered. With this in mind it was decided that the outer-diameter of the bearing should not exceed 16 mm in order to fit comfortably inside a rib. A review of off-the-shelf bearings then identified that the inner-diameter (i.e. spar diameter) could not exceed 12 mm.

3. The minimum spar thickness was identified as an important constraint; the most robust method to fabricate a small-scale spar is to machine it from a single block of material, as this removes the need for awkward application of adhesives etc. and prevents free-play occurring at attachment points. For fixed spars, this is not a problem as they can easily be cut from sheets of material. For rotating spars that most likely have cylindrical sections at mounting locations along their length (see figure 5.3a), the machining process would be performed using a lathe; for long lengths of material whipping (vibration of the piece) occurs if the cross-sectional dimensions are too small; this had to be avoided. For the type of spar considered (high aspect ratio, aluminium, height approximately 12 mm) a minimum spar thickness of 3 mm was chosen to avoid whipping.

To be able to assemble and disassemble the wing the entire length of the spar had to be able to slide through the bearings. This meant that the cross-section at all points along the spar had to fit inside the bearing inner-diameter (see figure 5.3b) i.e. the spar cross-sectional dimensions had to satisfy

$$d_s^2 + b_s^2 \leq D_i^2 \tag{5.1}$$

where d_s is the spar height, b_s is the spar thickness, and D_i is the bearing inner-diameter. In section 4.3, it was established that the effectiveness of the

(a) Rotating spar fabricated from single piece of material.

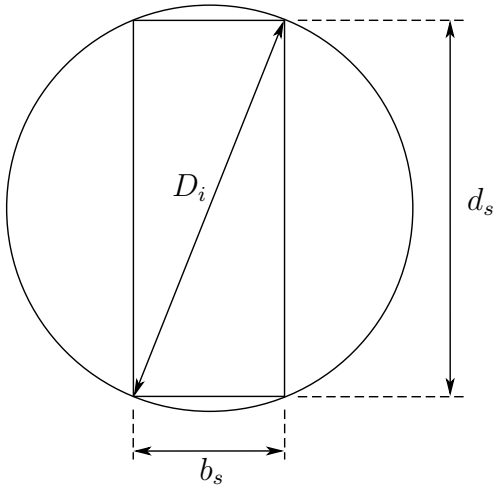

(b) Rotating spar cross-section.

Figure 5.3: Diagrams of the rotating spar.

concept, in general, improves as the ratio of d_s to b_s increases. Therefore, to maximise this ratio, D_i was maximised (12 mm), and b_s was minimised (3 mm), resulting in $d_s = 11.6$ mm.

At this early stage it was intended to use a light-weight, low-stiffness material to shape the leading-edge. This aerofoil leading-edge shape was intended to occupy approximately 10% of the chord and one of the reasons for having a thin leading-edge spar was to support this leading-edge shape, as shown in figure 5.4a. Taking this and the bearing diameter and clearance into account, it was estimated that the centre of the rotating spars should lie between $\frac{x}{c} = 0.167$ and $\frac{x}{c} = 0.585$. Using the recommendation from section 4.3 that the rotating spars should be located as far apart as possible in the chordwise direction positioned the forward rotating spar at $\frac{x}{c} = 0.167$ and the rear rotating spar at $\frac{x}{c} = 0.585$.

Similarly, the wing also required a spanwise component to support the trailing-edge; however, in this case a simple flat-plate type spar could be used since the upper and lower skin surfaces meet here close to parallel to each other. To give the skin adequate support it was intended to use a trailing-edge spar that also occupied 10% of the chord. Figure 5.4b provides details of the design. For the

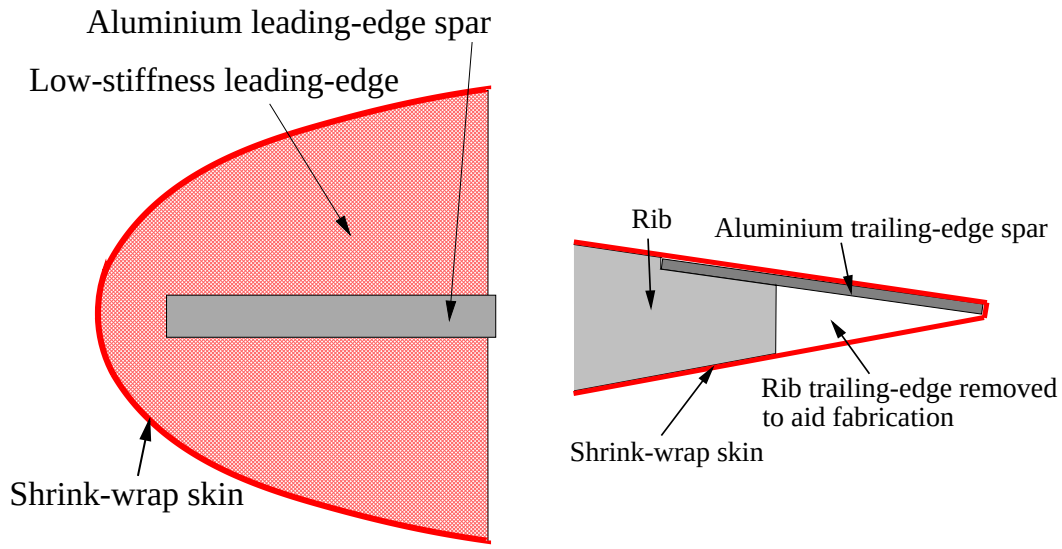

(a) Leading-edge. (b) Trailing-edge.

Figure 5.4: Leading- and trailing-edge design.

baseline design, both the leading- and trailing-edge spars were intended to be relatively flexible, since a high stiffness for these spars would reduce the effectiveness of the concept; therefore, 2 mm was chosen for the spar height, since 2 mm aluminium plates are readily available off-the-shelf.

Summary of the baseline wing

To summarise, the baseline wing planform used was a half-wing of span 730 mm, chord of 250 mm ($\mathcal{A}\mathrm{R} = 5.84$), and sweptback to an angle of 15°. The aluminium structure consisted of two fixed spars (height 2 mm, thickness 25 mm) lying flush with the leading- and trailing-edges ($\frac{x}{c} = 0.05$ and $\frac{x}{c} = 0.95$), two rotating spars (height 11.6 mm, thickness 3 mm) located at $\frac{x}{c} = 0.167$ and $\frac{x}{c} = 0.585$ and multiple ribs (NACA 0012 profile). The rotating spars were mounted in roller bearings of inner-diameter 12 mm and outer-diameter 16 mm. 9 ribs were considered adequate to provide and maintain a good aerodynamic profile over the span. The maximum design speed was 25 $\mathrm{m{\cdot}s^{-1}}$ and the design wind-off angle of incidence was 5°.

5.2.3 Effect of rotating spars on flutter behaviour

In the subsequent section, it will be shown using a finite element model that the wind tunnel wing model will be free from flutter throughout the tests; however, this provides little insight into the effect of the rotating spars on the flutter behaviour, and the analytical model developed in chapter 3 is limited to predicting static aeroelastic behaviour and therefore also provides no means of examining the flutter behaviour. It is possible, however, to understand the variation of the flutter speed with spar orientation by examining the structural behaviour and relating this to well known flutter trends.

For most practical wings, the frequency ratio $\omega_h/\omega_\theta < 1$, where ω_h is the first bending frequency and ω_θ is the first torsional frequency. Since the [90 90] case provides the wing with the highest flexural rigidity (see figure 4.4 for a more detailed flexural rigidity trend), and since the flexural rigidity is affected to a much greater extent than the torsional rigidity by the rotating spars concept, it can be stated that the effect of the rotating spars is to decrease the frequency ratio ω_h/ω_θ and therefore increase the separation of the two frequencies. Since classical bending-torsion flutter is caused by the coalescence of these two modal frequencies, this decrease in the frequency ratio has an aeroelastically stabilising effect, therefore delaying flutter. A typical variation of flutter speed with frequency ratio is shown in figure 5.5a [15]; there is a well-defined dip in the flutter speed corresponding to a frequency ratio of around unity.

The other major influence on the flutter behaviour for the rotating spars wing is caused by the shift of the elastic axis relative to the aerodynamic centre; the [0 90] case positions the elastic axis furthest aft and the [90 0] case positions it furthest forward (see figures 4.2 and 4.3 for more detailed elastic axis trends). A rearward shift in the position of the elastic axis (therefore increasing the elastic coupling) typically has an aeroelastically destabilising effect, resulting in a decreased divergence and flutter speed. A typical variation of flutter speed with position of the elastic axis is shown in figure 5.5b [15].

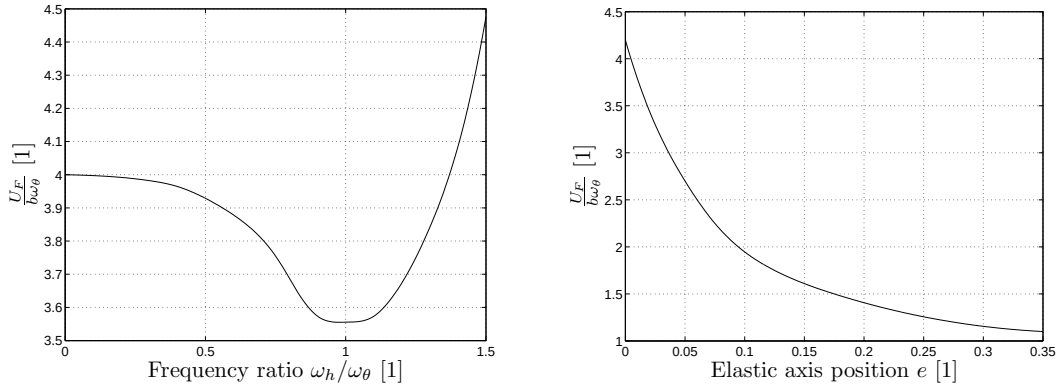

(a) Effect of frequency ratio.

(b) Effect of elastic axis position.

Figure 5.5: Typical variation of sectional dimensionless flutter speed (for classical binary bending-torsion flutter) with structural parameters.

The effect of rotating the spars away from the [90 90] position is to therefore decrease the frequency ratio (stabilising), and to either increase (destabilising) or decrease (stabilising) the elastic coupling; these conflicting contributions imply that a qualitative assessment of the flutter behaviour is difficult to make, and an analytical flutter model is required.

5.2.4 Analytical refinement of the model

Introduction

There are two major reasons why the analytical model developed and used in chapters 3 and 4 respectively was not used to predict the performance of the wind tunnel wing; first and foremost, the assumed modes vortex lattice model developed in chapter 3 is a static aeroelastic model and therefore has no capability of predicting the flutter speed of a wing. Without this prediction, the use of a wind tunnel model that, for some spar configurations, has reduced stiffness values is a somewhat reckless task, as the wing may easily be destroyed with little warning before any data is collected.

Additionally, the assumed modes model is of a wing with two spars (both rotating) and a variable number of ribs (ribs of constant torsional stiffness along

their length); in reality, non-rotating leading- and trailing-edge spars were also required as already mentioned in order to provide the aerodynamic shape and to maintain the wing planform shape. Extending the assumed modes model to a four-spar wing is extremely challenging, and the assumption of uniform rib properties along their lengths would also no longer be applicable, as the ribs in the wind tunnel model follow the profile of a NACA 0012 aerofoil.

Instead, a finite element model was made using NASTRAN™, which provided a closer approximation of the structure of a four-spar wing with aerofoil-shaped ribs than the assumed modes model could offer, and also provided an indication of the flutter speeds. The disadvantages to using this approach were that no indication of drag forces were provided, and optimisation of the design was not considered due to the relatively expensive computational requirements relative to the assumed modes model.

The decision not to optimise the design, however, was not seen as a major obstacle; with reference to the previous section, the various recommendations and constraints employed resulted in the definition of a baseline wing. This wing required only a small amount of fine-tuning via a trial-and-error process to ensure that aeroelastic instabilities would not be a problem during the testing and also to improve the effectiveness of the rotating spars concept. The variables used to refine the model were the height of the fixed spars, and the height and thickness of the rotating spars.

Finite element approximation of the model

The NASTRAN™ finite element representation of the wing structure is shown in figure 5.6. The four spars were modelled using beam elements (CBEAM) and the ribs were modelled via plate elements (CTRIA3) [11]. The spars were restrained in all six degrees of freedom at the root. The two centre spars (the rotating spars) were connected to the ribs in five degrees of freedom, with the unrestrained degree of freedom being rotation about the spars' longitudinal axis;

this ensured that twisting moments of the wing about a spanwise axis could not be transmitted from the ribs to the rotating spars, therefore making the model more realistic.

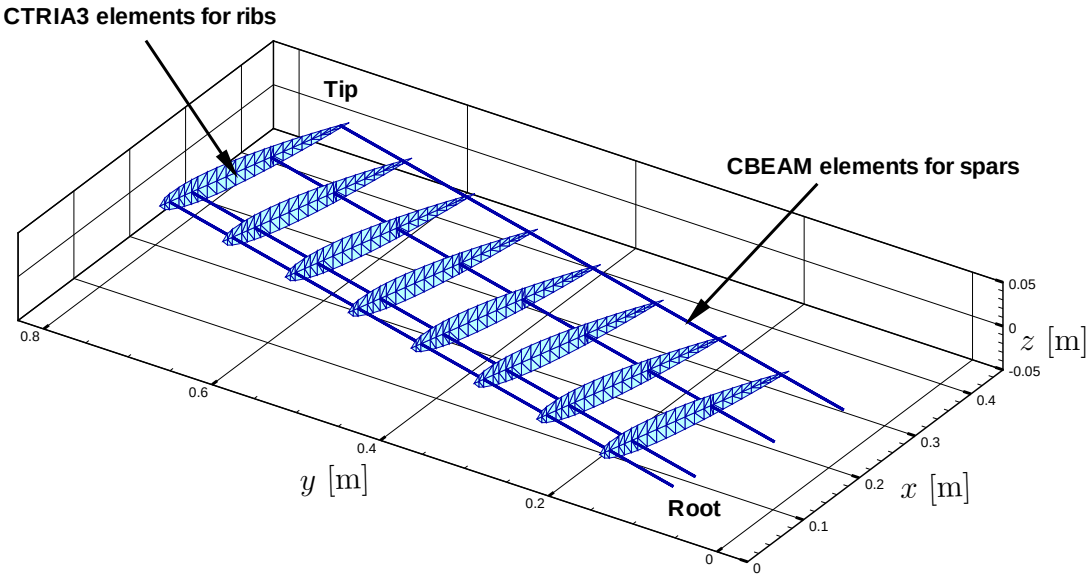

Figure 5.6: Finite element representation of the structural model.

The FE model did not contain a rib at the root since this was a rigid boundary; in the real wing, the inclusion of this rib was for non-structural reasons (to provide the aerodynamic shape at the root). The rib caps, low-stiffness material that was used to provide the aerodynamic shape at the leading-edge, and shrink-wrap skin were not included in the structural model; it was intended to manufacture the rib caps from a low-stiffness material (e.g. thin cardboard, since it is easy to work with) and the assumption was therefore made that the stiffness of this was insignificant in comparison to the ribs. Similarly, the assumption was made that the membrane skin had little effect on the overall stiffness of the wing; this was a convenient simplification, as the effect such a skin has on the structure of the wing depends upon many variable factors including the heat of application of the shrink-wrap, and therefore is difficult to accurately estimate. Similarly, the exclusion of the leading-edge low-stiffness material was predicted not to noticeably alter the wing stiffness and also made construction of the FE

model more straightforward.

The NASTRAN™ finite element representation of the wing aerodynamic model is shown in figure 5.7. 310 CAERO1 aerodynamic panels were used to provide the lifting-surface approximation of the wing, and these panels were placed at the mid-plane of the aerofoil. SPLINE2 algorithms provided the linear beam spline for transmitting the aerodynamic loads and motion between the aerodynamic and the structural model [116].

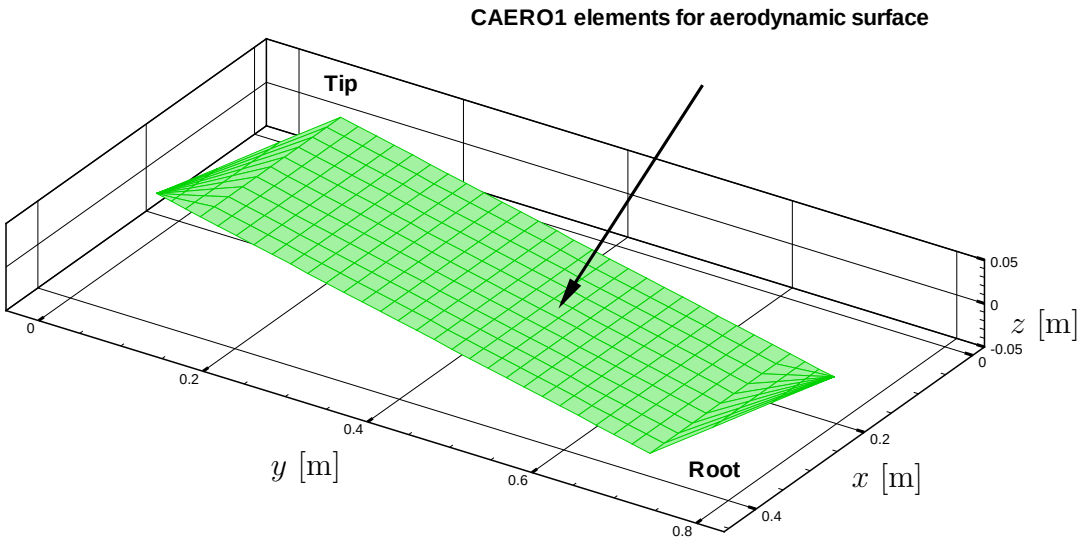

Figure 5.7: Finite element representation of the aerodynamic model.

As mentioned in section 3.5 and again in section 4.2.1, the angle of orientation of each rotating spar is described throughout by $[\phi_f \ \phi_r]$, the angle in degrees between the wing chordline and the principal axis z' of the spar for the forward and rear spar respectively, where $I_{z'z'} \leq I_{y'y'}$ e.g. the wing's bending stiffness is maximum at the [90 90] configuration, and is minimum at the [0 0] configuration.

Refinement of the baseline wing to the final design

Several aeroelastic analyses were performed using the baseline model, namely trim (at 25 m·s^{-1}), divergence (both SOL 144) and flutter (SOL 145 using the *p-k* method) [116]. This was done for spar configurations [0 0], [0 90], [90 90] and [90 0] since extremes can occur at any of these configurations.

The maximum and minimum C_L values from the trim analyses were then used to give an indication of the effectiveness of the concept using M_L, defined in section 4.3 as

$$M_L = C_L|_{\max} - C_L|_{\min} \tag{4.13}$$

and the divergence and flutter speeds, U_d and U_F respectively, were noted. The results are shown in table 5.1.

Table 5.1: Performance of the baseline wing design.

Parameter	[0 0]	[0 90]	[90 90]	[90 0]
C_L [1]	0.26702	0.39321	0.32565	0.28203
U_d [m·s^{-1}]	∞	50.545	100.351	∞
U_F [m·s^{-1}]	36.986	40.844	40.691	37.960

It can be seen from these results that the design is very effective (M_L = 0.12619 i.e. lift can be altered by up to 47%). However, it can also be seen that the lowest critical airspeed is 36.986 m·s^{-1} (flutter for the [0 0] configuration), which was deemed to be too close to potential operating speeds, should there be major discrepencies between the finite element and actual model.

The design variables were then altered within the ranges displayed in table 5.2 in a trial-and-error type approach to maximise M_L subject to sufficiently high values of U_d and U_F. It should be re-iterated at this point that the rotating spar cross-sectional dimensions had to conform to the inequality statement given by Eq. 5.1. Additionally, the off-the-shelf aluminium plates that were considered for the leading- and trailing-edge spars had thicknesses 1.2 mm, 2 mm, 3 mm, 3.175 mm, and 6 mm, which therefore corresponds to the possible spar thicknesses.

Table 5.2: Parameter ranges for the refinement of the wing design.

Variable	Min. value	Max. value
Leading-edge spar thickness [mm]	1.2	6
Trailing-edge spar thickness [mm]	1.2	6
Rotating spar height d_s [mm]	3	11.6
Rotating spar thickness b_s [mm]	3	11.6

Table 5.3 shows the chosen values for these parameters for use with the final wing design, and table 5.4 shows the results of the aeroelastic analyses using this wing.

Table 5.3: Parameter values for the refined wing design.

Variable	Final design value
Leading-edge spar thickness [mm]	3
Trailing-edge spar thickness [mm]	1.2
Rotating spar height d_s [mm]	11.3
Rotating spar thickness b_s [mm]	4

Table 5.4: Performance of the refined wing design.

Parameter	[0 0]	[0 90]	[90 90]	[90 0]
C_L [1]	0.26070	0.34982	0.31900	0.28106
U_d [m·s^{-1}]	∞	67.549	132.046	∞
U_F [m·s^{-1}]	49.048	55.162	52.455	46.345

From these results it can be seen that the aeroelastic stability of the wing has been improved without too much loss of effectiveness; the divergence speeds have been considerably increased, while the onset of flutter, most importantly, has also been delayed (by around 10 m·s^{-1}). Typical frequency and damping trends for the

refined wing design are shown in figure 5.8. With p an eigenvalue of the aeroelastic

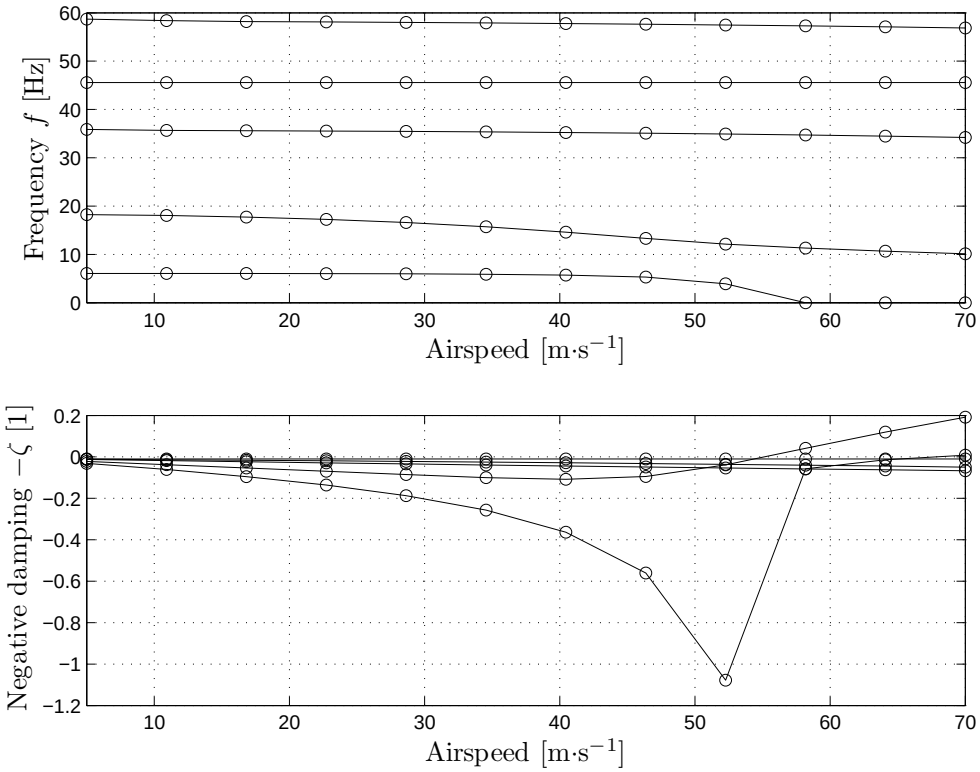

Figure 5.8: Frequency and damping trends for the first five modes of the refined wing design ([0 90] configuration).

system, each damping value used in the plot is given by $\zeta = \mathrm{Re}\{p\}/\mathrm{Im}\{p\}$ [159]. The plots show damping becomes negative for a mode at around 55 m·s^{-1} and for another mode at around 67 m·s^{-1}, and inspection of the frequency plot confirms the latter of these as a divergence mode, since the frequency reduces to zero.

5.2.5 Buckling check

It was noted in section 3.2.3 that rectangular beams of slender cross-section under a bending load are susceptible to lateral buckling failure. The analytical model developed in chapter 3 ignored this as it was intended as a simple tool for providing an insight into how the rotating spars concept could be used to improve the aerodynamic performance of a wing. However, for the experimental

wing where structural integrity is important, the following demonstrates that the spars will remain stable throughout the tests.

The critical stress at which a cantilever beam of narrow rectangular cross-section becomes unstable as a force is applied at the free end is given by [131]

$$\sigma_{cr} = 2.006 \frac{h}{l I_{y'y'}} \sqrt{E I_{z'z'} G J} \tag{5.2}$$

For an aluminium beam with Poisson's ratio of 0.33, this can be expressed approximately as

$$\sigma_{cr} = 2.460 \frac{b^2}{hl} E \tag{5.3}$$

In Eqs. 5.2 and 5.3, b and h are the cross-sectional dimensions, where $h > b$, and l is the length of the spar. Spar dimensions are given in table 5.3 and the leading- and trailing-edge h dimension is 25 mm, and all spars have a length of 755.75 mm. This gives a critical stress of 318 MPa for the two rotating spars, 81 MPa for the leading-edge spar and 13 MPa for the trailing-edge spar. The aluminium alloy that was used yields around 110 MPa, therefore the rotating spars will yield before buckling is possible, whereas the leading- and trailing-edge spars will not.

Next, it must be established whether it is possible for the critical buckling loads on each spar to be reached during the tests; this critical end force is given by [131]

$$P_{cr} = \frac{4.013}{l^2} \sqrt{E I_{z'z'} G J} \tag{5.4}$$

Again assuming a Poisson's ratio of 0.33, this can be expressed approximately as

$$P_{cr} = 0.4101 \frac{h b^3}{l^2} E \tag{5.5}$$

This gives a critical end force of 36 N for the two rotating spars, 33 N for the leading-edge spar and 2.1 N for the trailing-edge spar. The maximum theoretical lift and drag forces predicted are 40 N and 8 N respectively (see section 5.2.2). The rotating spars will therefore be closest to buckling when in the 90° position,

and it is conservatively assumed that 50% (20 N) of the lift force is carried by this spar. As a consequence of the alignment of the leading- and trailing-edge spars (see figure 5.4), buckling of these members may only occur as a result of drag loading; conservatively, it is assumed that the drag force is distributed evenly amongst the four spars and therefore the leading- and trailing-edge spars will be subject to a force of no greater than 2 N. These force and stress results are summarised in tables 5.5 and 5.6 respectively.

Table 5.5: Force requirement for lateral buckling of the spars.

Component	$P_{\max}$ [N]	P_{cr} [N]	Are forces large enough for buckling?
Rotating spars	20	36	No
Leading-edge spar	2.0	33	No
Trailing-edge spar	2.0	2.1	No

Table 5.6: Failure mode of spars.

Component	σ_Y [MPa]	σ_{cr} [MPa]	Failure mode
Rotating spars	110	318	Yield
Leading-edge spar	110	81	Lateral buckling
Trailing-edge spar	110	13	Lateral buckling

The trailing-edge spar is the only component that may be close to buckling during the tests according to these results; for this spar, lateral buckling is predicted to occur before the material yields, and the critical buckling load is only 5% higher than the maximum load expected during the tests. However, a great deal of conservatism has been employed throughout this prediction; firstly the aerodynamic loads used are theoretical maximums and not attainable. Secondly,

these loads were conservatively distributed amongst the spars; in reality the rotating spar will carry less than 50% of the lift, and the leading- and trailing edge spars will carry less than 25% of the drag forces. Furthermore, the ribs act to stiffen the lateral flexural rigidity of the spars; this effect has been conservatively ignored. Finally Eqs. 5.2 - 5.5 are correct for a force acting at the free end of the cantilever; the aerodynamic loads are distributed over the span in reality. For a uniform distribution this increases the critical force/stress to 300% of the end load prediction [131]; although aerodynamic loads are not distributed evenly across the span, this trend suggests that the critical forces/stresses will increase considerably.

5.3 Construction phase

5.3.1 Overview of the model

The wind tunnel wing model comprised of three major components:

1. The wing; this was the component of interest in the study i.e. the aeroelastic lifting-surface. The major components in the wing were two fixed spars, two rotating spars, nine ribs containing roller-bearings for mounting the rotating-spars in, cardboard rib caps for supporting the skin, and the shrink-wrap skin itself.

2. The actuator housing; this was a high-stiffness framework located inboard of the wing root that contained the two servos required to actuate the rotating spars.

3. The wing mount; this was a high-stiffness arrangement of steel plates located inboard of the actuator housing. Its purpose was to transmit loads between the wing and the load-balance.

These three components were designed such that the actuator housing and the wing mount could be considered to be rigid relative to the elastic motions of the wing structure.

5.3.2 Description of the wing

The internal structural components of the wing were all manufactured from aluminium. The nine ribs were cut from 3 mm thick sheets, and two 15.9 mm holes were then cut into each of these to provide interference fits for the 16 mm outer-diameter roller bearings. This fit was further secured with a low viscosity bearing retaining adhesive. Notches were also cut at the leading- and trailing-edges of the ribs for positioning the fixed spars. Figures 5.9a and 5.9b show these rib details. Also shown in figure 5.9a is the 3 mm thick leading-edge spar which was held in place with adhesive.

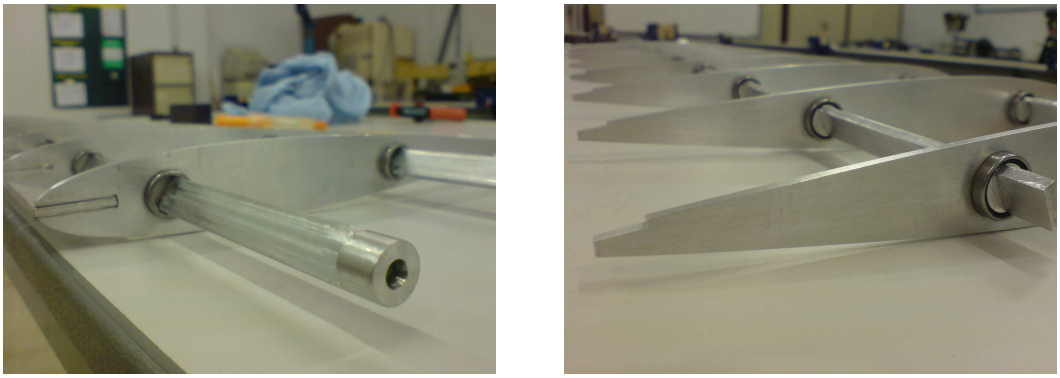

(a) Leading-edge. (b) Trailing-edge.

Figure 5.9: Rib details.

The rotating spars were each fabricated in a lathe from a single aluminium rod to create alternating cylindrical and rectangular sections, with the outside of the 12 mm diameter cylindrical sections forming the inner-race for the roller bearings. The distinction between these different sections is apparent in both figures 5.9a and 5.9b. Thin aluminium discs were also manufactured to allow the rotating spars to attach easily to the servo arms.

The complete assembled wing structure (excluding the rib caps) is shown in figure 5.10. In this figure, the 1.2 mm thick trailing-edge spar is also visible. This spar was positioned using the trailing-edge rib notches and secured with adhesive.

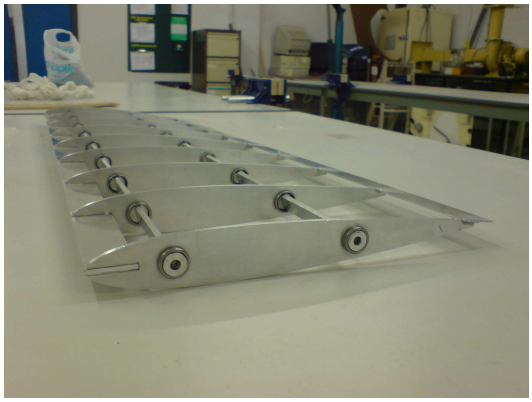

Figure 5.10: The complete internal structure excluding rib caps.

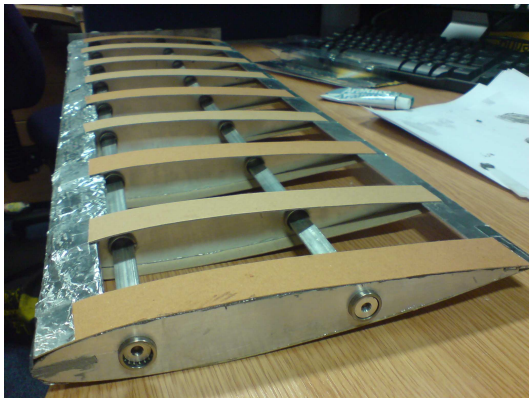

Figure 5.11: Leading-edge profile and rib caps.

High-density foam was used to maintain the leading-edge profile of the aerofoil between adjacent ribs. The foam sections were cut to a template using a hot-wire foam cutter. This was then glued to the leading-edge spar and aluminium tape was wrapped around it to strengthen the attachment further. This leading-edge profile is visible in figure 5.11.

Strips of cardboard were cut and attached to the upper and lower surfaces of the ribs to form rib caps. These rib caps are also visible on the wing in figure 5.11. Finally, the wing was covered with a shrink-wrap skin (SOLARFILM).

5.3.3 Description of the actuator housing

The primary purpose of the actuator housing was to support the two servos and to ensure that they were correctly placed and aligned to rotate the spars. The housing also transmitted the aerodynamic loads from the wing assembly to the wing mount, and was designed to be effectively rigid in comparison with the wing structure. For this reason, steel was chosen to construct the various components

of the housing that included three 10 mm thick bars and three 3 mm thick plates. A thick aerofoil-shaped piece of aluminium that was otherwise going to waste was also used. This component was bolted onto the wing mount parallel to the airflow, and the arrangement of the steel bars ensured that the wing was sweptback at an angle of 15° to the airflow. This becomes clear upon inspection of figures 5.12a and 5.12b.

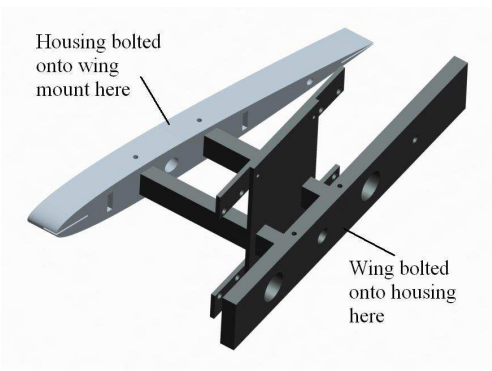

(a) CAD model.

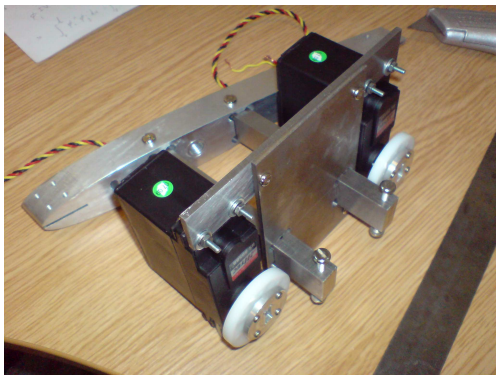

(b) Part of the housing with the servos attached.

Figure 5.12: Actuator housing.

The bars were held together by screws, and the plate assembly was then welded to the bars. The servos were secured to the plates using screws.

5.3.4 Description of the wing mount

The wing mount consisted of a framework of five 10 mm thick steel plates and was used to transmit the aerodynamic loads from the wing and actuator housing assembly to the load-balance above the wind tunnel test-section. The mount was designed to carry these loads with minimal deflection and therefore was considered to be a rigid structure relative to the wing. It is clear to see the various components of the wing mount from figure 5.13. Briefly, the assembly consists of a swept vertical plate with holes at the base (for attaching the actuator housing and therefore the wing), a horizontal plate to create the necessary horizontal offset between the balance and the wing root, an angle plate to connect and

support the horizontal and vertical plates, and two tapered vertical plates to connect the horizontal plate to the load-balance. The horizontal plate and the two tapered plates had material removed from the interior to reduce the weight of the assembly, as it was near the limit of the load-balance. The plates were attached to one-another using screws.

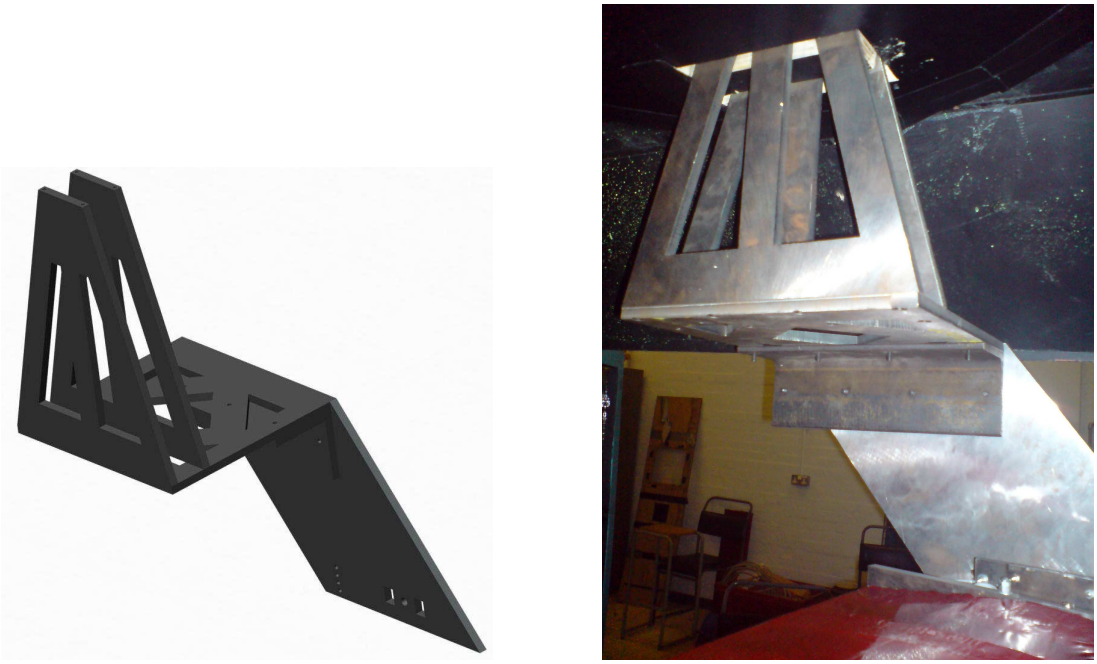

Figure 5.13: CAD model and photo of the wing mount.

5.3.5 The complete assembly

The wing was attached to the actuator housing and this was in turn attached to the wing mount. Figure 5.14 shows a CAD model of the complete assembly (excluding leading-edge profile, rib caps, and skin), as well as a photo of the complete assembly in the wind tunnel.

5.4 Equipment

In sections 5.2 and 5.3, the design and construction of the wind tunnel wing model was described. In this section, a brief overview of the other equipment

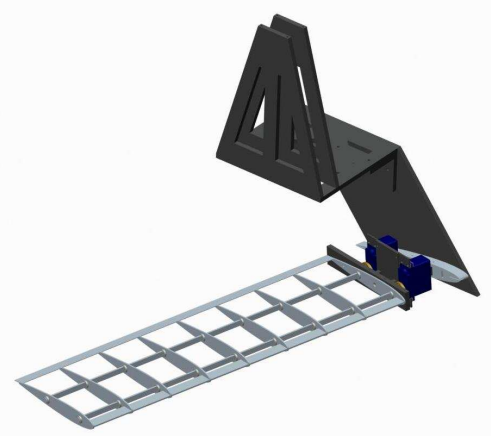

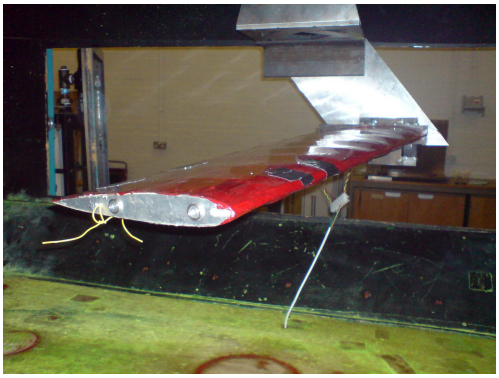

Figure 5.14: Complete wing model.

required to perform the tests shall be presented.

5.4.1 Wind tunnel

The static aeroelastic tests were performed in a low-speed wind tunnel (test-section shown in figure 5.15). The maximum speed of the tunnel was approximately 50 m·s^{-1}, although, as described in section 5.2.2, the operating speeds were limited to 0 m·s^{-1}< U < 28 m·s^{-1}, 32 m·s^{-1}< U < 34 m·s^{-1}, and 37 m·s^{-1}< U < 50 m·s^{-1} as a consequence of instabilities caused by aerodynamic resonances.

The test-section had an octagonal cross-section (see figure 5.2b for dimensions) and was 1.65 m long.

5.4.2 Load-balance

An Elven Precision Ltd six-component load-balance (visible above the wind tunnel test-section in figure 5.15) was used to measure the aerodynamic loads on the wing. The mechanical range of the six channels were; drag: ±67 N, sideforce: ±135 N, lift: ±220 N, rolling moment: ±3.5 N·m, pitching moment: ±11 N·m and yawing moment: ±3.5 N·m. All six channels used transducers with a range of ±5 V.

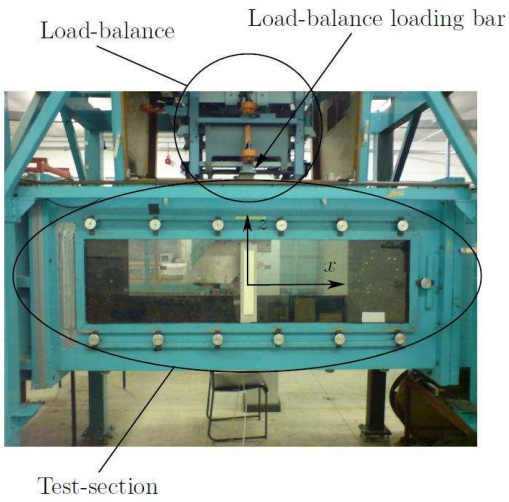

Figure 5.15: Wind tunnel test-section and load balance.

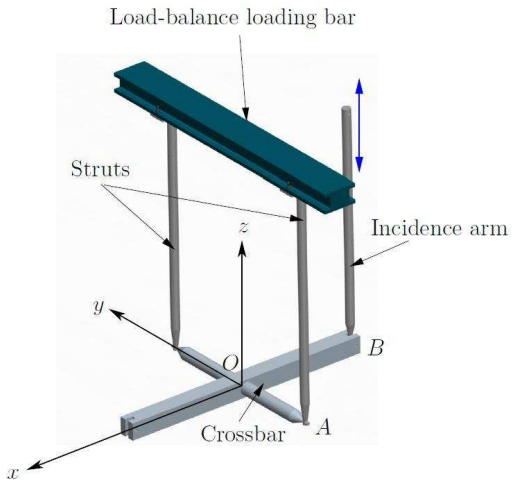

Figure 5.16: Calibration apparatus for the load-balance.

Calibration of the load-balance

To determine the relationship between the voltage output of the transducers and the load input applied to them, and also to establish whether cross-coupling between the six channels was significant or not, calibration of the load balance was performed (CAD model of calibration equipment shown in figure 5.16).

The input loads can be related to the voltage from the transducers using

$$\begin{bmatrix} P_x & P_y & P_z & P_p & P_q & P_r \end{bmatrix}^T = \boldsymbol{C} \begin{bmatrix} V_x & V_y & V_z & V_p & V_q & V_r \end{bmatrix}^T \tag{5.6}$$

which can be written as

$$\boldsymbol{p} = \boldsymbol{C}\boldsymbol{v} \tag{5.7}$$

where V_i is the output voltage from the transducer associated with direction i, P_i is the input load in direction i, and the six aerodynamic directions are x (drag), y (sideforce), z (lift), p (rolling moment), q (pitching moment), and r (yawing moment). $\boldsymbol{C}$ is a 6×6 calibration matrix, and for a correctly aligned load-balance,

will be diagonal. This was found, approximately, to be the case with

$$\boldsymbol{C} = \begin{bmatrix} 17.295 & 0 & 0 & 0 & 0 & 0 \\ 0 & -36.190 & 0 & 0 & 0 & 0 \\ 0 & 0 & -54.713 & 0 & 0 & 0 \\ 0 & 0 & 0 & -1.5098 & 0 & 0 \\ 0 & 0 & 0 & 0 & -3.0602 & 0 \\ 0 & 0 & 0 & 0 & 0 & -1.2945 \end{bmatrix} \tag{5.8}$$

5.4.3 Laser displacement system

A KEYENCE laser displacement system was used to provide high accuracy measurements of the wing deflections. The system consisted of two sensor heads (LK-501 using a 690 nm class 3B laser), each with a controller (LK-2501) and a 24 V DC power supply. The system was capable of sampling at 977 Hz (sampling period of 1024 μm) and was set to operate in its long-range mode (250 - 750 mm). The output signal was ± 5 V providing a sensitivity of 50 mm$\cdot$V^{-1}.

5.4.4 Servos

Servos were chosen to actuate the rotating spars because they can provide accurate rotational positioning, offer large torque ranges for a relatively small size, and are easily available off-the-shelf to meet a variety of specifications. Since the aim of these tests was purely a demonstration of the adaptive internal structures concept and its ability to optimise the aerodynamic performance, no consideration was given to minimising weight etc., and therefore servos were chosen that provided the maximum output torque possible whilst being able to fit within the wing chord. To meet these specifications, two Hitec HS-805BB servos were used and can be seen in figure 5.12b.

Control of the servos

The servos each had three input wires: power (4.8 - 6.0 V DC), signal (3 - 5 V peak-to-peak square wave), and a 0 V common return. It was the signal that required careful consideration to achieve accurate control of the servos.

The pulse-width of the control signals controlled the position of the servos, with a neutral (central) position quoted as 1500 μs. Figure 5.17 describes pulse wave control. For the majority of the period of the signal T, the system was inactive. The servos required a signal every T seconds to control them. This signal was a short duration square wave pulse of pulse-width τ. The position of the servos varied linearly with τ.

For these particular servos, the period of the signal was 20 ms (i.e. the pulse refreshed at 50 Hz), and it was found that to increment the servos by 1° required an increment in the pulse-width of 9.222 μs.

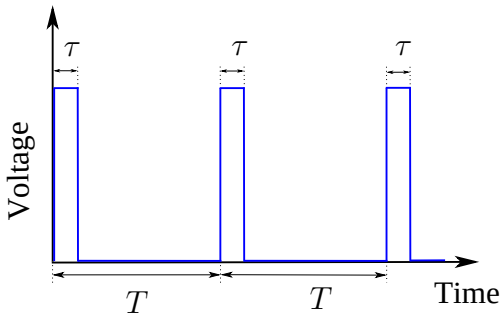

Figure 5.17: Pulse wave signal.

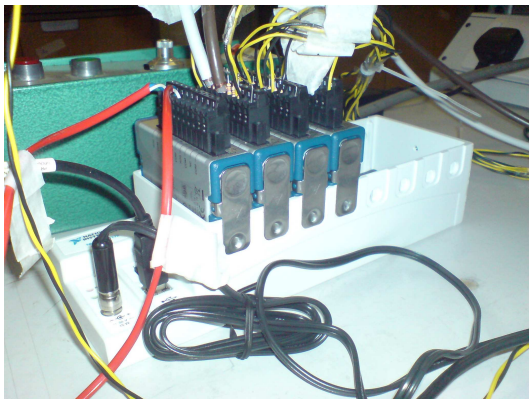

Figure 5.18: Data acquisition hardware.

Performance of the servos

The servos accepted a large range of pulse-widths, enabling the required 90° rotation to be easily achieved. A moderately high actuation frequency was required if roll-control was to be realised using this concept, and the servos did provide this by being capable of rotating through 90° in 0.21 s under zero-load conditions, and

although not measured precisely, under the maximum aerodynamic loads during test conditions this range of motion was achieved in well under a second. The maximum torque provided by each of the servos was 2.354 N·m.

5.4.5 Data acquisition hardware

The input and control signals were interfaced to a computer via National Instruments™ data acquisition hardware. This consisted of a cDAQ-9172 8-slot chassis, a NI 9263 4-channel analogue output module, and three NI 9215 4-channel simultaneous sampling differential analogue input modules. All modules used 16-bit resolution and could sample at up to 100 kS·s^{-1} per channel. The four modules are clearly visible occupying four of the chassis slots in figure 5.18.

The various input and output signals to the data acquisition hardware are detailed in table 5.7. Although lift and drag were the only aerodynamic loads of interest in the tests, all six components were recorded.

Table 5.7: Data acquisition hardware connections.

Slot 1 (Analogue output)		Slot 2 (Analogue input)	
Channel	Signal	Channel	Signal
1	Forward servo	1	Pressure transducer
2	Rear servo	2	Forward laser
3	Unused	3	Rear laser
4	Unused	4	Drag
Slot 3 (Analogue input)		**Slot 4 (Analogue input)**	
Channel	Signal	Channel	Signal
1	Sideforce	1	Yawing moment
2	Lift	2	Unused
3	Rolling moment	3	Unused
4	Pitching moment	4	Unused

5.4.6 Data acquisition software

All the tests were controlled and monitored using a computer. MATLAB® and LabVIEW™ were used together to write and operate the control program for the tests. This was interfaced to the data acquisition hardware via the appropriate drivers.

5.4.7 Other equipment

An amplified pressure transducer with a range of 1500 Pa was used to convert the wind tunnel pitot pressure into an electrical signal in order to monitor the dynamic pressure and therefore the airspeed of the tunnel. Calibration of the

pressure transducer revealed that

$$U = 17.638\sqrt{V} \tag{5.9}$$

where U is the test-section airspeed in $m{\cdot}s^{-1}$ and V is the amplitude of the output signal in volts.

A dual power supply was used to provide the two servos (6 V) and the pressure transducer (12 V) with power.

As can be seen in figure 5.2a, the test-section had removable sections; two side panels, a large circular roof section, and the entire floor section (not shown in figure 5.2a). The floor and side panels were removable in order to gain access to the interior of the tunnel, and the side panels were also interchangeable with window panels for observing tests. The circular hole in the roof was necessary to enable the load-balance to be yawed i.e. as the balance yawed, so too did the wing mount and wing. However, to seal the section, a disc was placed in the hole and this disc was attached to the balance frame and therefore rotated with the balance as it yawed. As a consequence, the disc design was dependent upon the wing mount design, and so a disc had to be made.

In the photo in figure 5.13, the outline of the disc can be seen, and the wing mount passes through two slots in it to connect to the balance. The laser sensor heads were attached to the disc, and slots were also cut in the disc to allow the laser to transmit through onto the wing surface.

5.5 Tests

5.5.1 Determination of airspeed range and integrity of measurements

Before commencing any of the planned tests, the operational envelope of the wing had to be established; the wing was intended to operate over the range

0 m·s^{-1}$\leq U \leq$ 25 m·s^{-1} (see section 5.2.2) but it was expected that below a certain speed, the variations in the aeroelastic loads and deflections with the spar orientations would be too small to establish trends due to low signal-to-noise ratios. Also, above a certain airspeed there was the possibility that the servos may not be able to overcome the stiction forces on the spars caused by large bending deflections.

Therefore, over a range of airspeeds with the spars at the [0 0], [0 90], [90 0] and [90 90] configurations (i.e. the extremes) data was collected and the wing was observed. It was found that below about 17 m·s^{-1} trends were difficult to observe due to very small ranges in loads and deflections, and above 23 m·s^{-1} the servos struggled to position the spars at the intended orientation due to the large stiction forces. To ensure that neither of these limitations would cause problems during testing, the airspeed range for testing was set at 18 m·s^{-1}$\leq U \leq$ 22 m·s^{-1}, which represented a 49% change in the dynamic pressure during testing.

The wing's design angle of incidence was 5°; after setting up the test rig an inclinometer measured the actual angle of incidence as 5.3° which was considered to be close enough to the design value not to cause problems.

To gain an insight into the expected relative signal-to-noise ratios of the input channels, at the maximum airspeed of 22 m·s^{-1} the forward and rear spar orientations, ϕ_f and ϕ_r respectively, were varied between 0° and 90° using 7.5° increments in order to establish the maximum and minimum measurements from each channel, and these were used to calculate the range of data for each channel. These ranges are shown in table 5.8 as percentages of the maximum range of the transducer for the respective channels e.g. at 22 m·s^{-1} the voltage output from the transducer associated with the lift channel varied by up to 0.0881 V as the spars were rotated; this was 0.881% of the 10 V range of the transducer.

Table 5.8: Typical variation in signal voltage as a percentage of transducer range at 22 m·s^{-1}.

Channel	ΔV [%]
Fwd laser	7.10
Rear laser	7.98
Drag	0.430
Side	0.393
Lift	0.881
Roll	0.211
Pitch	0.017
Yaw	0.916

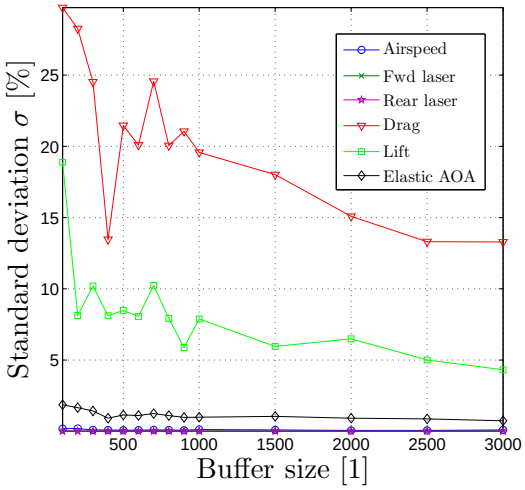

Figure 5.19: Variation of standard deviation of channels with buffer size at 22 m·s^{-1}.

This table highlights two things; firstly, that in general the signal-to-noise ratio of the trends was anticipated to be relatively poor, since all channels vary by less than 8% of their transducer's range. The other significant conclusion to draw from the table is that all the load channels varied by less than 1% of their transducer's range and therefore it was expected that the trends of these measurements would be considerably more noisy than the trends of the deflections measured by the laser displacement system. Ideally, the measurement range from all channels should have been around 90% of the transducer ranges, but unfortunately the tests had to be performed with the equipment available.

In order to improve the signal-to-noise ratio of the trends, averaging of the data had to be performed. To minimise the time required collecting data during the tests, an investigation was performed to establish how long the data had to be averaged for to reduce the noise to a level where the trends became recognisable. The channels of interest in the test were the lift and drag force measurements,

the pressure transducer (for the airspeed) and the two laser displacement measurements. One laser sensor head was used to measure the leading-edge bending deflection near the tip of the wing, whilst the other sensor head measured the trailing-edge bending displacement at the same span location. Therefore, it was possible also to measure the change in angle of incidence of the wing at this spanwise location. To perform the investigation:

1. At an airspeed of 22 $\text{m}\cdot\text{s}^{-1}$, with a buffer size of 100 samples, and at a resolution of 100 Hz the mean of each parameter of interest was found.

2. Step 1 was repeated 20 times to find the standard deviation for each channel as a percentage of the maximum range of the channel at that airspeed (except U, the range was 0 $\text{m}\cdot\text{s}^{-1} \leq U \leq 22$ $\text{m}\cdot\text{s}^{-1}$).

3. The buffer size was increased and steps 1 and 2 were repeated.

4. Step 3 was repeated for all buffer sizes considered.

Figure 5.19 shows the results. Confirming the predictions, the drag and lift data contained the most noise, with the other channels having an acceptable signal-to-noise ratio for all buffer sizes considered. Clearly, the driver for achieving acceptable results was reducing the noise component in the drag signal. However, it can be seen that the standard deviation of the drag appears to converge at around 13% and requires averaging over 25 - 30 s to achieve this. There was a strong argument to average over a much shorter time, and by doing so only worsening the data slightly. For this reason, a buffer size of 500 was chosen (standard deviation in drag of around 20%, but only 5 s of averaging required). A third-order lowpass Butterworth filter was also used to improve the signal-to-noise ratio.

5.5.2 Effect of non-aerodynamic surfaces on the loads

Before any aerodynamic data relating to the wing could be recorded, the effect on the loads of the wing mount, actuator housing, and servos had to be taken into account. To do this, the wing mount, actuator housing and servos (see figure 5.20a) were placed in the test-section and the airspeed was incremented from zero to just above the maximum test speed. At each airspeed the voltage output from the load-balance was noted. This procedure was performed three times to average out the data. The results are shown in figure 5.20b.

(a) CAD model of the wing mount with actuator housing and servos attached.

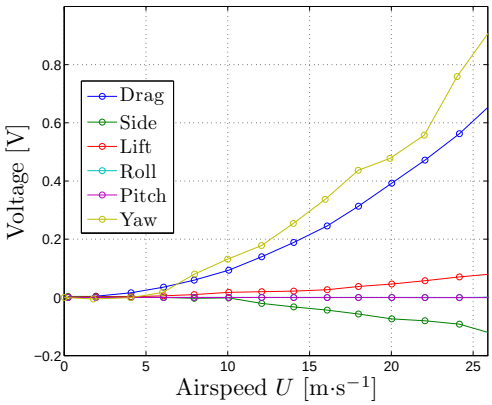

(b) Load-balance voltages produced by the wing mount only over a range of airspeeds.

Figure 5.20: Calibration of the wing mount, actuator housing and servos.

The results demonstrate that the wing mount, actuator housing and servos most noticeably generated a drag force and yawing moment. The yawing moment was caused by the drag force, since the assembly was not at the centre of the test-section. These results were as expected, given the poor aerodynamic shape of the actuator housing and servos in particular, which gave rise to a large profile drag. A spline interpolation was then used based on this data to determine the required offset for all channels at any given airspeed.

5.5.3 Structural parameter tests

Prior to performing aeroelastic tests on the wing, some structural tests were performed to gain an insight into the extent to which the rotating spars impact various structural parameters. Due to the time-consuming nature of this task, the tests were only performed at combinations of spar orientations 0°, 30°, 60° and 90°, and were repeated three times to average out the data. The results of these were also compared with results of analyses performed using the finite element model described in section 5.2.4.

Chordwise position of the elastic axis

Details of a method to establish the chordwise position of the elastic axis were given in section 4.2.1 and involves loading the wing at the leading- and trailing-edge and measuring the torsional deflection. This was performed for the test wing by hanging weights from it, and for the FE model by using a linear static solution sequence (SOL 101) [11].

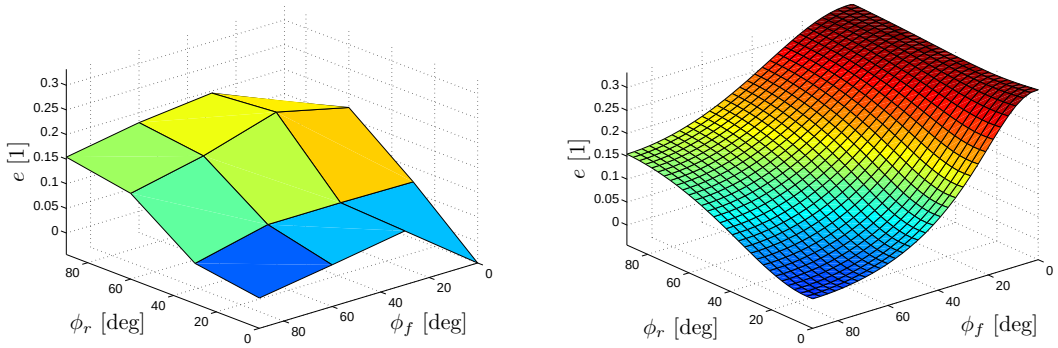

(a) Tests. (b) FEA prediction.

Figure 5.21: Variation of wing elastic axis position with spars' orientations.

The results of the test were inconclusive and are shown in figure 5.21a. Some values agree with the predicted values (figure 5.21b). However, for some spar configurations (in particular when $\phi_f = 0°$), the values differ from that of the FEA (finite element analysis) prediction. The analytical prediction suggests the ability to alter e (the dimensionless chordwise position of the elastic axis aft of the

aerodynamic centre) over the range $0 \leq e \leq 0.35$. In reality, the tests suggested a smaller range of $-0.05 \leq e \leq 0.2$. The trend established in the FEA prediction agrees well with the trend shown in section 4.2.1 (the study with the assumed modes model).

Flexural rigidity

Details of a method to establish the wing's flexural rigidity were given in section 4.2.1 and involves loading the wing tip at the elastic axis with a vertical force P in order to produce a pure bending deflection and measuring the resulting tip bending deflection, h_{tip}. This was performed for the test wing by hanging weights from it, and for the FE model by using a linear static solution sequence (SOL 101) [11]. Eq. 4.2 was then used to calculate the flexural rigidity i.e.

$$K_h = \frac{Pl^3}{3h_{\text{tip}}} \tag{4.2}$$

where l is the length of the wing from root to tip.

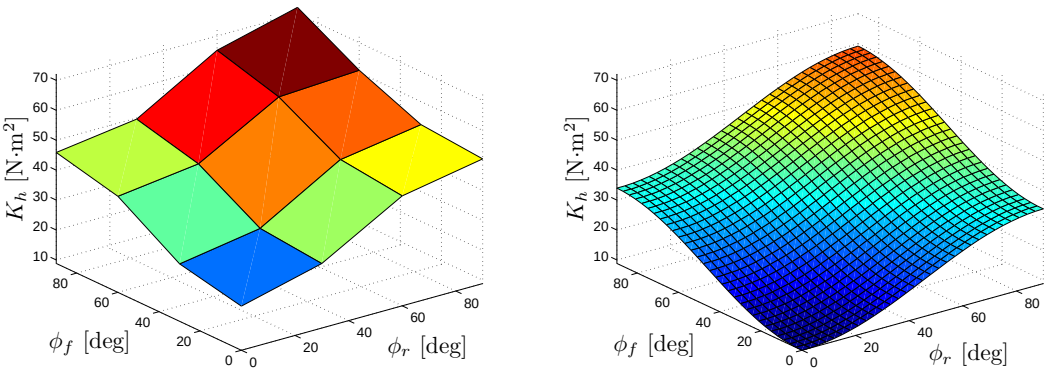

(a) Tests. (b) FEA prediction.

Figure 5.22: Variation of wing flexural rigidity with spars' orientations.

Figure 5.22 shows the results of both the analytical prediction and the tests. The test results agree well with the predicted results. The only noticeable difference is that the test results are offset by approximately +10 N·m^2 relative to the analytical results. This additional flexural rigidity is most likely due to the

shrink-wrap skin on the test wing, and to a lesser extent, from the leading-edge foam, neither of which were represented in the finite element model. The trends in both these graphs agree well with with the trend shown in section 4.2.1 and can be explained using a similar argument. Figure 5.22a shows that the rotating spars adaptive internal structure concept enables a change in the bending stiffness of this wing of in excess of 200%.

Torsional rigidity

Details of a method to establish the wing's torsional rigidity were given in section 4.2.1 and involves loading the wing tip with a moment, M, in order to produce a pure torsional deflection and measuring the resulting tip torsional deflection, θ_{tip}. This was performed for the test wing by hanging weights from it, and for the FE model by using a linear static solution sequence (SOL 101) [11]. Eq. 4.2 was then used to calculate the torsional rigidity i.e.

$$K_\theta = \frac{Ml}{\theta_{\text{tip}}} \tag{4.7}$$

where l is, as before, the length of the wing.

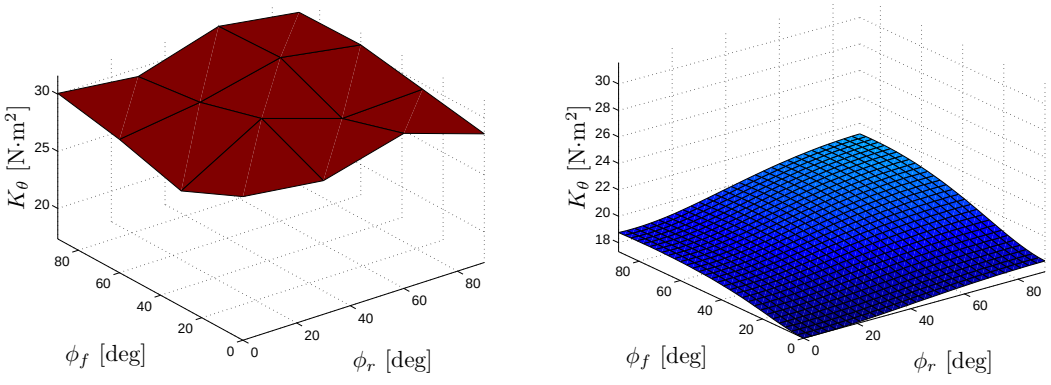

(a) Tests. (b) FEA prediction.

Figure 5.23: Variation of wing torsional rigidity with spars' orientations.

The results of the test were inconclusive and are shown in figure 5.23a. Clearly, the test results lack a trend, unlike the FEA prediction (figure 5.23b).

This can be most easily explained by considering that the torsional rigidity of the wing does not alter much relative to the flexural rigidity; therefore, noise becomes much more apparent in the data. The trend established in the FEA prediction agrees well with the trend shown in section 4.2.1 (the study with the assumed modes model).

First bending frequency

To investigate the effect of the rotating spars on the first bending frequency of the wing, dynamic tests were performed. This was performed for the test wing by performing 'twang' tests (i.e. pulling on string attached to the wing for as short a time as possible in order to achieve as close to an impulse response as possible) and recording the resulting displacement response, and for the FE model by using a normal modes solution sequence (SOL 103) [11]. A fast Fourier transform (FFT) analysis of the time history then allowed the frequency content of the response to be probed. Unfortunately, the responses were too noisy to establish obvious trends in all modes other than the first (bending).

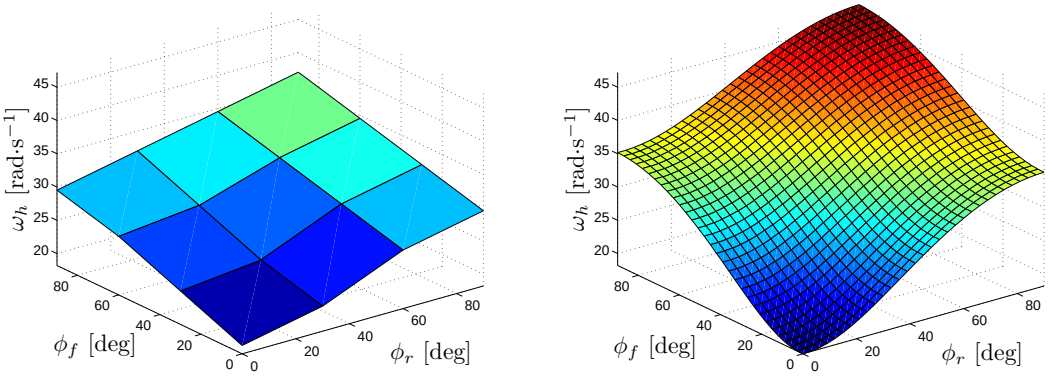

(a) Tests. (b) FEA prediction.

Figure 5.24: Variation of first bending frequency with spars' orientations.

Figure 5.24 shows that the test results agree well with the analytically predicted results. There is a slight amplitude discrepancy between the two that is more noticeable at higher frequencies. This difference indicates that the predicted

first bending frequency is slightly too high.

5.5.4 Aeroelastic parameter tests

To carry out the aeroelastic parameter study on the wing, data was collected for all channels at all spar configurations (ϕ_f and ϕ_r were varied between 0° and 90° using 7.5° increments) over a range of airspeeds (18, 19, 20, 21, and 22 m·s^{-1}). This was repeated ten times at each airspeed to offer improved averaging; this was considered necessary due to the low signal-to-noise ratio of the drag channel in particular. Similar analyses were performed using the finite element model described in section 5.2.4 with a static aeroelastic solution sequence (SOL 144) [116]. The results are categorised as deflection parameters and loads parameters, and for brevity only the plots of $U = 22$ m·s^{-1} are presented; at all other test airspeeds the trends were similar, although over a smaller range.

Deflections

Figures 5.25 and 5.26 show the leading- and trailing-edge tip bending deflections for the wing at 22 m·s^{-1}. Figure 5.27 shows the elastic angle of incidence at the tip for these tests.

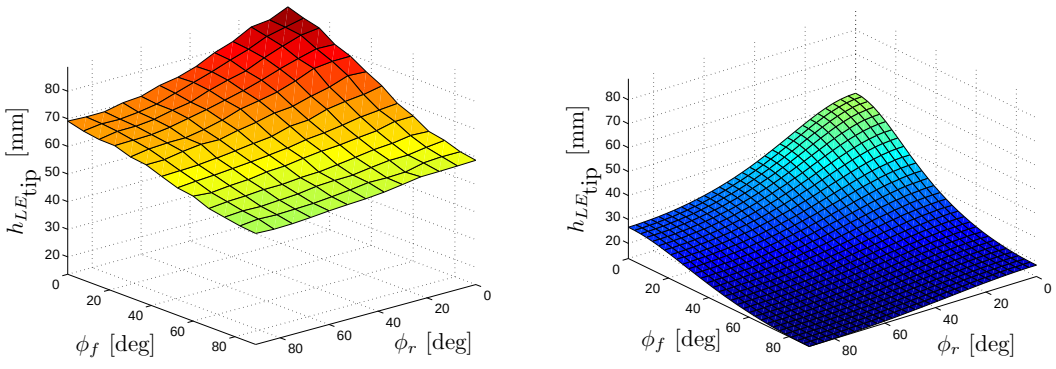

(a) Tests. (b) FEA prediction.

Figure 5.25: Variation of wing leading-edge tip bending deflection with spars' orientations at 22 m·s^{-1}.

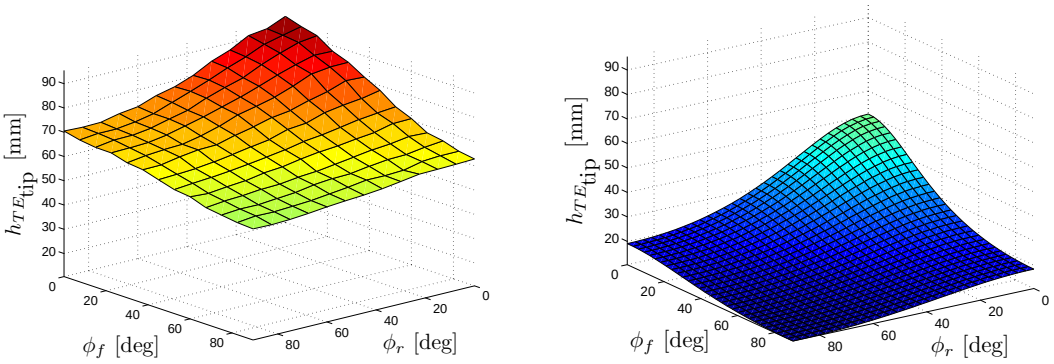

(a) Tests. (b) FEA prediction.

Figure 5.26: Variation of wing trailing-edge tip bending deflection with spars' orientations at 22 m·s^{-1}.

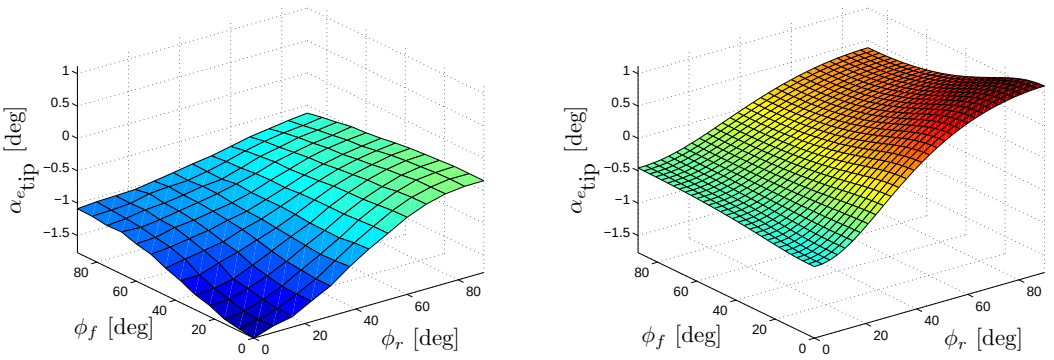

(a) Tests. (b) FEA prediction.

Figure 5.27: Variation of tip elastic angle of incidence with spars' orientations at 22 m·s^{-1}.

Qualitatively, the tests agree well with the analytical predictions, as well as with the analytical parameter study that was performed in section 4.2.2.

Quantitatively however, the test results differed slightly from the FEA predictions. This was primarily due to the effect of gravity during the tests and the differences between the methods used to zero the deflections; for the tests, the displacements were referenced to the wing in the [90 90] configuration at zero airspeed which represented a slightly negative bending deflection due to gravity. Furthermore, gravity acted to twist the wing slightly nose-down, therefore reducing the angle of incidence by an increasing amount along the span. These

effects were considered to be relatively insignificant in terms of the aerodynamic behaviour and therefore no attempt was made to capture them in the analytical model, which ignored initial deflections due to gravity. It does, however, explain why the predictions of the bending deflections were too low and why the predictions of the elastic angle of incidence were too high. Importantly though, the data is approximately offset by a fixed amount over all spar configurations, and therefore it can be seen that the wing tip bending deflections could be varied by up to around 40 - 50 mm at 22 m·s^{-1}, and that the wing tip angle of incidence could be varied by up to approximately 1.5° which is significant in terms of aerodynamic performance.

Loads

Figure 5.28 shows the variation of the lift coefficient at 22 m·s^{-1} for all spar configurations. Once again, the test trend agrees well with the analytically predicted trend as well as with the trend established in section 4.2.2. Quantitatively, the lift coefficients from the tests also agree well with the predicted results, ranging from approximately 0.266 to 0.338, which represents a substantial 26.7% change in lift.

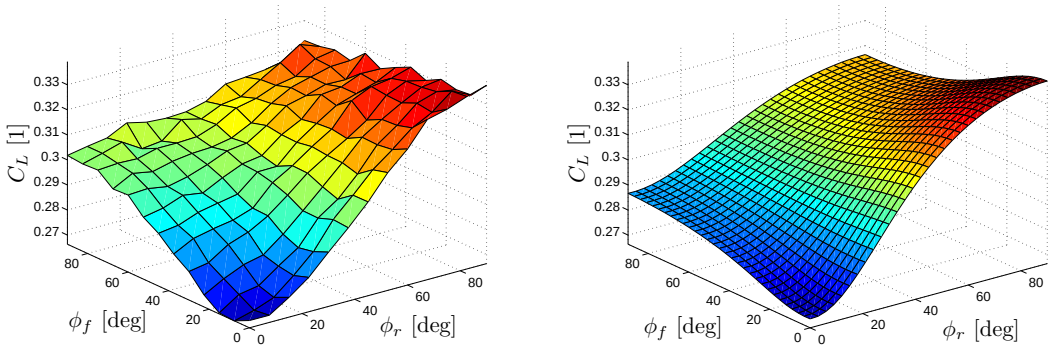

(a) Tests. (b) FEA prediction.

Figure 5.28: Variation of C_L with spars' orientations at 22 m·s^{-1}.

The relatively poor signal-to-noise ratio in the drag measurements is apparent in figure 5.29, reinforcing the findings presented in figure 5.19. No drag modelling

is offered by NASTRAN™ therefore a quantitative comparison between the FE model results and the test results could not be performed for the drag. The trend, however, agrees well with the trend of induced drag identified in the parameter study in section 4.2.2 (study using the assumed modes model). At 22 m·s^{-1} it was possible to alter the drag coefficient of the wing by about 17.1%.

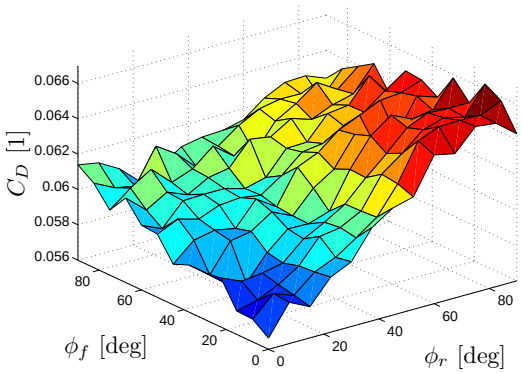

Figure 5.29: Variation of C_D with spars' orientations at 22 m·s^{-1} (tests only).

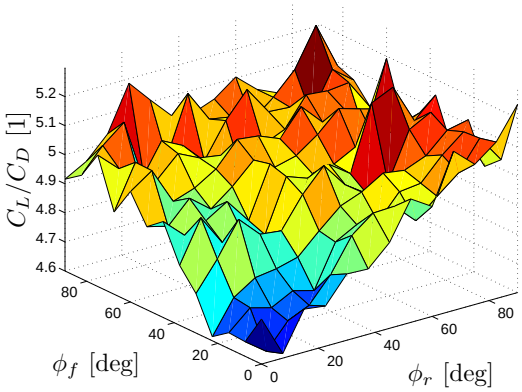

Figure 5.30: Variation of C_L/C_D with spars' orientations at 22 m·s^{-1} (tests only).

This was also the case for the lift-to-drag ratio; no FEA prediction could be made due to the lack of drag information, but the test trend (see figure 5.30) follows the trend of the inviscid lift-to-drag ratio established in section 4.2.2. The high level of noise in the signal is even more apparent in this plot, and makes it difficult to estimate actual values. However, the results suggest that the adaptive internal structures concept provides the ability to alter the lift-to-drag ratio of this wing by 10 - 15%, which represents a significant range.

5.5.5 Control of the loads via a regression model

To achieve drag reduction using the concept required a control algorithm that used the reference trim lift coefficient value $C_{L_{\text{ref}}}$ as an input and output the required spar orientations that would achieve this value whilst simultaneously minimising drag.

Initial efforts to realise this objective concentrated on using the existing data from the parameter study to curve fit for the entire data range, rather than a feedback approach, since it is a relatively time effective method, requiring only an initial population of a data set, and therefore real-time control could be achieved almost instantaneously. Due to the random noisy content of the data, it was decided that smoothing would be more appropriate than interpolating. Therefore, a polynomial regression model was fitted in a least squares sense to both the lift and drag coefficient data presented in section 5.5.4. It was found that a fourth-order polynomial was adequate, with the forward and rear spar orientations as well as the airspeed as the three independent variables, and C_L and C_D as the dependent variable in each of the models i.e.

$$C_L = f\left(\phi_f, \phi_r, U\right) \tag{5.10}$$

and

$$C_D = g\left(\phi_f, \phi_r, U\right) \tag{5.11}$$

where f and g are the lift and drag regression functions respectively. Figure 5.31 illustrates this for the data recorded at 22 m·s^{-1}, with the actual measured data superimposed on top of the regression surface.

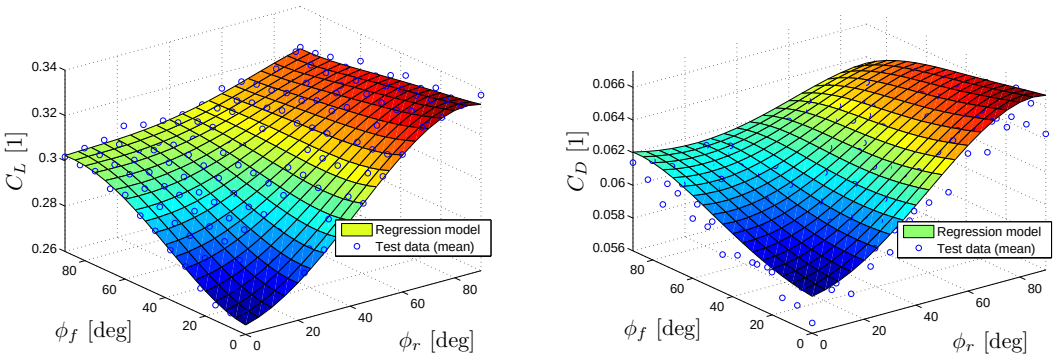

(a) Lift coefficient.

(b) Drag coefficient.

Figure 5.31: Polynomial regression model and actual data for the lift and drag at 22 m·s^{-1}.

Trimming the wing

The first task was to attempt to trim the wing i.e. regardless of drag, alter either ϕ_f or ϕ_r to achieve a desired reference lift coefficient value $C_{L_{\text{ref}}}$. For simplicity, only one of the spar orientations was altered at a time initially. For a fixed forward spar orientation, the routine can be described as follows:

1. The current airspeed U and chosen fixed forward spar orientation ϕ_f were input into the regression model such that Eq. 5.10 became

$$C_L = f(\phi_r) \tag{5.12}$$

2. This was then rearranged and the desired reference trim lift coefficient value was input to give

$$C_{L_{\text{ref}}} - f(\phi_r) = 0 \tag{5.13}$$

3. The rear spar orientation was then adjusted to correspond with the root of Eq. 5.13. If multiple roots were found within the range $0° \leq \phi_r \leq 90°$, any could be used as they all produced valid solutions.

4. Steps 1 - 3 were repeated continually in order to attempt to maintain $C_{L_{\text{ref}}}$.

For a fixed rear spar orientation, the procedure was similar. This was performed for both of these approaches using a variety of $C_{L_{\text{ref}}}$ values and a variety of fixed ϕ_f or ϕ_r values.

The results are shown in figure 5.32. The vertical red lines indicate the boundaries of the regression model. The error is presented here as a percentage of the possible range of C_L at 22 m·s^{-1}. From these results it is clear to see that this approach was unsuccessful; despite the regression model fitting the original data quite well, it appears to be offset significantly from the new data, with errors of 10 - 40% within the airspeed range. These large errors were most likely the result of the significant noise in the data that affected both the regression model and the live data.

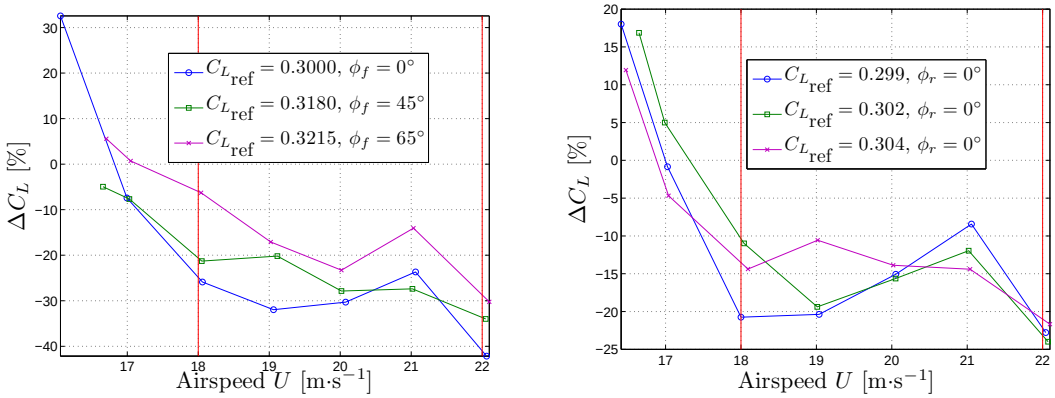

(a) ϕ_f fixed. (b) ϕ_r fixed.

Figure 5.32: Difference between actual and reference lift using regression model to trim the wing over a range of airspeeds.

Minimising the drag at the trim state

With the failure of the regression approach to trimming the wing, success was not expected in achieving the additional step of minimising drag whilst simultaneously trimming the wing, also using the regression approach. However, this was attempted in order to rule it out as a possibility. The procedure used can be summarised as follows:

1. For a large resolution of ϕ_f and ϕ_r within the ranges $0° \leq \phi_f, \phi_r \leq 90°$ and a large resolution of U within the range 18 m·s^{-1}$\leq U \leq$ 22 m·s^{-1}, Eqs. 5.10 and 5.11 were used to calculate all the corresponding values of C_L and C_D respectively.

2. The current airspeed U was then used to eliminate all of those solutions that fell outside the range of data $U \pm \delta U$, where δU was a sufficiently small tolerance of the airspeed.

3. The reference lift coefficient $C_{L_{\text{ref}}}$ was then used to eliminate all of those remaining solutions that fell outside the range of data $C_{L_{\text{ref}}} \pm \delta C_L$, where δC_L was a sufficiently small tolerance of the reference lift coefficient.

4. The remaining solutions were inspected to find the one corresponding to a

minimum C_D. The associated ϕ_f and ϕ_r values were then used to control the servos.

5. Steps 2 - 5 were repeated continually in order to attempt to maintain $C_{L_{\text{ref}}}$ subject to minimising C_D.

This was performed for two different reference lift coefficient values. The results are shown in figure 5.33. Once again, the vertical red lines indicate the boundaries of the regression model, and the error in C_L is presented as a percentage of the possible range of C_L at 22 m·s^{-1}.

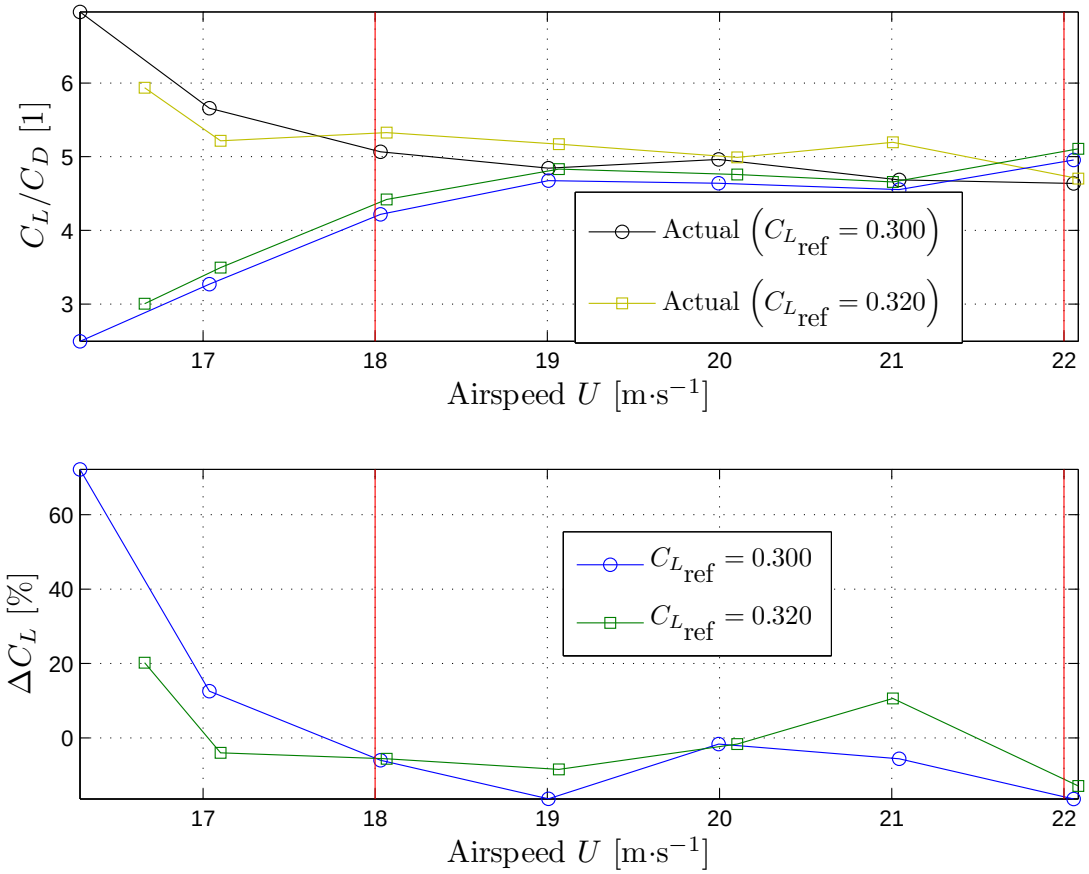

Figure 5.33: Difference between actual and reference lift-to-drag ratio and lift coefficient using regression models to minimise the drag at the trim state over a range of airspeeds.

As expected, the test has proven the method to be unsuccessful, with errors of up to 20% in the lift-to-drag ratio. Given the poor results of the previous task,

the error between the actual and reference lift coefficient values is surprisingly low (within ±10%). Despite this, there is a clear lack in the robustness associated with this approach. This was further demonstrated in the next task which replaced the load measurements with data from the laser displacement system.

5.5.6 Control of the deflections via a regression model

The results of section 5.5.5 showed that the regression model approach to accurately controlling the wing loads failed. However, the presence of poor signal-to-noise ratios in the measurements of the loads meant that it was not clear whether the failure was the result of this or the combined result of this as well as a lack of robustness in the approach.

To investigate this, the noisy input signals to the algorithm were eliminated by replacing them with data from the laser displacement system; more specifically, a polynomial regression function, h, was fitted in a least squares sense to the tip elastic angle of incidence data and is defined as

$$\alpha_{e_{\text{tip}}} = h\left(\phi_f, \phi_r, U\right) \tag{5.14}$$

and a procedure similar to the trim procedure outlined in section 5.5.5 was used to adjust ϕ_r in order to attain $\alpha_{e_{\text{tip}_{\text{ref}}}}$, the reference tip elastic angle of incidence. Large errors between the actual measured value of $\alpha_{e_{\text{tip}}}$ and the reference (target) value would indicate failure of the method. Since the input data (deflections) was relatively free from noise, this failure could be attributed to the robustness of the regression model itself.

Maintaining a reference angle of incidence

At a fixed airspeed and with a fixed forward spar orientation, the regression model was used to find the required ϕ_r to obtain a reference $\alpha_{e_{\text{tip}}}$. The actual value of $\alpha_{e_{\text{tip}}}$ measured by the lasers was also recorded. This was repeated over

a range of $\alpha_{e_{\text{tip}_{\text{ref}}}}$ for three different airspeeds.

As a separate task the above was performed with a single reference $\alpha_{e_{\text{tip}}}$ over a large range of airspeeds. The results of both of these tasks is shown in figure 5.34.

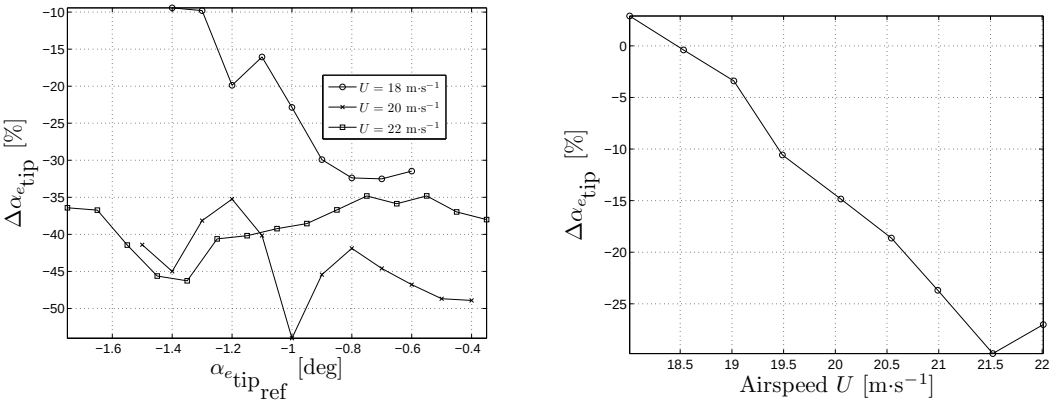

(a) Variation with reference $\alpha_{e_{\text{tip}}}$.

(b) Variation with airspeed.

Figure 5.34: Variation of error in $\alpha_{e_{\text{tip}}}$ with reference $\alpha_{e_{\text{tip}}}$ and airspeed using a regression model approach.

Figure 5.34 is significant as it shows that the method failed, since the errors were generally between 35% and 55% for the variation of $\alpha_{e_{\text{tip}_{\text{ref}}}}$, and increasing up to 30% with airspeed, which is unacceptable. Since the deflection input data to the regression model had a relatively high signal-to-noise ratio, the conclusion was made that the regression approach lacked robustness and therefore was not appropriate for controlling the wing loads.

5.5.7 Control of the loads via an optimisation approach

In section 5.5.6 it was demonstrated that a regression approach could not be used for controlling the wing loads, even if high signal-to-noise ratios in the load measurements were available. The next attempt to control the loads used the simple steepest descent optimisation routine described in section 4.5.4. However, unlike the analytical model, the test rig did not provide the capability of real-time control of the rigid angle of incidence to trim the wing, and therefore this

was achieved by varying ϕ_f and ϕ_r, a problem that was also intended to be solved using the optimisation algorithm. In summary, this approach to controlling the wing loads used an optimisation routine (trim) inside another optimisation routine (maximisation of lift-to-drag ratio).

The first part of this section presents results of the inner optimisation loop only i.e. trim, while the second part presents results of the outer optimisation loop only i.e. maximisation of the lift-to-drag ratio, C_L/C_D, with no reference lift value. Due to the failure of both of these tasks, and the time-consuming nature of optimisation approaches, no attempt was made to investigate the full drag reduction at the trim state.

Trimming the wing

ϕ_f and ϕ_r were varied in a steepest-descent optimisation algorithm with minimising $|C_L - C_{L_{\text{ref}}}|$ as the objective function (the steepest descent algorithm was explained in detail in section 4.5.4), where C_L was the live lift coefficient measured by the load balance. Initially, the input was varied in one direction at a time only (i.e. either ϕ_f or ϕ_r). In order to test the robustness of the approach, the airspeed was varied and the response of C_L and the spar orientations were monitored, and then $C_{L_{\text{ref}}}$ was varied and the response of C_L and the spar orientations were monitored. For brevity, the results of varying ϕ_r only are shown.

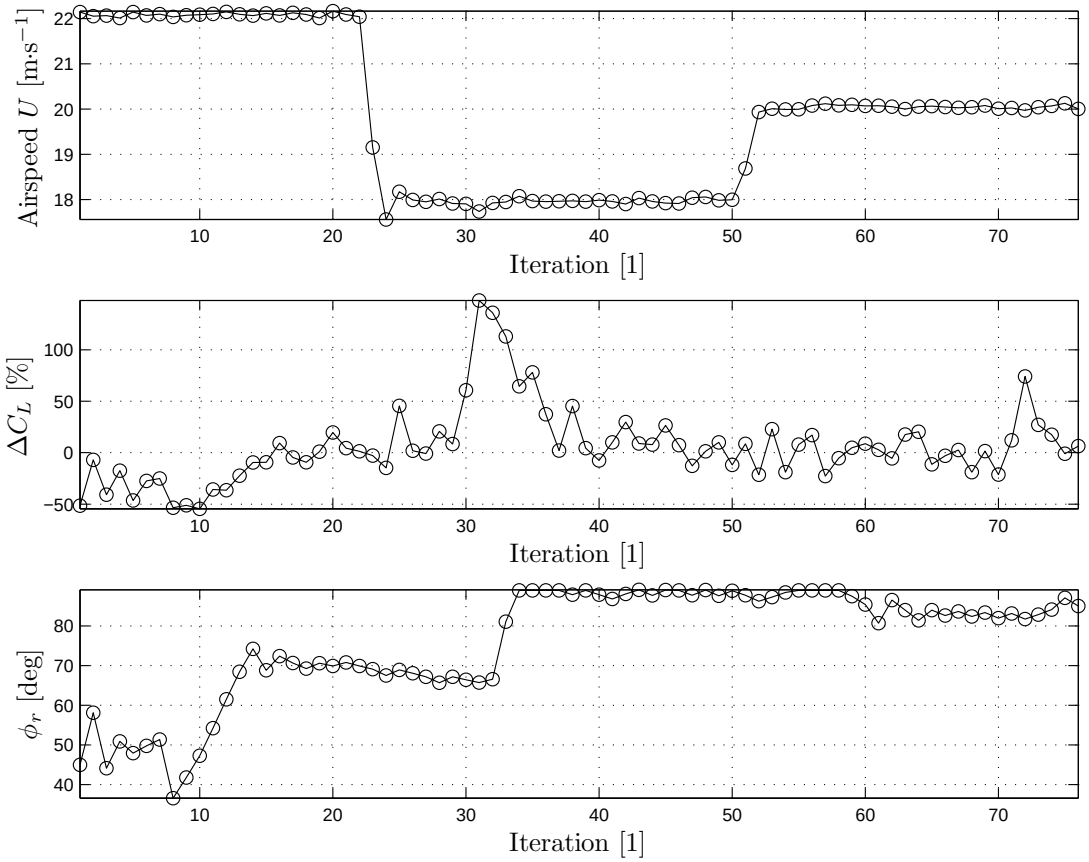

Figure 5.35: Tracking of ΔC_L and ϕ_r as the airspeed is varied.

Figure 5.35 shows the results of a test where the airspeed was initially 22 m·s^{-1} and then after a while was decreased to 18 m·s^{-1} before being increased to 20 m·s^{-1} where it remained for the remainder of the test. Throughout this $C_{L_{\text{ref}}}$ was constant. Responses in the plots of ΔC_L and ϕ_r that show changes corresponding to the changes in the airspeed plot would indicate that the optimisation routine was successful. However, there is no evidence of any correlation between the response of these parameters and the airspeed, and so it is clear that this attempt to trim the wing was unsuccessful.

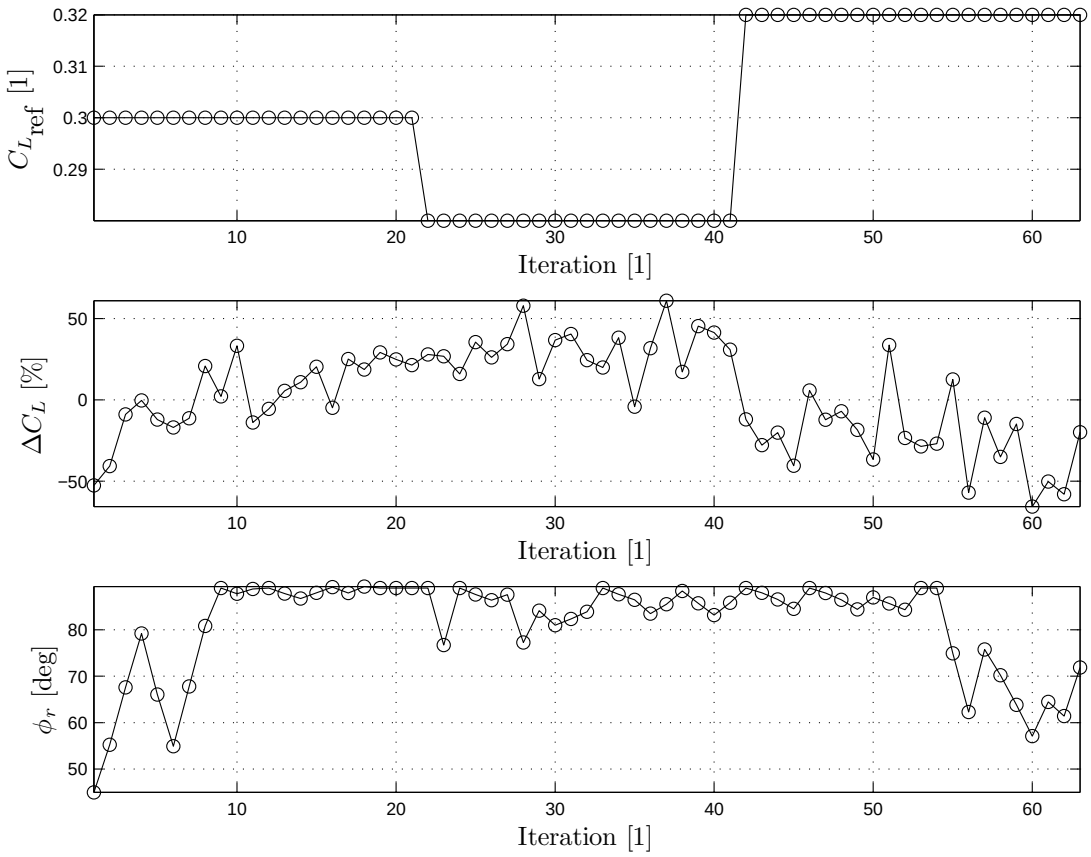

Figure 5.36: Tracking of ΔC_L and ϕ_r as $C_{L_{\text{ref}}}$ is varied.

Figure 5.36 shows the results of a test performed at a fixed airspeed where $C_{L_{\text{ref}}}$ was initially 0.30 and then after a while was decreased to 0.28 before being increased to 0.32 where it remained for the remainder of the test. Once again there is no evidence of any correlation between the response of these parameters and the reference lift value.

Maximising lift-to-drag ratio

In this task, ϕ_f and ϕ_r were varied in a steepest-ascent optimisation algorithm with maximising C_L/C_D as the objective function. This was not performed at the trim state i.e. there was no constraint in place to maintain a constant C_L. In order to test the robustness of the approach, the airspeed was varied and the response of C_L/C_D and the spar orientations were monitored.

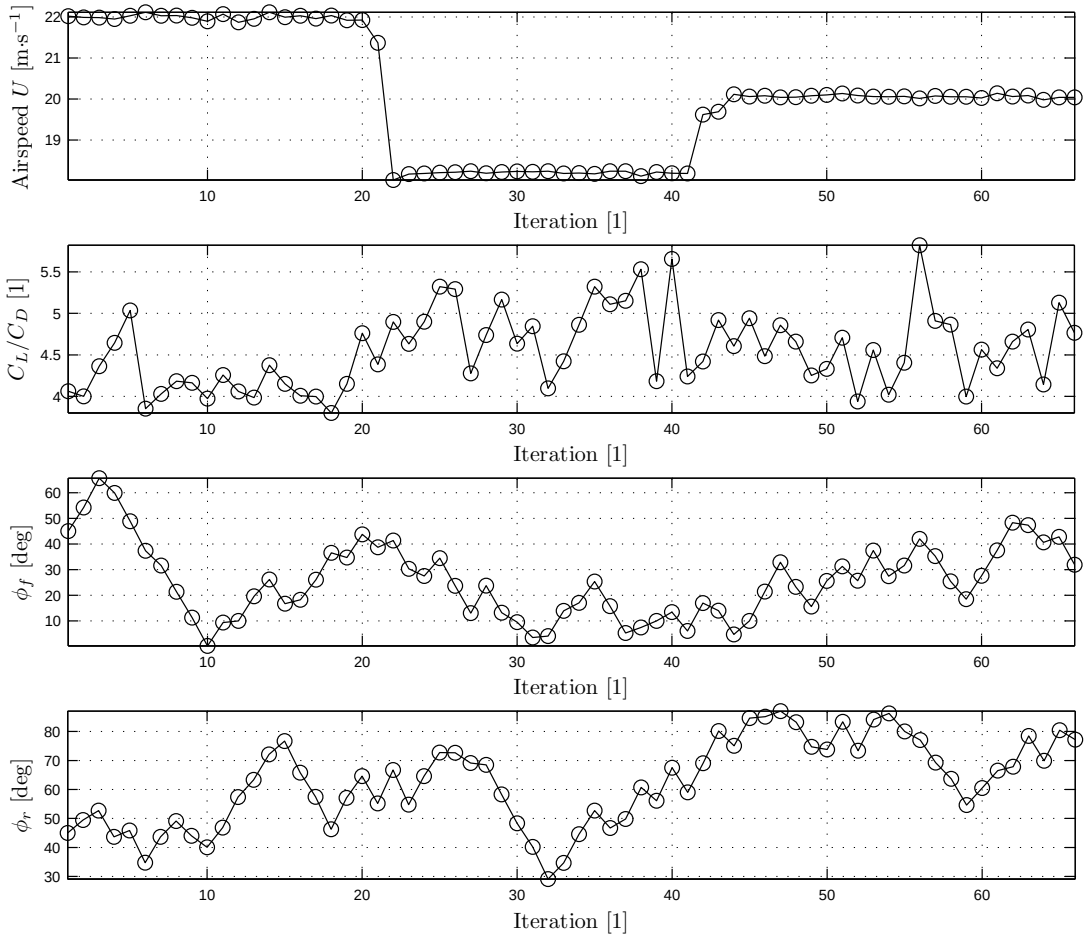

Figure 5.37: Tracking of lift-to-drag ratio, ϕ_f and ϕ_r as the airspeed is varied.

The results are shown in figure 5.37. Again, there is no correlation between the response of C_L/C_D, ϕ_f or ϕ_r as the airspeed varies indicating that the optimisation approach to controlling the wing loads was unsuccessful.

The primary reason for the failure of these optimisation approaches was identified as being related to the poor signal-to-noise ratio of the load-balance measurements and not the optimisation algorithm itself. This was confirmed by replacing the loads measurements with data from the laser displacement system, which had a much better signal-to-noise ratio; this is the focus of the next section.

5.5.8 Control of the deflections via an optimisation approach

The results of section 5.5.7 revealed that it was not possible to control the wing loads via an optimisation approach. Importantly though, the reason for this failure was assigned to the poor integrity of the C_L and C_D data that the optimisation algorithm used as inputs i.e. the noise in these signals added a significant time-varying component to the measurements that essentially implied the optimal solution was time-varying. As explored in section 5.5.1, the reason for this noise was due to the fact that the range of the load-balance channels was very large relative to the range of data that was measured.

To test the robustness of the optimisation algorithm, data from the laser displacement system was used to replace the load inputs to the algorithm. More specifically, the objective of minimising the drag whilst maintaining a reference lift value was replaced with the objective of maximising the bending deflection of the wing whilst maintaining a reference elastic angle of incidence.

Again, rather than possibly wasting test time on this task, initially the simpler challenge of maintaining a reference elastic angle of incidence with no regard for the bending deflection was performed. Since this was a sub-routine within the overall task, failure of this would imply failure of the more challenging task without the need to perform the time-consuming test.

Maintaining a reference angle of incidence

For simplicity ϕ_f was held constant and ϕ_r was varied in a steepest descent optimisation manner to achieve a reference tip elastic angle of incidence of $-1.2°$ (within error bounds) i.e. the objective function used was to minimise $|\alpha_{e_{\text{tip}}} - \alpha_{e_{\text{tip}_{\text{ref}}}}|$. This was firstly performed using an initial ϕ_r of $20°$ and repeated four times. This was then repeated with an initial ϕ_r of $70°$ in order to demonstrate the robustness of the approach. Table 5.9 summarises the results.

Table 5.9: Results demonstrating the repeatability of the optimisation routine to achieve a reference $\alpha_{e_{\text{tip}}}$ by varying ϕ_r.

Run	$\phi_{r_{\text{initial}}}$ [deg]	$\phi_{r_{\text{conv}}}$ [deg]	N_{iter} [1]	$\alpha_{e_{\text{tip}_{\text{conv}}}}$ [deg]	$\Delta\alpha_{e_{\text{tip}}}$ [%]
1	20	31.6	7	-1.258	-4.087
2	20	39.0	12	-1.167	2.325
3	20	42.5	13	-1.123	5.426
4	20	31.1	19	-1.284	-5.919
5	20	35.7	10	-1.198	0.141
6	70	36.0	10	-1.221	-1.480
7	70	36.3	38	-1.180	1.409
8	70	33.5	7	-1.277	-1.903
9	70	38.4	8	-1.230	-2.114
10	70	43.6	12	-1.135	4.580

The table shows that the results were repeatable, with all ten runs resulting in a solution ($\alpha_{e_{\text{tip}_{\text{conv}}}}$) with less than a 6% error ($\Delta\alpha_{e_{\text{tip}}}$) from the reference tip elastic angle of incidence. Additionally, the results show convergence of ϕ_r within the range $31.1° \leq \phi_{r_{\text{conv}}} \leq 43.6°$, which is an acceptably small range given that noise is present in the input data. Significantly, the results indicate that the algorithm will converge on an acceptable solution regardless of the starting point of the iterations i.e. $\phi_{r_{\text{initial}}}$. In general, convergence was achieved with a relatively low number of iterations, N_{iter}, although run 7 clearly struggles more than the others.

As an additional investigation, for a range of $\alpha_{e_{\text{tip}_{\text{ref}}}}$ (0.2° increments between $-2.0°$ and $-0.6°$), the optimisation routine was performed. This was carried out for a range of airspeeds (18 m·s^{-1}, 20 m·s^{-1}, 22 m·s^{-1}). The objective was to establish a clear trend between $\alpha_{e_{\text{tip}_{\text{ref}}}}$ and the converged ϕ_r. The existence of a trend would suggest that the algorithm is reliable and can be used given input data with a sufficiently high signal-to-noise ratio. The results are shown in figure

5.38.

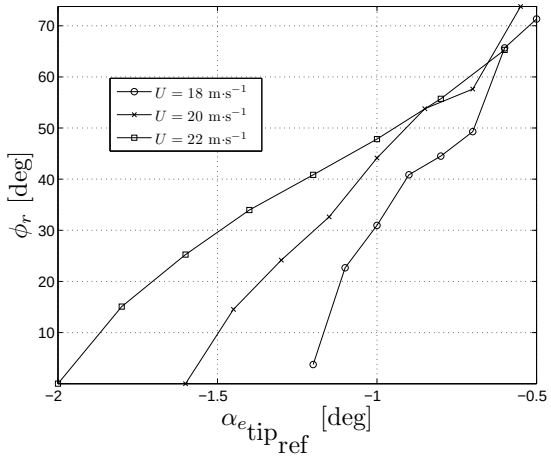

Figure 5.38: Variation of converged ϕ_r with $\alpha_{e_{\mathrm{tip}_{\mathrm{ref}}}}$.

From this plot, it is apparent that the optimisation routine has identified the near-linear relationship between the required ϕ_r and the reference angle of incidence. While this actual trend is not of interest in this study, the fact that this optimisation method has uncovered it implies that such a method could be used for controlling the wing loads.

Finally, to demonstrate the ability of the routine to respond to changes in the reference tip elastic angle of incidence, the optimisation routine was allowed to run with the removal of the convergence criteria. Every so often, the reference angle of incidence was altered. The results are presented in figure 5.39.

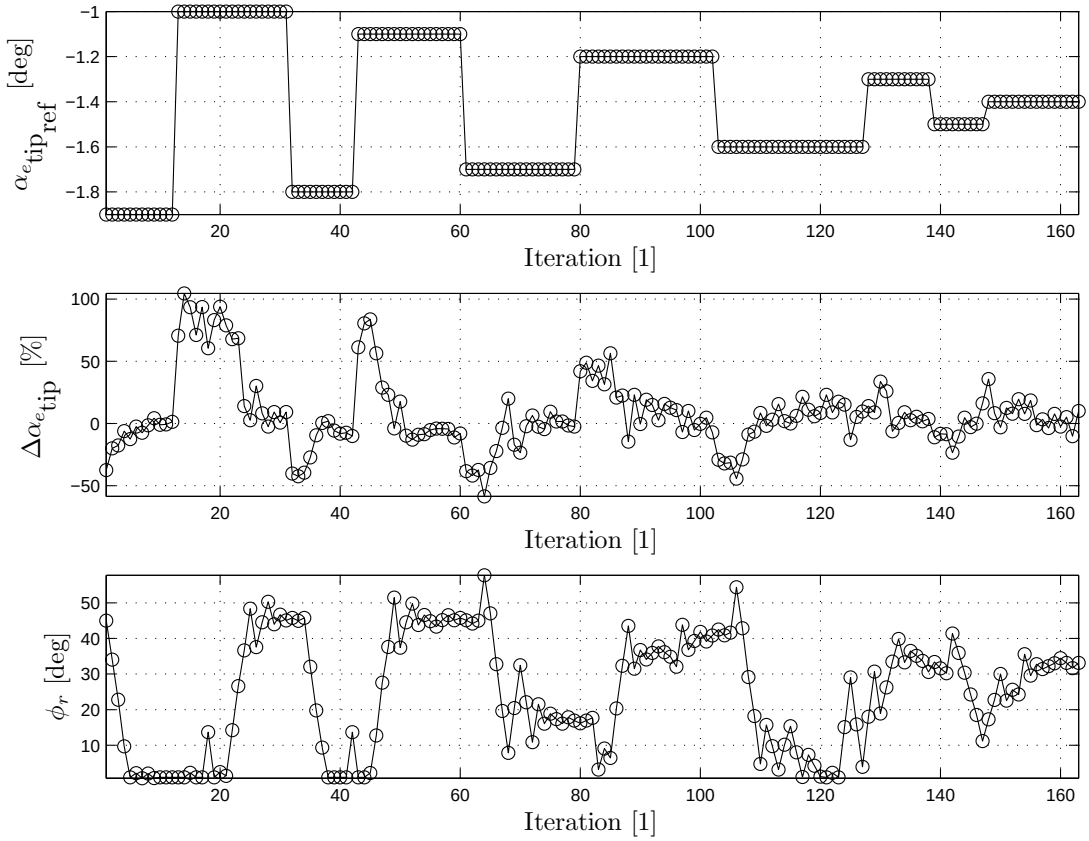

Figure 5.39: Tracking of $\Delta\alpha_{e_{\text{tip}}}$ and ϕ_r as the reference $\alpha_{e_{\text{tip}}}$ is varied.

From the plots it is clear that, with a delay of several iterations, as the reference elastic angle of incidence is varied, the rear spar orientation ϕ_r responds which results in a change in the actual elastic angle of incidence. Most importantly, the error between the reference and actual values returns to a low value after each step change in reference value.

Maximising leading-edge tip bending deflection, whilst maintaining a reference tip elastic angle of incidence

The aim of this task was to demonstrate that the leading-edge bending deflection could be maximised whilst maintaining a reference tip elastic angle of incidence. Successful demonstration of this would imply that the optimisation routine could be used for the more relevant task of minimising drag at the trim state. The

optimisation routine was as follows:

1. At an initial spar orientation configuration, $\alpha_{e_{\text{tip}}}$ was measured and then used to calculate $|\alpha_{e_{\text{tip}}} - \alpha_{e_{\text{tip}_{\text{ref}}}}|$.

2. ϕ_r was incremented by a small angle $d\phi_r$ and $\alpha_{e_{\text{tip}}}$ was measured again and used to calculate $|\alpha_{e_{\text{tip}}} - \alpha_{e_{\text{tip}_{\text{ref}}}}|$.

3. The results from steps 1 and 2 were used to calculate the gradient of $|\alpha_{e_{\text{tip}}} - \alpha_{e_{\text{tip}_{\text{ref}}}}|$ at the current location of ϕ_r. This gave an indication of how to alter ϕ_r in order to minimise the function.

4. Steps 1 - 3 were repeated using the new value of ϕ_r until $\alpha_{e_{\text{tip}}}$ was sufficiently close to $\alpha_{e_{\text{tip}_{\text{ref}}}}$. At this point the leading-edge tip bending deflection, $h_{LE_{\text{tip}}}$, was measured.

5. ϕ_f was incremented by a small angle $d\phi_f$ and steps 1 - 4 were repeated. The two values of $h_{LE_{\text{tip}}}$ at the reference $\alpha_{e_{\text{tip}}}$ value were then used to calculate the gradient of $h_{LE_{\text{tip}}}$ at the current location of ϕ_f. This gave an indication of how to alter ϕ_f in order to maximise $h_{LE_{\text{tip}}}$.

6. Step 5 was repeated using the new value of ϕ_f until $h_{LE_{\text{tip}}}$ could not be increased further.

The above procedure was very time-consuming due to having one loop operating inside another, and with 5 seconds of data collected at each data point in order to reduce noise via averaging. For this reason this task was performed once only. The results are shown in figure 5.40. Note that in this figure the convergence of the inner loop is represented by a single iteration i.e. the iteration axes correspond to the iterations of the outer loop.

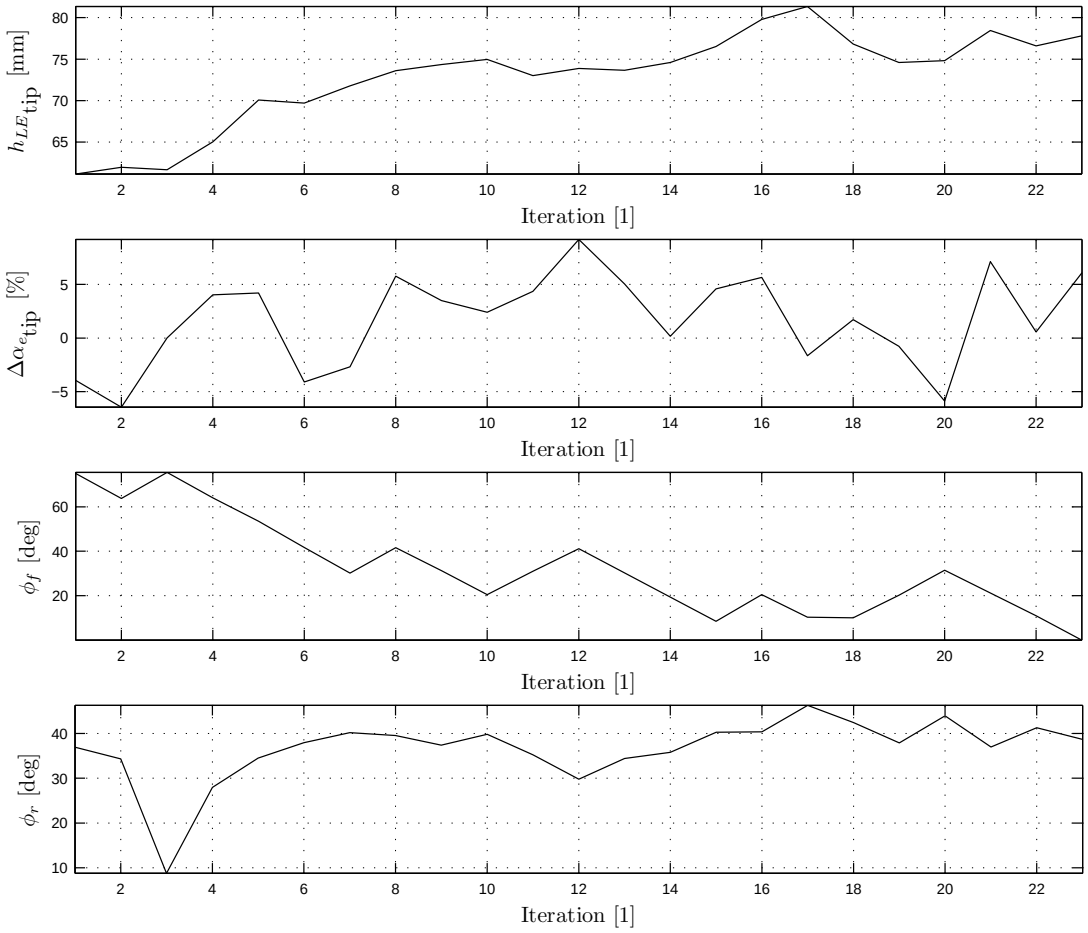

Figure 5.40: Convergence history.

The plots show that, in general, the tip bending deflection works its way towards a maximum of 75 - 80 mm from an initial deflection of approximately 60 mm. Also, it can be seen that the error between the actual tip elastic angle of incidence and the reference value has been kept below $\pm 10\%$ throughout. The lower two plots show that to achieve these objectives the optimisation routine has decreased ϕ_f towards 0° and positioned ϕ_r at around 40°.

These results show that the optimisation routine used here was successful and could be used with similar success to minimise drag at the trim state provided that the measurement of lift and drag can be be performed with a good signal-to-noise ratio.

5.6 Conclusions

This chapter has described the realisation of a wind tunnel model of a wing incorporating the rotating spars adaptive internal structures concept. The design guidelines outlined by analytical studies performed in chapter 4 were used as the basis of the model, and then this was fine-tuned using analytical aeroelastic analyses of the wing.

The construction phase of the wind tunnel model was described; this section dealt with conveying how the idealistic models used in the analytical studies were realised in order to arrive at a practical and successful test model. An overview of the support equipment used to perform the wind tunnel tests was also provided.

The bulk of the chapter described tests that were performed on the wing and presented the results. To summarise the main findings of these tests:

- Measurements of the aerodynamic loads could only be achieved with substantially lower signal-to-noise ratios than measurements of the deflections. This had significant implications for collecting data (averaging of many samples required) and for actively controlling the wing loads.

- The structural and aeroelastic parameter studies revealed that the results agreed well, in general, with the analytical predictions. Furthermore, the test and analytical trends agreed well with the analytical trends of the simplified 2-spar wing model established in chapter 4.

- Polynomial regression models failed to accurately control the wing loads via adaption of the wing structure, despite the regression models representing the original data very well. The primary cause for this in the tests was the poor signal-to-noise ratio of the load measurements. However, further tests using the deflections in place of the loads showed that even if the signal-to-noise ratio of the loads were improved, the regression model approach is likely to fail.

- Simple gradient optimisation approaches to controlling the wing loads were shown to have the potential to succeed. Although these failed in controlling the loads, this was attributed to the low signal-to-noise ratio of the load measurements; this was proven by successfully controlling the (less noisy) wing deflections with the same algorithm.

The tests highlighted that the sizing of the rotating spar actuators is a critical part of the design; it was the maximum torque of the servos that limited the wing to 22 $m \cdot s^{-1}$. Unfortunately, the tests had to be performed using the load balance and wind tunnel combination available; the wind tunnel geometry placed an upper limit on the size of the wing, and this upper limit led to a maximum variation in the aerodynamic loads of less than 1% of the range of the load balance which resulted in the low signal-to-noise ratios that were encountered during testing. Every effort should be made in future tests to ensure that the size of the wing is better matched to the load balance range. This would allow tests to be performed in much less time and would enable accurate control of the loads to be realised.

Chapter 6

Adaptive wing tip devices for loads alleviation

6.1 Introduction

All aircraft are subject to atmospheric turbulence of varying degrees of severity. The effect of atmospheric gusts and turbulence as well as aircraft-induced loads caused by manoeuvring on flexible aircraft structures is the excitation of flexible and rigid body aircraft modes [93]. This can lead to a number of problems; structurally, large bending moments can be generated leading to high internal stresses. If sufficient, these stresses will result in failure of the structure. Additionally, large deformations can occur which may result in nonlinear behaviour; this has significant implications at the analytical design stage of such aircraft, since computationally expensive nonlinear aeroelastic analyses must be performed [92]. Passenger effects range from a mild discomfort that is little more than an annoyance to the far more severe and dangerous situation of being forced violently against seat-belts, and unsecured items and/or passengers being tossed around.

6.1.1 Next generation surveillance aircraft

For some recent High Altitude Long Endurance (HALE) unmanned aerial vehicle (UAV) designs gust loads are particularly problematic as they not only result in high bending stresses, but also a possible degradation in their mission performance.

HALE aircraft are UAVs that perform surveillance type roles; recent military operations (e.g. Iraq and Afghanistan) highlight the trend and demand for an increasing use of UAVs. It is perhaps intelligence gathering missions that UAVs are most suited to; these roles often demand, amongst other capabilities, uninterrupted surveillance/reconnaissance for extended time periods, and it is this high endurance demand that UAVs handle very well. Some of these missions also require 360° coverage as well as a low frequency sensing capability [122].

Figure 6.1 shows the Northrop Grumman Global Hawk which has been used in Iraq and Afghanistan; this particular HALE UAV has a similar configuration to the manned Lockheed U-2 aircraft, particularly with the high aspect ratio wings [151]. However, as with almost all conventional aircraft, the Global Hawk is the result of a design that incorporates the payload (sensors) into the available airframe space after vehicle design, and as a consequence the sensing capabilities are limited by the aircraft configuration.

Figure 6.1: Northrop Grumman Global Hawk [150].

Figure 6.2: A joined-wing HALE UAV concept [152].

In order to overcome these performance limitations and achieve an optimum sensing capability, a completely different design methodology is being employed to design the next generation of HALE UAVs; the air vehicle is being designed around the required sensor systems. This has resulted in some unusual and novel UAV designs. High endurance is still crucial in these designs and so high aspect ratio wings are still present. Wing spans are being increased further however to accommodate larger sensor arrays that allow sensor operation at lower frequencies. The most radical change in configuration is the use of joined-wing designs, as this assists convenient integration of sensor equipment that provides 360° coverage, and also offers a stiffer wing structure without the use of lower aspect ratio and therefore less efficient wings [115]. The USAF classifies this future concept as SensorCraft [152]. Figure 6.2 shows a conceptual joined-wing SensorCraft design.

However, the large flexible high aspect ratio structures present in these designs are very susceptible to gust loads; large bending stresses are generated close to the wing root as a result, and for joined-wing planforms one of the critical design cases is the buckling of the rear wing structure due to gust loading [115]. Additionally, shape integrity is important for these aircraft in order to achieve optimum sensor performance, and large deformations as a result of gust loads could violate this requirement [92, 97]. This makes the use of a gust load alleviation system very desirable to a joined-wing SensorCraft design, as this will lead to a reduction in structure and therefore weight.

In this chapter a novel loads alleviation wing tip device is described and the effectiveness of it is demonstrated via a parameter study using an approximate aeroelastic wing model, and also in a case study using a finite element model of a joined-wing SensorCraft concept. Other aeroelastic analyses are also performed to show how the flutter and divergence behaviour is affected by the device, and to demonstrate the additional trim capability of it. The results of these analyses show that an adaptive capability would be useful. Next, the case study shows

how the alleviation of loads and therefore internal stresses is used to reduce the aircraft mass by up to 30%.

6.2 Loads alleviation systems

6.2.1 State of the art

Many current aircraft are fitted with gust load alleviation (GLA) or manoeuvre load alleviation (MLA) systems. For instance, the Lockheed L-1011-500 TriStar, which was introduced in the late '70s, used the Active Control System (ACS) to reduce loads due to turbulence and manoeuvres; accelerometers located at the wing tips and in the fuselage detected these motions and deflected the outboard ailerons accordingly [163].

Much of the latter Airbus family use the Loads Alleviation Function (LAF) of the flight computer to deflect the ailerons upwards and to deploy the spoilers upon detection of excessive motions, again by accelerometers. For lighter aircraft, such as the A320, the critical wing bending strength is defined by discrete gust cases, and therefore the LAF on the A320 is designed to deflect the surfaces to minimise the gust loads. For heavier aircraft, such as the A330 and A340, the critical wing bending strength is defined by manoeuvre loads, and so the LAF on these Airbus models are designed to deflect the surfaces to minimise the manoeuvre loads [43, 44]. The A380 is able to detect whether it is experiencing turbulence or manoeuvring, and controls the surface deflection response to minimise the corresponding loading, making it the first aircraft to optimise for both of these requirements [156].

The effectiveness of a loads alleviation system can be greatly enhanced by predicting the motion before it happens and there have been some attempts to enable this with regards to gust load alleviation using LIDAR, such as the NASA Airborne Coherent Lidar for Advanced In-Flight Measurements (ACLAIM) programme [125].

6.2.2 Proposed loads alleviation concept

The proposed loads alleviation concept is straightforward in nature; the device forms the outboard portion of the wing and is attached to the conventional inboard section with five degrees of freedom fixed, and the remaining pitch degree of freedom restrained by a torsional spring. This spring element can be as simple as a rod with an associated and appropriate torsional stiffness value. Figure 6.3 shows a rectangular wing with the device attached.

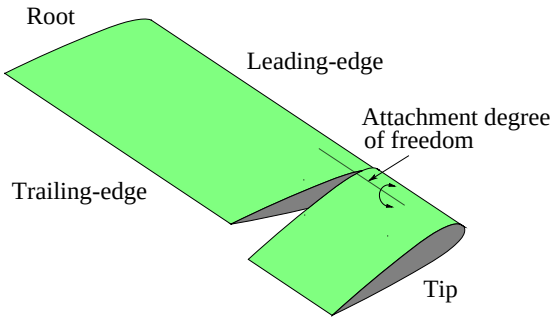

Figure 6.3: Wing tip loads alleviation concept.

Crucially, the chordwise attachment location must lie ahead of the aerodynamic centre for the concept to be effective; consider the wing encountering a sudden up-gust in the airflow. The inboard section of the wing, with its aerodynamic centre lying (typically) ahead of the elastic axis of the wing will twist nose-upwards, increasing its angle of incidence and associated aerodynamic loads. However, the outboard section, with its aerodynamic centre lying aft of the elastic axis (the attachment element) will rotate nose-downwards, decreasing its angle of incidence and associated aerodynamic loads. The intended effect of this is a smaller increase in net aerodynamic loads when compared with an unmodified wing encountering an identical gust. This means that critical gust and manoeuvre bending stresses as well as large deflections can be decreased, therefore leading to weight reductions and an improved shape integrity of the structure.

The precise chordwise and spanwise attachment location and the torsional stiffness have a major effect on the performance of the concept, and how well it is

suited to a particular gust, manoeuvre, or flight condition; these relationships are demonstrated throughout the chapter. Therefore some form of adaptive control would be very useful as it would allow the device to maintain optimal performance throughout the flight envelope. By adaptive, it is implied that its parameters can be altered with a low frequency, but is essentially still passive in nature. This is in contrast to an active device which is considered to respond with a far greater frequency, such as those discussed in section 6.2.1.

The concept originates from the 1970s with EADS who, in response to the oil crisis of 1973, researched it for use on the Airbus A300 to improve the aerodynamic efficiency [121]. Here it is also relevant to mention previous studies [5, 8, 9, 30, 32] performed within the Active Aeroelastic Aircraft Structures (3AS) programme which have examined the application of all-moving vertical tails to improve the aeroelastic effectiveness of tail fins; this has been shown to offer mass, drag and load reductions. However, this also identified that to provide optimum effectiveness throughout flight whilst avoiding aeroelastic instabilities required the tail attachment torsional stiffness and/or position to be adaptive.

A passive approach to the loads alleviation problem has several advantages over an active approach; firstly, there is no requirement for a complex active sensing and response system and therefore the concept is less likely to fail and will undoubtedly not suffer from the same weight penalty as an active system. Since the system is less likely to fail, the need for system redundancy is also removed; again, this will benefit the passive device in the form of weight savings relative to an active device.

An adaptive capability also offers the possibility of roll control for aircraft that have no requirement for fast manoeuvring, and a secondary consideration is that an adaptive capability could be exploited to minimise the wing drag at different flight conditions. Adjustment of the torsional stiffness of the attachment is the most likely approach to achieve an adaptive mechanism, as it is more practical than altering the chordwise or spanwise attachment position during flight.

6.3 Development of a dynamic aeroelastic model for a wing incorporating a wing tip device

6.3.1 Introduction

To gain an insight into the typical behaviour of a wing with the tip device, a parameter study was performed. The decision was taken to use a simplified model for a number of reasons; first of all, it was trends that were of interest in the study and therefore numerical accuracy was not viewed as critical. Further to this, the computational expense associated with calculating unsteady aerodynamic influence coefficients would reduce the effectiveness of the model as a tool to establish trends. For this reason, a simple in-house dynamic aeroelastic model was written using MATLAB®. This section presents the derivation of the equations of motion using a Lagrangian approach and also the development of a quasi-steady strip theory aerodynamic model.

Model description

The model is shown in figure 6.4 in the structural coordinate system $Oxyz$, where z is in the upwards direction. The wing is assumed to be rectangular in planform, unswept and uncambered, and of semi-span l and chord c. The tip device is located between $x = x_P$ and $x = l$ and is free to rotate about a spanwise axis located $e_\gamma c$ aft of the aerodynamic centre (quarter chord) and y_γ aft of the leading-edge. This rotation is restrained by a torsional spring of stiffness k. The main wing has an elastic axis located ec aft of the aerodynamic centre and y_e aft of the leading-edge. The main wing and device both have a flexural rigidity EI while only the main wing has a torsional rigidity given by GJ; the assumption is made that the device is rigid in torsion. It is further assumed that the density of the wing and device are constant and equal, ρ_W, with a uniform mass distribution; therefore the inertial axis is located at $y = c/2$, the semi-chord. The wing is also assumed to deflect in torsion through small angles and similarly the device is

assumed to rotate through small angles.

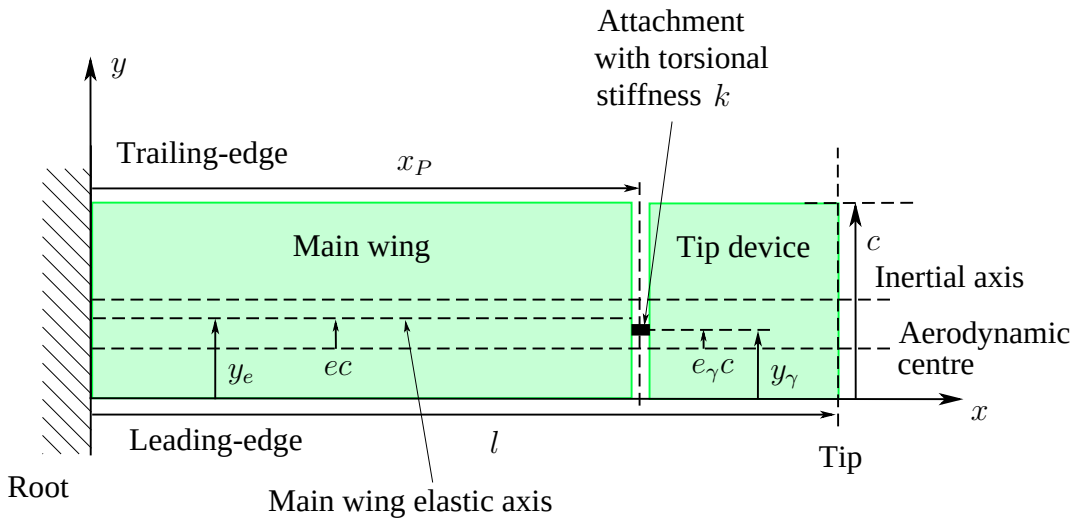

Figure 6.4: Wing with tip device in the structural coordinate system.

6.3.2 Structural model

In section 3.2.1 the Principle of Virtual Displacements was used to obtain the equations of motion for an aeroelastic system. Lagrange's energy equations is an alternative method to this and will be demonstrated in this section. In general, for the i^{th} generalised coordinate q_i, Lagrange's equation for an undamped system is given by [141, 158]

$$\frac{d}{dt}\left[\frac{\partial T}{\partial \dot{q}_i}\right] - \frac{\partial T}{\partial q_i} + \frac{\partial U}{\partial q_i} = Q_i \tag{6.1}$$

where T is the system kinetic energy, U is the system potential energy and Q_i are the generalised forces. The generalised coordinates are a set of independent parameters which are sufficient to describe the system's motion [158].

Displacement field

The displacement field for the wing in bending and torsion is given by the same earlier derived expression in section 3.2.1 for that of a spar (with the offset coordinate system from the elastic axis at y_e taken into account):

$$\mathbf{u}_W(x,y,z,t) = \begin{bmatrix} -zh'(x,t) & z\theta(x,t) & \Big(h(x,t) - (y-y_e)\,\theta(x,t)\Big) \end{bmatrix}^T \qquad 0 \le x \le x_P \tag{3.21}$$

where $h(x,t)$ is the bending displacement of the wing's elastic axis in the upwards direction, and $\theta(x,t)$ is the nose-up torsional deformation of the wing about the elastic axis. This expression assumes that the wing is of high aspect ratio. The simplification is made that displacement is limited to the z-axis and therefore Eq. 3.21 becomes

$$u_W(x,t) = h(x,t) + (y_e - y)\,\theta(x,t) \qquad 0 \le x \le x_P \tag{6.2}$$

h and θ can be represented by a finite summation of assumed mode shapes and associated amplitudes (see the Rayleigh-Ritz method in section 3.2.2) allowing the resulting equations of motion to be readily solved:

$$\begin{aligned} h(x,t) &\approx \boldsymbol{\psi}^T(x)\boldsymbol{\zeta}(t) \\ &= \sum_{a=1}^{A} \psi_a(x)\zeta_a(t) \end{aligned} \tag{6.3}$$

$$\begin{aligned} \theta(x,t) &\approx \boldsymbol{\phi}^T(x)\boldsymbol{\beta}(t) \\ &= \sum_{b=1}^{B} \phi_b(x)\beta_b(t) \end{aligned} \tag{6.4}$$

$\boldsymbol{\psi}$ and $\boldsymbol{\phi}$ are Ax1 and Bx1 matrices (i.e. vectors) containing appropriate shape functions ψ_a and ϕ_b respectively, and $\boldsymbol{\zeta}$ and $\boldsymbol{\beta}$ are vectors of length A and B

containing unknown time-varying amplitudes ζ_a and β_b respectively; for the assumed modes approach, $\boldsymbol{\zeta}$ and $\boldsymbol{\beta}$ are the generalised coordinates and define the amount of each assumed mode present in the motion [141]. Therefore Eq. 6.2 becomes

$$u_W = \sum_{a=1}^{A} \psi_a \zeta_a + (y_e - y) \sum_{b=1}^{B} \phi_b \beta_b \qquad 0 \leq x \leq x_P \tag{6.5}$$

For the wing tip device, the displacement field has an additional component associated with the nose-up rotation γ of it relative to the main wing, and the torsional component is analysed at the attachment point x_P, as indicated by ϕ_{b_P}:

$$u_D = \sum_{a=1}^{A} \psi_a \zeta_a + (y_e - y) \sum_{b=1}^{B} \phi_{b_P} \beta_b + (y_\gamma - y)\, \gamma \qquad x_P \leq x \leq l \tag{6.6}$$

Kinetic energy

The kinetic energy for the main wing is given by [50]

$$T = \frac{1}{2} \int_V \rho_W (\dot{u}_W^2 + \dot{u}_D^2) dV \tag{6.7}$$

where ρ_W is the density of the wing and V is the volume of the wing. Assuming a uniform mass distribution, Eq. 6.7 can be written as

$$T = \frac{\bar{\bar{m}}_W}{2} \int_A (\dot{u}_W^2 + \dot{u}_D^2) dA \tag{6.8}$$

where $\bar{\bar{m}}_W$ is the mass of the wing per unit area and A is the cross-sectional area of the wing. Substituting Eq. 6.5 into this gives

$$\begin{aligned} T = {} & \frac{\bar{\bar{m}}_W}{2} \int_0^{x_P} \int_0^c \left(\sum_{a=1}^{A} \psi_a \dot{\zeta}_a + (y_e - y) \sum_{b=1}^{B} \phi_b \dot{\beta}_b \right)^2 dy\, dx \\ & + \frac{\bar{\bar{m}}_W}{2} \int_{x_P}^{l} \int_0^c \left(\sum_{a=1}^{A} \psi_a \dot{\zeta}_a + (y_e - y) \sum_{b=1}^{B} \phi_{b_P} \dot{\beta}_b + (y_\gamma - y)\, \dot{\gamma} \right)^2 dy\, dx \end{aligned} \tag{6.9}$$

Therefore

$$\begin{aligned}
\frac{d}{dt}\left[\frac{\partial T}{\partial \dot{\zeta}_a}\right] &= \bar{\bar{m}}_W \int_0^{x_P}\int_0^{c} \psi_a \left(\sum_{a=1}^{A} \psi_a \ddot{\zeta}_a + (y_e - y) \sum_{b=1}^{B} \phi_b \ddot{\beta}_b \right) dy\, dx \\
&\quad + \bar{\bar{m}}_W \int_{x_P}^{l}\int_0^{c} \psi_a \left(\sum_{a=1}^{A} \psi_a \ddot{\zeta}_a \right. \\
&\quad \left. + (y_e - y) \sum_{b=1}^{B} \phi_{b_P} \ddot{\beta}_b + (y_\gamma - y)\, \ddot{\gamma} \right) dy\, dx \\
&= \bar{\bar{m}}_W \int_0^{x_P} \psi_a \left(c \sum_{a=1}^{A} \psi_a \ddot{\zeta}_a + \left(c y_e - \frac{c^2}{2} \right) \sum_{b=1}^{B} \phi_b \ddot{\beta}_b \right) dx \\
&\quad + \bar{\bar{m}}_W \int_{x_P}^{l} \psi_a \left(c \sum_{a=1}^{A} \psi_a \ddot{\zeta}_a + \left(c y_e - \frac{c^2}{2} \right) \sum_{b=1}^{B} \phi_{b_P} \ddot{\beta}_b \right. \\
&\quad \left. + \left(c y_\gamma - \frac{c^2}{2} \right) \ddot{\gamma} \right) dx
\end{aligned} \tag{6.10}$$

Similarly

$$\begin{aligned}
\frac{d}{dt}\left[\frac{\partial T}{\partial \dot{\beta}_b}\right] &= \bar{\bar{m}}_W \int_0^{x_P} \phi_b \left(\left(c y_e - \frac{c^2}{2} \right) \sum_{a=1}^{A} \psi_a \ddot{\zeta}_a \right. \\
&\quad \left. + \left(c y_e^2 - c^2 y_e + \frac{c^3}{3} \right) \sum_{b=1}^{B} \phi_b \ddot{\beta}_b \right) dx \\
&\quad + \bar{\bar{m}}_W \int_{x_P}^{l} \phi_{b_P} \left(\left(c y_e - \frac{c^2}{2} \right) \sum_{a=1}^{A} \psi_a \ddot{\zeta}_a \right. \\
&\quad + \left(c y_e^2 - c^2 y_e + \frac{c^3}{3} \right) \sum_{b=1}^{B} \phi_{b_P} \ddot{\beta}_b \\
&\quad \left. + \left(c y_e y_\gamma - \frac{(y_e + y_\gamma)\, c^2}{2} + \frac{c^3}{3} \right) \ddot{\gamma} \right) dx
\end{aligned} \tag{6.11}$$

and

$$\begin{aligned}
\frac{d}{dt}\left[\frac{\partial T}{\partial \dot{\gamma}}\right] &= \bar{\bar{m}}_W \int_{x_P}^{l} \left(\left(c y_\gamma - \frac{c^2}{2} \right) \sum_{a=1}^{A} \psi_a \ddot{\zeta}_a \right. \\
&\quad \left. + \left(c y_e y_\gamma - \frac{(y_e + y_\gamma)\, c^2}{2} + \frac{c^3}{3} \right) \sum_{b=1}^{B} \phi_{b_P} \ddot{\beta}_b \right.
\end{aligned}$$

$$+ cy_\gamma^2 - y_\gamma c^2 + \frac{c^3}{3}\Bigg) dx \tag{6.12}$$

Potential energy

The potential energy for the wing due to bending and torsional deformations is given by [37]

$$U_W = \frac{EI}{2}\int_0^l \left(\frac{\partial^2 h}{\partial x^2}\right)^2 dx + \frac{GJ}{2}\int_0^{x_P}\left(\frac{\partial \theta}{\partial x}\right)^2 dx \tag{6.13}$$

where E is Young's modulus, G is the shear modulus, I is the second moment of area of the wing about the elastic axis in the Oxz-plane and J is the St. Venant torsion constant. Section 3.2 provides the full derivation of the latter two terms and of the above equation (in terms of virtual strain energy). The torsional rigidity of the attachment spring provides an additional source of potential energy; this is given by [59, 76]

$$U_\gamma = \frac{1}{2}k\gamma^2 \tag{6.14}$$

Therefore, expressed in Lagrange's notation and upon substitution of the assumed modes and generalised coordinates, the total potential energy in the wing is

$$U = \frac{EI}{2}\int_0^l \left(\sum_{a=1}^{A}\psi_a''\zeta_a\right)^2 dx + \frac{GJ}{2}\int_0^{x_P}\left(\sum_{b=1}^{B}\phi_b'\beta_b\right)^2 dx + \frac{1}{2}k\gamma^2 \tag{6.15}$$

Therefore

$$\frac{\partial U}{\partial \zeta_a} = EI\int_0^l \psi_a''\sum_{a=1}^{A}\psi_a''\zeta_a\, dx \tag{6.16}$$

and

$$\frac{\partial U}{\partial \beta_b} = GJ\int_0^{x_P}\phi_b'\sum_{b=1}^{B}\phi_b'\beta_b\, dx \tag{6.17}$$

and

$$\frac{\partial U}{\partial \gamma} = k\gamma \tag{6.18}$$

Lagrange's equations, given by Eq. 6.1, for multiple generalised coordinates may now be expressed as

$$\mathbf{A}\ddot{\boldsymbol{\eta}} + \mathbf{E}\boldsymbol{\eta} = \mathbf{Q} \tag{6.19}$$

where $\mathbf{A}$ is the structural inertia matrix given by Eq. 6.21, $\mathbf{E}$ is the structural stiffness matrix given by Eq. 6.22, $\mathbf{Q}$ is the vector of generalised forces and $\boldsymbol{\eta}$ is a vector of generalised coordinates, given by

$$\boldsymbol{\eta}^T = \begin{bmatrix} \boldsymbol{\zeta}^T & \boldsymbol{\beta}^T & \gamma \end{bmatrix} \tag{6.20}$$

Notice also that in $\mathbf{A}$ and $\mathbf{E}$ the summations have been replaced with the product of vectors (see Eqs. 6.3 and 6.4), and the mass per unit area $\bar{\bar{m}}_W$ has been replaced with the mass per unit length $\bar{m}_W$.

$$\mathbf{A} = \bar{m}_W \begin{bmatrix} \left(\int_0^l \boldsymbol{\psi}\boldsymbol{\psi}^T\,dx\right) & \begin{pmatrix}\left(y_e - \frac{c}{2}\right)\left(\int_0^{x_P} \boldsymbol{\psi}\boldsymbol{\phi}^T\,dx\right) \\ +\int_{x_P}^l \boldsymbol{\psi}\,dx\,\boldsymbol{\phi}_P^T\end{pmatrix} & \left(\left(y_\gamma - \frac{c}{2}\right)\int_{x_P}^l \boldsymbol{\psi}\,dx\right) \\ \begin{pmatrix}\left(y_e - \frac{c}{2}\right)\left(\int_0^{x_P} \boldsymbol{\phi}\boldsymbol{\psi}^T\,dx\right) \\ +\boldsymbol{\phi}_P^T\int_{x_P}^l \boldsymbol{\psi}^T\,dx\end{pmatrix} & \begin{pmatrix}\left(y_e^2 - y_e c + \frac{c^2}{3}\right)\left(\int_0^{x_P} \boldsymbol{\phi}\boldsymbol{\phi}^T\,dx\right) \\ +\boldsymbol{\phi}_P\boldsymbol{\phi}_P^T\int_{x_P}^l dx\end{pmatrix} & \left(\left(y_e y_\gamma - \frac{(y_e+y_\gamma)c}{2} + \frac{c^2}{3}\right)\boldsymbol{\phi}_P\int_{x_P}^l dx\right) \\ \left(\left(y_\gamma - \frac{c}{2}\right)\int_{x_P}^l \boldsymbol{\psi}^T\,dx\right) & \left(\left(y_e y_\gamma - \frac{(y_e+y_\gamma)c}{2} + \frac{c^2}{3}\right)\int_{x_P}^l dx\,\boldsymbol{\phi}_P^T\right) & \left(\left(y_\gamma^2 - y_\gamma c + \frac{c^2}{3}\right)\int_{x_P}^l dx\right) \end{bmatrix} \tag{6.21}$$

$$\mathbf{E} = \begin{bmatrix} EI\int_0^l \boldsymbol{\psi}''\boldsymbol{\psi}''^T\,dx & \mathbf{0}_{A,B} & \mathbf{0}_{A,1} \\ \mathbf{0}_{B,A} & GJ\int_0^{x_P}\boldsymbol{\phi}'\boldsymbol{\phi}'^T\,dx & \mathbf{0}_{B,1} \\ \mathbf{0}_{1,A} & \mathbf{0}_{1,B} & k \end{bmatrix} \tag{6.22}$$

6.3.3 Aerodynamic model

For the aerodynamics, a simplified quasi-steady strip theory approximation will be used. The errors that result from such an approximation are not important since it is trends that are of interest. Conversely, while a full unsteady aerodynamic model is quantitatively more accurate, the major disadvantage of such an approach is the computational expense required to calculate the unsteady aerodynamic influence coefficients.

Virtual work

For the i^{th} generalised coordinate, the generalised forces are [141]

$$Q_i = \frac{\partial\left(\delta^* W\right)}{\partial\left(\delta q_i\right)} \tag{6.23}$$

where $\delta^* W$ is the virtual work of the system. From Eq. 3.63, the virtual work for the current wing (modified for the inclusion of the wing tip device and zero sweep) can be written as

$$\begin{aligned}\delta^* W = &\int_0^{x_P} \bar{L}_W\, \delta h_{ac_W}\, dx + \int_{x_P}^{l} \bar{L}_D\, \delta h_{ac_D}\, dx \\ &+ \int_0^{x_P} \bar{M}_{ac_W}\, \delta\theta\, dx + \int_{x_P}^{l} \bar{M}_{ac_D}\, dx\, (\delta\theta_P + \delta\gamma)\end{aligned} \tag{6.24}$$

where $\bar{L}_W$ and $\bar{L}_D$ are the lift per unit span on the wing and device respectively, $\bar{M}_{ac_W}$ and $\bar{M}_{ac_D}$ are the pitching moment (about the aerodynamic centre) per unit span on the wing and device respectively and δh_{ac_W} and δh_{ac_D} are the virtual bending displacements at the aerodynamic centre of the wing and device respectively.

Aerodynamic loads

To obtain expressions for the lift per unit span, firstly consider the upwash on the wing and device; for the wing, the upwash at the aerodynamic centre as a

result of simultaneous flexural and torsional motions, as well as a gust velocity w_g and uniform wind-off incidence α_r is given by [141]

$$w_W(x,t) = w_g(t) + U\Big(\alpha_r + \theta(x,t)\Big) - \dot{h}(x,t) \qquad 0 \le x \le x_P \quad (6.25)$$

where U is the airspeed and the small angle approximation has been applied to linearise the expression. Therefore, for a wing with a lift curve slope of a_W, the lift per unit span can be written as [15]

$$\bar{L}_W = \frac{\rho U}{2} c a_W \Big(w_g + U(\alpha_r + \theta) - \dot{h}\Big) \qquad 0 \le x \le x_P \quad (6.26)$$

where ρ is the air density. Substituting the shape functions and generalised coordinates (Eqs. 6.3 and 6.4) into this gives

$$\bar{L}_W = \frac{\rho U}{2} c a_W \Big(w_g + U\Big(\alpha_r + \sum_{b=1}^{B} \phi_b \beta_b\Big) - \sum_{a=1}^{A} \psi_a \dot{\zeta}_a\Big) \qquad 0 \le x \le x_P \quad (6.27)$$

The equivalent expression for the wing tip device requires the effective angle of incidence expression to be modified to account for the pitch angle of the device and rigid torsion assumption i.e.

$$\bar{L}_D = \frac{\rho U}{2} c a_W \Big(w_g + U\Big(\alpha_r + \sum_{b=1}^{B} \phi_{b_P} \beta_b + \gamma\Big) - \sum_{a=1}^{A} \psi_a \dot{\zeta}_a\Big) \qquad x_P \le x \le l \quad (6.28)$$

where it is assumed that the lift curve slope of the device is identical to that of the main wing. For steady aerodynamics, the uncambered wing assumption will produce zero pitching moment about the aerodynamic centre. However, to avoid serious aeroelastic modelling errors, a quasi-steady aerodynamic model should retain an approximation of the pitch damping term that results from a full unsteady model [141], and this term gives rise to a non-zero pitching moment about the aerodynamic centre; for the main wing this can be expressed per unit

span as

$$\bar{M}_{ac_W} = \frac{\rho U}{8} c^3 M_{\dot{\theta}} \dot{\theta} \qquad 0 \leq x \leq x_P \tag{6.29}$$

where $M_{\dot{\theta}}$ is the unsteady pitching moment aerodynamic derivative. In terms of the shape functions and generalised coordinates, Eq. 6.29 is

$$\bar{M}_{ac_W} = \frac{\rho U}{8} c^3 M_{\dot{\theta}} \sum_{b=1}^{B} \phi_b \dot{\beta}_b \qquad 0 \leq x \leq x_P \tag{6.30}$$

The equivalent expression for the wing tip device again requires to be modified to account for the pitch angle of the device and rigid torsion assumption i.e.

$$\bar{M}_{ac_D} = \frac{\rho U}{8} c^3 M_{\dot{\theta}} \left(\sum_{b=1}^{B} \phi_{b_P} \dot{\beta}_b + \dot{\gamma} \right) \qquad x_P \leq x \leq l \tag{6.31}$$

Virtual displacements

Next, the virtual bending displacement about the aerodynamic centre needs to be expressed in terms of the generalised coordinates. Again noting the small angle assumption that has been made, the virtual bending displacement at the aerodynamic centre of the wing is

$$\delta h_{ac_W} = \delta h + ec\, \delta\theta \qquad 0 \leq x \leq x_P \tag{6.32}$$

where ec is the distance that the elastic axis lies aft of the aerodynamic centre. For the wing tip device, the rigid torsion assumption and additional offset created by the angle γ modifies Eq. 6.32 to

$$\delta h_{ac_D} = \delta h + ec\, \delta\theta_P + e_\gamma c\, \delta\gamma \qquad x_P \leq x \leq l \tag{6.33}$$

where $e_\gamma c$ is the distance that the attachment spring lies aft of the aerodynamic centre.

Generalised forces

Upon substitution of Eqs. 6.32 and 6.33 into Eq. 6.24, and replacing the virtual terms with the shape functions and generalised coordinates, the virtual work becomes

$$\delta^* W = \int_0^{x_P} \bar{L}_W \Big(\sum_{a=1}^{A} \psi_a \, \delta\zeta_a + ec \sum_{b=1}^{B} \phi_b \, \delta\beta_b \Big) dx + \int_{x_P}^{l} \bar{L}_D \Big(\sum_{a=1}^{A} \psi_a \, \delta\zeta_a + ec \sum_{b=1}^{B} \phi_{b_P} \, \delta \, \beta_b + e_\gamma c \, \delta\gamma \Big) dx + \int_0^{x_P} \bar{M}_{ac_W} \sum_{b=1}^{B} \phi_b \, \delta\beta_b \, dx + \int_{x_P}^{l} \bar{M}_{ac_D} \, dx \Big(\sum_{b=1}^{B} \phi_{b_P} \, \delta\beta_b e_\gamma c \, \delta\gamma \Big) \tag{6.34}$$

Performing the partial differentiation of the virtual work with respect to each of the generalised coordinates (Eq. 6.23), and substituting in the full expressions for $\bar{L}_W$, $\bar{L}_D$, $\bar{M}_{ac_W}$ and $\bar{M}_{ac_D}$ (Eqs. 6.27, 6.28, 6.30 and 6.31) gives

$$\frac{\partial \left(\delta^* W \right)}{\partial \left(\delta\zeta_a \right)} = \frac{\rho U}{2} c a_W \int_0^{x_P} \psi_a \Big(w_g + U \Big(\alpha_r + \sum_{b=1}^{B} \phi_b \beta_b \Big) - \sum_{a=1}^{A} \psi_a \dot{\zeta}_a \Big) dx + \frac{\rho U}{2} c a_W \int_{x_P}^{l} \psi_a \Big(w_g + U \Big(\alpha_r + \sum_{b=1}^{B} \phi_{b_P} \beta_b + \gamma \Big) - \sum_{a=1}^{A} \psi_a \dot{\zeta}_a \Big) dx \tag{6.35}$$

Similarly

$$\frac{\partial \left(\delta^* W \right)}{\partial \left(\delta\beta_a \right)} = \frac{\rho U}{2} c^2 a_W e \int_0^{x_P} \phi_b \Big(w_g + U \Big(\alpha_r + \sum_{b=1}^{B} \phi_b \beta_b \Big) - \sum_{a=1}^{A} \psi_a \dot{\zeta}_a \Big) dx + \frac{\rho U}{2} c^2 a_W e \int_{x_P}^{l} \phi_{b_P} \Big(w_g + U \Big(\alpha_r + \sum_{b=1}^{B} \phi_{b_P} \beta_b + \gamma \Big) - \sum_{a=1}^{A} \psi_a \dot{\zeta}_a \Big) dx$$

$$+\frac{\rho U}{8}c^3 M_{\dot{\theta}}\int_0^{x_P}\phi_b\sum_{b=1}^{B}\phi_b\dot{\beta}_b\,dx$$

$$+\frac{\rho U}{8}c^3 M_{\dot{\theta}}\int_{x_P}^{l}dx\,\phi_{b_P}\left(\sum_{b=1}^{B}\phi_{b_P}\dot{\beta}_b+\dot{\gamma}\right) \tag{6.36}$$

and

$$\frac{\partial\left(\delta^* W\right)}{\partial\left(\delta\gamma\right)}=\frac{\rho U}{2}c^2 a_W e_\gamma\int_{x_P}^{l}\left(w_g+U\left(\alpha_r+\sum_{b=1}^{B}\phi_{b_P}\beta_b+\gamma\right)-\sum_{a=1}^{A}\psi_a\dot{\zeta}_a\right)dx$$

$$+\frac{\rho U}{8}c^3 M_{\dot{\theta}}\int_{x_P}^{l}dx\left(\sum_{b=1}^{B}\phi_{b_P}\dot{\beta}_b+\dot{\gamma}\right) \tag{6.37}$$

Using Eqs. 6.35 - 6.37 with Eq. 6.23 and substituting these generalised forces for multiple generalised coordinates into the expression given by Eq. 6.19 allows the equations of motion to be expanded to

$$\mathbf{A}\ddot{\boldsymbol{\eta}}+\rho U\mathbf{B}\dot{\boldsymbol{\eta}}+\left(\rho U^2\mathbf{C}+\mathbf{E}\right)\boldsymbol{\eta}=\left(\rho U^2\alpha_r+\rho U w_g\right)\mathbf{a}_r \tag{6.38}$$

where $\mathbf{A}$ is the structural inertia matrix (see Eq. 6.21), $\mathbf{B}$ is the aerodynamic damping matrix given by Eq. 6.40, $\mathbf{C}$ is the aerodynamic stiffness matrix given by Eq. 6.41, $\mathbf{E}$ is the structural stiffness matrix (see Eq. 6.22) and $\mathbf{a}_r$ is a vector of aerodynamic disturbances given by Eq. 6.39. Eq. 6.38 is the classic form of the dynamic aeroelastic equations of motion (compare with Eq. 1.2), modified to include a vector of aerodynamic disturbances and zero structural damping.

$$\mathbf{a}_r=\begin{bmatrix}\dfrac{ca_W}{2}\left(\int_0^{x_P}\boldsymbol{\psi}\,dx+\int_{x_P}^{l}\boldsymbol{\psi}\,dx\right)\\[2ex]\dfrac{c^2 a_W e}{2}\left(\int_0^{x_P}\boldsymbol{\phi}\,dx+\boldsymbol{\phi}_P\int_{x_P}^{l}dx\right)\\[2ex]\dfrac{c^2 a_W e_\gamma}{2}\int_{x_P}^{l}dx\end{bmatrix} \tag{6.39}$$

$$\mathbf{B} = \begin{bmatrix} \left(\frac{ca_W}{2}\int_0^l \boldsymbol{\psi}\boldsymbol{\psi}^T\,dx\right) & \mathbf{0}_{A,B} & \mathbf{0}_{A,1} \\ \left(\begin{array}{c}\frac{c^2a_We}{2}\left(\int_0^{x_P}\boldsymbol{\phi}\boldsymbol{\psi}^T\,dx\right)\\ +\boldsymbol{\phi}_P^T\int_{x_P}^l\boldsymbol{\psi}^T\,dx\end{array}\right) & \left(\begin{array}{c}\frac{-c^3M_{\dot\theta}}{8}\left(\int_0^{x_P}\boldsymbol{\phi}\boldsymbol{\phi}^T\,dx\right)\\ +\boldsymbol{\phi}_P\boldsymbol{\phi}_P^T\int_{x_P}^l dx\end{array}\right) & \left(\frac{-c^3M_{\dot\theta}}{8}\boldsymbol{\phi}_P\int_{x_P}^l dx\right) \\ \left(\frac{c^2a_We_\gamma}{2}\int_{x_P}^l\boldsymbol{\psi}^T\,dx\right) & \left(\frac{-c^3M_{\dot\theta}}{8}\int_{x_P}^l dx\,\boldsymbol{\phi}_P^T\right) & \left(\frac{-c^3M_{\dot\theta}}{8}\int_{x_P}^l dx\right) \end{bmatrix} \tag{6.40}$$

$$\mathbf{C} = -\begin{bmatrix} \mathbf{0}_{A,A} & \left(\begin{array}{c}\frac{ca_W}{2}\left(\int_0^{x_P}\boldsymbol{\psi}\boldsymbol{\phi}^T\,dx\right)\\ +\int_{x_P}^l\boldsymbol{\psi}\,dx\,\boldsymbol{\phi}_P^T\end{array}\right) & \left(\frac{ca_W}{2}\int_{x_P}^l\boldsymbol{\psi}\,dx\right) \\ \mathbf{0}_{B,A} & \left(\begin{array}{c}\frac{c^2a_We}{2}\left(\int_0^{x_P}\boldsymbol{\phi}\boldsymbol{\phi}^T\,dx\right)\\ +\boldsymbol{\phi}_P\boldsymbol{\phi}_P^T\int_{x_P}^l dx\end{array}\right) & \left(\frac{c^2a_We}{2}\boldsymbol{\phi}_P\int_{x_P}^l dx\right) \\ \mathbf{0}_{1,A} & \left(\frac{c^2a_We}{2}\int_{x_P}^l dx\,\boldsymbol{\phi}_P^T\right) & \left(\frac{c^2a_We_\gamma}{2}\int_{x_P}^l dx\right) \end{bmatrix} \tag{6.41}$$

6.3.4 Solving the aeroelastic equations of motion

Modal analysis of the unforced system

For free vibration, Eq. 6.38 reduces to

$$\mathbf{A}\ddot{\boldsymbol{\eta}} + \mathbf{E}\boldsymbol{\eta} = \mathbf{0} \tag{6.42}$$

With the assumption that the system oscillates harmonically with an undamped natural frequency ω, then the solution takes the form [141]

$$\boldsymbol{\eta}(t) = \mathbf{x}\sigma \exp(j\omega t) \tag{6.43}$$

where $\mathbf{x}$ is the shape/mode of vibration and σ is an amplitude. Substituting Eq. 6.43 into Eq. 6.42 gives

$$-\omega^2\mathbf{A}\mathbf{x} + \mathbf{E}\mathbf{x} = \mathbf{0} \tag{6.44}$$

Setting $\lambda = \omega^2$ gives

$$(\mathbf{E} - \lambda\mathbf{A})\,\mathbf{x} = \mathbf{0} \tag{6.45}$$

This is an eigenvalue problem that results in $A+B+1$ (the number of degrees of freedom) solutions for λ, the eigenvalues. The corresponding vectors $\mathbf{x_i}$, $i = 1, 2, \cdots A+B+1$ are the eigenvectors (mode shapes) of the system. For the i^{th} natural frequency, the corresponding mode shape describes the relative displacement of the physical coordinates.

Static aeroelastic response

For the static aeroelastic response, Eq. 6.38 reduces to

$$\left(\rho U^2\mathbf{C} + \mathbf{E}\right)\boldsymbol{\eta} = \rho U^2\alpha_r\mathbf{a}_r \tag{6.46}$$

Rearranging for the unknown generalised coordinates gives

$$\boldsymbol{\eta} = \left[\rho U^2 \mathbf{C} + \mathbf{E}\right]^{-1} \rho U^2 \alpha_r \mathbf{a}_r \tag{6.47}$$

and the generalised coordinates associated with bending, torsion and device pitching can then be extracted from $\boldsymbol{\eta}$ according to

$$\boldsymbol{\eta}^T = \begin{bmatrix} \boldsymbol{\zeta}^T & \boldsymbol{\beta}^T & \gamma \end{bmatrix} \tag{6.20}$$

where γ is the pitching of the device. $\boldsymbol{\zeta}$ and $\boldsymbol{\beta}$ can then be used with the shape functions given by Eqs. 6.3 and 6.4 to find $h(x)$ and $\theta(x)$, the bending and torsional displacements at spanwise coordinate x. γ, $h(x)$ and $\theta(x)$ are sufficient to completely describe the deformation of the wing under static aerodynamic loading. The coefficient of lift is given by

$$C_L = a_W \left(\alpha_r + \frac{1}{l} \int_0^l \alpha_e(x)\, dx \right) \tag{6.48}$$

where α_e is the elastic contribution to the angle of incidence i.e.

$$C_L = a_W \left(\alpha_r + \frac{1}{l} \int_0^{x_P} \theta\, dx + \frac{1}{l} (\theta_P + \gamma) \int_{x_P}^l dx \right) \tag{6.49}$$

Substituting the shape functions and generalised coordinates (Eqs. 6.3 and 6.4) into this gives

$$C_L = a_W \left(\alpha_r + \frac{1}{l} \int_0^{x_P} \sum_{b=1}^{B} \phi_b \beta\, dx + \frac{1}{l} \left(\sum_{b=1}^{B} \phi_{b_P} \beta + \gamma \right) \int_{x_P}^l dx \right) \tag{6.50}$$

Static aeroelastic stability analysis

For the static stability analysis, Eq. 6.38 reduces to

$$\left(\rho U^2 \mathbf{C} + \mathbf{E}\right) \boldsymbol{\eta} = \mathbf{0} \tag{6.51}$$

which can be expressed as

$$\Big(\mathbf{E} - q\left(-2\mathbf{C}\right)\Big)\boldsymbol{\eta} = \mathbf{0} \tag{6.52}$$

where q is the dynamic pressure. The lowest real and positive solution to this eigenvalue problem represents the divergence pressure q_d of the system [15].

Dynamic aeroelastic stability analysis [141]

For the dynamic stability analysis Eq. 6.38 reduces to

$$\mathbf{A}\ddot{\boldsymbol{\eta}} + \rho U\mathbf{B}\dot{\boldsymbol{\eta}} + \left(\rho U^2\mathbf{C} + \mathbf{E}\right)\boldsymbol{\eta} = \mathbf{0} \tag{6.53}$$

Introducing the trivial expression

$$\mathbf{I}\dot{\boldsymbol{\eta}} - \mathbf{I}\dot{\boldsymbol{\eta}} = \mathbf{0} \tag{6.54}$$

where $\mathbf{I}$ is the identity matrix of size $(A + B + 1) \times (A + B + 1)$ and combining it with Eq. 6.53 gives

$$\begin{bmatrix} \mathbf{I} & \mathbf{0} \\ \mathbf{0} & \mathbf{A} \end{bmatrix} \begin{bmatrix} \dot{\boldsymbol{\eta}} \\ \ddot{\boldsymbol{\eta}} \end{bmatrix} - \begin{bmatrix} \mathbf{0} & \mathbf{I} \\ -\left(\rho U^2\mathbf{C} + \mathbf{E}\right) & -\rho U\mathbf{B} \end{bmatrix} \begin{bmatrix} \boldsymbol{\eta} \\ \dot{\boldsymbol{\eta}} \end{bmatrix} = \begin{bmatrix} \mathbf{0} \\ \mathbf{0} \end{bmatrix} \tag{6.55}$$

Rearranging gives Eq. 6.55 in first order form:

$$\begin{bmatrix} \mathbf{I} & \mathbf{0} \\ \mathbf{0} & \mathbf{I} \end{bmatrix} \begin{bmatrix} \dot{\boldsymbol{\eta}} \\ \ddot{\boldsymbol{\eta}} \end{bmatrix} - \begin{bmatrix} \mathbf{0} & \mathbf{I} \\ -\mathbf{A}^{-1}\left(\rho U^2\mathbf{C} + \mathbf{E}\right) & -\mathbf{A}^{-1}\rho U\mathbf{B} \end{bmatrix} \begin{bmatrix} \boldsymbol{\eta} \\ \dot{\boldsymbol{\eta}} \end{bmatrix} = \begin{bmatrix} \mathbf{0} \\ \mathbf{0} \end{bmatrix} \tag{6.56}$$

i.e.

$$\mathbf{I}\dot{\mathbf{z}} - \mathbf{Q}\mathbf{z} = \mathbf{0} \tag{6.57}$$

where the identity matrix $\mathbf{I}$ is now of size $2\left(A+B+1\right) \times 2\left(A+B+1\right)$ and

$$\mathbf{Q} = \begin{bmatrix} \mathbf{0} & \mathbf{I} \\ -\mathbf{A}^{-1}\left(\rho U^2 \mathbf{C} + \mathbf{E}\right) & -\mathbf{A}^{-1}\rho U \mathbf{B} \end{bmatrix} \tag{6.58}$$

and

$$\mathbf{z} = \begin{bmatrix} \boldsymbol{\eta}^T & \dot{\boldsymbol{\eta}}^T \end{bmatrix}^T \tag{6.59}$$

Again, a harmonic oscillation is assumed and the solution takes the form

$$\mathbf{z} = \mathbf{y}\tau \exp\left(\lambda t\right) \tag{6.60}$$

where $\mathbf{y}$ is the shape of vibration and τ is an amplitude. Substituting Eq. 6.60 into Eq. 6.57 results in

$$\left(\mathbf{Q} - \lambda \mathbf{I}\right)\mathbf{y} = \mathbf{0} \tag{6.61}$$

This is an eigenvalue problem that for an oscillatory system results in $A+B+1$ complex conjugate pairs of eigenvalues. For the i^{th} mode, the eigenvalues are given by

$$\lambda_i = -\zeta_i \omega_i \pm j\omega\sqrt{1-\zeta_i^2} \tag{6.62}$$

where ω_i and and ζ_i are the undamped natural frequency and damping ratio respectively. For positive real parts of the eigenvalues the system is unstable. Furthermore, if the eigenvalues are real, the roots are non-oscillatory. Therefore Eqs. 6.58, 6.61 and 6.62 can be used to evaluate the stability of a mode at an airspeed of interest and to determine whether it is oscillatory or not.

Transient response to a discrete gust

For the transient response to a discrete gust, Eq. 6.38 reduces to

$$\mathbf{A}\ddot{\boldsymbol{\eta}} + \rho U \mathbf{B}\dot{\boldsymbol{\eta}} + \left(\rho U^2 \mathbf{C} + \mathbf{E}\right)\boldsymbol{\eta} = \rho U w_g \mathbf{a}_r \tag{6.63}$$

Using a similar method to that demonstrated in Eqs. 6.53 - 6.56 allows Eq. 6.63 to be written in first order form as

$$\begin{bmatrix} \mathbf{I} & \mathbf{0} \\ \mathbf{0} & \mathbf{I} \end{bmatrix} \begin{bmatrix} \dot{\boldsymbol{\eta}} \\ \ddot{\boldsymbol{\eta}} \end{bmatrix} - \begin{bmatrix} \mathbf{0} & \mathbf{I} \\ -\mathbf{A}^{-1}\left(\rho U^2 \mathbf{C} + \mathbf{E}\right) & -\mathbf{A}^{-1}\rho U \mathbf{B} \end{bmatrix} \begin{bmatrix} \boldsymbol{\eta} \\ \dot{\boldsymbol{\eta}} \end{bmatrix} = \begin{bmatrix} \mathbf{0} \\ \rho U w_g \mathbf{a}_r \end{bmatrix} \tag{6.64}$$

In this form the aeroelastic equations of motion are easily solved by numerical time integration [37]. For the current model, the ode45 solver (Dormand-Prince Runge-Kutta method [164]) provided by MATLAB® was used. Once $\boldsymbol{\eta}$ is found at a given time, it is straightforward to obtain the physical deformation of the wing (as described for the static aeroelastic response) and therefore the transient response can be obtained when this procedure is performed over the time history. A '1-cosine' gust was used for the analyses; the function that describes this is given by [141]

$$w_g(t) = \frac{w_{g_0}}{2}\left(1 - \cos\frac{2\pi U}{L_g}t\right) \tag{6.65}$$

where w_{g_0} is the maximum gust velocity and L_g is the length of the gust.

6.4 Parameter study using the aeroelastic model

The analyses described in section 6.3.4 were performed for the baseline wing (i.e. the wing without the device) and for the wing with the device. The model parameters used were $l = 1$ m, $c = 0.25$ m, $\bar{m}_W = 0.9375$ kg·m^{-3}, $e = 0.1$, $EI = 34.5$ N·m^2, $GJ = 65$ N·m^2, $a_W = 2\pi$, $\rho = 1.225$ kg·m^{-3} and $M_{\dot{\theta}} = -1.2$.

6.4.1 Analyses of the baseline system

To create the baseline system, x_P is set to l, and the matrices and vectors in 6.38 are reduced to remove the degree of freedom associated with the rotation of the device. The first five modes are described in table 6.1. The inertial coupling that exists in the structure gives rise to coupled mode shapes.

Table 6.1: Undamped natural frequencies of the baseline system.

Mode	Frequency [Hz]
(a) First bending	3.389
(b) Second bending and first torsion	20.889
(c) Second torsion	29.161
(d) Third bending and third torsion	58.717
(e) Fourth torsion	88.421

For the static aeroelastic response analysis, performed at $U_b = 10\ \mathrm{m{\cdot}s^{-1}}$ (baseline airspeed), with a wind-off incidence of 5°, the global lift coefficient was found to be $C_L = 0.55520$. The divergence speed was found to be $8.1869 U_b$, with mode (c) being the critical mode (see table 6.1).

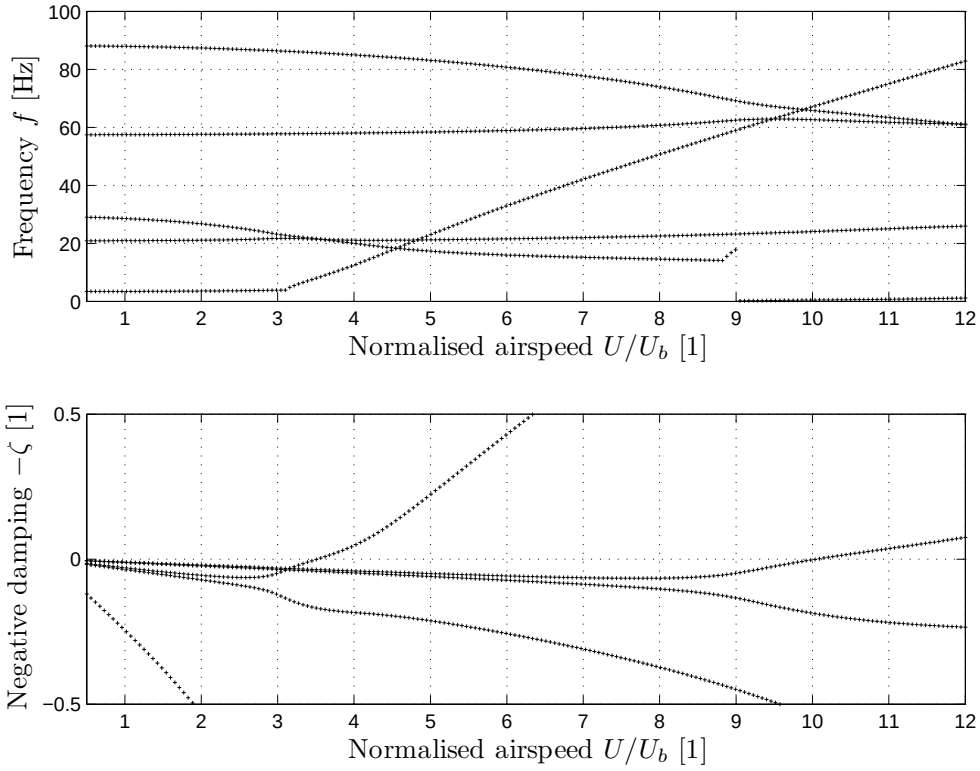

Figure 6.5: Frequency and damping trends for the first five modes of the baseline system.

The structure was found to flutter at $3.5628U_b$, with the coalescing frequencies of mode (b) and mode (c) providing the flutter mechanism. The frequency and damping plots for the first 5 modes are shown in figure 6.5. The damping plots show the onset of instability at around $3.5U_b$, and the frequency trends corresponding to this airspeed exhibit the coalescing frequency behaviour associated with classical binary flutter. The plots show another instability occurring at around 9 - $10U_b$; from the frequency plot this can be identified as the previously mentioned divergence mode (zero frequency).

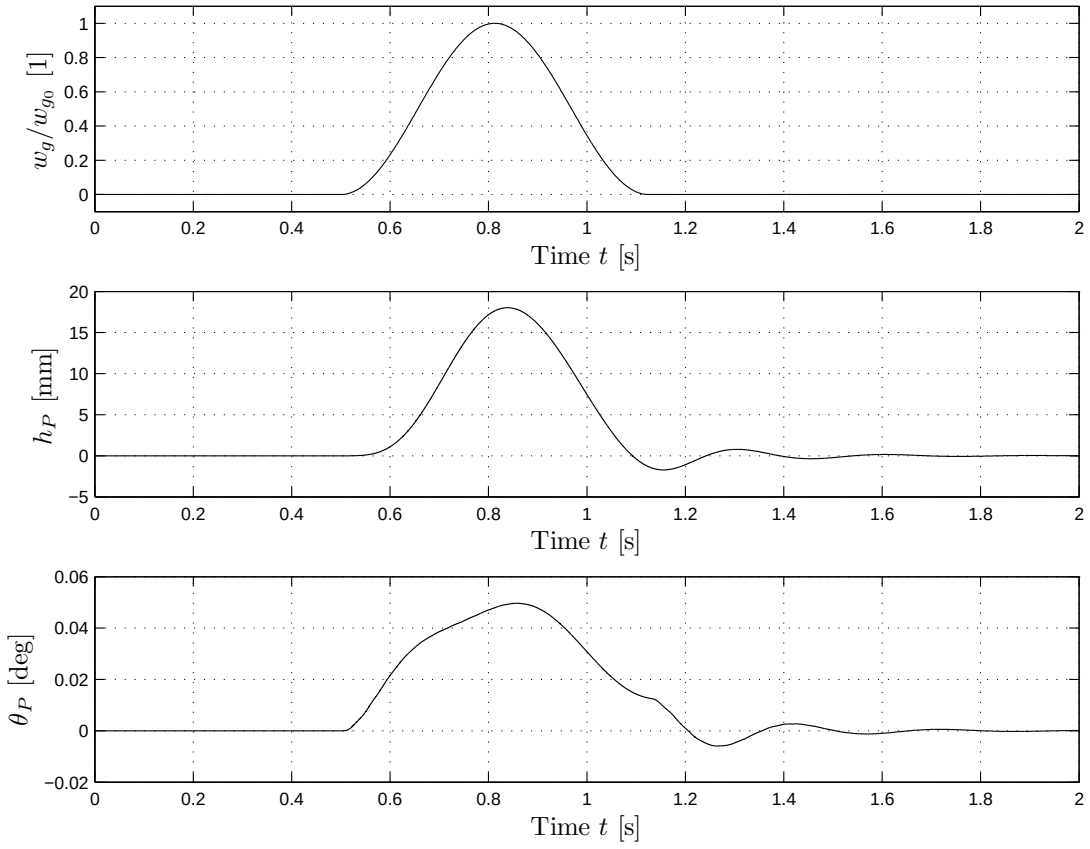

Figure 6.6: Gust response for the baseline system.

The gust analysis was performed at the baseline airspeed U_b. A '1-cosine' gust was used for the analysis. Using FAA regulations [1], the maximum gust w_{g_0} that the scaled aircraft should be designed for is $0.0986U_b$. The specified gust gradient distance (the distance required for the gust to build to a peak) is 12.5

mean chord lengths of the aircraft, with this chord measurement being 0.25 m.

The response of the wing (figure 6.6) was measured at point P, a point on the elastic axis at 60% span; this point was used as all future modifications would be made at points outboard of this, and therefore it would allow for a direct comparison. At this point, the maximum (absolute) plunge $h_{P_{\max}}$ of of the wing was found to be 18.021 mm.

6.4.2 Analyses of the modified system

The first five modes for the modified system are described in table 6.2 for $x_P/l = 0.7, y_P/c = 0$ and $k = 10$ N·m·rad^{-1}. Comparison with the modes of the baseline system given in table 6.1 reveals that the first four modes of the baseline system are present in the modified system (each with a device pitching motion included), and with the exception of second torsion, have near identical undamped natural frequencies. The first two modes of the baseline system have also been separated in the modified system by the additional mode of the device pitching.

Table 6.2: Undamped natural frequencies when the loads alleviation device is employed ($x_P/l = 0.7, y_P/c = 0, k = 10$ N·m·rad^{-1}).

Mode	Frequency [Hz]
(a) First bending and device pitching	3.136
(b) Device pitching	10.373
(c) Second bending, first torsion and device pitching	22.088
(d) Second torsion and device pitching	40.827
(e) Third bending, third torsion and device pitching	59.677

Figure 6.7a illustrates the variation of the divergence speed with attachment stiffness k for several different chordwise and spanwise positions of attachment. It can be seen that the device improves the divergence behaviour of the wing; this is due the fact that the attachment points lie ahead of the aerodynamic centre of

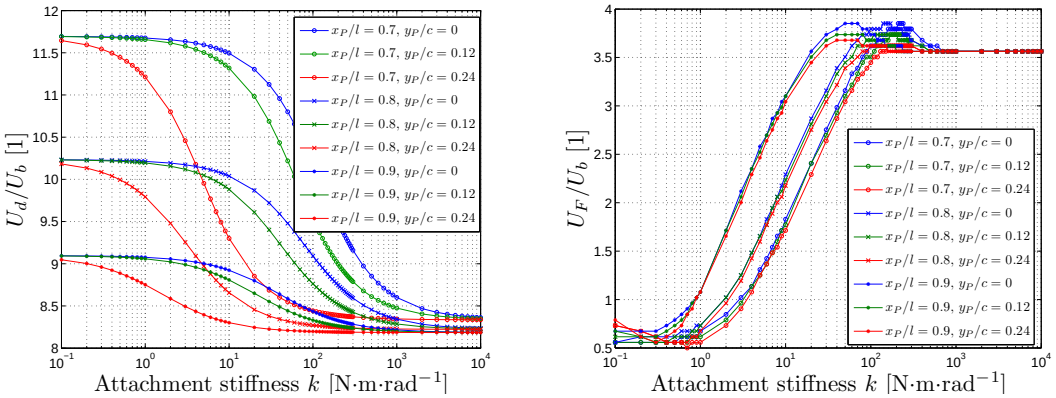

(a) Normalised divergence speed.

(b) Normalised flutter speed.

Figure 6.7: Aeroelastic stability behaviour when the loads alleviation device is employed.

the device and so a nose-down moment results, decreasing the angle of incidence of the device as the stiffness decreases. The result is reduced aerodynamic loads on the wing. Furthermore, the plot shows that in terms of divergence behaviour, the closer to the leading-edge of the wing the attachment point is, the better; this reflects the greater length of the moment arm between the aerodynamic centre and the axis of rotation. Finally, the closer the attachment point is to the wing root, the higher the divergence speed; as the main/inboard wing becomes shorter, its torsional stiffness increases, therefore increasing the divergence speed. The divergence speed at high stiffnesses agrees well with the baseline model ($8.1869U_b$), as expected.

Figure 6.7b illustrates the modified wing's flutter speed variation with attachment stiffness for different chordwise and spanwise positions of attachment. It is clear that the gust alleviation device has a detrimental effect on the flutter behaviour of the aircraft; as the stiffness of the device decreases, so too does the flutter speed. The significant range of stiffnesses that have a major impact on the flutter speed is approximately 1 - 100 N·m·rad^{-1}. The high stiffness flutter speeds agree well with the baseline model's prediction ($3.5628U_b$), as expected. It is also clear from figure 6.7b that the closer the attachment point is to the leading-edge and to the wing tip, the better, with regards to flutter behaviour.

The frequency and damping plots for the first 5 modes of the modified system (with $x_P/l = 0.7, y_P/c = 0$ and $k = 10$ N·m·rad^{-1}) are shown in figure 6.8. Comparison with figure 6.5 (equivalent plots for the baseline system) shows that the flutter speed has reduced significantly ($U_F = 1.8292U_b$, in agreement with figure 6.7b) as a result of the coupling of modes (a) and (b) (identified in table 6.2). A second incidence of flutter can be seen at around $5.2U_b$ due to the coupling of modes (c) and (d). Finally, the zero frequency instability (divergence) is not visible in the range of airspeeds considered, as expected.

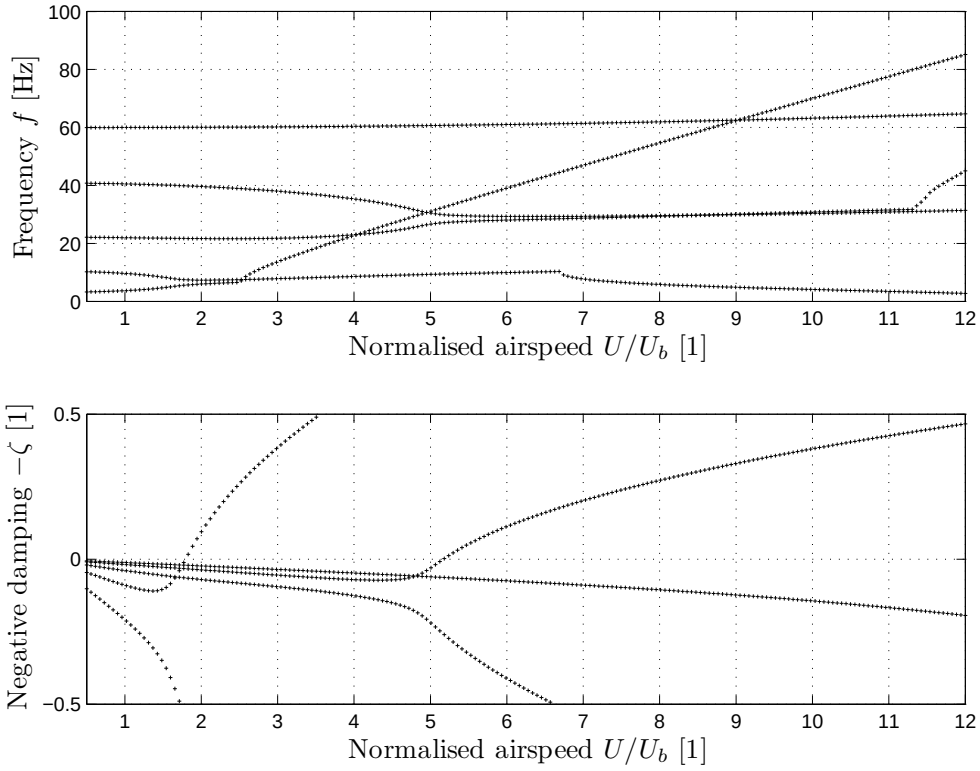

Figure 6.8: Frequency and damping trends for the first five modes when the loads alleviation device is employed ($x_P/l = 0.7, y_P/c = 0, k = 10$ N·m·rad^{-1}).

Figure 6.9a shows the variation of maximum plunge of the wing (at the attachment point P) with attachment stiffness, for several different chordwise and spanwise positions of attachment, during the response to the gust; these trends are significant as they provide an indication of the trends of the maximum stress in the structure. The minimum stiffness that was considered is approximately 3

N·m·rad^{-1}; below this the wing is fluttering, as shown in figure 6.7b.

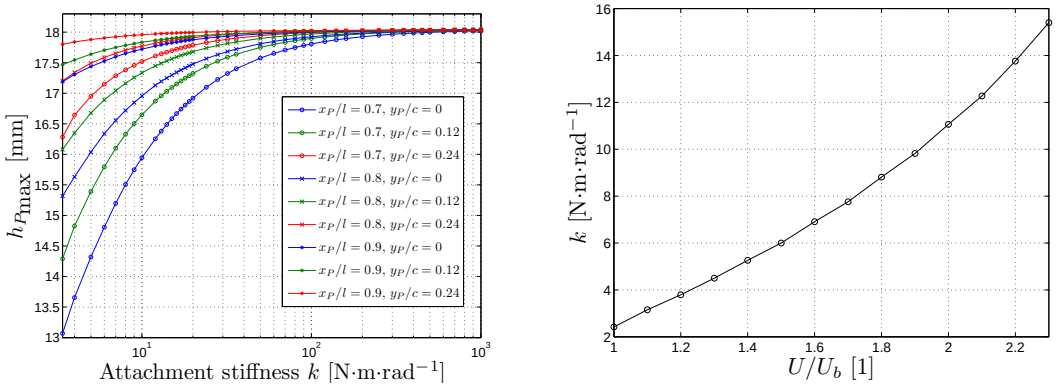

(a) Variation of maximum bending deflection at P at U_b.

(b) Variation of required attachment stiffness with airspeed to minimise $h_{P_{\max}}$ $(x_P/l = 0.7, y_P/c = 0)$.

Figure 6.9: Gust behaviour when the loads alleviation device is employed.

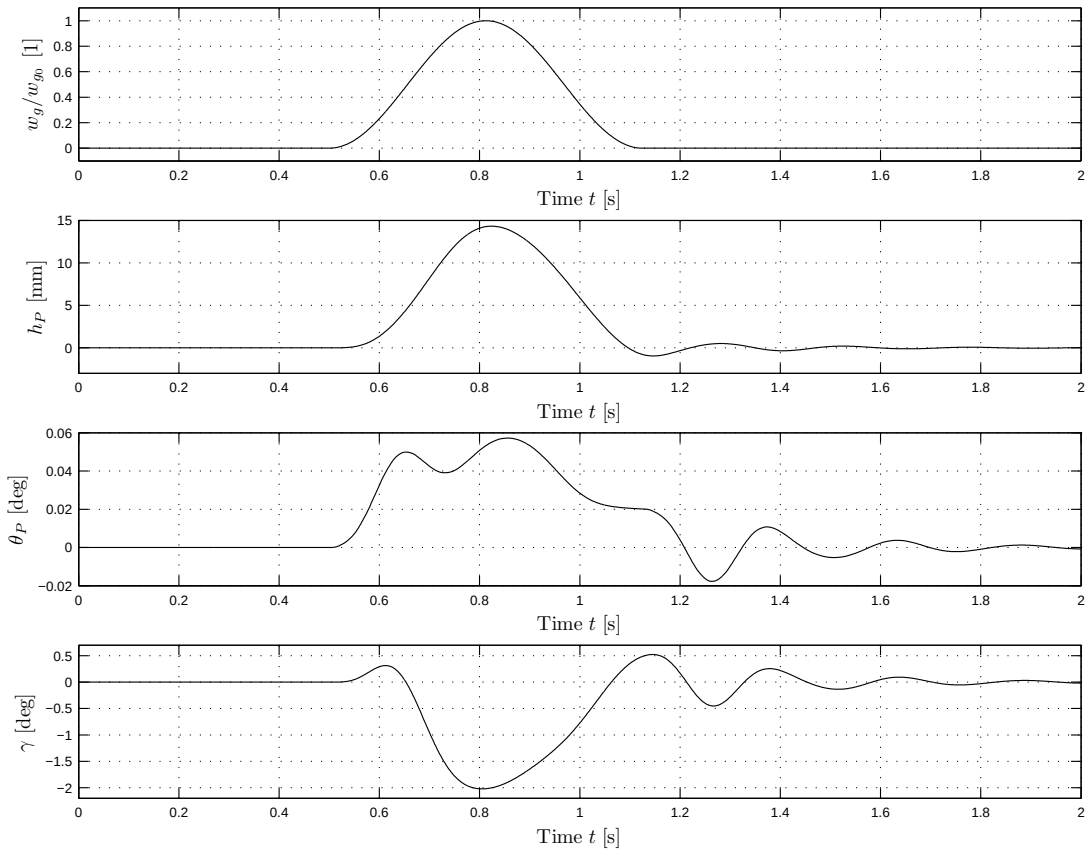

Figure 6.10: Gust response at U_b when the loads alleviation device is employed $(x_P/l = 0.7, y_P/c = 0, k = 5$ N·m·rad$^{-1})$.

The loads alleviation device allows the maximum bending deflection at P to be reduced from 18.021 mm to 13.070 mm (27.474% reduction). It can be seen that the further forward towards the leading-edge, and the further inboard towards the wing root the attachment point is, the more effective the device is at alleviating the deflections. Figure 6.9b shows that as the airspeed is varied, the attachment stiffness must also be varied in order to minimise the deflection of the structure that results from the gust, which demonstrates the advantage of an adaptive stiffness capability.

Figure 6.10 shows the response of the wing due to the gust when the device is employed. Comparison of this plot with figure 6.6 (the equivalent plots for the baseline system) shows a reduction in the bending deflection of the wing for the modified system, and to achieve this the device has rotated through 2°. The reduced damping in the system is also apparent from the wing's torsional response in particular.

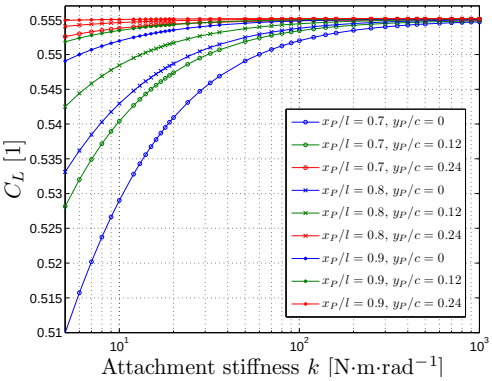

(a) Variation of lift coefficient with attachment stiffness at U_b.

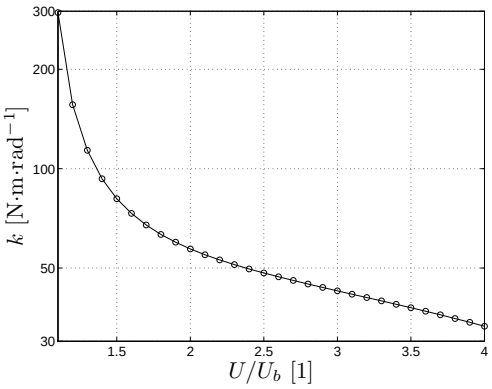

(b) Variation of required attachment stiffness with airspeed to trim the wing to the baseline C_L ($x_P/l = 0.7, y_P/c = 0$).

Figure 6.11: Static aeroelastic response when the loads alleviation device is employed.

From the static aeroelastic response analyses (see figure 6.11a), it was found that the device enables the lift coefficient to be reduced from 0.55520 to 0.51000 (8.141% reduction) at U_b; this demonstrates the trim capability of the device. This was further explored by establishing the range of k necessary to trim the

wing to the baseline C_L over a range of airspeeds (see figure 6.11b), which reinforces the benefits of an adaptive stiffness capability. At higher dynamic pressures the variation in C_L will be more significant and therefore a low frequency roll capability is also a possibility.

6.5 Case study for stress reduction

6.5.1 Description of the baseline platform

The platform chosen for the study was the Boeing 410E SensorCraft concept. From past collaborations with the US AFRL, much was known about this concept and therefore it represented a convenient choice of platform [16, 17, 107]. Furthermore, from previous work a scaled finite element representation of this baseline UAV was available [2, 97]. The aircraft has a joined-wing blended wing-body configuration with the forward wings swept back by 55° and with a dihedral of 7°, and the rear wings swept forward by 56° and with a anhedral of 9°. The full-scale model has a semi-span of approximately 23 m. The FE model used for the study was scaled to provide a basis for future wind tunnel tests and consists of an aluminium sub-structure and a shrink-wrap skin.

6.5.2 Aeroelastic analyses of the baseline system

The FE representation of the Boeing 410E SensorCraft concept was a 1:15 geometrically scaled right-hand half-model. The NASTRAN™ structural model (shown in figure 6.12) represents the fuselage, tailplane and skin with plate elements (CQUAD4), the spars (2 per wing) and tail boom with beam elements (CBEAM), and the ribs (12 in the forward wing, 10 in the rear) with plate elements (CTRIA3) [11].

The NASTRAN™ aerodynamic model (shown in figure 6.13) represents the lifting-surfaces (the two wings, the fuselage, and tailplane) with 600 CAERO1

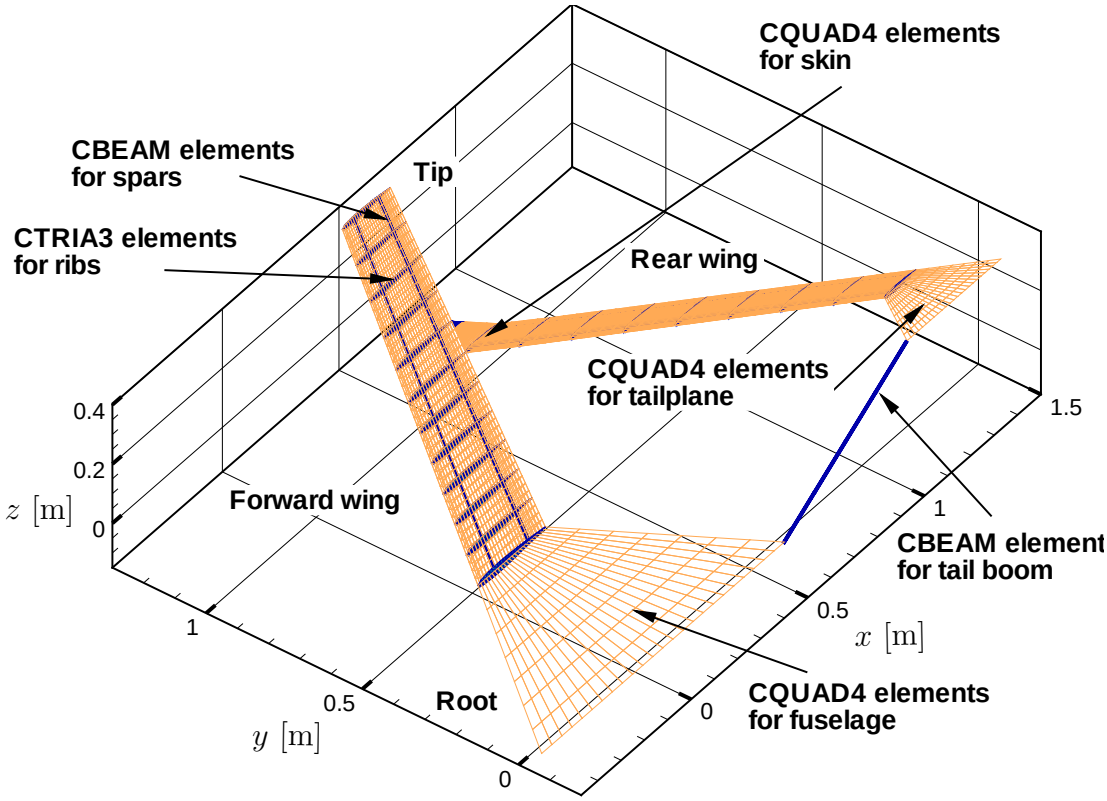

Figure 6.12: Finite element representation of the baseline structural model in the aerodynamic coordinate system.

aerodynamic panels. SPLINE1 algorithms provided the linear beam spline for transmitting the aerodynamic loads and motion between the aerodynamic and the structural model [116].

To establish the baseline system behaviour, the first step in the study was to perform the divergence (SOL 144), flutter (SOL 145 using the p-k method) and gust (SOL 146) analyses [116] of the unmodified wing model. Since it was intended to use the results of this study in future experimental studies, the analyses was performed using sea-level atmospheric conditions and an airspeed of 30 m·s^{-1} i.e. typical low-speed wind tunnel conditions. The divergence speed was found to be 80.846 m·s^{-1}, with bending of the forward wing being the critical mode. The structure was found to flutter at 66.373 m·s^{-1}, with the coalescing frequencies associated with mode 1 (rear wing bending and torsion) and mode 2 (first wing bending of both forward and rear wings). The dynamic aeroelastic analysis failed

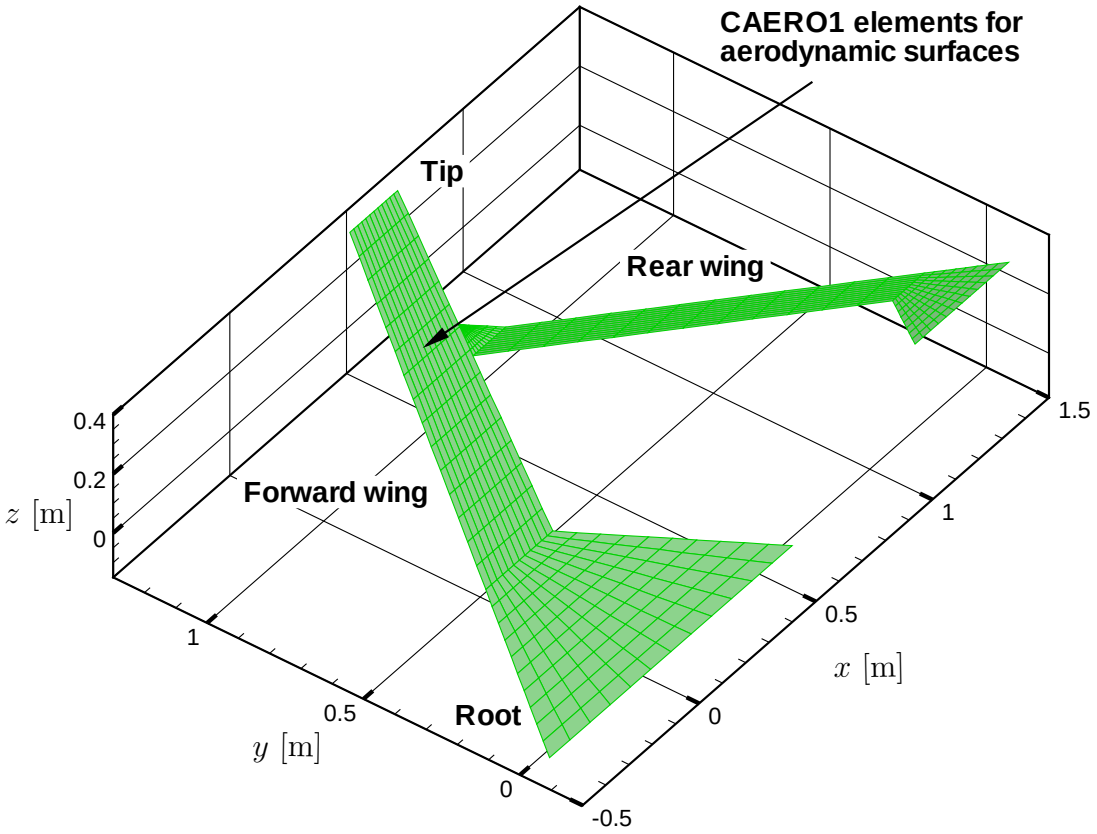

Figure 6.13: Finite element representation of the baseline aerodynamic model in the aerodynamic coordinate system.

to identify the divergence mode that occurred at 80.846 m·s^{-1}; instead it found another flutter mode here. The author was advised by MSC.Software technical support to accept the static analysis divergence solution in the case of such an inconsistency. The frequency and damping plots for the first 5 modes are shown in figures 6.14. With p an eigenvalue of the aeroelastic system, each damping value used in the plot is given by $\zeta = \mathrm{Re}\{p\}/\mathrm{Im}\{p\}$ [159].

The gust analysis was performed with a freestream velocity of 30 m·s^{-1}. A '1-cosine' gust was used for the analysis. As before, FAA regulations [1] dictated the maximum gust w_{g_0} that the scaled aircraft should be designed for as 2.957 m·s^{-1}.

The maximum (absolute) stress (which occurs in the rear spar of the forward wing at the root), σ_{root}, encountered during the response (see figure 6.15) to

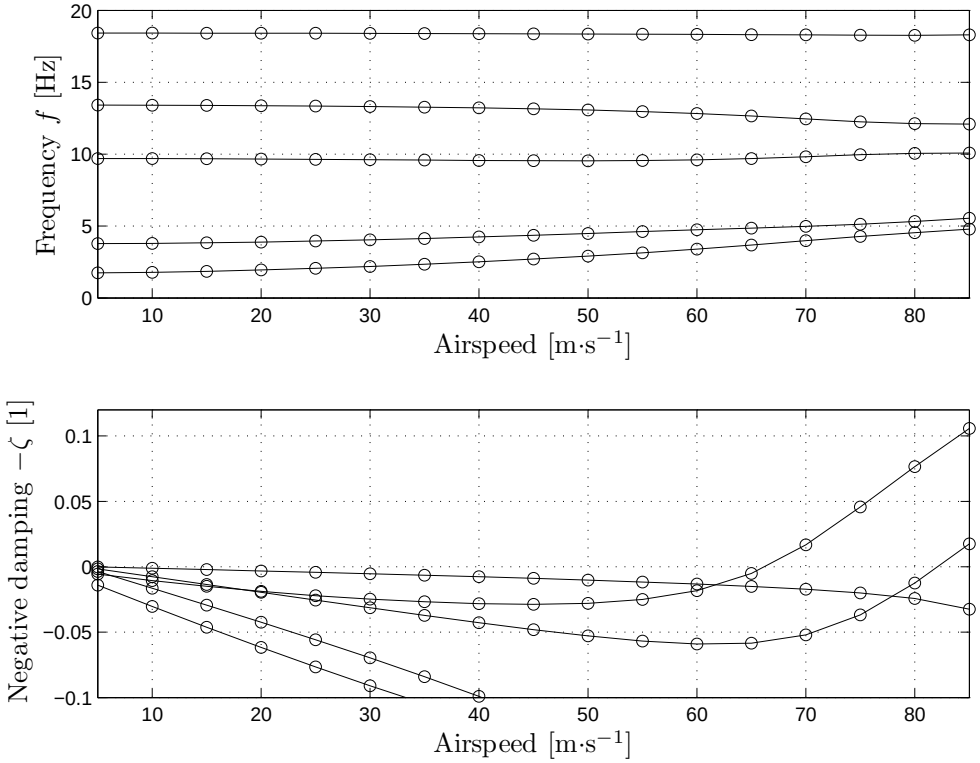

Figure 6.14: Frequency and damping trends for the first five modes of the baseline system.

the gust was found to be 146.361 MPa. A peak (absolute) twist of the wing at the tip was found to be 1.6805°. The response was also measured at the point P on the span (86%) where the wing would be modified; at this point the maximum (absolute) twist $\theta_{P_{\max}}$ encountered was 1.4825° and the maximum (absolute) bending $h_{P_{\max}}$ of the wing was 50.316 mm.

6.5.3 Aeroelastic analyses of the modified system

The wing was altered to include a loads alleviation device. This device replaced part of the outboard section of the forward wing (86 - 100% span) and was attached to the main wing via a torsional spring close to the leading-edge at point P, allowing it to pitch relative to the main wing with an associated stiffness (see figure 6.16 where the device has been aligned off-centre for demonstration purposes). The attachment spring was represented with a spring element (CELAS2),

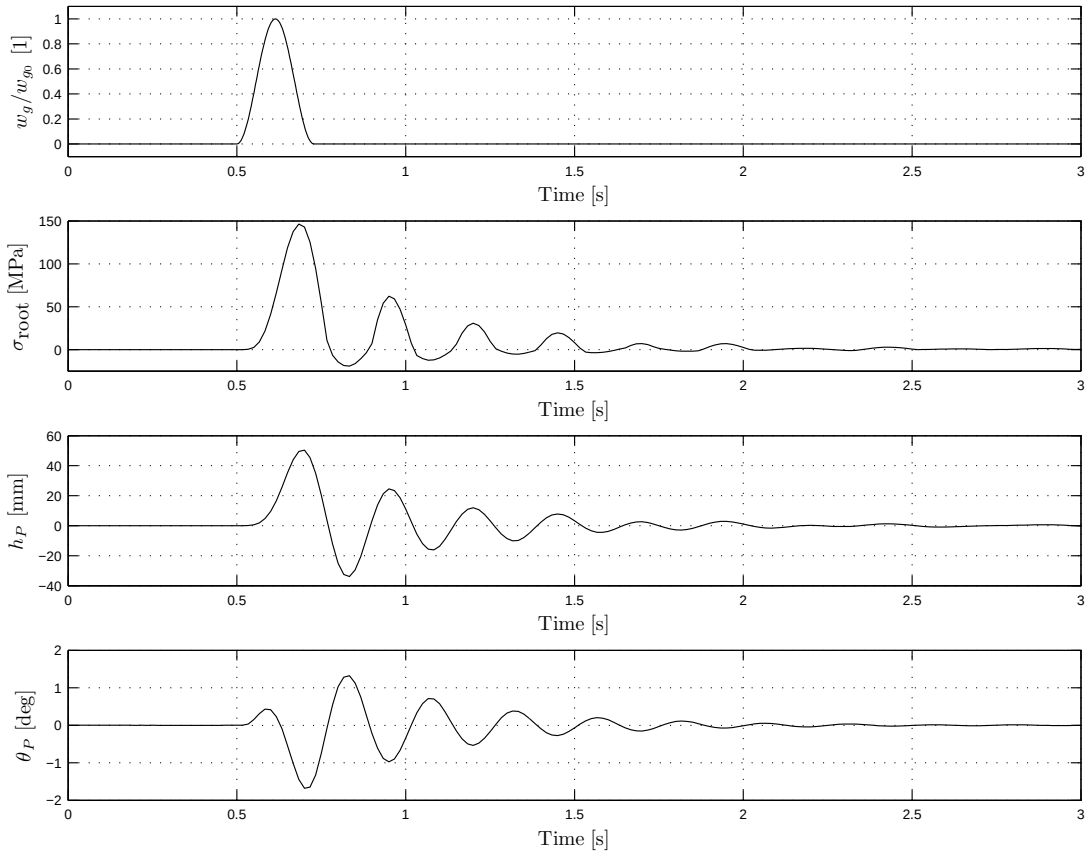

Figure 6.15: Gust response for the baseline system.

and an additional rib was placed at the attachment chordline. As the main wing pitches up in response to a gust (and by doing so increasing aerodynamic loads and resultant stresses), the device rotates about the spring (as the aerodynamic centre lies aft of this axis), decreasing its incidence and therefore decreasing aerodynamic loads.

Of interest in this study was the aeroelastic behaviour of the wing as both the stiffness of the attachment, as well as the chordwise position of the attachment point P were varied. Three attachment points that coincided with existing nodes in the model were considered; these are given in the aerodynamic coordinate system (unlike in sections 6.3 and 6.4) as $x_P/c = 0.0$, $x_P/c = 0.08307$ and $x_P/c = 0.1666$, with c the local chord length and x_P the chordwise distance from the leading-edge. Note that $x_P = 0$ corresponds to the leading-edge of

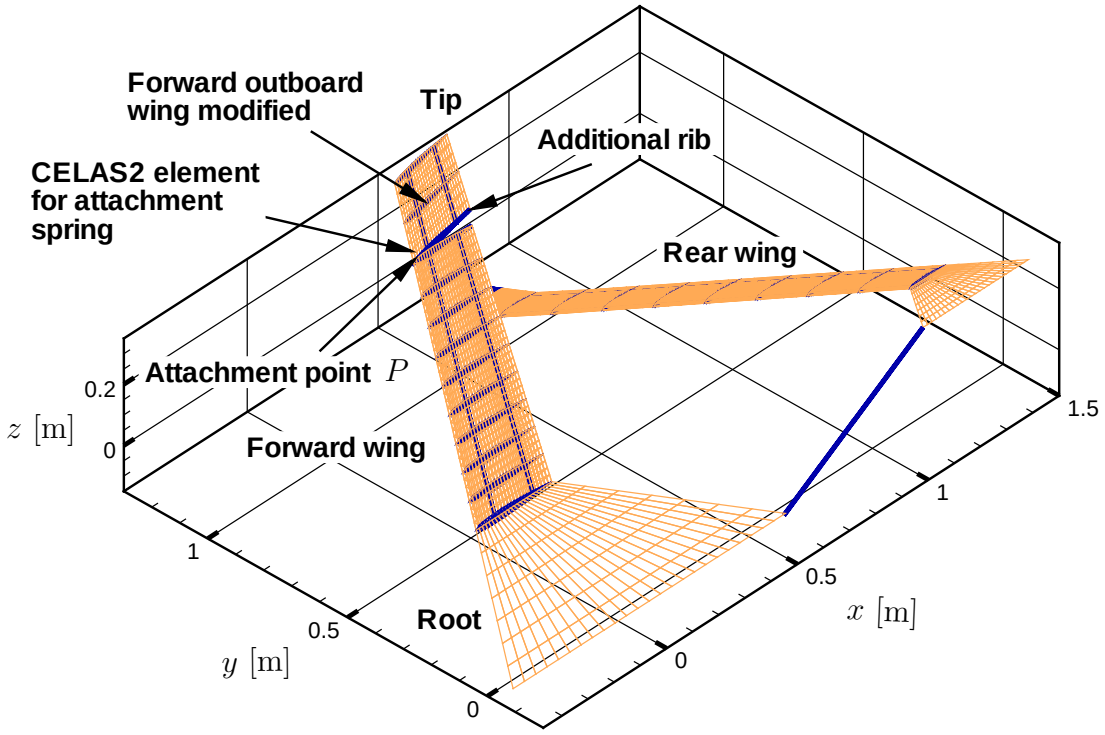

Figure 6.16: Finite element representation of the modified structural model in the aerodynamic coordinate system.

an arbitrary section and therefore the corresponding y-axis is parallel but not coincident to the aerodynamic y-axis shown in figures 6.12, 6.13 and 6.16.

Figure 6.17 illustrates the variation of the divergence speed with attachment stiffness k for several different chordwise positions of attachment. The critical divergence mode was found to be bending of the forward wing for stiffnesses approximately greater than 50 N·m·rad^{-1} and pitching of the device as well as rear wing bending for stiffnesses below this value.

Although the divergence speed barely alters over the range of stiffnesses considered, the device improves the divergence behaviour of the wing slightly, confirming the findings of section 6.4.2. With regards to the placement of the attachment, figure 6.17 also confirms the trends established in that section. The difference in the divergence speed at high stiffnesses from the original model (80.846 m·s^{-1}) is most likely due to structural modifications to include the device. However, the critical modes are identical.

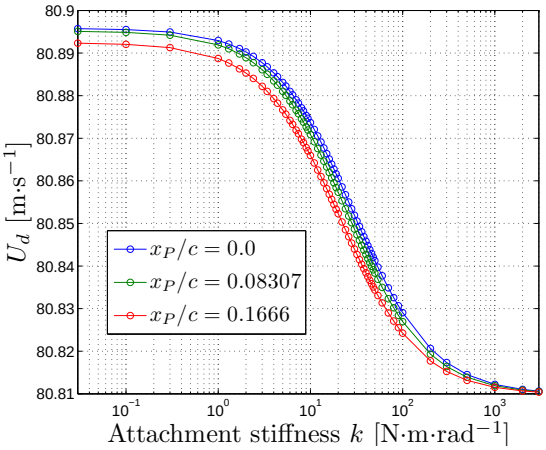

Figure 6.17: Divergence behaviour when the loads alleviation device is employed.

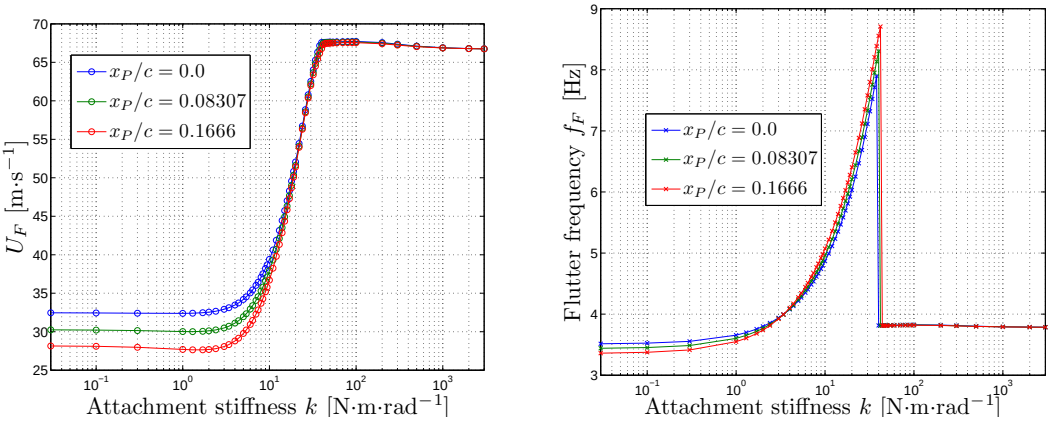

(a) Flutter speed.

(b) Flutter frequency.

Figure 6.18: Flutter behaviour when the loads alleviation device is employed.

Figure 6.18a illustrates the modified wing's flutter speed variation with attachment stiffness for various chordwise attachment points. The plots reinforce the results of the parameter study in section 6.4.2 in which it was established that the gust alleviation device has a detrimental effect on the flutter behaviour.

The significant range of stiffnesses that have a major impact on the flutter speed is approximately 5 - 40 N·m·rad^{-1}. At the upper end of this range a sharp levelling-off of the flutter speed is observed. This is caused by a change of modes causing the flutter, as can be more dramatically seen in figure 6.18b (variation of flutter frequency). The high stiffness flutter speeds agree well with the baseline model's prediction, as expected. Again, it is evident from figure 6.18a that the

closer the attachment point is to the leading-edge, the better, with regards to flutter behaviour.

Figure 6.19a shows the maximum stress in the wing during the response to the gust. For attachment points at $x_P/c = 0.08307$ and $x_P/c = 0.1666$ the plot ends abruptly because below the corresponding value of torsional stiffness the wing is fluttering. At 30 m·s^{-1} with the attachment point at the leading-edge

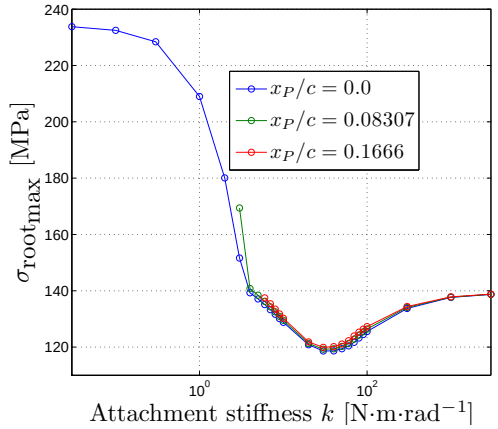

(a) Maximum stress in structure.

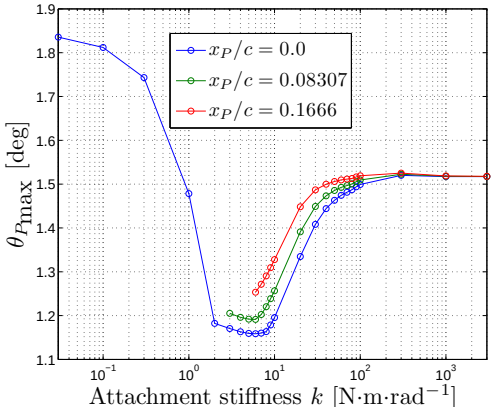

(b) Maximum twist of wing at attachment point.

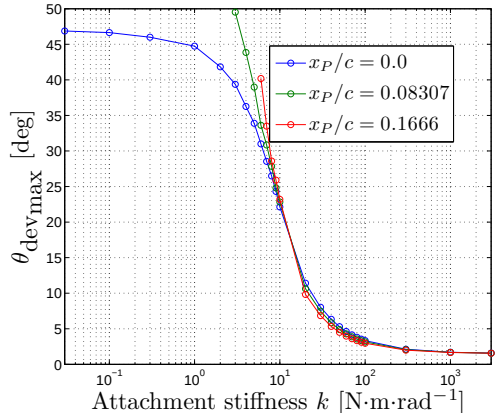

(c) Maximum pitch of device.

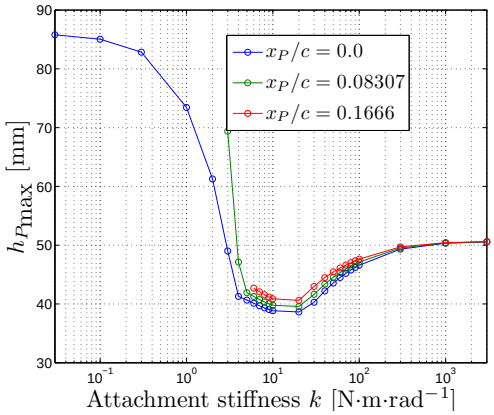

(d) Maximum bending of wing at attachment point.

Figure 6.19: Gust behaviour when the loads alleviation device is employed.

($x_P/c = 0.0$), the wing is free from flutter over the entire range of stiffnesses considered (see figure 6.18a). Figures 6.19b - 6.19d (displacement plots) show this behaviour too.

The loads alleviation device allows the maximum stress to be reduced from

146.361 MPa to 118.477 MPa (19.052% reduction). As expected, above a certain stiffness value, a decrease in the stiffness alleviates the stress in the structure. However, below this point the stress begins to increase again. This is due to the decrease of damping in the system. It can also be seen that the further forward the attachment point is, the more effective the device is at alleviating the stress. Figures 6.19b - 6.19d also show that a forward-placed attachment point is best at minimising displacements of the main wing.

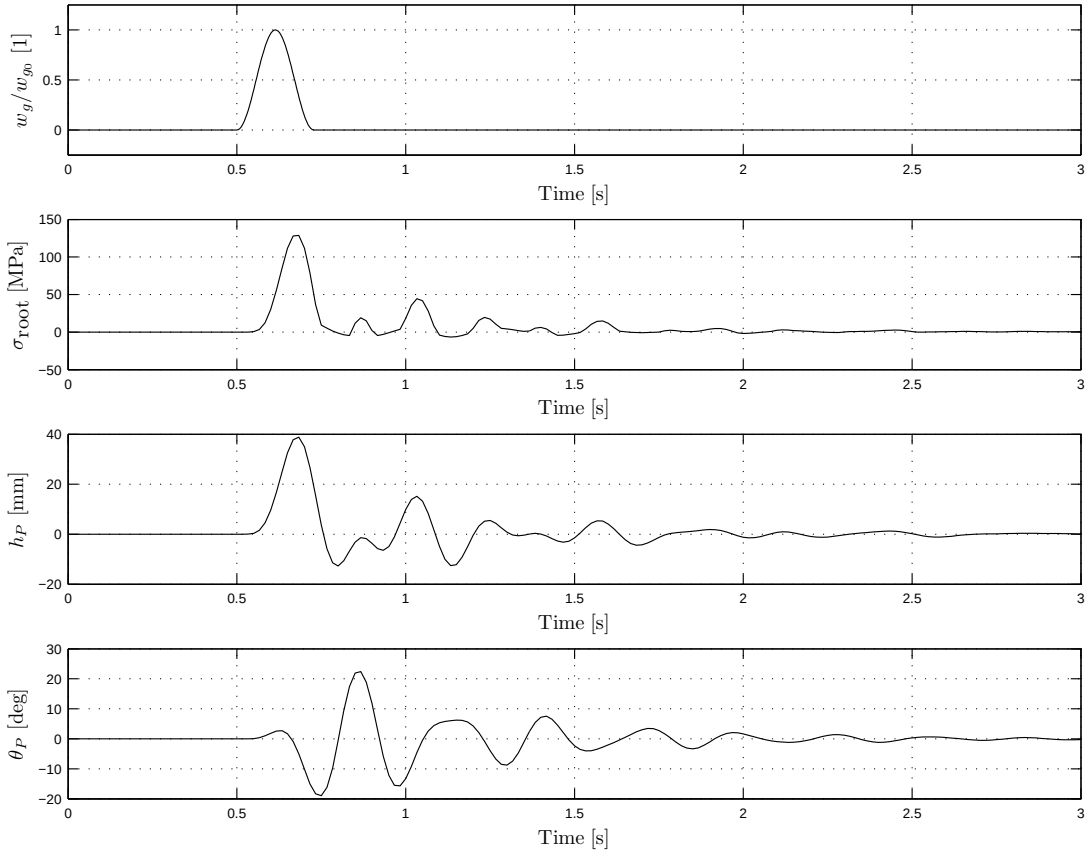

Figure 6.20: Gust history and response of wing with $k = 10$ N·m·rad^{-1} ($x_P/c = 0.0$).

Figures 6.20 and 6.21 show the behaviour of the wing due to the gust for two different values of stiffness ($k = 10$ N·m·rad^{-1} and $k = 30$ N·m·rad^{-1}), both at 30 m·s^{-1} and with an attachment point of $x_P/c = 0.0$. The most obvious difference is, as expected, the device pitches to much higher incidences with an associated lower stiffness. Also of interest, a non-exponential decay of the

response amplitude is seen for the lower stiffness, due to the lower damping in the system allowing an additional mode to become significant.

The high stiffness values of maximum stress (once again found in the rear spar of the forward wing at the root) are slightly below the original wing's value of 146.361 MPa; this can be attributed to structural modifications in the model. However, the corresponding values of wing twist, tip twist and bending (analysed at the attachment point to eliminate angular contributions from the device) are in good agreement with the original wing (1.4825°, 1.6805°, 50.316 mm respectively).

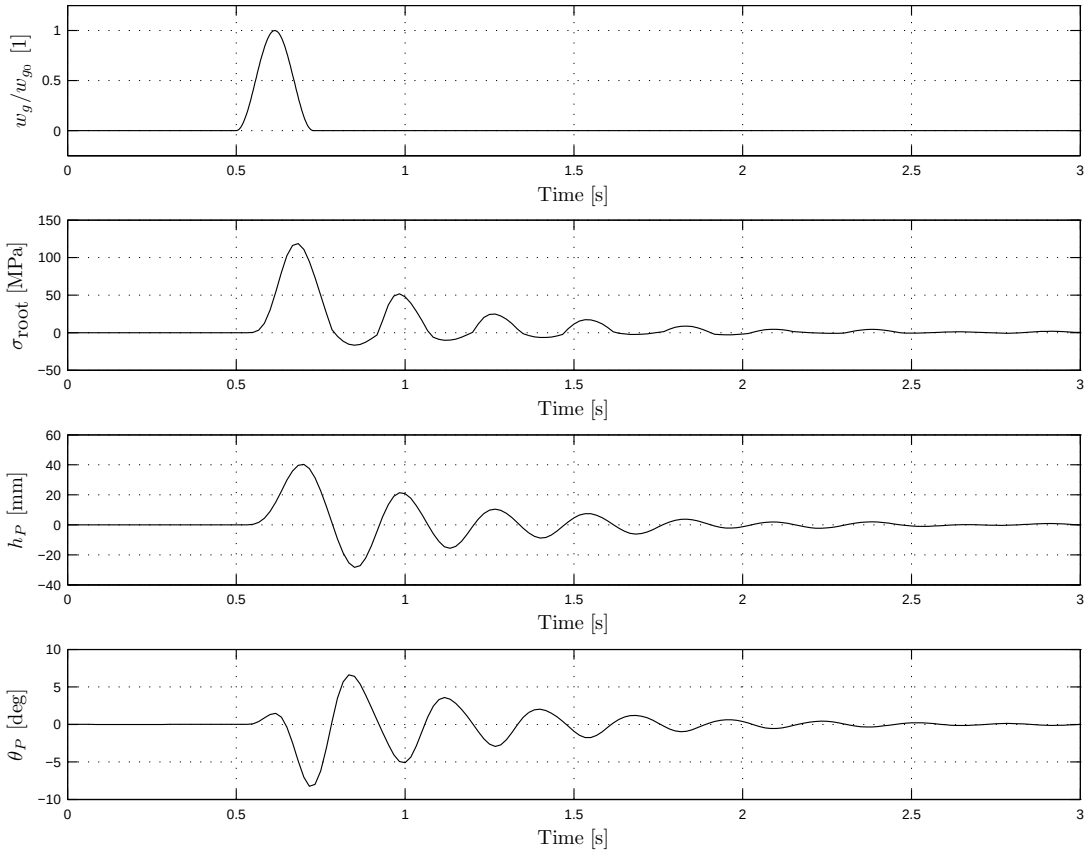

Figure 6.21: Gust history and response of wing with $k = 30$ N·m·rad^{-1} ($x_P/c = 0.0$).

6.6 Case study for mass reduction

In short, the motivation for incorporating a loads alleviation device onto an aircraft is to save mass, since the alternative method of improving the response would be to use a stiffer and therefore heavier aircraft structure. To demonstrate this, the model used in section 6.5 was used for a mass reduction exercise; from section 6.5 the maximum stress encountered in the baseline wing in response to a gust was 146.361 MPa and for the modified wing it was 118.477 MPa; using the maximum stress of the baseline model as the reference maximum allowable stress, the task then was to remove material from the modified structure to increase the maximum stress from 118.477 MPa to the reference value.

Two approaches to this problem were considered: uniform removal of material from all of the aircraft structure excluding the wing tip device, and an optimisation of the aircraft structure excluding the wing tip device with minimum mass and the reference stress value as the objective functions.

6.6.1 Uniform mass reduction

In this approach, all structural components (as shown in figure 6.12) in the model except those contained within the wing tip device region had identical percentages of certain dimensions reduced. For example, a 15% reduction in element dimension reduced the following dimensions by 15%: spar heights and thicknesses, rib thicknesses, skin thickness, fuselage thickness, tailplane thickness, tail boom height and thickness. This was done for approximately 50 different element reduction increments and for each of these models the maximum stress in response to the gust was recorded.

The results are shown in figure 6.22. The reference stress value is represented in figure 6.22a by the solid red line. It can be seen that, as the component dimensions are reduced, the maximum stress in the structure during the gust response increases, as expected. The stress returns to the reference value between

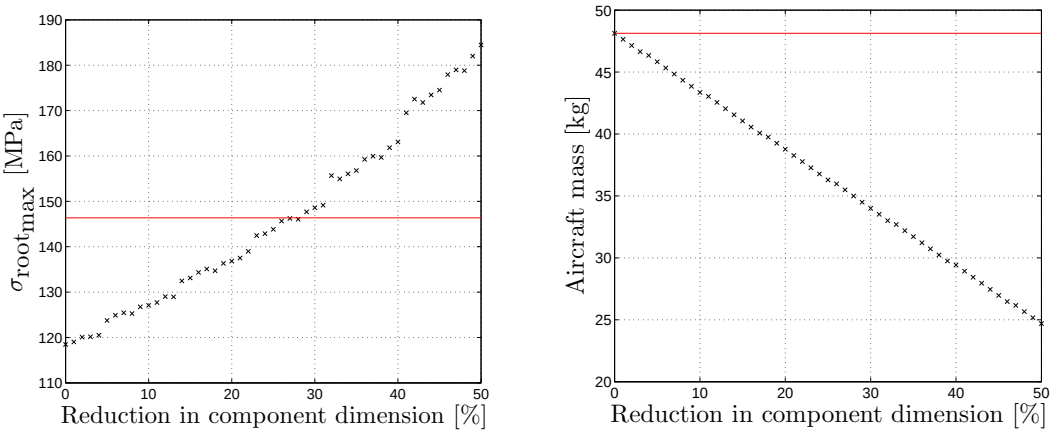

(a) Stress. (b) Mass.

Figure 6.22: Reduction in component sizes to return stress to reference value and reduce aircraft mass.

27% and 29% reduction in the component dimensions. In figure 6.22b the solid red line represents the original mass of the aircraft (48.133 kg). The mass reduces approximately linearly as the component dimensions decrease. At the reference stress value (corresponding to a 27 - 29% reduction in the component dimensions) the mass of the aircraft is 34.498 - 35.488 kg. This is equivalent to a 26.270 - 28.327% reduction in the aircraft mass.

6.6.2 Mass reduction via optimisation

The second approach to reducing the aircraft mass was to use a genetic algorithm optimisation (see section 4.4.3) routine to vary the component dimensions with a minimum aircraft mass and the reference stress value as the objective functions. Table 6.3 shows the range of the variables used in the optimisation, and the number of increments (N_i) considered.

Table 6.3: Parameter ranges.

Parameter	Min.	Max.	N_i
All rib thicknesses [mm]	1.1	20	2^4
Fuselage and tailplane thickness [mm]	10	30	2^3
Tail boom height and thickness [mm]	10	30	2^3
All spar thicknesses [mm]	1.1	20	2^4
Fwd. wing fwd. spar height [mm]	1.1	12.2	2^4
Fwd. wing rear spar height [mm]	1.1	6.5	2^4
Rear wing fwd. spar height [mm]	1.1	8.4	2^4
Rear wing rear spar height [mm]	1.1	4.4	2^4

The optimisation routine resulted in a maximum stress in the structure in response to a gust of 146.398 MPa (0.0253% difference from the reference stress) and the aircraft mass being reduced to 35.452 kg which is a reduction of 26.345%. The convergence iteration history, presented in figure 6.23, shows that the routine converges after approximately 20 iterations.

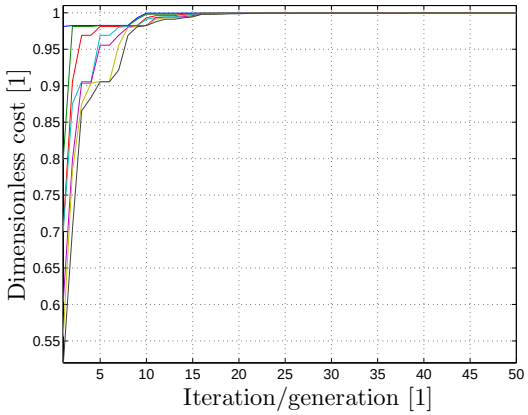

Figure 6.23: Convergence of cost function for the seven best genes/solutions.

Comparison of mass reduction results

The two approaches to the mass reduction problem arrived at very similar results, with the uniform mass reduction method reducing the aircraft mass by approximately 26 - 28%, and the optimisation approach reducing it by 26%. This is a significant mass saving which highlights the potential of the proposed loads alleviation device.

The component dimensions for the two methods as well as for the baseline wing are presented in tables 6.4 - 6.6. From these results it is clear to see the extent of the reductions, although some of the component dimensions have increased from the baseline model in the optimisation approach. One significant problem with the uniform reduction method is highlighted in these results; some of the solution values are not practical because they are so small that the components would be extremely difficult, if not impossible to manufacture. For instance, the forward spar in the forward wing has cross-sectional dimensions of 2.2 mm and 0.8 mm; clearly this could not be manufactured, given that the spar is over 1 m long and fabricated from aluminium. In contrast, the optimisation routine used realistic dimension ranges.

Table 6.4: Rib parameters.

Parameter	Baseline	Uniform mass reduction	Optimisation approach
Fwd. wing rib thicknesses (root to tip) [mm]	13.7	9.9	6.1
	11.2	8.1	6.1
	4.9	3.5	16.2
	12.4	8.9	6.1
	7.4	5.3	16.2
	3.6	2.6	3.6
	13.7	9.9	13.7
	1.1	0.8	3.6
	15.0	10.8	4.9
	17.5	12.6	13.7
Rear wing rib thicknesses (root to tip) [mm]	12.4	8.9	6.1
	16.2	11.7	13.7
	16.2	11.7	13.7
	12.4	8.9	20.0
	17.5	12.6	12.4
	20.0	14.4	17.5
	18.7	13.5	8.7
	6.1	4.4	20.0
	3.6	2.6	2.4
	18.7	13.5	4.9

Table 6.5: Spar parameters.

Wing	Spar	Parameter	Baseline	Uniform mass reduction	Optimisation approach
Fwd.	Fwd.	Height [mm]	2.0	1.4	7.8
		Thickness [mm]	4.8	3.5	3.6
	Rear	Height [mm]	3.0	2.2	1.1
		Thickness [mm]	1.1	0.8	1.1
Rear	Fwd.	Height [mm]	2.0	1.4	4.0
		Thickness [mm]	3.0	2.2	18.7
	Rear	Height [mm]	4.8	3.5	1.1
		Thickness [mm]	1.1	0.8	18.7

Table 6.6: Other component parameters.

Parameter	Baseline	Uniform mass reduction	Optimisation approach
Fuselage thickness [mm]	18.6	13.4	12.9
Tailplane thickness [mm]	30.0	21.6	18.6
Tail boom height [mm]	10.0	7.2	15.7
Tail boom thickness [mm]	10.0	7.2	27.1

6.7 Conclusions

The work presented in this chapter has helped to describe and develop an effective method for passive loads alleviation. An approximate aeroelastic model was developed and used as a tool to perform a parameter study into the concept, resulting in a 27% reduction in flexural deformation. Next, a case study was performed using a finite element representation of a SensorCraft platform; this included applications of the device to reduce the gust-induced stress by 19%, as well as to reduce the mass of the aircraft by 28%.

The studies with the approximate model and the finite element model both exhibited similar aeroelastic trends and identified the adaptive attachment stiffness requirement. In terms of the divergence behaviour, it is apparent that the loads alleviation device is beneficial to the wing; as the stiffness of the attachment decreases, the divergence dynamic pressure increases. However, this is not the case with flutter; in general, a decrease in attachment stiffness lowers the flutter dynamic pressure. However, above a certain stiffness, a further change in the stiffness has little effect on the flutter behaviour, as neither of the two modes involved in flutter at these stiffness values is associated with the device.

With regards to the gust response behaviour, in general the lower the stiffness of the device attachment, the more effective the device is at reducing gust-induced stress peaks; however, below a certain stiffness value the stress and deflections of the response increase again with decreasing stiffness, which reflects the fact that damping in the system is decreasing.

It was also shown that by varying the stiffness and location of the attachment, the lift could be altered; this has applications for roll control and also for trimming the aircraft.

It is the recommendation of the author that an attachment point as close to the wing's leading-edge as possible be used; this raises both the divergence and flutter dynamic pressures, and decreases gust-induced stresses and deflections,

as well as increasing the effectiveness of the device as a control surface. However, a compromise must be found with regards to the spanwise location of the attachment; as this point moves further away from the tip the divergence speed increases, the gust-induced stresses and deflections decrease and the effectiveness of the device as a control surface increases. However, there is a simultaneous reduction in the flutter speed, and this reinforces the adaptive stiffness requirement.

Chapter 7

Conclusions and future work

7.1 Conclusions

Two novel adaptive wing structures concepts have been explored. The development of a static aeroelastic model incorporating the rotating spars concept was presented, and analytical as well as experimental studies into the concept have been performed. Both of these approaches incorporated methods for automating control of the structure with varying degrees of success. The development of a dynamic aeroelastic model incorporating the loads alleviation device was demonstrated, and analytical studies using this and finite element models were performed.

The parameter studies and optimisation routines performed using the analytical model of the rotating spars wing led to the following conclusions:

- The structural parameter that is most affected by the concept is the wing's flexural rigidity, which is of significance for swept wings. The chordwise position of the elastic axis is also noticeably affected, whereas it is challenging to alter the torsional rigidity by any significant amount.
- Since most aeroelastic phenomena are torsional in nature, the inability of

the concept to enable significant changes in the torsional rigidity of the wing suggests that, for an arbitrary planform, the concept will not be effective.

- However, by carefully designing the wing, the large changes in flexural rigidity can be employed to benefit the performance; this can be realised through the use of a wing with sweep. The sweep introduces a bending-torsion coupling, therefore using the variations in the flexural rigidity to tailor the aerodynamic performance. In reality, this effect is reduced for forward swept wings since they are less aeroelastically stable than swept-back wings and therefore undergo large deformations at lower speeds than sweptback wings.

- Wings that have a medium-to-high aspect ratio ($\mathcal{AR} \geq 6$) are best suited to take advantage of the bending coupling that exists on swept planforms.

- The ratio of second moments of area of a rotating spar should be large ($I_{11}/I_{22} \geq 10$) to maximise the effectiveness of the concept. Care must be taken, however, to ensure that the spar will not be susceptible to lateral buckling.

- For a wing with two rotating spars, they should be positioned as far apart as possible to maximise the effectiveness of the concept. More precisely, the effectiveness of the concept improves as the distance that the elastic axis can vary by relative to the aerodynamic centre increases.

- The spar orientations required to minimise drag at the trim state change as the airspeed changes therefore demonstrating the requirement for an adaptive capability.

- An optimisation routine to minimise the drag at the trim state was performed successfully, providing the basis for control of the spars on the experimental wing.

The wind tunnel tests demonstrated the successful implementation of the rotating spars concept on an experimental swept wing. However, the tests also identified some challenges that were not obvious from the analytical studies. To summarise the findings of these tests:

- The results of the structural and aeroelastic parameter studies agreed well with the finite element predictions and showed that the lift-to-drag ratio of the wing could be altered by up to 15%.

- Measurements of the aerodynamic loads from the load balance were subject to high levels of noise, which presented problems when attempting to automate drag reduction of the trimmed wing. This was due to equipment limitations meaning that the range of the load balance was several orders of magnitude greater than the range of the loads generated by the wing.

- As a result of these high noise values, a regression approach to trim the wing and achieve minimum drag at the trim state failed.

- The optimisation routine used in the analytical study to minimise drag at the trim state also failed as a result of the noise.

- Using signals with lower noise levels (from the laser displacement system) allowed the regression and optimisation approaches to be tested for robustness. Once again, the regression approach failed. However, the optimisation approach resulted in the desired behaviour, and therefore it is the recommendation of the author that this type of approach be used rather than a regression model in future attempts to automate the trim or drag reduction procedures. The disadvantage of this approach is that it is a time-consuming method of control, which is in contrast to the near instantaneous regression approach; however, the frequency demands to maintain the optimum wing shape throughout the flight envelope are very low.

In addition to the points above, the following conclusions regarding the scaling-up of the rotating spars concept to full-size aircraft were noted:

- Most modern aircraft employ a semi-monocoque wing structure; in this design, a stressed skin is used and carries the majority of the load. The skin and spar caps provide the flexural rigidity, and the torsional load is resisted by the wing box, which comprises of the spar webs and upper and lower skins between the two main spars.

- The rotating spars concept works by altering the flexural rigidity of the spars; a large variation in the flexural rigidity of the spars will have only a small effect on the overall rigidity of a semi-monocoque wing, and therefore gains in aerodynamic performance will be unsubstantial.

- The degree of freedom required to permit rotation of the spars would interrupt the flow of shear in the semi-monocoque wing box structure, redistributing it around the periphery of the aerofoil structure; the leading- and trailing-edge skins would require stiffening, therefore increasing the weight of the wing.

- The concept has been applied throughout this work to an unstressed wing structure. This type of structure is well set-up for the concept as the majority of the structural strength is provided by the spars. However, it is not indicative of modern aircraft wing structures which use semi-monocoque wing structures.

- Practicality issues unrelated to structural problems would also arise if the rotating spars concept was used in modern aircraft. Spars typically double as fuel tank walls; rotating spars could not serve this purpose, creating the need for additional standalone bulkheads. The clearance required within the wing for rotation of the spars would also reduce the volume of usable space.

The parameter studies using the developed dynamic aeroelastic model of the wing incorporating the loads alleviation device, and the finite element case study with this device led to the following conclusions:

- In general, lower attachment torsional stiffness values and attachment positions closer to the leading-edge and further from the tip are most effective at reducing the stresses and deflections present in the structure in response to a gust. However, below a certain stiffness value the stresses and deflections increase again with decreasing stiffness, which reflects the decreasing damping in the system as the pitching mode of the device becomes less stable.

- In general, the loads alleviation device lowers the flutter dynamic pressure of the wing, and as the stiffness of the attachment decreases, so too does the flutter dynamic pressure. Consequently, care must be taken to avoid flutter within the flight envelope. Conversely, the device promotes static stability within the system, with the divergence dynamic pressure increasing as the attachment stiffness decreases.

- For the case study, a 19% reduction in the maximum stress in the structure in response to a gust was achieved. A separate exercise was performed to maintain original stress levels whilst using the loads alleviation device to reduce the aircraft mass; two independent approaches to this exercise showed that the device enabled the mass to be reduced by around 30%.

7.2 Suggestions for further work

Continuing work needs to be performed to realise the potential of both the adaptive structures concepts. For advancement in the research of the rotating spars concept the following areas were identified as critical to progress the work:

- Extend the assumed modes static aeroelastic model to provide the capability of a dynamic analysis; this would allow important constraints such as flutter to be included in the parameter studies and optimisation routines.

- The concept is most effective for rotating spars where the flexural rigidity in the plane of bending is large in comparison with the lateral flexural rigidity; however, such beams are susceptible to lateral buckling. It would therefore be useful to include a lateral buckling stability analysis as part of the rotating spars assumed modes structural model; this would make the analysis more realistic as it currently ignores this failure mechanism.

- Additionally, the inclusion of viscous flow would allow improved drag predictions to be made, therefore making the analytical study more realistic. This would require a completely fresh approach to the model (aeroelastic CFD), but given that drag reduction is the primary aim of the concept, the effort would be justified.

- I-beams and C-channel beams are predominantly used for constructing efficient wing spars, providing the required structural strength with the minimum weight. For proof-of-concept, it was convenient to use spars of rectangular cross-section in the current study. However, progress needs to made regarding the development of spar cross-sectional shapes that can be effectively incorporated into the rotating spars concept while simultaneously offering an efficient distribution of material. Further to that, the spars should also be resistant to lateral buckling.

- Future wind tunnel tests of the concept should ideally use a load balance with a measurement range better suited to the range of data expected from the model. This will reduce the time required to collect data since less averaging is required, and more significantly will enable the goal of automatic drag reduction to be achieved.

- It would also be of interest to explore and compare different actuators. The tests described in this work used servos as actuators since they are available off-the-shelf, but they are not necessarily the best option. The next step after this would be to perform a feasibility study; this would consider whether the likely mass and energy requirements of a rotating spars wing can be justified by the drag reductions it offers over a conventional wing. A comparison with other morphing concepts would also be useful.

Future work that would further research into the adaptive loads alleviation wing tip device was also identified:

- Extension of the in-house dynamic aeroelastic model to encompass more generic wing planforms; this would enable studies to be performed into how planform parameters such as sweep and taper affect the performance of the wing tip device.

- Research to establish the most suitable actuators and mechanisms to realise the adaptive capacity of the device; factors to consider include the energy requirements of an actuator and the practicality of embedding actuators and mechanisms in a typical modern aircraft wing.

- Incorporation of the loads alleviation device with adaptive capabilities into a wind tunnel model would be the logical progress to make. Parameter studies and attempts to automate the adaptive nature of the device would help to reinforce the analytical results.

- A detailed comparison of the wing tip device with alternative well-established loads alleviation technologies would be interesting and helpful. Key details to compare include performance, system weight and volume, reliability, energy requirements, fatigue life and anticipated maintenance requirements.

References

[1] Revised discrete gust load design requirements. *Federal Register*, 61(28):5217, 1996.

[2] A. Ainul, J.E. Cooper, and O. Sensburg. Development of a gust alleviation device. In *International Forum on Aeroelasticity and Structural Dynamics*, Stockholm, Sweden, 2007.

[3] M. Amprikidis and J.E. Cooper. Development of smart spars for active aeroelastic structures. In 44^{th} *AIAA/ASME/ASCE/AHS/ASC Structures, Structural Dynamics & Materials Conference*, Norfolk, Virginia, 2003.

[4] M. Amprikidis and J.E. Cooper. Experimental validation of wing twist control using adaptive internal structures. In 45^{th} *AIAA/ASME/ASCE/AHS-/ASC Structures, Structural Dynamics & Materials Conference*, Reno, Nevada, 2004.

[5] M. Amprikidis and J.E. Cooper. Development of an adaptive stiffness attachment for an all-moving vertical tail. In 46^{th} *AIAA/ASME/ASCE/AHS-/ASC Structures, Structural Dynamics & Materials Conference*, Austin, Texas, 2005.

[6] M. Amprikidis, J.E. Cooper, C. Rogerson, and G.A. Vio. Adaptive internal structures for active aeroelastic aircraft. In *International Forum on Aeroelasticity and Structural Dynamics*, Amsterdam, The Netherlands, 2003.

[7] M. Amprikidis, J.E. Cooper, C. Rogerson, and G.A. Vio. On the use of adaptive internal structures for wing shape control. In 46^{th} *AIAA/ASME-/ASCE/AHS/ASC Structures, Structural Dynamics & Materials Conference*, Austin, Texas, 2005.

[8] M. Amprikidis, J.E. Cooper, and O. Sensburg. Experimental investigation of an all-movable vertical tail model. In 44^{th} *AIAA/ASME/ASCE/AHS-/ASC Structures, Structural Dynamics & Materials Conference*, Norfolk, Virginia, 2003.

[9] M. Amprikidis, J.E. Cooper, and O. Sensburg. Initial development of an active aeroelastic all movable vertical tail. In 44^{th} *AIAA/ASME/ASCE-/AHS/ASC Structures, Structural Dynamics & Materials Conference*, Norfolk, Virginia, 2003.

[10] H. Ashley and M. Landahl. *Aerodynamics of wings and bodies*. Dover Publications, New York, USA, 1985.

[11] No author given. *MSC.Nastran 2005 r3 Quick Reference Guide*. MSC.Software Corporation, Santa Ana, California, 2006.

[12] Y. Bar-Cohen. *Biomimetics: biologically inspired technologies*. CRC Press, Florida, USA, 2005.

[13] S. Barbarino, S. Ameduri, L. Lecce, and A. Concilio. Wing shape control through an SMA-based device. *Journal of Intelligent Material Systems and Structures*, 20(3):283–296, 2009.

[14] J.D. Bartley-Cho, D.P. Wang, C.A. Martin, J.N. Kudva, and M.N. West. Development of high-rate, adaptive trailing edge control surface for the Smart Wing Phase 2 wind tunnel model. *Journal of Intelligent Material Systems and Structures*, 15(4):279–291, 2004.

[15] R.L. Bisplinghoff, H. Ashley, and R.L. Halfman. *Aeroelasticity*. Addison-Wesley, Massachusetts, USA, 1955.

[16] V. Bond and M. Blair. Free vibration modal data for the SensorCraft concept Boeing 410 E4-21R2. AFRL report of Boeing 410E finite element data, 2006.

[17] V. Bond, R. Canfield, J.E. Cooper, and M. Blair. Scaling for a static non-linear response of a joined-wing aircraft. In 12^{th} *AIAA/ISSMO Multidisciplinary Analysis and Optimization Conference*, Victoria, British Columbia, 2009.

[18] K.L. Bonnema and B. Stephen. AFTI/F-111 Mission Adaptive Wing flight research program. In 4^{th} *AIAA Flight Test Conference*, San Diego, California, 1988.

[19] P. Bourdin, A. Gatto, and M.I. Friswell. The application of variable cant angle winglets for morphing aircraft control. In 24^{th} *Applied Aerodynamics Conference*, San Francisco, California, 2006.

[20] P. Bourdin, A. Gatto, and M.I. Friswell. Aircraft control via variable cant-angle winglets. *Journal of Aircraft*, 45(2):414–423, 2008.

[21] J. Bowman, B. Sanders, B. Cannon, J. Kudva, S. Joshi, and T. Weisshaar. Development of next generation morphing aircraft structures. In *AVT-168 Morphing Aircraft Symposium*, Évora, Portugal, 2009.

[22] G. Brown, R. Haggard, and B. Norton. Inflatable structures for deployable wings. In 16^{th} *AIAA Aerodynamic Decelerator Systems Technology Conference and Seminar*, Boston, Massachusetts, 2001.

[23] R.G. Budynas. *Advanced strength and applied stress analysis*. WCB/McGraw-Hill, Massachusetts, USA, second edition, 1999.

[24] P.C. Chen, D. Sarhaddi, R. Jha, D.D. Lui, K. Griffin, and R. Yurkovich. Variable Stiffness Spar approach for aircraft manoeuvre enhancement using ASTROS. *Journal of Aircraft*, 37(5):865–871, 2000.

[25] S. Chick, P.J. Sánchez, D. Ferrin, and D.J. Morrice. Practical introduction to simulation optimization. In *2003 Winter Simulation Conference*, New Orleans, Louisiana, 2003.

[26] E.K.P. Chong and S.H. Zak. *An introduction to optimization*. Wiley-Interscience series in discrete mathematics and optimization. Wiley, New York, USA, second edition, 2001.

[27] A.R. Collar. The first fifty years of aeroelasticity. *Aerospace Journal*, 10(3):350–391, 1978.

[28] J.E. Cooper. *Gradient methods*. Introductory course to design optimisation, The University of Manchester and ERCOFTAC, 2005.

[29] J.E. Cooper and M. Amprikidis. On the use of adaptive aeroelastic structures to optimise aeroelastic performance. In *CEAS/KATnet Conference on Key Aerodynamic Technologies*, Bremen, Germany, 2005.

[30] J.E. Cooper, M. Amprikidis, S. Ameduri, A. Concilio, J. San Millán, and M. Castañón. Adaptive stiffness systems for an active all-moving vertical tail. In 1^{st} *European Conference for Aerospace Sciences (EUCASS)*, Moscow, Russia, 2005.

[31] J.E. Cooper, V. Hodigere-Siddaramaiah, G.A. Vio, S. Miller, and G. Dimitriadis. Adaptive aeroelastic structures for improved aircraft performance. In *World Forum on Smart Materials and Smart Structures Technology*, Chongqing and Nanjing, China, 2007.

[32] J.E. Cooper, O. Sensburg, and M. Amprikidis. A variable stiffness concept

for efficient aircraft vertical tail design. EOARD Contract FA8655-02-1-3085, September 2003.

[33] G.A.O. Davies. *Virtual work in structural analysis*. Wiley, Chichester, England, 1982.

[34] L.D. Davis et al. *Evolutionary algorithms*, volume 111 of *The IMA volumes in mathematics and its applications*. Springer, New York, USA, 1999.

[35] M. Dorigo and C. Blum. Ant colony optimization theory: a survey. *Theoretical Computer Science*, 344(2), 2005.

[36] M. Dorigo and Stützle. *Ant colony optimization*. The MIT Press, Massachusetts, USA, 2004.

[37] E.H. Dowell et al. *A modern course in aeroelasticity*. Solid mechanics and its applications. Kluwer Academic, London, England, fourth edition, 2004.

[38] R. Eberhart and J. Kennedy. A new optimizer using particle swarm theory. In 6^{th} *International Symposium on Micro Machine and Human Science*, Nagoya, Japan, 1995.

[39] D. Eller and S. Heinze. An approach for induced drag minimization and its experimental evaluation. In *45th AIAA/ASME/ASCE/AHS/ASC Structures, Structural Dynamics & Materials Conference*, 2004.

[40] R. Enoiu and G. Dragusin. Application of vortex lattice methods to analyze the performance of a glider. *Fascicle of Management and Technological Engineering*, 6(16):488–497, 2007.

[41] J.R. Florance, C.V. Spain, W.A. Silva, J. Heeg, T.G. Ivanco, and C.D. Wieseman. Variable Stiffness Spar wind tunnel model development and testing. In 45^{th} *AIAA/ASME/ASCE/AHS/ASC Structures, Structural Dynamics & Materials Conference*, Palm Springs, California, 2004.

[42] P.E. Fontenoy. *Aircraft carriers: an illustrated history of their impact*. ABC-CLIO, California, USA, 2006.

[43] T. Ford. Continuing wing production. *Aircraft Engineering and Aerospace Technology*, 70(1):9–14, 1998.

[44] T. Ford. Fly-by-wire and interactions. *Aircraft Engineering and Aerospace Technology*, 71(5), 1999.

[45] Y.C. Fung. *An introduction to the theory of aeroelasticity*. Dover Publications, New York, USA, 1993.

[46] A. Gatto, F. Mattioni, and M.I. Friswell. Experimental investigation of bistable winglets to enhance wing lift takeoff capability. *Journal of Aircraft*, 46(2):647–655, 2009.

[47] J.M. Gere. *Mechanics of materials*. Pacific Grove, California, USA, 2004.

[48] F. Gern, D.J. Inman, and R.K Kapania. Structural and aeroelastic modeling of general planform wings with morphing airfoils. *AIAA Journal*, 40(4):628–637, 2002.

[49] D.E. Gevers. *U.S. Patent Number 5,645,250*. U.S. Patent and Trademark Office, District of Columbia, USA, 1997.

[50] J.H. Ginsberg. *Advanced engineering dynamics*. Cambridge University Press, Cambridge, England, second edition, 1998.

[51] F. Glover and G.A. Kochenberger. *Handbook of metaheuristics*. Kluwer Academic, Massachusetts, USA, 2003.

[52] W. Green and G. Swanborough. *An illustrated anatomy of the world's fighters*. MBI Publishing Company, Minnesota, USA, 2001.

[53] I. Griva, S.G. Nash, and A. Sofer. *Linear and nonlinear optimization.* Society for Industrial and Applied Mathematics, Pennsylvania, USA, second edition, 2009.

[54] K. Gurney. *An introduction to neural networks.* CRC Press, London, UK, 1997.

[55] J.R. Hansen. *The bird is on the wing: aerodynamics and the progress of the American airplane.* TAMU Press, Texas, USA, 2004.

[56] R.L. Haupt and S.E. Haupt. *Practical genetic algorithms.* Wiley-Interscience, New Jersey, USA, 2004.

[57] E.J. Hearn. *Mechanics of materials*, volume 1 of *International Series on Materials Science and Technology.* Pergamon Press, Oxford, England, second edition, 1985.

[58] E.J. Hearn. *Mechanics of materials*, volume 2 of *International Series on Materials Science and Technology.* Pergamon Press, Oxford, England, second edition, 1985.

[59] C.P. Heins. *Bending and torsional design in structural members.* D.C. Heath, London, England, 1975.

[60] J. Hesser and R. Männer. *Towards an optimal mutation probability for genetic algorithms.* Lecture notes in Computer Science. Springer, Berlin, Germany, 2006.

[61] D.H. Hodges and G.A. Pierce. *Introduction to structural dynamics and aeroelasticity.* Cambridge aerospace series. Cambridge University Press, Cambridge, England, 2002.

[62] V. Hodigere-Siddaramaiah. *Adaptive internal structural concepts.* PhD thesis, University of Manchester, 2009.

[63] V. Hodigere-Siddaramaiah, J.E. Cooper, G.A. Vio, and G. Dimitriadis. Drag minimisation using adaptive aeroelastic structures. In 48^{th} *AIAA-/ASME/ASCE/AHS/ASC Structures, Structural Dynamics, and Materials Conference*, Honolulu, Hawaii, 2007.

[64] N.J. Hoff. *The analysis of structures: based on the minimal principles and the principle of virtual displacements*. Wiley, New York, USA, 1956.

[65] E.L. Houghton and P.W. Carpenter. *Aerodynamics for engineering students*. Butterworth-Heinemann, Oxford, England, fifth edition, 2003.

[66] J.D. Jacob, S.W. Smith, D. Cadogan, and S. Scarborough. Expanding the small UAV design space with inflatable wings. In *AeroTech Congress and Exhibition*, Los Angeles, California, 2007.

[67] P.J. Jacob and A.D. Ball. Empirical validation of the performance of a class of transient detector. In *AISB International Workshop*. Springer, April 1997.

[68] A. Johnson and K. Sherwin. *Foundations of mechanical engineering*. Nelson Thornes, Cheltenham, UK, second edition, 2001.

[69] J. Kacprzyk, O. Castillo, P. Melin, and W. Pedrycz. *Soft computing for hybrid intelligent systems*. Springer, Berlin, Germany, 2008.

[70] J. Katz and A. Plotkin. *Low-speed aerodynamics*. Cambridge University Press, Cambridge, England, second edition, 2001.

[71] J.F. Kennedy and R.C. Eberhart. *Swarm intelligence*. Morgan Kaufmann Publishers, California, USA, 2001.

[72] K.C. Khurana. *Aviation management: Global perspectives*. Global India Publications, New Delhi, India, 2009.

[73] S. Kirkpatrick. Optimization by simulated annealing: quantitative studies. *Journal of Statistical Physics*, 34(5), 1984.

[74] B. Kocivar. PS aviation editor takes a ride in the F-14. *Popular Science*, pages 88–90, July 1977.

[75] B. Kocivar. Tilt-rotor VTOL. *Popular Science*, pages 68–70, February 1978.

[76] C.F. Kollbrunner and K. Basler. *Torsion in structures: an engineering approach*. Springer-Verlag, Berlin, Germany, 1969.

[77] S. Kota, R. Osborn, G. Ervin, and D. Maric. Mission Adaptive Compliant Wing - design, fabrication and flight test. In *AVT-168 Morphing Aircraft Symposium*, Évora, Portugal, 2009.

[78] J.N. Kudva. Overview of the DARPA Smart Wing Project. *Journal of Intelligent Material Systems and Structures*, 15(4):261–267, 2004.

[79] A.M. Kuethe and C. Chow. *Foundations of aerodynamics: bases of aerodynamic design*. Wiley, New York, USA, fourth edition, 1986.

[80] C. Lan and J. Roskam. *Airplane aerodynamics and performance*. Design, Analysis and Research Corporation, Kansas, USA, 2003.

[81] J.G. Leishman. *Principles of helicopter aerodynamics*. Cambridge University Press, New York, USA, second edition, 2006.

[82] E. Livne and T.A. Weisshaar. Aeroelasticity of nonconventional airplane configurations - past and future. *Journal of Aircraft*, 40(6):1047–1065, 2003.

[83] M.C. Love. *Better takeoffs and landings*. McGraw-Hill, Massachusetts, USA, 1995.

[84] M. Marques, P. Gamboa, and E. Andrade. Design and testing of a variable camber flap for improved efficiency. In *AVT-168 Morphing Aircraft Symposium*, Évora, Portugal, 2009.

[85] B.W. McCormick. *Aerodynamics, aeronautics, and flight mechanics*. Wiley, Chichester, England, second edition, 1995.

[86] A.M.R. McGowan. Recent results from NASA's Morphing Project. In *Smart Structures and Materials 2002: Industrial and Commercial Applications of Smart Structures Technologies*, San Diego, California, 2002.

[87] A.M.R. McGowan, L.G. Horta, J.S. Harrison, and D.L. Raney. Research activities within NASA's Morphing Program. In *AVT-030 Structural Aspects of Flexible Aircraft Control*, Ottawa, Ontario, 1999.

[88] A.M.R. McGowan, D.D. Vicroy, R.C. Busan, and A.S. Hahn. Perspectives on highly adaptive or morphing aircraft. In *AVT-168 Morphing Aircraft Symposium*, Évora, Portugal, 2009.

[89] T.H.G. Megson. *Structural and stress analysis*. Elsevier Butterworth-Heinemann, London, UK, second edition, 2005.

[90] P.S. Meilinger. *Airwar: theory and practice*. Frank Cass Publishers, Abingdon, England, 2003.

[91] S. Miller and J.E. Cooper. Wing design incorporating a passive loads alleviation device. In *RAeS Aircraft Structural Design Conference*, Liverpool, UK, 2008.

[92] S. Miller and J.E. Cooper. Development of an adaptive wing tip device. In 50^{th} *AIAA/ASME/ASCE/AHS/ASC Structures, Structural Dynamics, and Materials Conference*, Palm Springs, California, 2009.

[93] S. Miller, J.E. Cooper, and G.A. Vio. Adaptive wing tip devices for gust alleviation, trim and roll control. In *AVT-168 Morphing Aircraft Symposium*, Évora, Portugal, 2009.

[94] S. Miller, V. Hodigere-Siddaramaiah, and J.E. Cooper. Morphing wings using adaptive structures. In *School and Symposium on Smart Structural Systems Technologies*, Porto, Portugal, 2010.

[95] S. Miller, V. Hodigere-Siddaramaiah, J.E. Cooper, and G.A. Vio. Control of rotating spars for an adaptive aeroelastic wing. In *AVT-168 Morphing Aircraft Symposium*, Évora, Portugal, 2009.

[96] S. Miller, G.A. Vio, J. Cooper, J. Vale, L. da Luz, A. Gomes, F. Lau, A. Suleman, L. Cavagna, and A. De Gaspari. SMorph - Smart Aircraft Morphing Technologies Project. In 51^{th} *AIAA/ASME/ASCE/AHS/ASC Structures, Structural Dynamics, and Materials Conference*, Orlando, Florida, 2010.

[97] S. Miller, G.A. Vio, and J.E. Cooper. Optimisation of a scaled sensorcraft model with passive gust alleviation. In 12^{th} *AIAA/ISSMO Multidisciplinary Analysis and Optimization Conference*, Victoria, British Columbia, 2008.

[98] M. Mitchell. *An introduction to genetic algorithms.* Cambridge, Massachusetts, USA, 1998.

[99] I. Moir and A. Seabridge. *Aircraft systems.* Wiley, Chichester, England, third edition, 2008.

[100] H.P. Monner, M. Sinapius, and S. Opitz. DLR's morphing activities within the European network. In *AVT-168 Morphing Aircraft Symposium*, Évora, Portugal, 2009.

[101] J. Moran. *An introduction to theoretical and computational aerodynamics.* Wiley, New York, USA, 1984.

[102] A. Natarajan, R.K. Kapania, and D.J. Inman. Aeroelastic optimization of adaptive bumps for yaw control. *Journal of Aircraft*, 41(1):175–185, 2004.

[103] M.C.Y. Niu. *Airframe structural design: practical design information and data on aircraft structures*. Conmilit Press, Hong Kong, 1988.

[104] J. Nocedal and S. Wright. *Numerical optimization*. Springer, New York, USA, 1999.

[105] B. Paluch and C. Toussaint. Design and testing of an aircraft active twist wing demonstrator. In *AVT-168 Morphing Aircraft Symposium*, Évora, Portugal, 2009.

[106] E. Pendleton. Back to the future. Active aeroelastic wing technology & the X-53. an approach to morphing. In *AVT-168 Morphing Aircraft Symposium*, Évora, Portugal, 2009.

[107] P. Pereira, L. Almeida, A. Suleman, V. Bond, R. Canfield, and M. Blair. Aeroelastic scaling and optimization of a joined-wing aircraft concept. In 48^{th} *AIAA/ASME/ASCE/AHS/ASC Structures, Structural Dynamics, and Materials Conference*, Honolulu, Hawaii, 2007.

[108] W.F. Phillips. *Mechanics of flight*. Wiley, New York, USA, 2004.

[109] D.S.G. Pollock. *A handbook of time-series analysis, signal processing and dynamics*. Academic Press, California, USA, 1999.

[110] K.G. Powell. *Vortical solutions of the conical Euler equations*, volume 28 of *Notes on numerical fluid mechanics*. Vieweg, Braunschweig, Germany, 1990.

[111] M.J.D. Powell. Restart procedures for the conjugate gradient method. *Mathematical Programming*, 12(1):241–254, 1977.

[112] S.G. Powers, L.D. Webb, E.L. Friend, and W.A. Lokos. Flight test results from a supercritical Mission Adaptive Wing with smooth variable camber. *NASA Technical Memorandum*, 1992.

[113] S.S. Rao. *Engineering optimization: theory and practice*. Wiley, New York, USA, 1996.

[114] S.S. Rao. *Mechanical vibrations*. Pearson Education, New Jersey, USA, fourth edition, 2004.

[115] C.C. Rasmussen, R.A. Canfield, and M. Blair. Joined-wing Sensor-Craft configuration design. *Journal of Aircraft*, 43(5):1470–1478, 2006.

[116] W.P. Rodden and E.H. Johnson. *MSC.Nastran Version 68 Aeroelastic Analysis User's Guide*. MSC.Software Corporation, Santa Ana, California, 2002.

[117] O. Samoylovitch and D. Strelets. Determination of the Oswald efficiency factor at the aeroplane design preliminary stage. *Aircraft Design*, 3(3):167–174, 2000.

[118] J.B. Samuel and D. Pines. Design and testing of a pneumatic telescopic wing for Unmanned Aerial Vehicles. *Journal of Aircraft*, 44(4):1088–1099, 2007.

[119] B. Sanders, D. Cowan, and L. Scherer. Aerodynamic performance of the Smart Wing control effectors. *Journal of Intelligent Material Systems and Structures*, 15(4):293–303, 2004.

[120] B. Sanders, F.E. Eastep, and E. Forster. Aerodynamic and aeroelastic characteristics of wings with conformal control surfaces for morphing aircraft. *Journal of Aircraft*, 40(1):94–99, 2003.

[121] J. Schweiger, A. Suleman, and J.E. Cooper. Review of the European research project 'Active Aeroelastic Aircraft Structures' with respect to future trends for morphing aircraft design. In *AVT-168 Morphing Aircraft Symposium*, Évora, Portugal, 2009.

[122] J.J. Sitz. *Aeroelastic analysis of a joined-wing SensorCraft*. PhD thesis, Air Force Institute of Technology, 2004.

[123] S.N. Sivanandam and S.N. Deepa. *Introduction to genetic algorithms*. Springer, Berlin, Germany, 2008.

[124] M.P. Snyder, B. Sanders, F.E. Eastep, and G.J. Frank. Vibration and flutter characteristics of a folding wing. *Journal of Aircraft*, 46(3):791–799, 2009.

[125] D. Soreide et al. Coherent lidar turbulence measurement for gust load alleviation. *NASA Technical Memorandum*, 1996.

[126] B. Stanford, M. Abdulrahim, R. Lind, and P. Ifju. Investigation of membrane actuation for roll control of a Micro Air Vehicle. *Journal of Aircraft*, 44(3):741–749, 2007.

[127] R. Tatham. Shear centre, flexural centre and flexural axis: an attempt to clear up current confusion and provide definitions differentiating between the three terms. *Aircraft Engineering and Aerospace Technology*, 23(7):209–210, 1951.

[128] F. Thompson and G.G. Haywood. *Structural analysis using virtual work*. Chapman and Hall, London, England, 1986.

[129] B. Tillman. *MiG Master: The story of the F-8 Crusader*. Naval Institute Press, Maryland, USA, second edition, 1990.

[130] S. Timoshenko. *Strength of materials, Part 1, Elementary Theory and Problems*. Van Nostrand Reinhold, London, England, third edition, 1955.

[131] S. Timoshenko and J. Gere. *Theory of elastic stability*. McGraw-Hill, Singapore, second edition, 1963.

[132] L.W. Traub, R. Snyder, and T. Pellino. Preliminary experimental investigation of a morphable biplane: the X-wing. *Journal of Aircraft*, 47(3):1068–1072, 2010.

[133] J. Vale, F. Lau, and A. Suleman. Design and development of strategies and structures for wing morphing. In *AVT-168 Morphing Aircraft Symposium*, Évora, Portugal, 2009.

[134] W.C.M. van Beers and J.P.C. Kleijnen. Kriging for interpolation in random simulation. *Journal of operational research society*, 54(3):255–262, 2003.

[135] R. Vos, Z. Gurdal, and M. Abdalla. Mechanism for warp-controlled twist of a morphing wing. *Journal of Aircraft*, 47(2):450–457, 2010.

[136] A.C. Walker. *Torsion*. Modular textbooks in engineering. Chatto and Windus, London, England, 1975.

[137] T.A. Weisshaar. Morphing aircraft technology - new shapes for aircraft design. In *AVT-141 Multifunctional Structures/Integration of Sensors and Antennas*, Vilnius, Lithuania, 2006.

[138] T.A. Weisshaar. Morphing aircraft symposium AVT-168 technical evaluation report. In *AVT-168 Morphing Aircraft Symposium*, Évora, Portugal, 2009.

[139] R.W. Wlezien, G.C. Horner, A.M.R. McGowan, S.L. Padula, M.A. Scott, R.J. Silcox, and J.O. Simpson. The aircraft Morphing Program. In 39^{th} *AIAA/ASME/ASCE/AHS/ASC Structures, Structural Dynamics & Materials Conference and AIAA/ASME/AHS Adaptive Structures Forum*, Long Beach, California, 1998.

[140] C. Wong and K. Kontis. Flow control by spanwise blowing on a NACA 0012. *Journal of Aircraft*, 44(1):338–340, 2007.

[141] J. Wright and J. Cooper. *Introduction to aircraft aeroelasticity and loads*. Wiley, Chichester, England, 2007.

[142] Z. You, J. Crabtree, and G. Lederman. Large-scale shape change in aircraft wings. In *AVT-168 Morphing Aircraft Symposium*, Évora, Portugal, 2009.

[143] M. Zyczkowski et al. *Strength of structural elements*. PWN, Warsaw, Poland, 1991.

Additional sources of information

[144] G. Alexander, A. Brown, D. Jackson, J. Scott, M. Swanson, A. Vander-Wyst, M. Walker, J. Whitman, and J. Yoon. Mikoyan Gurevich MiG-23, [Accessed: October 2009]. Available from http://www.aerospaceweb.org/-aircraft/fighter/mig23/.

[145] No author given. 787 landing gear test and new 787 order coming soon?, [Accessed: July 2010]. Available from http://nyc787.blogspot.com/search-/label/787-10.

[146] No author given. A modified F/A-18A undergoes wing torsion testing in the Flight Dynamics Laboratory at NASA's Dryden Flight Research Center, Edwards, California, [Accessed: July 2010]. Available from http://www.-dfrc.nasa.gov/gallery/photo/AAW/Small/EC01-0112-2.jpg.

[147] No author given. Aircraft of World War II - Warbird Forums, [Accessed: October 2008]. Available from http://www.ww2aircraft.net/forum/other-mechanical-systems-tech/makhonine-telescoping-wing-8527.html.

[148] No author given. BellBoeing V-22 Osprey, [Accessed: July 2010]. Available from http://www.military-today.com/helicopters/bellboeing_v_22_-osprey.htm.

[149] No author given. Concorde technical specs: droop nose system, [Accessed: July 2010]. Available from http://www.concordesst.com/nose.html.

[150] No author given. RQ-4 Global Hawk, [Accessed: September 2008]. Available from http://www.globalaircraft.org/planes/rq-4_global_hawk.pl.

[151] No author given. RQ-4A/B Global Hawk high-altitude, long endurance, unmanned reconnaissance aircraft, USA, [Accessed: September 2008]. Available from www.airforce-technology.com/projects/global.

[152] No author given. SensorCraft, [Accessed: September 2008]. Available from www.spyflight.co.uk/sensorcraft.htm.

[153] No author given. The Shuttleworth Collection - Military Pageant air display: Hawker Siddeley Harrier GR7, [Accessed: July 2010]. Available from http://www.airmuseumsuk.org/a% -irshow/2004/Shut040801/8-00/pages/056%20Hawker%20Siddeley% -%20Harrier%20GR%207%20ZD-347%20No4%20Sqn%20RAF.htm.

[154] No author given. Strange vehicles: Canadair CL-84 Dynavert, [Accessed: July 2010]. Available from http://www.diseno-art.com/encyclopedia/strange_vehicles/canadair_cl-84_dynavert.html.

[155] No author given. Variable-sweep wings, [Accessed: October 2008]. Available from http://www.century-of-flight.net/Aviation%20history/evolution%20of%20technology/Variable-Sweep%20Wings.htm.

[156] R. Bray. Supersize wings. *Ingenia Online*, (31), 2007.

[157] P. Emanuele et al. Lockheed F-104 Starfighter, [Accessed: October 2008]. Available from http://www.flightlevel350.com/Lockheed_F-104_aircraft_facts.html.

[158] E. Gilles. Aeroelasticity 4 course notes. University of Glasgow, 2005.

[159] E. Gilles. Aeroelasticity 5 course notes. University of Glasgow, 2005.

[160] R.B. Green. High-speed aerodynamics 4 course notes. University of Glasgow, 2005.

[161] S. Maksim. Nikitin-Shevchenko IS-1, [Accessed: October 2008]. Available from http://www.aviastar.org/air/russia/nikitin_is-1.php.

[162] S. Maksim. Westland Pterodactyl IV, [Accessed: October 2008]. Available from http://www.aviastar.org/air/england/west_pterodactyl4.php.

[163] A. Malhão. Portuguese Lockheed L-1011 TriStar, [Accessed: September 2008]. Available from http://www.tristar500.net/features.htm.

[164] Mathworks. MATLAB® ode functions documentation, [Accessed: September 2008]. Available from http://www.mathworks.com/help/techdoc/ref/-ode23tb.html.

[165] T. Melin. Home page of the tornado vlm project, [Accessed: July 2008]. Available from http://www.redhammer.se/tornado/DL.html.

[166] S. Miller, V. Hodigere-Siddaramaiah, G.A. Vio, and J.E. Cooper. Use of rotating spars for an adaptive aeroelastic wing. *Submitted to Journal of Aircraft*, 2010.

[167] S. Miller, G.A. Vio, and J.E. Cooper. Gust load alleviation using a wing tip device. *Submitted to Journal of Aircraft*, 2010.

[168] A. Savine. RK, LIG-7 by G.I. Bakshaev, [Accessed: October 2008]. Available from http://ram-home.com/ram-old/rk.html.

[169] D. Senda. French Swinger: Dassault Mirage G, [Accessed: October 2008]. Available from http://home.earthlink.net/~p51ace/swingwing/miragեg.html.

[170] J. Wagner. Lockheed F-104 Starfighter, [Accessed: October 2008]. Available from http://http://www.military.cz/usa/air/post_war-/f104/pics/pics_en.htm.